Solid-state lasers with joule-level pulse energies and kilowatt average powers for industrial applications

Michael Jon Poulter

Institute of Photonics
University of Strathclyde
Wolfson Centre
106 Rottenrow
Glasgow G4 0NW
United Kingdom

February 2011

A thesis presented in fulfilment of the requirements for the degree of Doctor of Engineering

For my family and in memory of my father

Copyright statement

Signed: Date:

Abstract

The work presented in this thesis is concerned with the development of commercial Nd:YAG laser systems for a number of specific industrial applications. Common to all of these applications is the need to scale toward joule-level pulse energies for adequate light-matter interaction. These applications are unusual in that they also require kilohertz pulse-repetition-frequencies and therefore kilowatt average powers to enable commercially viable levels of yield and throughput. This thesis begins by defining the specific requirements for each of the target applications.

Laser system development begins with the design and characterisation of a laser gain-module, which is continuously-pumped using high-power diode lasers. A number of new and existing engineering design principles are then combined for the optimisation of nanosecond pulse, multi-spatial-mode standing-wave resonators. Pulsing at kilohertz repetition frequency is achieved by acousto-optical Q-switching. A suite of complementary mathematical models is presented that facilitates the design of laser resonators with industrially robust performance. Power-scaling at the fundamental wavelength of 1.064 μm is achieved by implementing a number of master-oscillator power-amplifier arrangements. This leads to average powers of around 1600 W at pulse-repetition-frequencies up to 20 kHz. The industrial laser systems developed produce maximum pulse energies of 0.32 J with 18 ns pulse durations, resulting in peak powers in excess of 18 MW. Unprecedented combinations of pulse energy and average power have also been achieved using intra-cavity second harmonic generation. 520 W average power has been demonstrated at 0.532 μm wavelength with similar pulse durations and repetition frequencies.

Acknowledgments

I think it is only right and proper that I first acknowledge the people who directly helped me throughout my doctorate. For this, my thanks go to Prof. Andy Harvey and his staff at Heriot-Watt University, without whom I would have struggled to stay on course. Particular recognition goes to my academic supervisor Dr. David Burns at the Institute of Photonics, University of Strathclyde. David has supported my research every step of the way and I hold him in the highest regard both as a mentor and friend.

I would like to extend a special thank you to my industrial supervisor Dr. Nick Hay who continued to support me and my work even when his obligation to do so ran out. Nick's professionalism and abilities in laser design are only surpassed by his unfeasibly kind nature and capacity to endure my not-so-witty banter. Thanks Nick!

There are a number of colleagues that I would also like to recognise for their input to this work. I'd like to thank Ben Fulford for his help with data collection and Mike Mason for the informed discussions on laser physics.

I am eternally grateful to my wonderful wife Karen for staying with me over the course of my doctorate and to my son James for letting Daddy have enough sleep to cope. This work is for you.

Lastly, I would like to thank my parents. None of this would have been possible without my mother's relentless drive to provide me with the confidence to succeed and my father's unwavering encouragement… I like to think that I would have made him proud.

Michael Poulter

Contents

1 Introduction

In 1958 Schawlow and Townes [1.1] introduced the laser as a concept by proposing a method for generating 'extremely monochromatic and coherent light'. The suggested scheme was an extension of a technique used for the amplification of microwave radiation that exploited stimulated emission, a quantum mechanical process that had been postulated by Einstein [1.2] over 40 years prior. The first practical demonstration of a laser closely followed in 1960 when Maiman [1.3] used a sample of ruby to create a source of bright coherent light. Today, lasers can be made to exhibit greatly varying degrees of brightness and coherence, making them ideal instruments for countless forms of measurement, communication and light-matter interaction. As such, lasers have enabled an astounding range of technologies and are now found in prolific use throughout scientific research, military, medical, and industrial applications.

Since its introduction, laser technology has diverged to produce two extremes in output characteristics. At one extreme, low power lasers (typically less than 1 W) have been developed to produce highly specialised optical properties for use in such applications as metrology, communication and imaging [1.4; 1.5]. These lasers tend to have excellent beam quality with high levels of temporal and spatial coherence, often operating on a single longitudinal mode. At the other extreme, ultra-high power lasers have been designed to generate pulses with petawatt (10^{15} W) peak powers for the investigation of fundamental physical phenomena, such as atomic fusion [1.6; 1.7]. These lasers usually exist

as national facilities and are sizeable enough to occupy entire buildings. Bridging these two extremes of operation are a multitude of lasers that exhibit powers suitable for more general light-matter interaction. These lasers have not only enabled the development of many new applications, but are also rapidly replacing traditional methods by providing faster, cleaner, less expensive and more reliable solutions.

There are two fundamental objectives associated with the development of a laser device. The first is to create an output that satisfies the process requirements for the intended application. This is often regarded as the critical objective for laser design. The second objective is to optimise the overall performance of the laser as a system. This leads to the contemplation of more general engineering characteristics such as size, control, reliability, reproducibility, serviceability and overall cost of ownership. Performance at the system level can have a significant effect on the success of a final design but is often less considered as part of laser development. The relative importance of the system design attributes depends on the application and intended field of use. For example, a high performance laser developed for use in frontier research may not be expected to comply with the stringent levels of reliability associated with a medical application, or the durability stipulated by a military standard. It is also not likely to be subjected to the cost-of-ownership targets demanded by industrial volume manufacturers.

The aim of the work presented in this thesis was to produce new engineering design principles for the development of higher power industrial solid-state laser systems. These principles have been specifically formulated for the optimisation of neodymium-doped yttrium aluminium garnet ($Nd^{3+}:Y_3Al_5O_{12}$ or Nd:YAG) lasers and their components to enable a number of specific applications. However, they can also be applied to the development of high-power solid-state lasers in general.

1.1 Industrial lasers and applications

High power solid-state laser technology has experienced particularly healthy growth in recent years. This has been largely due to the introduction of new manufacturing techniques and the evolution of more robust, increasingly cost effective high-power laser-diode pump sources. Higher power solid-state laser systems have enabled a variety of new industrial processes and are now competing for existing applications conventionally serviced by other laser types, particularly gas lasers. By far the most prevalent use for which is industrial materials processing, this includes marking, etching, cutting, machining, welding and surface treatment [1.8; 1.9]. In contrast, the new generation of solid-state lasers demonstrate higher efficiency, increased reliability and smaller physical footprint, whilst generally requiring less maintenance.

A number of specific industrial applications have emerged that require high-power pulsed operation at near-infrared and green wavelengths. It was suggested that the requirements for these applications can be satisfied using a common fundamental and corresponding second harmonic wavelength of the Nd:YAG laser. Before developing these lasers it was important to properly define the desired optical output and system performance requirements. These requirements are governed by the specific process conditions for the target applications, which are discussed in the following sections.

1.1.1 Plasma display panel production: Rapid laser patterning by projection etching

The conventional method for patterning in visibly transparent, electrically conductive thin-films on glass for plasma display panel (PDP) production typically consists of six stages [1.10; 1.11]. Initially, the conductive film, typically Indium Tin Oxide (ITO), is spin-coated with a photoresist. Selective exposure of the resist is then carried out using a photolithographic technique by which an image of the desired pixel electrode matrix, illuminated by a UV source, is

projected onto the panel. Structuring in the photoresist is then carried out using a wet chemical etch followed by a second chemical etch for patterning in the ITO layer. The photoresist is then stripped in an ashing process before the panel is finally cleaned. As an industrial procedure this multi-stage fabrication method is considered to be both time-consuming and expensive. Capital costs for the latest wet-etch process stations are reported to be in excess of $12M increasing to $120M over 3 years with the addition of consumable chemical and mask-set expenditure [1.12].

An alternative technique has however been demonstrated that uses high-power lasers in a single step process to directly ablate and therefore selectively remove small areas of ITO, without damaging the glass substrate below. Takai [1.13] and Venkat [1.14] discuss the laser source requirements for this process and highlight the particular efficacy of nanosecond-pulse solid-state lasers operating around 1 μm wavelength. This is primarily due to the fact that ITO exhibits strong absorption at the near-infrared, whilst the glass substrate remains largely transparent. In contrast to the wet-etch process, future rapid laser patterning (RLP) machine tools capable of similar 'takt' times are estimated to cost under $30M over the same 3 year period [1.12].

The first stage of the RLP process involves the uniform illumination of a single pixel mask (see figure 1.1). At this point the process beam is spatially homogenised using a cylindrical micro-lens array, which can also reshape the beam in order maximise transmission though the typically square shaped pixel mask. This can also be achieved by delivering the beam through recently developed highly multimode square-form optic fibres.

For the second stage, a de-magnified image of the illuminated mask is projected onto the ITO film, at which ablation occurs with the arrival of individual laser pulses. The image is then rapidly scanned across the display panel in order to generate the required pixel electrode matrix. To obtain suitably homogenous illumination at the mask it is advantageous to start with a low beam quality.

However, a laser output of no more than 25 - 30 times diffraction limited has been suggested to satisfy the brightness requirements and corresponding numerical aperture constraints imposed by the conventionally used imaging systems [1.14].

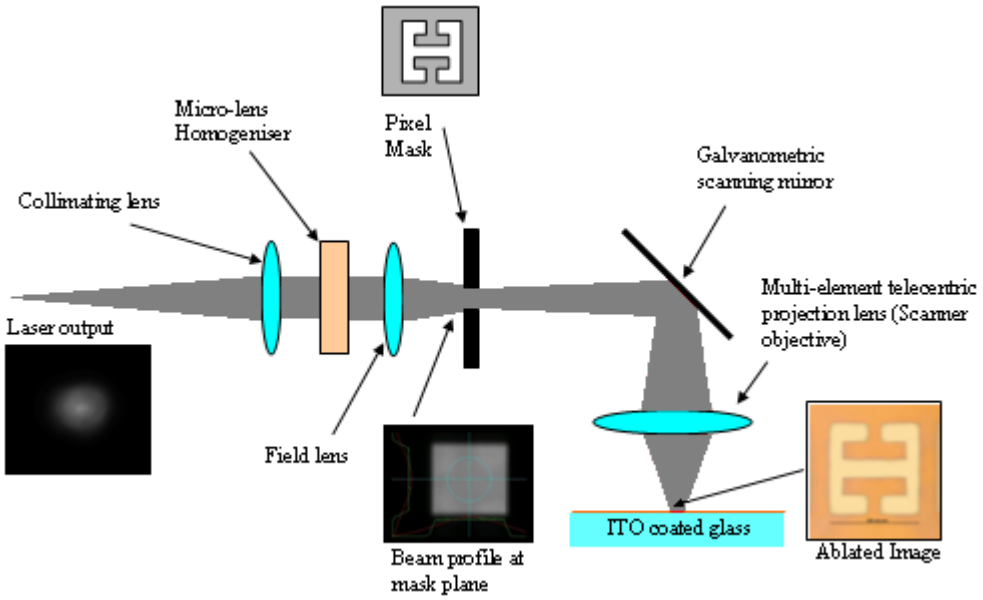

Figure 1.1 Schematic of the beam delivery optics used for rapid laser patterning (RLP).

The process parameters for the ablation of ITO vary as a function of film thickness. RLP, recently qualified at 1 μm wavelength and 35 ns pulse duration, requires minimum energy densities of 2.8 – 5.0 J.cm^{-2} for the adequate removal of a typical 100 - 200 nm thick layer of ITO [1.15; 1.16]. In order to produce desired pixel sizes of around 1 mm^2, pulse energies of up to 0.05 J are therefore required.

In 2006 this process was demonstrated using a state-of-the-art industrial Nd:YAG laser operating at 1.064 μm fundamental wavelength [1.15]. The laser was capable of delivering 0.05 J pulses at 6 kHz pulse repetition frequency (PRF), generating 300 W average power. This allowed for a patterning rate of 360,000 pixels per minute, which is considered too slow to enable RLP to compete with the traditional wet etch method. In order to increase process

throughput the laser would need to deliver 0.05 J pulses at a higher PRF. This leads to a direct scaling in the average power requirement. At 600 W average power and 12 kHz PRF the patterning rate would increase to 720,000 pixels per minute. Additional scaling to 800 W average power and 16 kHz would further increase the patterning rate to 960,000 pixels per minute, nearly 3 times faster than previously achievable. To meet a target process time of less than 100 seconds for a 2160 x 2460 mm 'generation 7' mother panel (producing multiple 42" displays), it follows that the simultaneous operation of 8 x 600 W or 6 x 800 W lasers would be required for each production line. Further scaling to 1.6 kW average laser power at 16 kHz PRF, providing 0.1 J pulses, would reduce the number of required laser systems to only 3 by equally splitting the output of each to provide the same result.

For volume production, it is important that the laser can deliver repeatable pulses for consistent ITO removal. The RLP process requires a statistical pulse to pulse energy variation of less than 3% to 1 standard deviation. High volume manufacturers of PDP displays also demand reliable, continuous (24/7) operation at a guaranteed laser performance for a minimum of 15,000 hours.

1.1.2 Extreme ultraviolet lithography: Laser produced plasma

To manufacture faster, higher performance microprocessors it is necessary to increase the number of active devices on a given integrated circuit. The demand for higher transistor densities leads to the need for smaller feature sizes, which are now in the region of tens of nanometers. This removes the feasibility of a direct write approach and necessitates the continued refinement of the existing step and repeat photolithographic method. This method is similar, although more complex, to the wet-etch technique described in section 1.1.1. Inevitably, the smallest achievable feature size using this method is limited by the diffraction effects induced at the lithographic mask. These effects are in turn largely governed by the properties of the light used for illumination, which is

conventionally provided by a rare-gas halide (excimer) laser. The source currently favoured for the production of latest generation microprocessors is the argon fluoride (ArF) laser, which generates a wavelength of 0.193 μm. However, theory dictates that to limit the extent of diffraction and fabricate smaller features, a reduction in the wavelength of the illuminating radiation is required.

The leading candidate for a scaleable route to next generation feature sizes of 32 nm and below is the production of 13.5 nm extreme ultraviolet (EUV) light from re-radiating plasma. It is widely accepted that the critical challenge presented by this approach is the creation of sufficient in-band EUV radiation from suitable target materials such as Xenon (Xe) or Tin (Sn) (see figure 1.2). The achievable wafer throughput of an exposure tool is directly related to the power that it generates. For high volume manufacturing, the requirement for useable in-band EUV powers of up to 115 W have been suggested [1.17].

In reality there are various methods of generating plasma for the production of EUV radiation [1.18], the most prominent of which include the synchrotron wiggler, gas discharge (including the Z-pinch, plasma focus and capillary discharge) and the laser produced plasma (LPP). The generation of EUV radiation by LPP has several reported advantages over the other methods. These include; low debris production, power stability, construction flexibility, minimal heat loading and larger un-obscured solid angles of emission for efficient collection. Although not without its challenges, it is hoped that LPP will enable an increase in attainable EUV power and processed wafer throughput, whilst maintaining a relatively low cost of ownership.

The overall construction of an LPP exposure tool is beyond the scope of this thesis. However, one key element to consider is the design of the high power laser driver that is required. S. Ellwi et al [1.20] describe the optimum parameters required for such a driver, relating each to the background plasma physics involved.

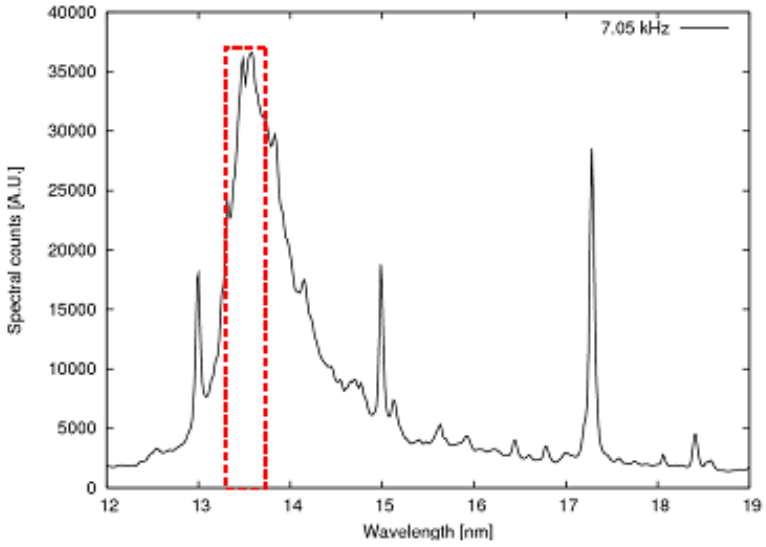

Figure 1.2 Typical EUV emission spectrum of Tin (Sn) when used as a target for LPP. The useful in-band region is outlined in red [1.19].

Fundamentally, the laser driver should enable optically thick plasma to be formed and then maintained at the correct temperature for efficient conversion to EUV, near the Plank limit. This temperature is typically in the region of 30 eV (approximately 350,000 K). The resultant focussed intensity required from the laser driver is therefore calculated to be around 10^{11} W.cm^{-2}. To ensure efficient EUV conversion, as well as reaching the correct temperature, it is also important to maintain it for an optimum length of time. This means that it is necessary to optimise the duration of the pulse delivered by the laser driver. For EUV conversion to occur, the pulse length must be long enough to exceed the relaxation timescale associated with ionisation equilibrium. Having initially produced interaction free electrons via high-field ionisation, the laser energy is transferred to the target material by collisional absorption. Only then is energy transferred to the ions via inelastic collisions and a steady state of ionisation achieved. For the temperatures involved here, this corresponds to $\sim$ 0.5 ns [1.21]. In addition to this, the duration of the driver pulse must also exceed the time taken for the expanding plasma to become optically thick to its own emitted radiation. For a typical xenon target that produces a 10 μm plasma

layer, it can be shown that the time taken for the expanding plasma to become optically thick to its own emitted radiation is ~ 1ns [1.22]. This sets a lower limit on the laser pulse duration for EUV emission to occur.

The upper limit for the duration of the driver pulse is governed by the finite lifetime t_{max} of the optically thick, critically dense plasma. Loss of critical density due to hydrodynamic expansion is related to the initial diameter of the target d_t, the critical electron density n_{cr}, the electron density of the unperturbed plasma n_{e0}, and the plasma sound speed c_s. The plasma lifetime can be estimated as

$$t_{\max} \approx \frac{d_t}{c_s}\left(\frac{n_{e0}}{n_{cr}}\right)^{1/3} \tag{1.1}$$

For example, under these conditions, a high-density xenon filament target with a diameter in the order of 50 μm will form optically thick plasma with a lifetime $t_{max} \sim 15$ ns [1.20], after which EUV will no longer be efficiently generated. Therefore, to satisfy the criteria for EUV conversion of typical target sizes of 50 - 100 μm, a high-power laser driver should be able to provide pulses of around 15 - 30 ns duration at pulse energies sufficient to generate an irradiance of at least 10^{11} W.cm^{-2}. For a 100 μm diameter target it follows that 30 ns pulses with energies in excess of 0.2 J are required.

The efficiency of conversion to EUV is dependent on the ion density generated and the wavelength of the laser driver used. For typical densities of $\sim 1 \times 10^{19}$ cm^{-3} the conversion efficiency is seen to drop at driver wavelengths below 1 μm [1.23]. There is however only a weak dependence of conversion efficiency on wavelength above 1 μm, which is typically less than only 1 % after collection. Therefore, for a 115 W production source it is projected that a laser driver would need to deliver between 15 - 20 kW average power to the target [1.20]. The total deliverable power for driving the LPP process can be scaled by multiplexing a number of individual laser beams onto the same target. However, the total number of laser systems should be kept to a minimum to avoid cost and space restrictions.

Of the industrial laser technologies considered for driving the LPP process, there are two most likely to be able to meet the wavelength and average power requirements. These are carbon dioxide (CO_2) lasers, operating on the 10.6 μm molecular transition, and Nd:YAG lasers emitting at the 1.064 μm fundamental. Industrial standard CO_2 lasers are historically used in continuous wave (CW) operation and are capable of producing average powers in excess of 10 kW. However, this drops considerably when they are converted for pulsed operation. Nanosecond-pulse CO_2 laser systems are available at 2 – 3 kW average powers but have, until recently [1.24], been limited to a few hundred hertz PRF. For continuous lithographic exposure, pulse repetition frequencies of greater than 6 kHz have been suggested [1.25].

As capital costs for these lasers systems become increasingly competitive, a number of important advantages have been suggested in favour of using solid-state lasers over CO_2 for LPP. Nd:YAG lasers can be easily adapted for operation at kilohertz PRF and have been shown to function more efficiently in this regime. This combined with generally lower service and maintenance outlay may also give the solid-state laser a cost of ownership advantage. Of greater importance however is the temporal pulse shape. The pulse generated by a CO_2 laser typically exists as a spike on top of a sizeable pedestal, which can be several hundred nanoseconds in duration [1.24; 1.25]. This essentially constitutes wasted energy in the LLP process and can have a significant impact on the conversion efficiency to EUV.

The Nd:YAG laser also has an advantage with respect to focusability. For the same beam quality and effective apertures an Nd:YAG laser, operating at 1 μm wavelength, can generate the same beam waist size as that of a CO_2 laser when using a focusing optic with ~ 10 times longer focal length. This can provide valuable space for multiplexing a number of beams to target and aid in the collection of the in-band EUV generated. Alternatively, concession of lower Nd:YAG beam qualities can lead to further scalability in laser output power. However, to maintain sufficient focusability, it has been suggested that the

quality of an Nd:YAG laser beam should be no more than 10 - 15 times diffraction limited [1.26].

For this application the objective is to generate a scaleable industrial Nd:YAG laser design capable of satisfying the requirements for a production standard EUV exposure tool. Desired pulse energies of at least 0.2 J operating at > 6 kHz PRF result in a minimum average power requirement of 1.2 kW. Prototype exposure tools are currently planned that need multiple lasers, each operating at 1.5 kW average powers initially, with the intension of scaling to 3 kW and beyond.

1.1.3 Industrial micromachining: The laser micro-jet

The micro-jet is a technique used in laser materials processing to effectively extend the depth of a focused laser beam by waveguiding in a filament water-jet. For this application the output from a high-power laser is coupled into water-jets with diameters of 30 - 150 μm [1.27]. It is well known that water exhibits a window in absorption centred at approximately 0.5 μm wavelength, which is suited to the output from an Nd:YAG laser operating at a common second harmonic (0.532 μm). As the refractive index of water is larger than that of air and the diameter of the jet is large compared to the laser wavelength the water-jet acts as a cylindrical waveguide that is analogous to a highly multi-mode step-index fibre. Using water-jets for the delivery of high-power laser light not only effectively extends the depth of focus but can also eliminate recast, remove process debris and reduce the heat-affected zone (HAZ) that inevitably occurs near the kerf of laser cut material. The laser micro-jet has been successfully employed for a multitude of micromachining applications including the cutting and scribing of silicon, polycrystalline diamond and copper.

The micro-jet head consists of a water chamber that is accesses by the focused laser beam through an anti-reflection coated quartz window, as illustrated in figure 1.3. Specially designed, laser-light resistant sapphire nozzles are used to

reduce destabilisation of the coaxially generated water-jet. Input water pressures of 50 - 500 bar are used to produce jet speeds of 50 – 420 $m.s^{-1}$. Purified, de-ionised and de-gassed water is used and re-cycled in order to minimise light absorption and decrease the likelihood of laser-induced water-jet breakdown [1.28]. At 0.532 µm wavelength the purified water jet has an absorption coefficient of $\sim 4.3 \times 10^{-4}$ cm^{-1}. This enables the laser light to be guided along lengths of up to 15 cm before jet integrity is lost, depending on the jet diameter and water pressure.

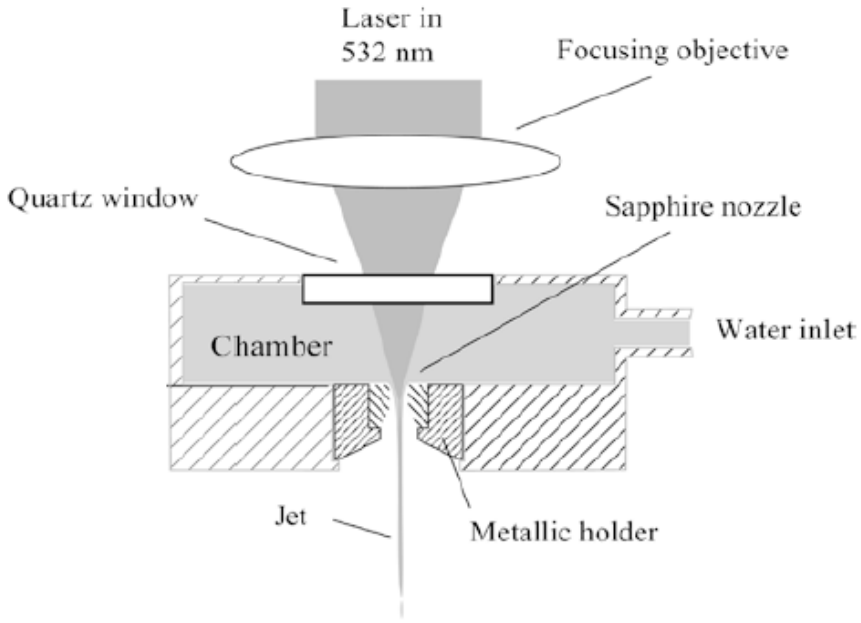

Figure 1.3 Cross-sectional view of the coupling head geometry for the laser micro-jet [1.27].

The laser source requirements for water-jet-guided micromachining applications are determined by the absorption characteristics of both the water and process substrate. Process irradiance requirements of 100 - 500 $MW.cm^{-2}$ have been reported with optimum pulse durations in the order of 150 ns [1.29]. However, at these irradiance levels non-linear effects can begin to cause major losses in the water-jet. Of particular significance is the abundant formation of red light at around 0.653 µm wavelength. It is believed

that this light is a result of stimulated Raman scattering (SRS) that is enhanced by morphology dependent resonances in the water-jet. Up to 30 % loss of transmitted power due to SRS has been observed over 8 cm interaction lengths for irradiances of ~ 400 $MW.cm^{-2}$. This effectively sets an upper limit on the amount of light that can be usefully coupled to the work piece. For the largest jet diameters of 150 µm, the imposed operating limits lead to working pulse energy requirements of 3 - 10 mJ. Although these levels of pulse energy can be easily generated using a frequency doubled Nd:YAG laser the throughput requirements for many micromachining applications dictate higher repetition frequencies than are naturally exhibited by these sources. For effective processing and desired scan speeds of around 200 $mm.s^{-1}$ the optimum PRF is in the range of 20 - 50 kHz. The corresponding average power requirements are therefore in the order of 60 - 200 W at 20 kHz, 90 - 300 W at 30 kHz and 150 - 500 W at 50 kHz.

The desired laser beam quality is determined by the numerical aperture requirements for coupling onto the smallest diameter water-jets. Low Fresnel-number, aberration-corrected lenses can be used to create sub-50 µm focus diameters and suitable numerical apertures with laser beams that are less than 40 times diffraction limited. However, this corresponds to a requirement of less than 25 times diffraction limited at the laser output if the beam is delivered to the micro-jet head via a 200 µm core diameter, 10 m long optic fibre of known optical aberration.

1.1.4 Liquid crystal display panel production: Low temperature poly-silicon annealing

The annealing of amorphous silicon (Si) to a poly-crystalline state (p-Si) has a well documented effect on increasing charge carrier mobility. This presents great potential benefits for applications that use large area electronics, such as solar-cells and flat panel displays.

Active-matrix liquid-crystal displays (AMLCD) contain a glass back-plate onto which a thin-film transistor (TFT) matrix is fabricated for addressing and switching pixels or sub-pixels. The TFT gate is created in a layer of silicon chemically deposited onto the back-plate with a thickness of 50 – 200 nm. Historically, this technique has been confined to the use of amorphous silicon as the conventional methods for crystallisation involve heating to temperatures high enough to also melt the glass substrate (600 - 1000 °C). However, in the late 1980's a technique was presented for fabricating poly-silicon TFTs at low substrate temperatures [1.30]. This technique used an excimer gas laser (xenon chloride, XeCl) operating at 0.308 μm wavelength to locally heat the surface of the amorphous silicon. The crystallisation process relies on the controlled delivery of energy over a short length of time such that the melt only just propagates to the glass-film interface leaving a number of small, solid grains for crystal seeding. This process, called super lateral growth, is used to prevent random spontaneous nucleation in the cooling silicon, thus allowing the formation of larger crystal grains and increased charge carrier mobility.

Laser crystallisation of silicon films by excimer laser annealing has since developed. The technique now uses complex optical systems to create line-beams below which the silicon layer is translated for the uniform treatment of large surface areas [1.31]. This process of sequential lateral solidification (SLS) allows controlled horizontal crystal growth from a full melt that is seeded by the previously solidified material, as illustrated in figure 1.4. The result is a further increase in crystal grain size, electron mobility and yield [1.32].

Low temperature poly-silicon annealing by SLS has enabled the production of smaller and faster switching TFTs, providing liquid crystal displays with design flexibility, improved aperture ratios and greater pixel densities. Moreover, the ability to fabricate fast TFTs has raised the possibility of a 'system on glass' approach to display manufacturing whereby the control electronics are also incorporated into the glass panel.

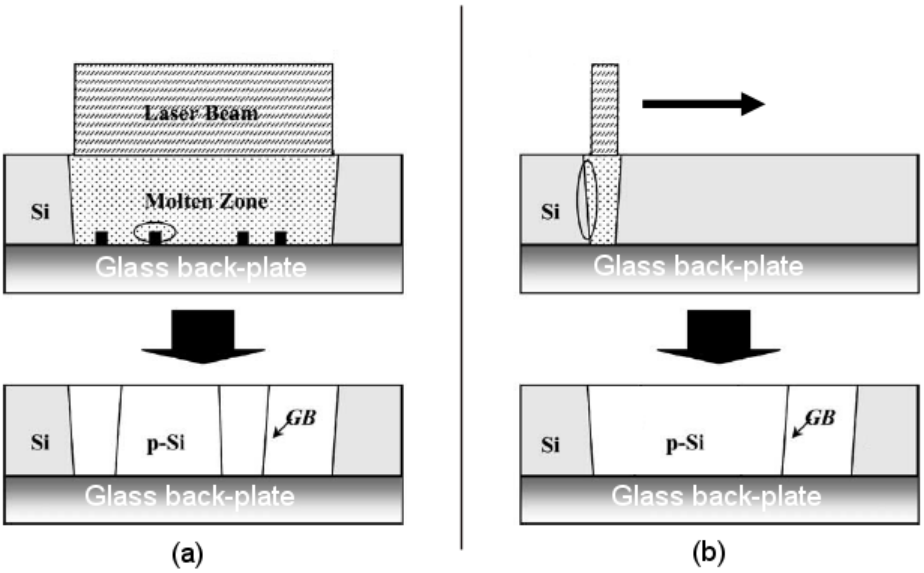

Figure 1.4 An illustration of the reduction in the number of grain-boundaries (GB) observed for laser crystallisation with (a) super lateral growth and (b) sequential lateral solidification [1.33].

There is however a number of limitations associated with excimer laser annealing for AMLCD fabrication. Productivity is restricted by slow process throughput due to the low PRF and significant service requirements that are features of the excimer source. There are also issues with consistency due to a narrow process window at ultraviolet wavelengths. Consequently, yield in the production of larger panels is hindered by the variability in the process between multiple passes of the laser light. As a result, the implementation of poly-silicon TFT panels has been confined to smaller, high performance displays.

As other viable industrial laser sources have developed, the search for a scaleable solution for low temperature poly-silicon annealing was extended to the visible green wavelengths at which larger process windows have been observed. In 1998, laser crystallisation was demonstrated using a 50 W CW copper vapour laser operating at 0.511 or 0.578 μm wavelength [1.34]. This was followed in 2000 by the implementation of a pulsed Argon ion (Ar^+) laser with 10 W average power, emitting at 0.514 μm [1.35]. However, to produce longer line beams and reduce the number of passes needed for the treatment of larger panels, much higher average powers were required. In recent years, output

powers generated by solid-state lasers operating at second harmonic wavelengths of around 0.5 μm have surpassed the levels attainable by the incumbent technologies.

The process requirements for annealing using these lasers have been theoretically modelled [1.36]. In this case the model assumes one-dimensional non-linear heat conduction in the silicon film, described as

$$C(T)\rho\frac{\partial T}{\partial t} = \frac{\partial}{\partial x}\left[K(T)\frac{\partial T}{\partial x}\right] + S(x,t) \tag{1.2}$$

where $C(T)$, $K(T)$ and ρ are the specific heat, thermal conductivity and density values for amorphous silicon respectively. The temperature $T(x, t)$ varies with depth into the silicon film x and time t. $S(x, t) = S(x).S(t)$ represents the energy imparted by a laser pulse, which is assumed to have a Gaussian temporal shape delivering energy with a time dependent component of the form

$$S(t) = \frac{1}{\Gamma\sqrt{\pi}}\exp\left[-\frac{t-t'}{\Gamma}\right]^2 \tag{1.3}$$

where Γ is the 1/e full-width half-maximum duration of the laser pulse and t' is the time at which the pulse reaches maximum irradiance. In the x dimension

$$S(x) = I_0(1-R_0)\alpha\exp[-\alpha.x] \tag{1.4}$$

where I_0 is the irradiance of the incident laser beam, R_0 is the reflectivity at the film interface and α is the absorption coefficient of amorphous silicon. R_0 and α vary between the solid and liquid states. A time dependant temperature profile of the thin-film can be generated by finding a solution for $T(x, t)$. This can be done by dividing the heated region into small equal sections of length Δx and applying boundary conditions associated with the process beginning at 300 K. From this it is possible to calculate the depth at which a given laser pulse will raise the amorphous silicon to a temperature above its melting point (around 1420 K). This simulation suggests that 10 ns pulses with energy densities of ~ 0.2 J.cm^{-2} are suitable for melting the surface of amorphous silicon, increasing

to > 0.8 J.cm^{-2} for the full liquefaction of a 200 nm thick layer. Preliminary experimentation using frequency doubled solid-state lasers has confirmed the need for this level of energy density with results of approximately 0.4 J.cm^{-2} reported for the crystallisation of a thinner 150 nm film [1.37].

Line-beam generating optics have now been developed for annealing with frequency doubled solid-state lasers, which have longer coherence lengths than the conventionally used excimer sources [1.38]. A typical 100 mm x 40 μm line requires laser pulse energies of ~ 0.025 J to obtain a minimum energy density of 0.4 J.cm^{-2} and ~ 0.05 J for the 0.8 J.cm^{-2} needed for the thicker films. These figures account for loss at the elements of the line generating optics, which can be as much as 35 %. Kilohertz pulse repetition frequencies have also been suggested in order to achieve adequately productive scan speeds [1.39].

It is now considered that the most significant attribute of a laser used for industrial poly-silicon annealing is pulse repeatability, followed by repetition frequency, pulse energy and pulse duration [1.33]. That is, the most critical parameters for LTPS are those which will ensure a high yield and a fast process rate. Although larger process windows are observed at ~ 0.5 μm wavelength, pulse to pulse consistency is still considered to be the most important parameter with the annealing process requiring less than 2 % variation in pulse energy, to 1 standard deviation. For larger line-beams and faster scan speeds the pulse energy and repetition frequency must be further scaled. AMLCD manufacturers have now tasked laser designers with preliminary targets of 600 W average power at pulse repetition frequencies greater than 5 kHz and pulse durations in the range of 10 - 200 ns.

The primary challenge for this application is to control the annealing process so that homogenous crystallisation across a substrate is ensured, while providing the high throughput and low operational costs required for effective industrial application. Requirements for high levels of laser system repeatability and reliability are therefore implicit.

1.2 State-of-the-art

Figure 1.5 illustrates the state-of-the-art at the beginning of this research in 2006 for commercially available high-power nanosecond-pulse, solid-state lasers operating at ~ 1 µm wavelength. All of the industrial lasers shown are multi-spatial-mode in operation (not diffraction limited). The data gathered includes performances for a number of solid-state laser schemes with a variety of gain-media types, gain-media geometries and pump configurations. With the exception of a small number of new ytterbium-doped glass (Yb^{3+}:glass) fibre lasers, the schemes that closest met the target application requirements were based on Nd:YAG rod arrangements. For operation at the highest powers, the Nd:YAG rods were either side or end pumped using aluminium gallium arsenide (AlGaAs) laser diodes.

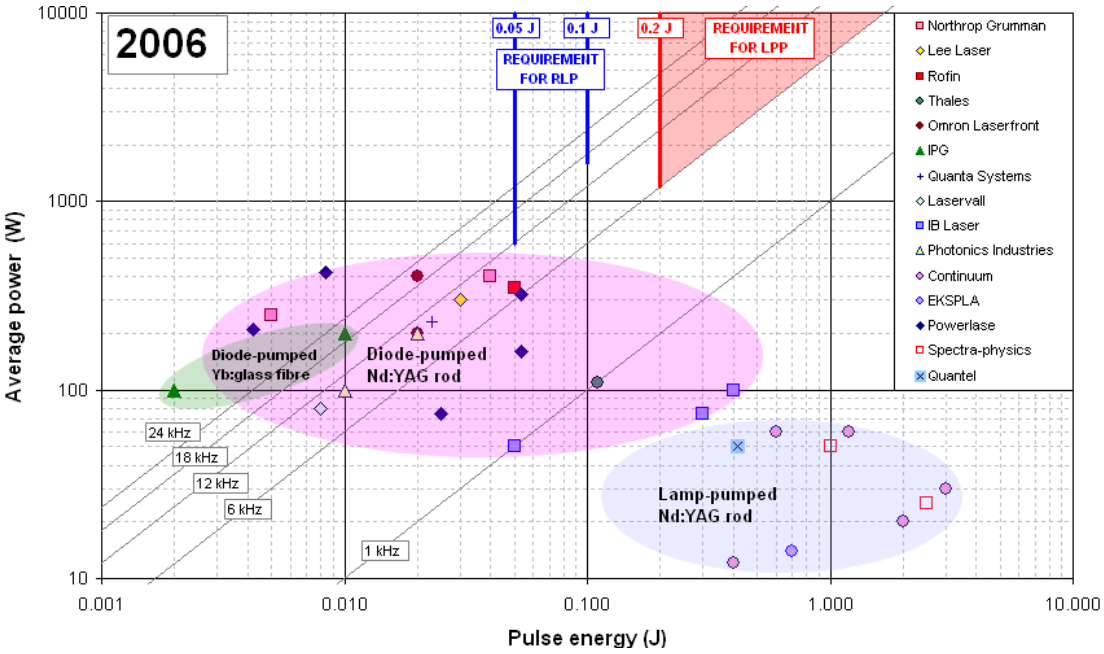

Figure 1.5 State-of-the-art for commercially available high-power, nanosecond-pulse, solid-state lasers operating at ~ 1 µm wavelength in 2006. The requirements for RLP and LLP applications are illustrated in blue and red respectively.

The laser output requirements for the RLP and LPP applications are highlighted on figure 1.5 in blue and red respectively, illustrating a disparity between the available and desired performance in 2006. The RLP process primarily required scaling of the average power by increased PRF at a pulse energy of 0.05 J above 12 kHz or 0.1 J above 16 kHz. The LPP process would however benefit from scaling of the average power by either increased pulse energy and/or repetition frequency above a minimum requirement of 0.2 J at 6 kHz.

Figure 1.6 illustrates the state-of-the-art for commercial frequency-doubled, high-power, nanosecond-pulse, solid-state lasers available in 2006. The target parameter spaces for the laser micro-jet and low temperature poly-silicon (LTPS) annealing applications are highlighted, again demonstrating a disparity between the available and desired laser performance at this time. In general, the water-jet-guided micromachining processes required scaling of the average power through increased pulse repetition frequency. In this case 3 – 10 mJ pulse energies are needed at 20 - 50 kHz PRF. In contrast, the LTPS application demonstrated the requirement for greater average power through increased pulse energy. The model presented in section 1.1.4 suggested that a minimum of 0.025 J above 5 kHz PRF is required, increasing to 0.05 J above 5 kHz PRF for annealing of the deepest silicon-films.

In 2006, frequency-doubled, lamp-pumped Nd:YAG based systems exhibited sufficiently high pulse energies for both the micro-jet and LTPS applications, but not at the repetition frequencies required. Diode-pumped neodymium-doped lithium yttrium fluoride (Nd^{3+}:$LiYF_4$ or Nd:YLF) rod lasers also made an appearance with sufficiently high energy storage capacity. However, these were also deficient in terms of PRF for the target applications at the second harmonic. Finally, frequency-doubled, diode-pumped Nd:YAG rod lasers were shown to offer appropriate PRF for the LTPS application but with lacking pulse energies. These pulse energies were sufficient for micromachining but, in this case, higher PRF and therefore higher average powers were needed to fully satisfy the laser micro-jet process requirements.

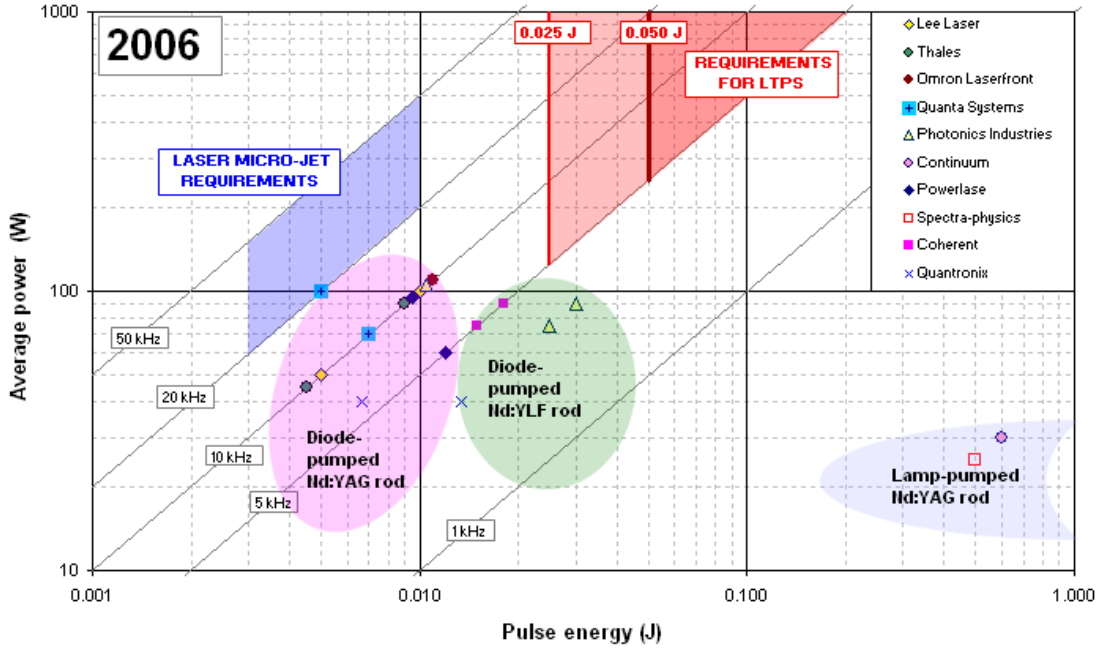

Figure 1.6 State-of-the-art for commercially available high power nanosecond-pulse solid-state lasers operating at ~ 0.5 μm wavelength in 2006. The laser micro-jet and LTPS application requirements are highlighted in blue and red respectively.

1.3 Summary

A number of target applications (detailed in section 1.1) have been demonstrated in principle using the highest power, nanosecond-pulse, solid-state lasers that were commercially available at the beginning of this research in 2006. However, in order to compete with alternative technologies and meet the minimum requirements for manufacturing productivity, there was a need for scaling of the laser output at both near-infrared and green wavelengths.

In terms of laser output optimisation, a number of requirements are common across all of the target applications. The polarisation of the generated laser light is not considered to be a defining factor in any of the application processes, with the possible exception of poly-silicon annealing for which investigations are ongoing. All of the target applications demand nanosecond pulse durations to satisfy interaction requirements and kilohertz repetition frequencies for increased process throughput. Importantly, near diffraction-limited beam

quality is not required. It is however demanded that the scaling to higher powers and pulse energies is achieved at minimum cost and with the same or better standard of reliability as that offered by the existing highest power industrial laser systems.

The objective of this research was therefore to develop nanosecond-pulse, Nd:YAG lasers capable of producing new levels of performance at the 1.064 μm fundamental and 0.532 μm second harmonic wavelengths. Target requirements for joule-level pulse energies at kilohertz repetition frequencies infer the need for multi-kilowatt average powers and megawatt peak powers at the fundamental wavelength. Preliminary requirements for average powers of up to 600 W at the second harmonic were also suggested in order to satisfy manufacturing productivity targets.

The following chapters detail the important considerations for nanosecond-pulse, solid-state laser development. They outline the design principles used, the theoretical application of these principles through mathematical modelling and their practical implementation by means of experimental investigation. In chapter 2 we discuss the concept of a high-power laser gain-module; a modular source of optical gain that integrates the solid-state gain medium with an optimised high-power pump configuration. Constituting the largest section of work, chapters 3 - 5 report on the subsequent development of high-power multi-spatial-mode laser resonators. Chapters 6 and 7 detail various methods of scaling to higher powers and pulse energies at the fundamental and second harmonic wavelengths. This includes the design and characterisation of master-oscillator power-amplifier (MOPA) systems and intra-cavity frequency converted sources. Finally, in chapter 8 we conclude by considering the performance of the laser as an industrial system and give suggestions for further work. Here we discuss how the formulated design principles can be used to optimise important laser system attributes such as efficiency, reproducibility and reliability, thus minimising the overall cost of ownership.

2 High power laser gain-module development

At the heart of commercial solid-state laser design is the desire to create a source of optical gain capable of generating the required output as efficiently and reliably as possible. In this chapter we report on the design and characterisation of a gain-module (often alternatively referred to as a laser-head or pump-module) for use in high-power multi-spatial-mode laser resonators and MOPA systems. Gain-module development for higher-power operation is based on testing the limits of a well known design that comprises an Nd:YAG rod transversely-pumped with directly-coupled laser-diodes. The important considerations for efficient, reliable and cost-effective gain-module design are discussed. This is followed by relevant optical modelling and experimental assessment of gain-module performance for use in subsequent chapters.

2.1 Gain-module design considerations

There are a number of design challenges associated with the development of a gain-module intended to function at very high-power. For reliable operation it is wise to assess the fundamental limits of the module and its components. In particular, the thermal fracture limit for the Nd:YAG rod should be well understood and characterised. Linked with this are factors relating to the

optical pump configuration such as the efficiency and distribution with which the diode light is absorbed.

Having developed an industrially robust gain-module we will then investigate its thermo-optical characteristics, which will govern how it performs as a component of a stable resonator. More specifically, it is important to appreciate the extent of the thermal lensing that can occur at high pump levels. This investigation is also extended to the residual effects observed as a result of stress-induced birefringence.

2.1.1 Heat dissipation and thermal fracture

The performance of a solid-state laser is often limited by its ability to cope with the effects that arise from the deposition of heat during optical pumping and the inevitable thermal gradients generated during its removal. Fundamentally, reduction in the total heat load can be achieved by controlling the output properties of the optical pump. In this case, narrow line-width laser diodes are used to remove the wasted spectral content exhibited by conventional broadband pump sources, such as flash or arc lamps. In some cases it is also possible to temporally duty-cycle the pump with minimal change to the overall laser output characteristics. However, at the highest powers, continuous switching of the laser diodes can lead to significant degradation in the operating lifetime; we will therefore consider the conditions associated with CW pumping only. Specific treatment of the effects that govern mechanical fracture and rupture stresses induced by heavy pumping in Nd:YAG can be found by Koechner [2.1; 2.2] and more recently Weber et al [2.3].

For a cylindrical, rod-type geometry, cooling is normally performed by passing water along the barrel of the rod. The resulting temperature T as a function of distance x along the rod radius is obtained by solving the one-dimensional heat conduction equation, which yields

$$T(x) = T(a) + \frac{Q}{4K}\left(a^2 - x^2\right) \tag{2.1}$$

where K is the thermal conductivity, Q is a constant heating rate per unit volume and a is the radius of the rod [2.1; 2.4]. The thermal gradient generated across a pumped solid-state rod causes mechanical stress due to the constraint of the expanding hotter material by that which is cooler. For a homogeneously pumped isotropic rod with a temperature distribution described by equation (2.1) the radial σ_r tangential σ_φ and axial σ_z normal stress components can be defined as

$$\sigma_r(x) = QU\left(x^2 - a^2\right) \tag{2.2}$$

$$\sigma_\varphi(x) = QU\left(3x^2 - a^2\right) \tag{2.3}$$

$$\sigma_z(z) = 2QU\left(2x^2 - a^2\right) \tag{2.4}$$

Here $U = \mu\xi\,[16K(1 - \nu)]^{-1}$ where μ is the thermal coefficient of expansion, ξ is the Young's modulus and ν is the Poisson's ratio for the material [2.1; 2.3; 2.5]. Ultimately, detrimental effects arise when the material, in this case Nd:YAG, absorbs enough heat from the optical pump for the resulting stresses to overcome its tensile strength, at which point the rod will fracture. Analysis of equations (2.2 – 2.4) indicates that the highest stresses will occur at the centre of the rod and at the barrel surface. Currently available high quality Nd:YAG, usually grown by the Czochralski technique exhibits excellent levels of bulk purity and crystal continuity. The weakest point of the rod is therefore often at the barrel surface. Small defects such as micro-fractures remnant from the boule cutting process are seen to restrict the limits for thermal fracture. We can define the total stress at the surface as a vector sum of the tangential and axial components [2.1]. The maximum circumferential hoop stress at the rod surface for a given pump power per unit length can therefore be expressed as

$$\sigma_{\max} = \frac{\mu\xi}{K(1-\nu)}\frac{P_h}{L_p} \tag{2.5}$$

where L_p is the pumped length of the rod and P_h is the power dissipated as heat. Under the oscillating conditions observed in a laser resonator the minimum thermal load can be approximated as

$$P_{h_{\min}} = P_{abs}\left(1-\eta_s\right) \tag{2.6}$$

where P_{abs} is the total pump absorbed in the rod and η_s is the *stokes shift* related efficiency (quantum defect) for the electronic transition. For the 1.064 μm transition of Nd:YAG $\eta_s = 0.76$. In reality however, it is difficult to accurately calculate the total amount of power that is dissipated as heat in the laser rod. Supplementary to the quantum defect there are a number of purported mechanisms for increasing the heat load such as the presence of Nd-ion 'dead sites', which do not contribute to inversion and exhibit non-radiative decay. Concentration quenching, excited state absorption (ESA), upconversion and hot pump chamber re-radiation can also contribute to heating in the rod [2.3; 2.6; 2.7; 2.8]. Most of these additional heating mechanisms depend on the doping concentration and the quality of the Nd:YAG used. Rather than assuming the minimum quantum defect contribution it is therefore often useful to practically assess the thermal loading, as will be reported in section 2.3.3.

In addition to the above mechanisms the thermal load is further increased under non-oscillating conditions. This is because the heating due to the emission of a stimulated photon is less than that of an average spontaneously emitted photon. At low pump irradiances, in the absence of upconversion, the exact difference in the thermal loading between oscillating and non-oscillating conditions is dependent on the level of concentration quenching present, which is in-turn a function of the doping concentration [2.9]. For typical doping concentrations of around 0.75 % at. Nd the reduction in fractional power dissipated as heat between non-oscillating and oscillating conditions is approximately 10 %. Aside from the increased likelihood of thermal fracture under non-oscillating conditions this also has significant implications for the

thermo-optical characteristics of the gain-module, which are discussed later in this chapter.

To ensure reliable operation it is vital that the Nd:YAG rod is pumped at a safe level below the threshold for thermal fracture. It is therefore useful to compare the result of equation (2.5) with the ultimate tensile strength (fracture limit) σ_u for Nd:YAG. In doing this we can define a maximum permissible heat load per unit length, which can be expressed as

$$\left(\frac{P_h}{L_p}\right)_{\max} = \frac{8\pi K(1-\nu)}{\mu\xi}\sigma_u \qquad (2.7)$$

For Nd:YAG the thermal conductivity K = 0.103 W.cm^{-1}.K^{-1} and is assumed constant as it varies no more than 10 % between 300 and 400 K [2.10]. The other material constants used for Nd:YAG in this study are: ν = 0.25, μ = 6.9 x 10^{-6} K^{-1} and ξ = 307 GPa, which are taken from manufacturer specifications.

The fracture limit of Nd:YAG is observed to vary greatly depending on the surface finish of the rod. Reported values for the tensile strength of Nd:YAG range from around 120 - 240 MPa [2.3], which results in a maximum permissible heat load per unit length of between 110 - 220 W.cm^{-1}. Steps can be taken to ensure a high permissible heat load per unit length by conditioning the normally ground surface finish of the rod by means of chemical etching or annealing processes [2.11; 2.12; 2.13]. Experimental determination of the fracture limit for the rods used in this work is reported in section 2.3.1.

2.1.2 Optical pump configuration

Maximisation of the overall laser system efficiency begins at the gain-module. In general the solid-state laser designer has little control over the electrical and optical efficiencies associated with the laser-diode pump source. Differences in efficiency between pump-diode manufacturers is also small, although there is a general increasing trend in efficiency seen as this technology develops [2.14].

The efficiency by which the pump is *transferred* to the Nd:YAG rod η_T is however controllable though considered gain-module design. To increase η_T it is advantageous to optimise two parameters. It is important to maximise the amount of light that is incident onto the rod as a significant proportion of the total pump can be imparted during the first pass. This involves consideration of the method by which the pump is directed toward the rod. We can quantify this parameter by defining a *first-pass view factor* that represents the fraction of light that is incident on the rod at the first pass. The use of pump coupling or conditioning optics can be used to relay the pump light, particularly when there is limited space, but any residual reflections will adversely affect the transfer efficiency. The second objective is to minimise the re-cycling loss of the pump by promoting efficient re-coupling of any remaining light back into the rod on subsequent passes. This can be characterised by a *secondary-pass view factor* (which represents the fraction of light incident on the rod that has been returned by the reflective pump chamber) plus the absorption and reflection losses associated with the process.

Another important factor is the pump *absorption* efficiency η_a, which is defined as the total fraction of pump that is absorbed once inside the Nd:YAG rod. This is determined by the average fractional absorption per pass of the rod and the total number of passes that occur before subsequent absorption can be regarded as negligible. The pump absorption efficiency is dependent on the dimensions of the rod, the doping concentration of Nd^{3+} ions (which should be at least sufficient to prevent pump saturation) and the pump wavelength distribution with respect to the absorption spectrum of Nd:YAG. It follows that η_T and η_a are interrelated whereby both factors are dependent on the number of significant rod passes. A radiation *coupling* efficiency η_c can be defined by taking the product of the transfer and absorption parameters, which can in turn be used to determine the total pump absorbed P_{abs} such that

$$\eta_c = \eta_T \eta_a \tag{2.8}$$

and $$P_{abs} = \eta_c P \tag{2.9}$$

where P is the total power output by the laser diodes.

A further characteristic that is determined by the optical pump configuration is the volumetric distribution of the absorbed pump. Non-uniform absorption on transit through the rod is inevitable and is generally related to the aforementioned factors that govern absorption efficiency. For example, the first pass absorption and pump-chamber configuration will affect the distribution, as well as the coupling efficiency. The transverse refractive focusing of the pump light through the cylindrical rod will also contribute to the absorption profile, which is largely fixed by the first order refractive index of the rod at the pump wavelength. For maximum system efficiency with respect to laser output it is advantageous to match the absorption related gain-distribution within the rod to the field distribution of the beam generated in a given laser resonator. Thorough consideration of this effect is given by Hall [2.15] and Koshel [2.16] and will be discussed later in this work. However, as the resonator configuration is often unknown at the time of gain-module development and is ultimately changeable, the ability to tailor the absorption profile to suit the spatial characteristics of the laser mode is limited. At high pump levels there can also be a trade-off to make between the fabrication of a less homogeneous gain profile for increased extraction efficiency and increased risk of thermal fracture. An initial aim for this work was therefore determined to design a gain-module with maximised pump coupling efficiency and a homogeneous absorption profile. This will allow operation at the highest reliable pump powers without thermal fracture. Homogeneous pumping will also simplify the characterisation of the thermo-optical properties such as thermal lensing and aid in the mathematical modelling of laser resonators, which is discussed at length in chapter 4.

2.1.3 Thermal lensing

The first order aberration that arises when a solid-state rod is pumped and cooled at its periphery is a positive lensing. This occurs due to the formation of radial thermal gradients and the dependence of the refractive index on temperature. Extensive investigation of the thermal effects that lead to lensing in optically pumped solid-state laser media has been carried out and continues to date. For rigorous theoretical and experimental treatment of these effects the reader is directed to work presented by the likes of Quelle [2.17], Reidel and Baldwin [2.18; 2.19], Foster and Osterink [2.20], Koechner [2.21], Kimura and Otsuka [2.22], Burnham [2.23], Gleason et al [2.24] and Weber et al [2.3].

For a homogeneously pumped rod the variation in the refractive index with distance along the radius of the rod x is described by $n(x) = n_r - (1/2)n_2x^2$ where n_r and n_2 are first and second order refractive index coefficients respectively. In a cylindrical geometry this parabolic variation in refractive index manifests perpendicular to the axis of light propagation and therefore constitutes a thermally induced lens of refractive power

$$D_{therm} = \frac{2\Delta T_{rod} L_p}{a^2} \frac{dn}{dT} \tag{2.10}$$

where a is the radius of the Nd:YAG rod, L_p is the length over which the rod which is pumped and dn/dT is the coefficient of the refractive index dependence on the temperature (for Nd:YAG n_r = 1.823 and dn/dT = 9.86 x 10^{-6} K^{-1}). ΔT_{rod} is the difference in temperature between the surface and centre of the rod, which is dependent on the amount of power dissipated as heat P_h and independent of the rod surface temperature [2.3]. We know from section 2.1.1 that an accurate quantification of the heat loading is difficult to theoretically predict. However, it is possible to extract an approximation for ΔT_{rod} from practical thermal lens measurements and estimate P_h using the expression

$$P_h = \Delta T_{rod} \left(4\pi K L_p\right) \tag{2.11}$$

Contrary to early reported experimental results the variation in thermal lens power with total incident pump is generally observed to be linear [2.25; 2.26], such that $D_{therm} \alpha n_2 \alpha \Delta T_{rod} \alpha P_h \alpha P_{abs} \alpha P$. We know that the thermal load increases in the absence of laser oscillation within the Nd:YAG rod and that for typical doping concentrations this fractional change is in the order of 10 % [2.9]. It follows that a proportional increase in the thermal lens power between oscillating and non-oscillating conditions should also be expected.

2.1.4 Photoelastic birefringence: Bifocusing and depolarisation

In addition to the temperature-dependant variation in refractive index a thermally loaded solid-state rod can also exhibit stress-induced birefringence due to the photoelastic effect. In this case, the inherently spherical indicatrix of the cubic YAG crystal lattice is modified to an ellipsoid, which has axes that are in the same direction as the normal stress components, defined by equations (2.2 – 2.4). For rod geometries, the variation of the refractive index in the radial (r) and the tangential (φ) orientations are therefore of most interest as they are seen to affect the respective polarisation components of the oscillating laser radiation. Similar to the first order temperature induced component the stress-induced index profiles are parabolic forming spherical lens components of refractive powers given by

$$D_{r,\varphi} = \frac{2\Delta T_{rod} L}{a^2}\left(\mu C_{r,\varphi} n_r^3\right) \qquad (2.12)$$

where L is the rod length, μ is the thermal coefficient of expansion and $C_{r,\varphi}$ are functions of the radial and tangential photoelastic coefficients for Nd:YAG, such that $C_r = 0.017$ and $C_\varphi = -0.0025$ [2.3]. This polarisation bifocusing can often prove troublesome, particularly when attempting to isolate and maintain a single spatial mode for diffraction limited operation. The implications of bipolar lensing with multi-spatial-mode oscillation will be discussed at length in chapter 4.

In addition to bifocusing the stress-induced birefringence can also cause phase retardation between the radial and tangential components resulting in non-uniform depolarisation across the transmitted beam. This is particularly problematic for resonators that require fixed, often linear polarisation to enable techniques such as electro-optic Q-switching or cavity dumping, for example. Depolarisation by photoelastic retardation is generally not detrimental to the performance of randomly polarised Nd:YAG oscillators operating at the fundamental wavelength, although there are however implications for intra-cavity non-linear wave mixing, which are discussed in chapter 7. For dedicated studies of stress-induced birefringence, including bifocusing and depolarisation compensation techniques, the reader is directed to references [2.25], [2.27] and [2.28].

2.2 Optical modelling: Non-sequential geometrical ray-tracing

The stated objective is to design a gain-module with maximised pump coupling efficiency and a homogeneous absorption profile. This will enable operation at the highest reliable pump powers without thermal fracture. Commercially available geometrical ray-tracing software (TracePro™) has been used to model the performance of various pump chamber designs. This technique employs a non-sequential Monte-Carlo-type computational algorithm to simulate the propagation of light rays within the pump chamber. Using this we are able to theoretically determine the transfer, absorption and total coupling efficiency of the pump, as well as its subsequent distribution within the Nd:YAG rod.

The accuracy of a ray-trace simulation is generally limited by the ability to adequately characterise the emission, transmission, absorption, scatter and reflection properties of the optical components being used. Of primary importance is the angular distribution of the laser diode pump source. Experimental data for this is typically supplied by the manufacturer as part of

performance characterisation. Using a new feature of the ray-tracing software it is possible to generate anisotropic emission from a surface such that perpendicular fast and slow axis divergences can be modelled. Figures 2.1 and 2.2 illustrate the resultant simulated output for a single laser diode bar of 10 mm in length. Notice how close the modelled angular distribution of the light matches the experimentally measured data. Each pump assembly consists of an end-on linear array of 4 diode bars separated by a pitch of 2 mm. This gives total pumped length of L_p = 46 mm which is near centralised on the rod of length L = 97 mm.

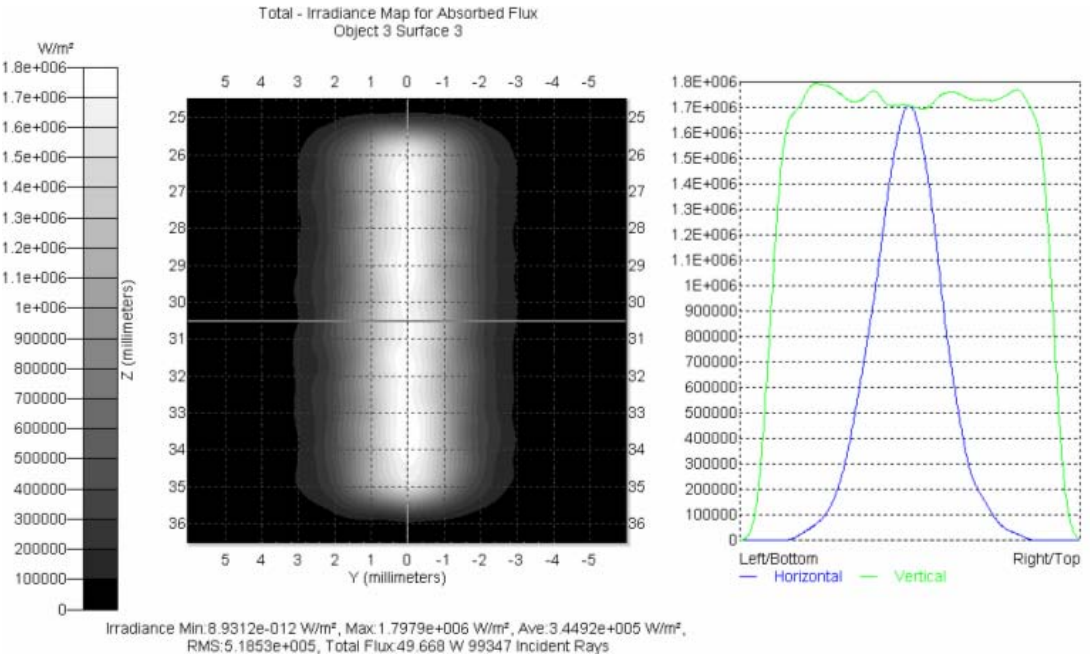

Figure 2.1 Ray-trace simulation of the laser diode pump source showing an irradiance map for the output of a diode bar at a plane perpendicular to the central axis of propagation.

The next step is to apply this pump source to an optical chamber and cooled laser rod configuration. Homogeneous pump distribution within the rod can be promoted by reducing the absorption per pass and increasing the number of passes. This can be achieved by reducing the doping concentration and/or diameter of the rod. However, this generally results in low pump coupling

efficiencies as there is a loss associated with every pass. By increasing the number of incident pump positions around the circumference of the rod it is possible to promote coupling efficiency and homogeneous distribution, as well as scalability of the total pump power. There is however a practical limit associated with this, which is set by the finite space available to mechanically locate the laser diode assemblies. A maximum of 5 incident pump positions can be achieved when directly coupling the high-power laser diodes used here. They are equally spaced at 72° angular intervals about the rod circumference.

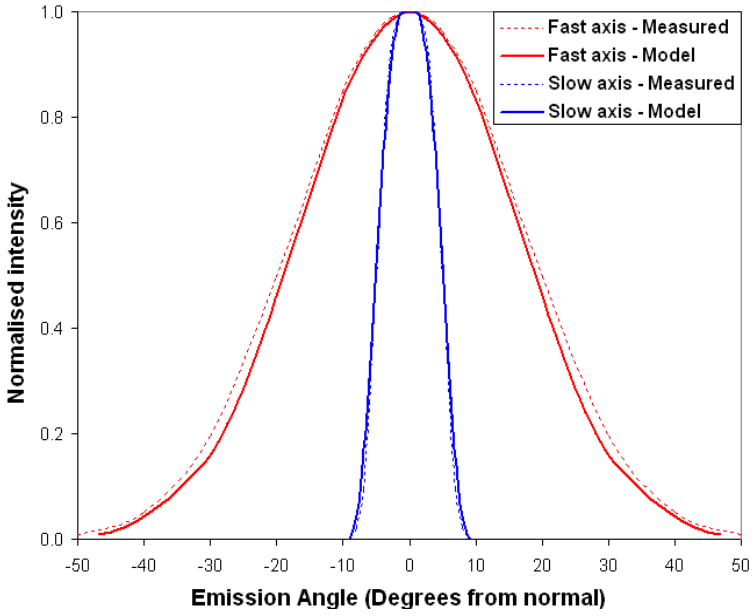

Figure 2.2 Ray-trace simulation results for the laser diode output showing a comparison of the simulated fast and slow axis distributions with respect to the measured characterisation data.

To optimise the pump coupling efficiency and maintain uniform distribution it is necessary to alter the dimensions and optical properties of the pump chamber components. The inside diameter of the reflective chamber should be made as small as possible relative to the rod in order to maximise recapture of the reflected pump. This dimension is restricted by the water jacket and associated flow tube that are required for sufficient cooling of the rod barrel surface. The thickness of the water jacket is dependent on the thermal load and the rate at

which water is required to pass the rod. Similarly, the minimum flow tube thickness is restricted by the requirement for operation at a safe level below the bursting pressure. This can be calculated given the required flow rate and tube material, which must be largely transparent to the pump radiation. The details of these calculations are beyond the scope of the work presented here.

In contrast to that required for uniform pump distribution the coupling efficiency can be maximised by increasing the absorption per pass and reducing the number passes (through increased the doping concentration and/or rod diameter). To promote uniformity in the pump distribution without significantly compromising efficiency it is common to condition the light by transmission or reflection at optically diffusive surfaces.

A number of pump chamber designs with various dimensions and material properties have been assessed by importing detailed, physically representative 3-dimensional computer aided drawings into the ray-tracing software. Figure 2.3 shows a cross section of the resulting optimised pump chamber design that comprises an Nd:YAG rod of 0.6 % at. Nd doping concentration and radius a = 2.25 mm. Surrounding this is a water jacket and flow-tube suitable for sustaining coolant flow rates of around 6.0 l.min^{-1}. The outer surface of the flow-tube has been given an optically diffuse finish using a standard bead-blast grinding method. This is replicated at the rod barrel, which was then annealed to increase the thermal fracture limit. A diffuse rod finish will also aid the elimination of parasitic oscillations that can occur between polished surfaces due to Fresnel reflection. Further homogenisation of the pump light is achieved by using a diffuse chamber reflector. In this case a bulk reflector material was sourced that would provide greater than 97 % scattered reflectivity at the 808 nm pump wavelength. However, the majority of the losses incurred at the walls of the pump chamber are due to the 2 mm wide pump entry slits, which reduce the circumferential reflective surface by nearly 30%. For modelling purposes it is assumed that approximately 50 % of the light passing through the pump entry slits is returned by reflection at the diode assembly.

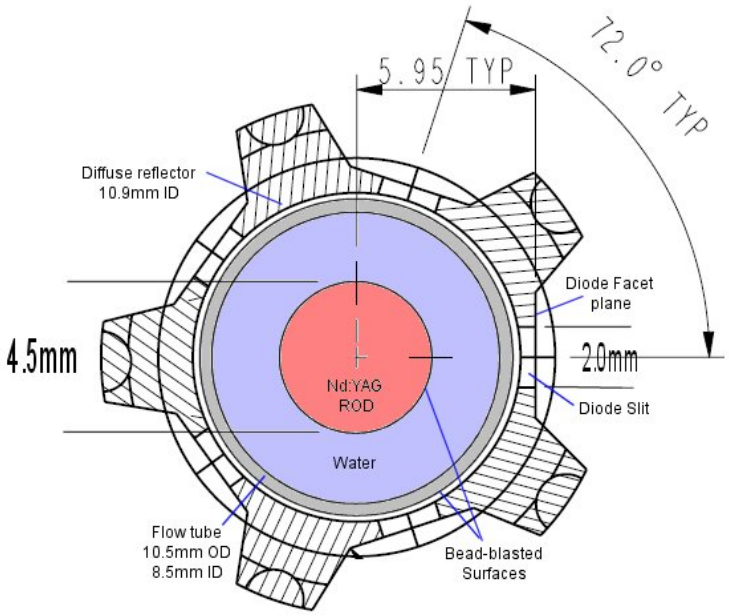

Figure 2.3 Schematic of the final pump chamber design in cross-section showing the component dimensions and 5-fold symmetry (illustrated without the laser diode assemblies).

The total absorption per unit length in the rod has been calculated by taking the specified absorption of 808 nm light at 0.6 % at. Nd doping concentration and modifying it to account for the fractional overlap between the wavelength distribution of the laser diode output and the spectral absorption of Nd:YAG. In this case the laser diodes used exhibit a lognormal spectral distribution around a peak wavelength of 808 nm (± 3 nm) and a FWHM width of 2.5 nm (± 0.5 nm). This gives an absorption coefficient of ~ 0.24 mm^{-1} at 0.6 % at. Nd.

Figure 2.4 (a) shows a screen shot for the ray-trace simulation. The results indicate that 66.5 % of the power output by the pump diodes is incident on the rod in the first pass. More importantly, 48.9 % of the total pump light is absorbed on the first pass, which includes light that is back reflected or back scattered at the rod-to-water interface. Running the simulation for multiple passes suggests a total pump coupling efficiency η_c = 0.80. We can estimate the total number passes required to obtain this coupling efficiency by assessing the secondary pass view factor, which was found to be 0.42, and assuming that the

fraction of incident light absorbed on secondary passes is the same as that seen on the first pass. Figure 2.4 (b) indicates that the majority of pump absorption has occurred after around 10 passes of the laser rod.

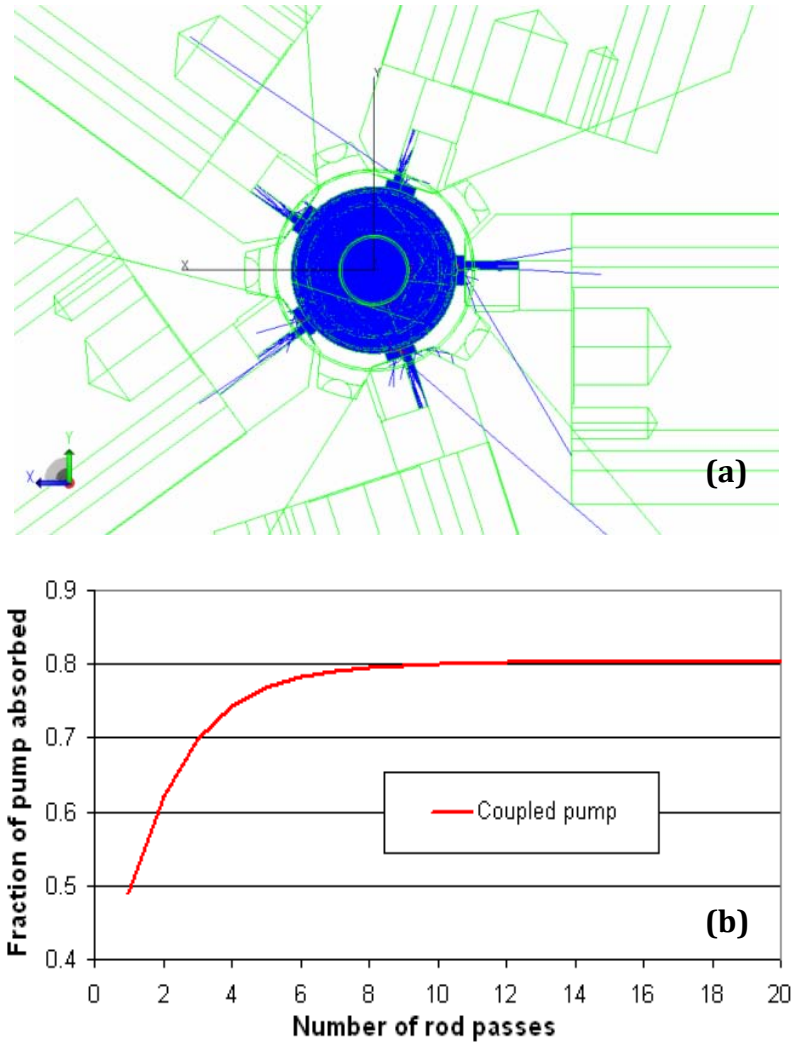

Figure 2.4 Ray-trace simulation results showing (a) a screen shot of the traced rays inside the pump chamber in cross-section and (b) the fraction of the total pump absorbed as a function of rod pass number for the final high-power gain-module design.

The 'volume flux collection' functionality of the ray-tracing software can be used to assess the average distribution of the absorbed pump in the laser rod. Figure 2.5 (a) shows a flux-collection-grid that covers the pumped volume with 200 x 200 x 1 cells in the *x*, *y* and *z* planes respectively. Figure 2.5 (b) gives an

illustration of the resulting absorbed flux. Taking a line-out in *x* (averaging over a central 20-cell wide band in *y*) returns an absorption profile that varies no more than 2 % peak-to-peak across the rod diameter.

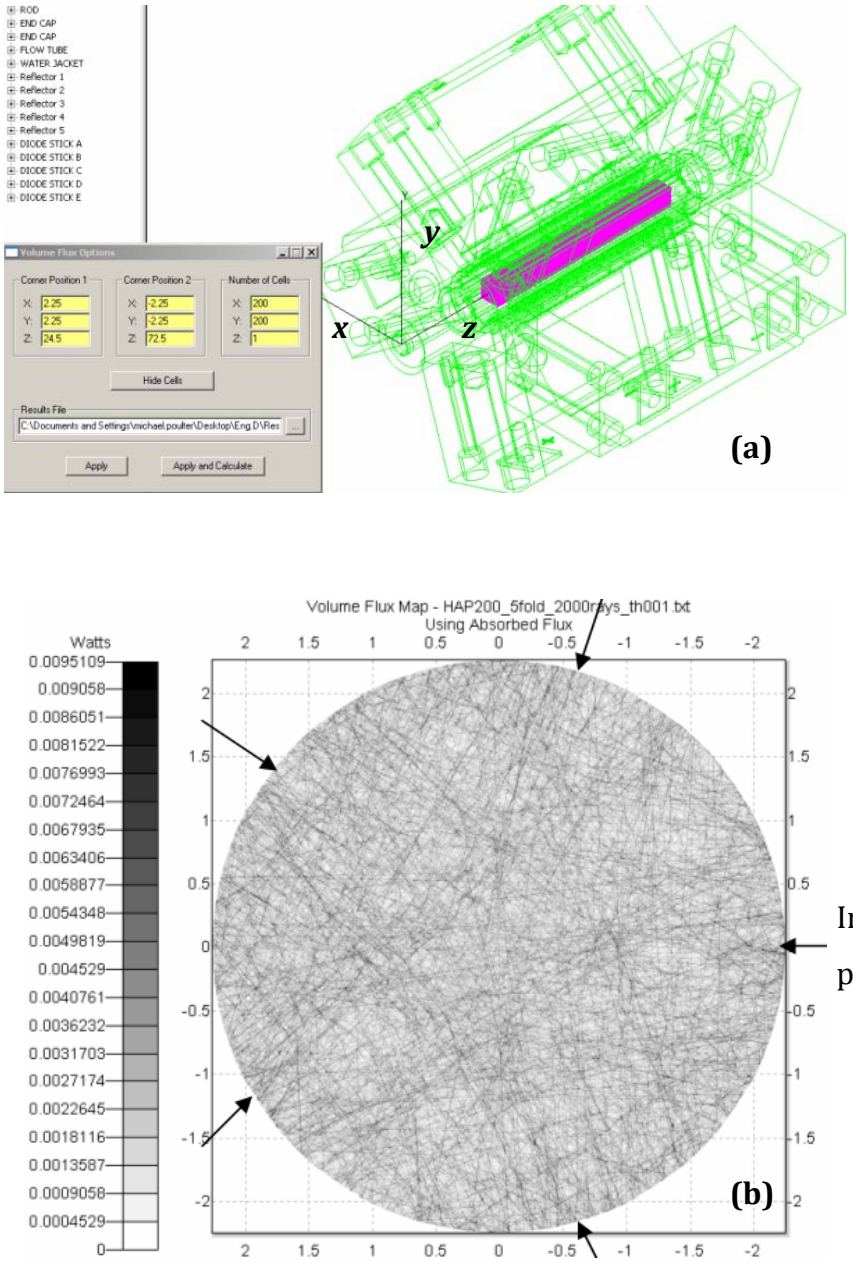

Figure 2.5 An illustration of (a) the size and position of the volume flux grid (shown in magenta) used to extract the distribution of the absorbed pump within the Nd:YAG rod and (b) the simulated average flux distribution in cross-section of the laser rod giving an indication of the pump absorption profile.

2.3 Experimental results

The following sections outline the results obtained during the experimental characterisation of the developed high-power gain-module and its components.

2.3.1 Rod fracture limit investigation

The Nd:YAG rods used in this work were typical of the current manufacturing standard. Here, the rods are cut from the peripheries of a larger boule that had been grown via the Czochralski technique and seeded to produce a cubic crystal structure. The rods are cut with <111> crystallographic orientation and finished with a 55 micro-inch barrel grind before being annealed to eliminate surface micro-fractures. Finally, the rod facets are polished to < λ/10 flatness (at λ = 0.633 μm wavelength), 10 - 5 scratch-dig surface quality and anti-reflection coated for 1.064 μm.

The technique for measuring rupture stress presented in reference [2.2] was used to assess the fracture limit for a sample of these laser rods. This method is a mechanical alternative that enables testing above the stress levels that can be thermally induced by the laser diodes. For an end-supported cylindrical beam with two equal and symmetrically placed loads we can calculate the ultimate tensile strength (rupture stress) using the expression

$$\sigma_u = \frac{16 z_l F_{\max}}{(2a)^3 \pi} \tag{2.13}$$

where z_l is the distance between the rod end support and the nearest load point. a is the rod radius and F_{max} is the total load at failure. The destructive mechanical testing of rods from 5 separate batches with 0.60 % (± 0.05 %) at. Nd doping concentration revealed a mean failure load of 132 (+ 4, - 3) N, which corresponds to a rupture stress of 222 (+ 7, - 4) MPa. Using equation (2.7) we can now calculate the maximum permissible heat load per unit pumped length of rod (P_h/L_p) = 204 (+ 7, - 4) W.cm^{-1}. These figures are

comparable with previously reported values [2.3] and are also consistent with the 175 - 200 $W.cm^{-1}$ limit for thermal fracture specified by the rod manufacturer.

2.3.2 General gain-module characterisation

A high-power gain-module was constructed according to the modelled design outlined in section 2.2. In this section we concentrate on the performance characterisation of this module and its significant components. The first of the salient components to be characterised are the laser diode pump assemblies, of which there are 5. Each diode assembly comprises a horizontal stack of 4 diode bars that are 10 mm in length and separated by a 2 mm pitch. This gives a 46 mm total pump length. Each diode bar consists of around 37 closely spaced edge emitters providing a maximum of 50 W output at approximately 57 A drive current. In order to ensure lifetimes in excess of 15,000 hours the diodes have been de-rated to operate at 50 A maximum drive-current. The output characteristics for the specific diode assemblies used for this particular gain-module are summarised in table 2.1 below.

Laser diode output data (at 25° C)	**Peak output wavelength at 57 A [nm]**	**FWHM linewidth at 57 A [nm]**	**Drive current treshold for oscillation [A]**	**Slope (above threshold) [W/A]**	**Electrical to optical efficiency [%]**	**Output power at 50 A drive current [W]**
Laser diode assembly 1	807.5	2.9	14.9	4.75	49.7	167
Laser diode assembly 2	807.3	2.4	14.8	4.73	49.6	166
Laser diode assembly 3	807.5	2.6	14.8	4.74	49.6	167
Laser diode assembly 4	806.7	2.3	14.9	4.71	50.6	165
Laser diode assembly 5	806.7	2.4	14.8	4.70	50.5	165
					Total output [W]	831

Table 2.1 Experimentally determined output characteristics of the 5 laser-diode pump assemblies used in a high-power gain-module constructed according to the design presented in section 2.2.

The Nd:YAG rod used in this module was found to have 0.65 % at. Nd average doping concentration, which is just within the tolerance for the specified design

value of 0.60 % (± 0.05 %). This doping density is nearly always seen to vary slightly along the length of the rod. Although the extent of this is difficult to quantify it is considered small enough to not significantly affect performance when applied to a laser resonator. In this case the rod facets are polished plane-parallel and electron-beam coated for anti-reflection at 1.064 μm wavelength. The rod and pump-diode cooling water loop is sealed using compression-fit O-rings and tested to 3.9 bar input pressure and 6.9 $l.min^{-1}$ flow rate.

To assess the relative performance of successive gain-modules each one is installed into a short CW test resonator and aligned for maximum output power. This resonator simply comprises the gain-module plus two plane cavity mirrors (high reflector and output coupler) placed ~ 60 mm from the rod ends. An output coupling is selected for maximum power output and kept constant at 30 % (70 % reflectivity at 1.064 μm). To maximise output power the gain-module cooling water is temperature tuned. This optimises overlap between the spectral output of the pump diodes and absorption in the Nd:YAG rod. Figure 2.6 shows the variation in output power with gain-module temperature measured at the input manifold to the laser diodes, which provides a 5-way equally partitioned flow distribution. This data is taken at 50 A drive-current and is unique to each gain-module as it depends on the assortment of peak output wavelengths and linewidths exhibited by the laser diodes used. In this case an estimated polynomial line of best fit suggests that an operating temperature of approximately 28.5 °C is most efficient. The gain-module temperature is therefore held at 28.5 (± 0.2) °C using a water to water heat exchanger and proportional-integral-derivative (PID) controller.

Note that for this gain-module a 4 °C variation in temperature constitutes only 3 % change in output power and that all of the optical components used are within the standard tolerances specified in section 2.2. The implications of varying component specification and tolerancing, including the effects on gain-module and laser resonator performance, are discussed in section 3.3.

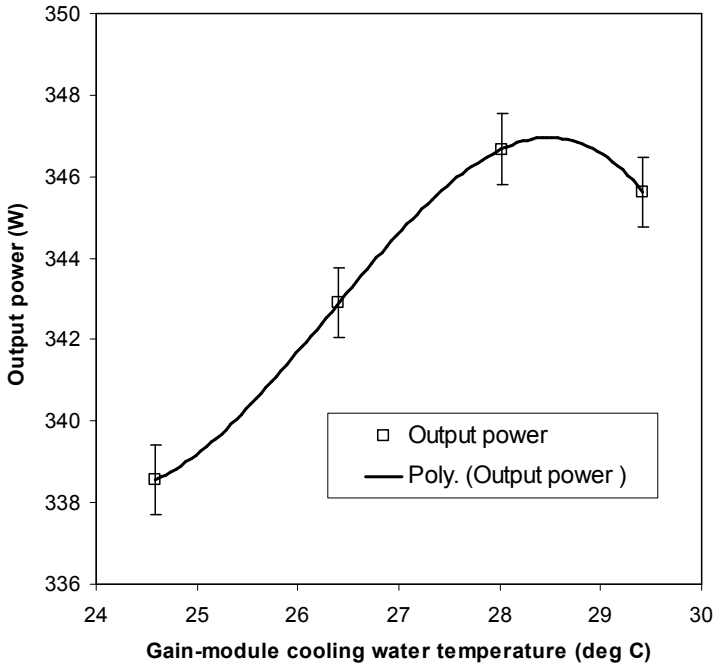

Figure 2.6 Experimentally determined output power at 831 W pump power (50 A drive-current) as function of gain-module cooling water temperature for a short (160 mm) test-resonator.

Figure 2.7 shows the output power as a function of total pump power for the short CW test resonator. An output of 346 W (± 17 W) was measured at the optimum 831 W (± 42 W) pump power giving an optical to optical efficiency of 41.6 % (± 4 %). The fitted linear trend line returns a slope efficiency value of 50.1 % (± 0.5 %) above 250 W pump and suggests a threshold for oscillation at ~ 150 W pump power (21.1 A laser diode drive-current). However, in reality, below 250 W pump the slope deviates from the linear trend with a measured threshold for oscillation occurring at 95 W total pump power (18.8 A laser diode drive-current). This is likely to be due to a shift in the laser diode emission wavelength at lower drive-currents. The shift is typically around 0.1 nm per amp drive-current, giving ~ 3 nm variation over the measured current range. This shift leads to a change in overlap between the pump emission and Nd:YAG absorption spectra, which in turn alters the level of population inversion.

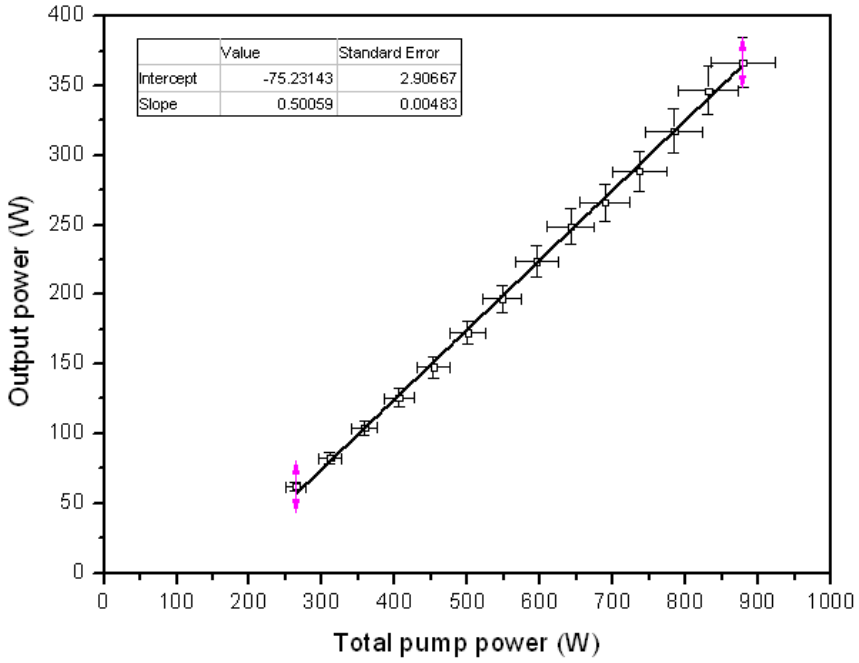

Figure 2.7 Experimentally determined output power as function of total pump for a short (160 mm) CW test-resonator constructed using the developed high-power gain-module.

2.3.3 Thermal lens power and heat load determination

The refractive power of the lens generated by a pumped laser rod has three general components, the largest of which is the lensing that is brought about by the temperature dependent refractive index variation across the diameter of the laser rod. Adding to this are the components related to the stress-induced birefringence and rod facet deformation through non-uniform thermal expansion. Although, for rod geometries with un-pumped end sections greater than ~ 1 rod diameter the latter of these components can be assumed to have a negligible effect on the total refractive power induced [2.3; 2.21].

Precise methods for measuring the lens power of pumped laser rods have been recently presented using arbitrary resonator stability characterisation and even spectrometry [2.26; 2.29; 2.30]. However, for analytical modelling purposes an adequately accurate measurement of lens power can be determined using the more simple method employed by Gleason and Eichler [2.24; 2.25]. This method involves using a collimated low-power helium-neon probe laser and measuring

the position of its focus with respect to the pumped laser rod. As an optical element, the pumped rod can be approximated to a thick lens. It can be shown that, to the first order, the position of the principle planes of this lens do not depend greatly on the thermal load and are located at a distance $h = L/(2n_r)$ from the rod facets, where L and n_r are the length and primary refractive index of the laser rod respectively [2.21]. This is valid in the majority of practical cases when the focal length is greater than the rod length.

Figure 2.8 shows the refractive power of the gain-module for non-oscillating conditions $D_{exp} = 1/f_{exp}$, where f_{exp} is the experimentally measured focal length. f_{exp} is defined as the distance from the focus of least confusion (between radial and tangential polarisation components) in the probe beam and the nearest principle plane of the rod-like lens. The variation in this focal length due to the difference in wavelength between the probe beam (at 0.633 μm) and that of the intended operating laser transition (at 1.064 μm) is calculated to be within the measurement error.

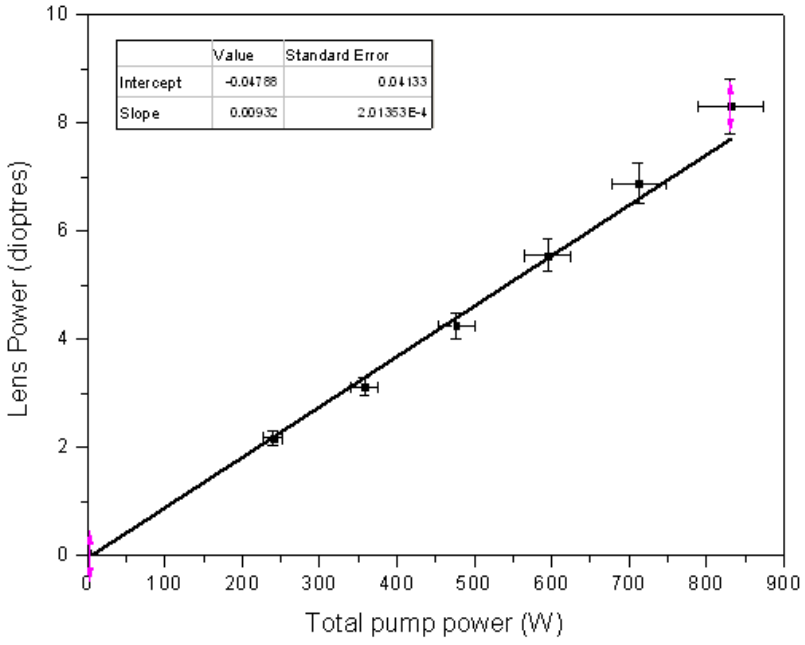

Figure 2.8 Experimentally determined gain-module lens power (inclusive of thermal lens and photoelastic birefringence components) as function of total pump power.

By applying linear regression to this experimental data we are able to extract a lens constant for the gain-module, which is characterised by the slope of the best fit line shown in figure 2.8 and expressed in dioptres per watt of total pump. For the lensing observed under the conditions with no laser oscillation the lens constant C_t' = 9.3 x 10^{-3} (± 2.0 x 10^{-4}) D.W^{-1}. In terms of resonator design, a more useful parameter is the lens constant for the gain-module under oscillating conditions where a reduced heat load is observed. For mathematical modelling purposes we may assume that the lens constant will scale proportionally with heat loading, which is reduced by ~ 10 % for oscillating conditions [2.9]. We can therefore deduce an approximation for the lens constant under oscillating conditions C_t = 8.4 x 10^{-3} D.W^{-1}. This value will be used to simulate resonator performance in chapter 4.

The corresponding lens power D_{exp} for the experimentally measured focus of least confusion in the probe beam can be expressed as follows

$$D_{\exp} = \frac{\left(D_{therm} + D_r\right) + \left(D_{therm} + D_\varphi\right)}{2} \tag{2.14}$$

By substituting equations (2.10) and (2.12) into equation (2.14) we are able to formulate an expression for the difference in temperature between the surface and the centre of the rod ΔT_{rod} such that

$$\Delta T_{rod} = a^2 D_{\exp}\left[2L_p \frac{dn}{dT} + L\mu n_r^3\left(C_r + C_\varphi\right)\right]^{-1} \tag{2.15}$$

At an optimum total pump power of 831 W the experimentally measured lens power of 8.3 (± 0.5) dioptres suggests that ΔT_{rod} = 43.5 (± 2.6) K. A more representative value for the power dissipated as heat in the laser rod can now be calculated using equation (2.11), which returns a heat load P_h = 259.0 (± 15.6) W. Given a pumped length of 4.6 cm we can therefore calculate that 56.3 (± 3.4) W.cm^{-1} is dissipated as heat per unit length at the optimum pump power. This is a factor of 3.6 (+ 0.4, - 0.3) below the limit for thermal fracture measured in section 2.3.1. Using the pump coupling efficiency

η_c = 0.80 deduced in section 2.2 we can calculate a value for the fractional thermal loading with respect to the absorbed pump. At 831 W total pump (and therefore 664 W absorbed pump power), the fractional heat loading is 0.39 (+ 0.05, - 0.04). This is significantly larger than the minimum quantum-defect limited level but consistent with the 0.37 - 0.43 values reported by Fan [2.6]. The corresponding thermal component of the practically measured lens power, calculated using equation (2.10), is 7.79 (± 0.47) D.

We can attempt to corroborate the mathematically derived value for the thermal lens power in the absence of oscillation by using finite element (FE) modelling code (LASCAD™). A similar fractional thermal loading of 0.32 was required to generate a temperature differential ΔT_{rod} of 43.5 K in the FE-model. Figure 2.9 shows the resulting temperature distribution for the 3-dimensional FE-model of the pumped Nd:YAG rod. The thermal lens component of the pumped rod (disregarding the stress-induced birefringence) can be calculated by applying a parabolic fit to the change in temperature-dependent refractive index and assessing the resulting optical path-length-difference (OPD) across the rod. Under this parabolic approximation the optical path-length-difference obeys the relation

$$OPD(x) = 0.5 D_{therm} x^2 \tag{2.16}$$

Analysing the slope of a linear trend line fitted to an OPD(x) versus x^2 plot returns a thermal lens component of D_{therm} = 8.0 D, which is within the error of the value mathematically derived using equation (2.10).

Note that the actual temperature at the centre of the rod $T_{rod}(0)$ will be larger than ΔT_{rod}. An estimation of this is given by

$$T_{rod}(0) = T_{surf} + \Delta T_{rod} = \left(\frac{P_h}{A_{surf} h_t} \right) + T_{coolant} + \Delta T_{rod} \tag{2.17}$$

where T_{surf} and A_{surf} are the temperature and area of the barrel surface for the pumped section of the laser rod, $T_{coolant}$ is the coolant water temperature and h_t

is a surface transfer coefficient [2.3]. For a cooling water temperature $T_{coolant}$ = 28.5 °C and a typical surface transfer coefficient of 2 W.cm^{-2}.K^{-1}, at the optimum total pump level of 831 W, T_{surf} = 48.4 °C and $T_{rod}(0)$ = 92.0 °C.

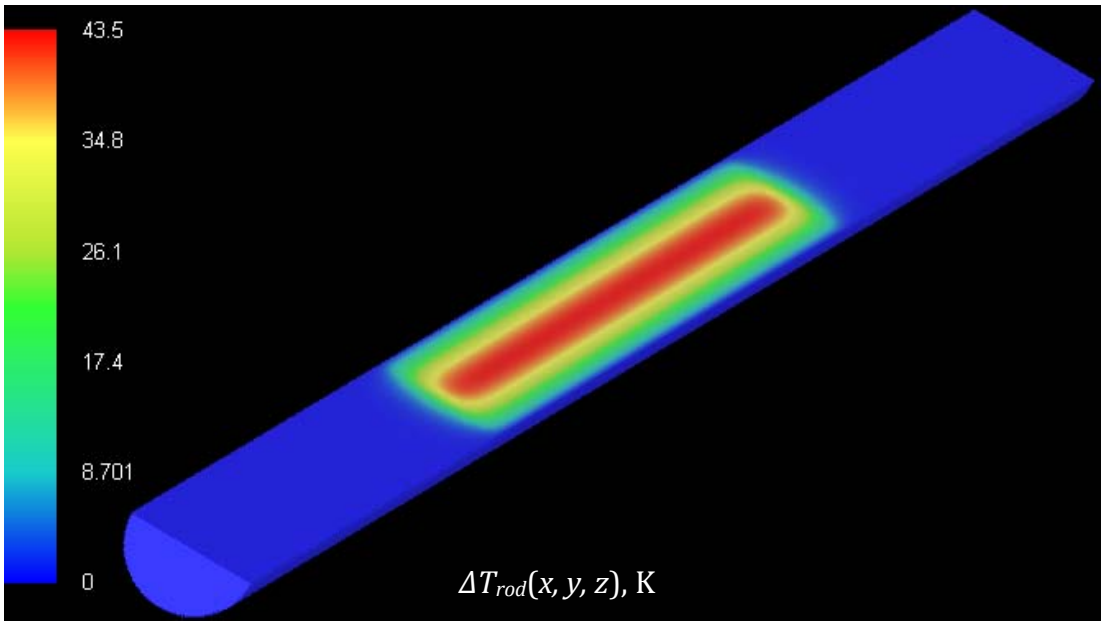

Figure 2.9 A 3-dimensional illustration of the temperature distribution within the rod relative to the surface temperature, produced by finite-element (FE) modelling of the high-power gain-module.

2.4 Summary

The high-power laser gain-module developed in this chapter uses a straightforward geometry comprising a water cooled Nd:YAG rod transversely pumped with high-power CW laser diodes. The laser diode light is directly coupled without the use of expensive delivery fibres, micro-lenses or optical ducts into a pump chamber that has been designed to maximise absorption efficiency and promote homogeneous thermal loading and gain distribution. Non-sequential ray-trace simulations of the gain-module suggest a total pump coupling efficiency η_c = 0.80. For long-term reliable operation the pump lasers are operated below the maximum rated drive-current giving an optimum total

pump power of 831 W shared near equally in a 5-fold symmetry. The resultant heating per unit length is a safe factor of 3.6 (+ 0.4, - 0.3) below the measured limit for thermal fracture at 204 (+ 7, - 4) $W.cm^{-1}$. This level of dissipated power corresponds to a fractional heat loading of 0.39 (+ 0.05, - 0.04) with respect to the absorbed pump and leads to an estimated average lens constant for the gain-module under oscillating conditions of $C_t = 8.4 \times 10^{-3}$ dioptres per watt of total incident pump. This value includes the effects of stress-induced birefringence observed between radial and tangential polarisations.

3 Multi-spatial-mode resonators: Part I – Design principles

Resonator development is central to laser system performance and will be reported in three parts. Part I outlines the background physics involved in the design of high-power standing-wave laser oscillators. In part II we introduce the methods by which multi-spatial-mode performance can be simulated and optimised prior to construction. The validity of the models produced is assessed in part III through detailed design and characterisation of single-rod and dual-rod Q-switched laser resonators.

This chapter (Part I) outlines the design principles used to manufacture industrially robust high-power laser resonators based on the Nd:YAG gain-module design reported in chapter 2. The objective is to highlight the properties used in the optimisation of multi-spatial-mode resonators and their component parts in order to achieve higher output powers and promote consistent, reliable and efficient Q-switched operation.

3.1 Spatial characteristics: Beam generation and propagation

When designing a multi-spatial-mode laser it is important to consider resonator stability and how this relates to robust industrial operation. The spatial mode structure generated in a stable resonator has a significant effect on important performance characteristics such as beam quality, waist size, far-field divergence, energy extraction efficiency and total output power. Spatial mode structure can also affect Q-switched pulse evolution, pulse repeatability and CW leakage (pre-lasing).

3.1.1 Spatial modes and resonator stability

In continuation of the work carried out by Schawlow and Townes, Fox and Li [3.1] investigated the use of Fabry-Perot interferometers for the production of regenerative feedback in lasers, or 'optical masers' as they were named at the time. It was observed that after many reflections a steady state is reached by which the relative field distribution generated does not vary from transit to transit and that the transverse amplitude of the field decays at an exponential rate. This steady-state field distribution can be regarded as a 'normal mode' of oscillation in the interferometer (or resonator). Many such normal resonator modes are permissible depending on the initial wave distribution and the losses due to diffraction. Fox and Li also observed that each of these transverse or *spatial* resonator modes has a characteristic self-replicating amplitude and phase. They will therefore each exhibit a unique field distribution orthogonal to the beam axis. This distribution can be mathematically expressed as an eigenfunction and be given rectangular or circular symmetry depending on the shape of the limiting aperture that is inducing the diffraction loss.

The field variations produced by the *transverse electro-magnetic* waves present in the resonator modes are denoted by TEM_{mn} for rectangular symmetry where

m and *n* represent the number of zero irradiance nodes normal to the beam axis in the vertical and horizontal directions, using Cartesian coordinates. For circular symmetry the transverse modes are characterised by cylindrical coordinates and are labelled TEM_{pl}, where *p* and *l* represent the number of radial and angular nodes respectively. Larger values of *m* and *n* or *p* and *l* signify higher order transverse modes and a change in the associated field distributions, a sample of which is illustrated in figure 3.1. The lowest order or *fundamental* spatial mode is labelled TEM_{00} and is typically that with least diffraction loss.

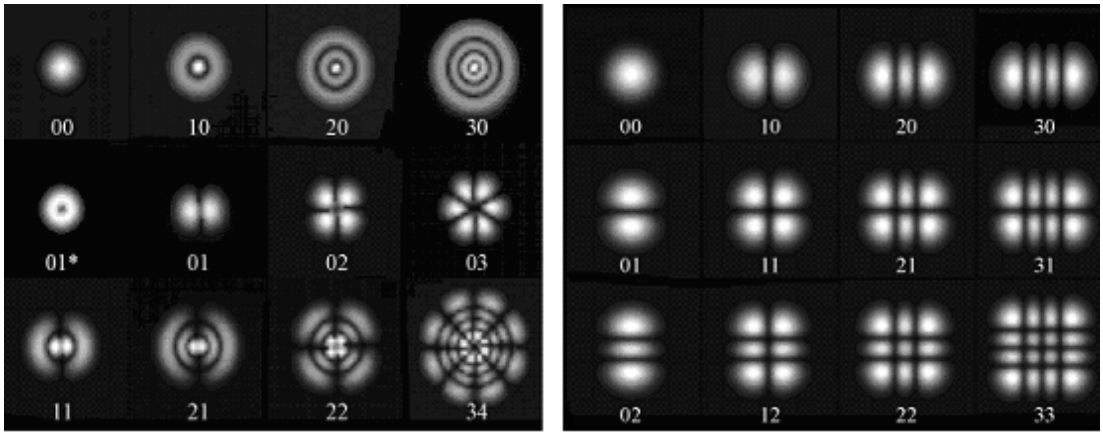

Figure 3.1: The transverse electromagnetic field distributions for normal resonator modes with rectangular and cylindrical symmetry [3.2].

The transverse electromagnetic field distributions produced with cylindrical symmetry can be described by the combination of Gaussian distributions and Laguerre polynomials, thus generating Laguerre-Gaussian beam profiles with irradiance distributions that follow the expression

$$I_{pl}(\alpha,\phi,z) = I_0\left[\frac{2\alpha^2(z)}{w^2(z)}\right]^l\left[L_p^l\,\frac{2\alpha^2(z)}{w^2(z)}\right]^2\left(\cos^2 l\gamma\right)\exp\left(-\frac{2\alpha^2(z)}{w^2(z)}\right) \qquad (3.1)$$

where *z* is the direction of propagation and (α, ϕ) are the polar coordinates in the plane transverse to the beam direction [3.2]. The radial irradiance distributions have been normalised to the spot size of a first order gaussian

profile *w(z)* and defined as the radius at which the irradiance of the TEM_{00} mode drops to $1/e^2$ of its peak value, which is located at the axis of beam propagation. L^l_p is the generalised Laguerre polynomial of order *p* and index *l*.

By the same method, Hermite-gaussian spatial profiles are produced in field distributions with rectangular symmetry by combining similar gaussian distributions with Hermite polynomials. The irradiance distribution of an (*m*, *n*) mode is thus given by

$$I_{mn}(x,y,z) = I_0\left[H_m\left(\frac{x\sqrt{2}}{w(z)}\right)\exp\left(\frac{-x^2}{w^2(z)}\right)\right]^2 \times \left[H_n\left(\frac{y\sqrt{2}}{w(z)}\right)\exp\left(\frac{-y^2}{w^2(z)}\right)\right]^2 \quad (3.2)$$

where H_m and H_n represent the *m*th and *n*th-order Hermite polynomials respectively.

A definitive review of light beam generation in laser resonators is offered by Kogelnik and Li [3.3] who present a study of paraxial rays and their passage through reciprocating optical systems. For paraxial rays the output position y_2 and angle with respect to the axis of propagation y_2' are linearly dependent on the corresponding input parameters y_1 and y_1' such that

$$\begin{vmatrix} y_2 \\ y_2' \end{vmatrix} = \begin{vmatrix} A & B \\ C & D \end{vmatrix} \cdot \begin{vmatrix} y_1 \\ y_1' \end{vmatrix} \quad (3.3)$$

The *ABCD* array is known as the ray transfer matrix for the optical component or system.

In order to determine the spatial mode content of an optical resonator and its ability to sustain a given oscillation Kogelnik and Li considered the system as a series of optical events that occur in a periodic sequence. This sequence can then be classified as either stable or unstable depending on its ability to confine the rays between subsequent passes. To satisfy conditions for stable self-sustained oscillation the round-trip ray transfer matrix for a resonator must obey the inequality

$$0 < \frac{(A+D)}{4} + 0.5 < 1 \tag{3.4}$$

The concept of resonator stability can be demonstrated by considering a passive optical system consisting of two spherical feedback mirrors that can change the sustainability of a given oscillation. For the stability condition to be met a ray leaving a point on a given plane inside the resonator will intersect the same point at the same plane after reflection from both mirrors. Resonator stability can be represented graphically, as shown in figure 3.2. The axes show the '*g*' parameters of the optical system, which in this case can be related to the spacing *d* and radii of curvature R_1 and R_2 of the two mirrors that make up the resonator such that

$$g_1 g_2 = \left(1 - \frac{d}{R_1}\right)\left(1 - \frac{d}{R_2}\right) = \frac{(A+D)}{4} + 0.5 \tag{3.5}$$

This results in a conditional requirement for stability on the (g_1, g_2) plane given by

$$0 < g_1 g_2 < 1 \tag{3.6}$$

The stability condition boundaries can therefore be conveniently displayed by plotting the two branches of the hyperbola corresponding to the equation $g_1 g_2 = 1$.

A general review of laser resonator technology can be found in two parts by Siegman [3.4; 3.5]. However, in order to find the exclusive treatment of resonator design for solid-state lasers we must look to publications such as those produced by Stickley [3.6] or Osterink and Foster [3.7]. Significantly, these works discuss how the thermal lensing in a solid-state gain medium, induced by optical pumping, can have a significant effect on the stability of a resonator. It is essential to consider this effect when attempting to control the performance of a solid-state laser. Before moving on to discuss thermally active resonators in detail we shall review the behaviour of Gaussian beams in free space propagation.

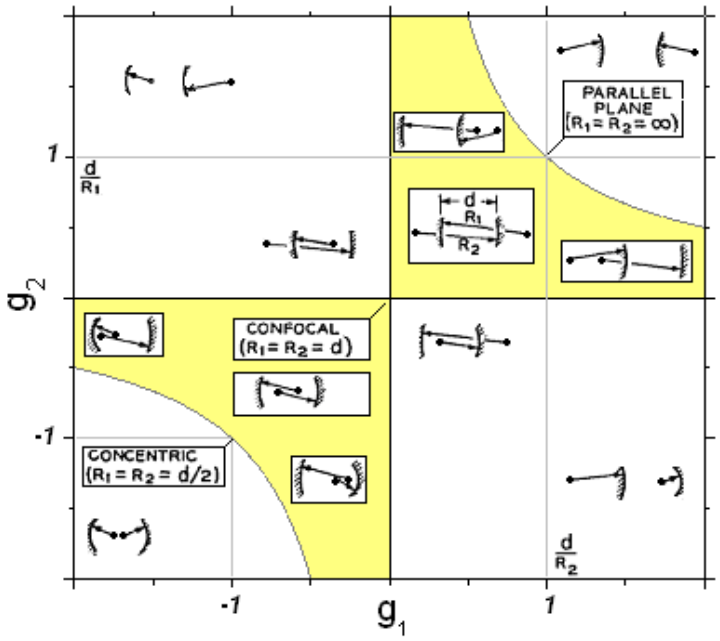

Figure 3.2: Resonator stability diagram. Unstable resonator systems lie in the un-shaded regions [3.3].

3.1.2 Gaussian beam propagation and the M^2 factor

Prior to considering the behaviour of higher order spatial modes it is useful to be able to define the properties associated with the TEM_{00} fundamental. Independent of rectangular or cylindrical symmetry, this mode exhibits a first order Gaussian irradiance distribution centred on the axis of propagation. The associated complex electric field amplitude for such a beam is valid both inside and outside of a laser resonator and has the form

$$E(u,z) = E_0\left(\frac{w_0}{w(z)}\right)\exp\left(\frac{-u^2}{w^2(z)}\right)\exp\left[-i\left(kz + \frac{ku^2}{2\beta(z)} - \zeta(z)\right)\right] \qquad (3.7)$$

where u is the transverse radial displacement from the axis of beam propagation and w_0 is the radius of the beam at a waist positioned at $z = z_0 = 0$. The wave number $k = 2\pi/\lambda$ where λ is the wavelength of the propagating wave and $\beta(z)$ is the radius of curvature exhibited by the wavefront of the beam. $\zeta(z)$ represents a longitudinal phase delay known as the Gouy phase shift that occurs

due to the propagation in the z direction such that $\zeta(z) = \tan^{-1}(\lambda z/\pi w_0^2)$. A contour of the resultant propagating gaussian beam is illustrated in figure 3.3, this is also referred to as a caustic curve.

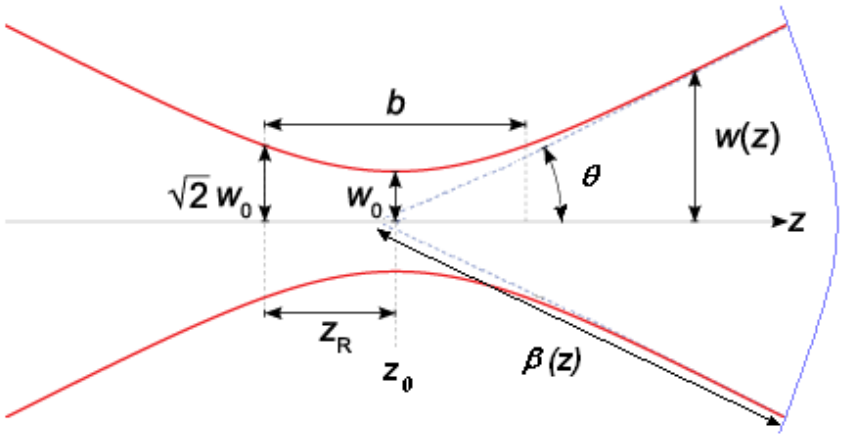

Figure 3.3: Contour (or caustic) of a gaussian beam waist (red) and the propagating wavefront (blue).

The beam radius $w(z)$ increases with displacement z from the waist position and is described by the equation

$$w^2(z) = w_0^2\left[1+\left(\frac{\lambda z}{\pi w_0^2}\right)^2\right] \tag{3.8}$$

At the waist position z_0 the wavefront is observed to be planar, that is $\beta(z) = \infty$. As the beam propagates away from this position a changing spherical curvature in the wavefront is observed, this is given by the relation

$$\beta(z) = z\left[1+\left(\frac{\pi w_0^2}{\lambda z}\right)^2\right] = z\left[1+\left(\frac{z_R}{z}\right)^2\right] \tag{3.9}$$

where $z_R = (\pi w_0^2)/\lambda$ and is defined as the distance from the beam waist to where the radius has increased by a factor of $\sqrt{2}$, this is known as the Rayleigh range. It is over twice the Rayleigh range that the beam is considered to be 'focused', this distance is commonly referred to as the confocal parameter $b = 2z_R$.

At $z >> z_R$ the beam is seen to expand linearly with distance from the waist position. In this condition we can define a *far-field* half-angle divergence for the beam θ given as

$$\theta = \frac{\lambda}{\pi w_0} \tag{3.10}$$

Care must be taken when using the far-field approximation to calculate a geometrical waist position, which is not at the same place as the hyperbolic gaussian waist. However, for most practical applications the difference is considered to be negligible.

For many lasers the treatment of gaussian beams is satisfied by the aforementioned equations. This is because the majority of lasers are designed to operate at or close to a single, invariably fundamental, spatial mode. However, for the optimisation of multi-spatial-mode resonators we must address the treatment of higher order modes and the effect they have in deviating from the fundamental gaussian beam propagation equations.

On inspection of the irradiance distribution equations (3.1) and (3.2) we can see that the lateral extent of higher order Hermite-gaussian or Laguerre-gaussian modes increases with the mode numbers m, n and p, l respectively. As the number of spatial modes increases the focusability of the beam decreases such that the smallest waist for a given half-angle divergence is increased, thus moving away from the diffraction limited condition. This is considered to be a reduction in the beam quality.

In a tutorial paper on 'How to (Maybe) Measure Laser Beam Quality', Siegman [3.8] discusses an approach to defining beam quality that uses the *variance method* by which the second moment of the irradiance profile is used to define beam width. The key to this method is that the second moment of a laser beam obeys a universal quadratic free-space propagation rule of the form

$$\sigma_x^2(z) = \sigma_{x0}^2 + \sigma_\theta^2 \times (z - z_0)^2 \tag{3.11}$$

which holds for any arbitrary real laser beam, whether it is gaussian or non-gaussian, fully coherent or partially incoherent, single or multiple spatial mode. σ_{x0} is the power density variance at the beam waist and σ_θ is the variance of the angular distribution of the beam leaving the waist.

From this it is found that the second-moment-based radius of an arbitrary non-diffraction limited beam *W(z)* will propagate in free space similar to that of an ideal gaussian beam, except for a multiplication factor *M* in the far-field angular distribution. The width of the beam at any point along the propagating z-axis is thus defined as

$$W^2(z) = W_0^2 + M^4 \times \left(\frac{\lambda}{\pi W_0}\right)^2 (z - z_0)^2 \tag{3.12}$$

where W_0 is the beam width at the waist. From this definition the near-field far-field product of any arbitrary beam can be expressed as follows.

$$W_0 \times W_x(z) = M^2 \times \frac{z\lambda}{\pi} \tag{3.13}$$

This shows that an M^2 parameter can be used to give a measure of how non-ideal the spatial properties of real laser beams are with respect to an ideal gaussian model. This *beam propagation factor*, or *figure of merit*, is therefore considered to be a basic measure of laser beam quality and can be expressed as a function of beam width in the near and far-fields as follows

$$M^2 = \frac{\pi W_0^2}{\lambda z}\sqrt{\left(\frac{2W(z)}{2W_0}\right) - 1} \tag{3.14}$$

The M^2 factor can essentially be regarded as the number of times diffraction limited a beam is. That is, the diffraction limited fundamental TEM_{00} mode has an M^2 value of 1. The second moment radius of the fundamental mode is the same as the $1/e^2$ irradiance value previously used. Larger beam waists are seen to occur with the linear superposition of higher order modes. In this case the beam radius measured to the second moment is not necessarily at the $1/e^2$

irradiance value. However, the gaussian beam propagation equations (3.1) to (3.10) still hold if λ is replaced by $M^2\lambda$. For example, the beam radius *W(z)* and far-field half-angle divergence Θ of a multi-mode beam are given by the following equations

$$W^2(z) = W_0^2\left[1+\left(\frac{M^2\lambda z}{\pi W_0^2}\right)^2\right] \tag{3.15}$$

$$\Theta = M^2\frac{\lambda}{\pi W_0} \tag{3.16}$$

It is useful to note that for the same M^2 a reduction in the waist size will result in a corresponding increase in the far-field divergence.

M^2 is now recognised as an ISO standard for quantifying laser beam quality [3.9]. Reliable measurements of the M^2 factor can be performed by detailed examination of the second moment radius at different planes through the waist or caustic curve in the beam [3.10]. The advantage of using the second moment as a measure of beam radius is that the subsequent mixed mode irradiance distribution is equal to the power weighted sum of the M^2 values for the component pure spatial modes. Although an increase in higher order mode content leads to an increase in M^2 it is not possible to recover the relative contributions of individual pure modes to a mixed, multi-mode combination unless exact information on the amplitude and phase at each point across the beam is obtained. This is difficult to achieve in practice and not usually necessary.

When applying the beam propagation equations to the multiple-spatial-mode structure sustained inside a stable laser resonator it is useful to consider an embedded first order gaussian beam that can be used as a mathematical reference within the multi-mode envelope, as illustrated in figure 3.4. The embedded gaussian is simply related to the multi-mode beam such that

$$W(z) = Mw(z) \tag{3.17}$$

and $\Theta = M\theta$ (3.18)

A *beam parameter product* can also be defined by multiplying the waist radius and half-angle divergence of the multi-mode beam as follows.

$$W_0.\Theta = (Mw_0)(M\theta) = M^2(w_0\theta) \tag{3.19}$$

From this we see that the beam propagation factor can again be obtained, yielding the relation

$$M^2 = \frac{W_0\Theta}{w_0\theta} \tag{3.20}$$

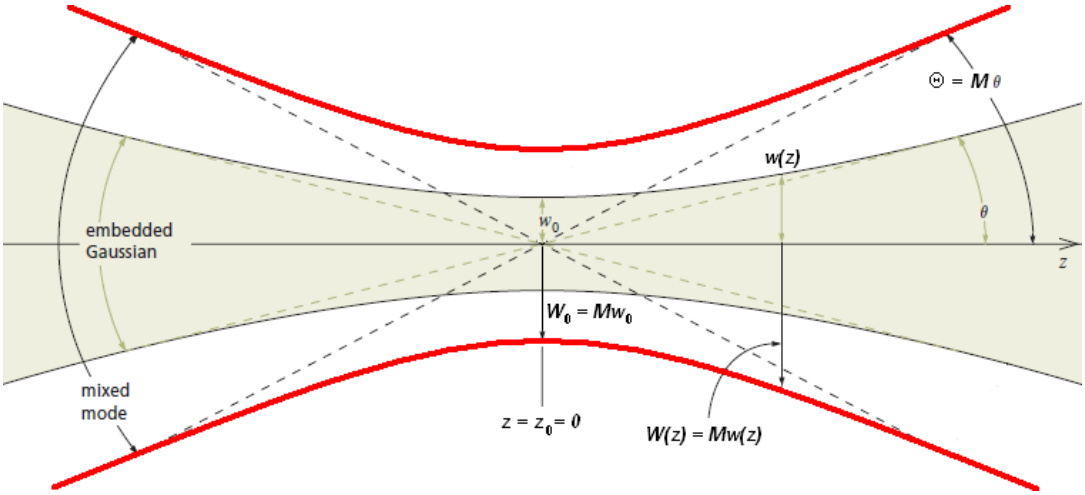

Figure 3.4 Contour of a multi-spatial-mode beam waist (red) and its embedded gaussian (grey).

We may now extend this treatment of gaussian beams to address the properties of the spatial modes generated by a stable resonator and investigate how spatial mode content can be optimised to benefit laser performance.

3.1.3 Dynamic stability and thermally active resonators

There are a number of conditions required to ensure effective operation of an industrial laser resonator. Efficient laser action is promoted if the beam generated inside the resonator fills the active medium and extracts as much of

the available gain as possible. In addition to this, the resonator must also enable the desired performance in terms of output power and beam properties. The laser as a product should be designed to best maintain these characteristics despite inevitable variations in pump power, mechanical alignment and component characteristics for the same laser and from system to system. Historically, most laser resonators are designed to function with the highest possible beam quality, operating at or close to the fundamental spatial mode. We will consider this condition before addressing the implications of multi-spatial-mode operation.

The variability in passive (empty) resonator stability with small changes in mirror curvature was investigated by Chesler and Maydan [3.11] who defined an index of axial sensitivity by assessing the change in g_1g_2 produced by a given perturbation. This model was adapted for active solid-state resonators by Steffen et al [3.12; 3.13] who incorporated a variable pump-induced thermal lens. In this case the resonator was considered resistant to perturbations in the thermal lens if the beam divergence and mode volume are insensitive to changes in the focal length f of the internal lens. The fundamental mode volume in a solid-state rod was maximised by placing it close to one mirror and making its length negligible compared to the resonator length.

A more flexible model for fundamental mode operation was suggested by Magni [3.14], which allows the optimisation of thermally active stable resonators without imposing any restriction on resonator dimensions or rod position. This model makes use of an equivalent resonator whereby the pumped rod of length L is treated as a thin lens in terms of the round trip ray transfer matrix. The mirror positions L_1 and L_2 are measured relative to the principle planes P_1 and P_2 of the rod when considered as a thick lensing element, as illustrated in figure 3.5. Again, particular emphasis was placed on the conditions by which the fundamental mode size at the equivalent thin lens is maximised, while keeping the resonator insensitive to fluctuations in the refractive power.

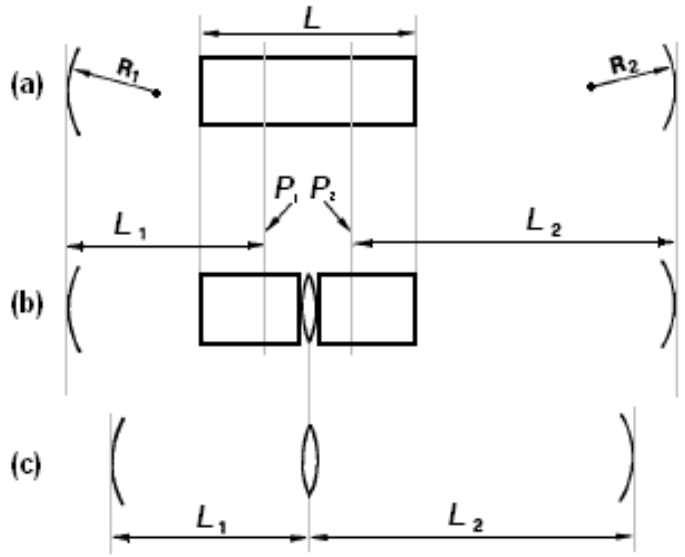

Figure 3.5 Equivalent resonators with (a) a rod-like lens; (b) a thin lens between two pieces of homogeneous media [exactly equivalent to (a) outside of the rod and approximately inside]; and (c) a thin lens [equivalent to (a) and (b) outside the rod]. The gaussian beam sizes on the lenses are the same in (b) and (c) and approximately equal to that in the middle of the rod in (a) [3.14].

This model shows that for a given resonator configuration there are always two permissible zones of stability that can occur with changing internal lens power $D = 1/f$. The origin of the two stability zones can be understood by revisiting the resonator stability diagram shown in figure 3.2. As the lens power is altered the point representing the resonator on the (g_1, g_2) plane moves along a straight line which intersects the hyperbola $g_1 g_2 = 1$. We therefore find that for a thermally active resonator

$$g_i = 1 - DL_j - \frac{L_i + L_j - DL_iL_j}{R_i} \tag{3.21}$$

where i and j are interchangeable such that $i, j = 1, 2$; $i \neq j$.

Figure 3.6 shows how the resonator stability changes with internal lens power highlighting the origin of the two permissible stability zones, one of which is always located in the third quadrant of the stability diagram (bottom left). The

direction by which the line of resonator stability moves across the (g_1, g_2) plane can be obtained by introducing the parameters u_1 and u_2 where

$$u_i = L_i\left(1-\frac{L_i}{R_i}\right) \tag{3.22}$$

The conditions for u_1 and u_2 that govern the direction of the stability line are also illustrated in figure 3.6.

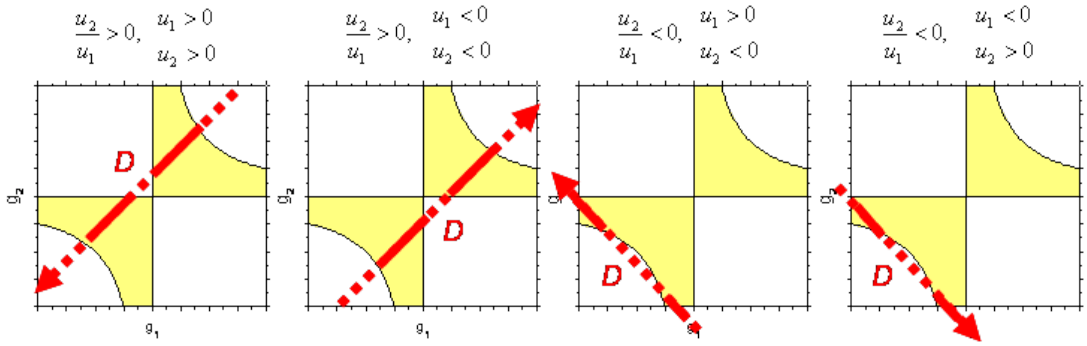

Figure 3.6: Resonator stability diagrams showing the origin of the two permissible stability zones that lie along lines of changing internal lens power for different resonator configurations. The conditions that govern the slope and direction of the line are shown above.

For reliable fundamental mode operation the gaussian-beam waist size (radius) at the equivalent thin lens (corresponding to the middle of the rod) w_a must be stationary with respect to the refractive power of the lens D thus giving the condition

$$\frac{dw_a}{d(1/f)} = \frac{dw_a}{dD} = 0 \tag{3.23}$$

where,

$$w_a^2 = \frac{\lambda}{\pi}\left[\frac{4u_1u_2g_1g_2+(u_1-u_2)^2}{(1-g_1g_2)g_1g_2}\right]^{1/2} \tag{3.24}$$

Fundamental mode resonators that satisfy the condition defined by equation (3.23) are said to be *dynamically stable*, as illustrated in figure 3.7. It is possible

to produce resonator configurations with dynamic stability where the two zones meet either at the origin of the (g_1, g_2) plane or at any point on the $g_1g_2 = 1$ hyperbola in the third quadrant. However, both of these conditions are located at boundaries of stability and therefore do not represent practically useful resonator configurations.

For resonators with a single lensing element the two stability zones always have the same width in terms of refractive power, which typically varies proportionally with absorbed pump. This width ΔD satisfies a relation with the minimum achievable fundamental mode size at the lens for both zones w_{am} described by the equation

$$\Delta D = \frac{2\lambda}{\pi w_{am}^2} \tag{3.25}$$

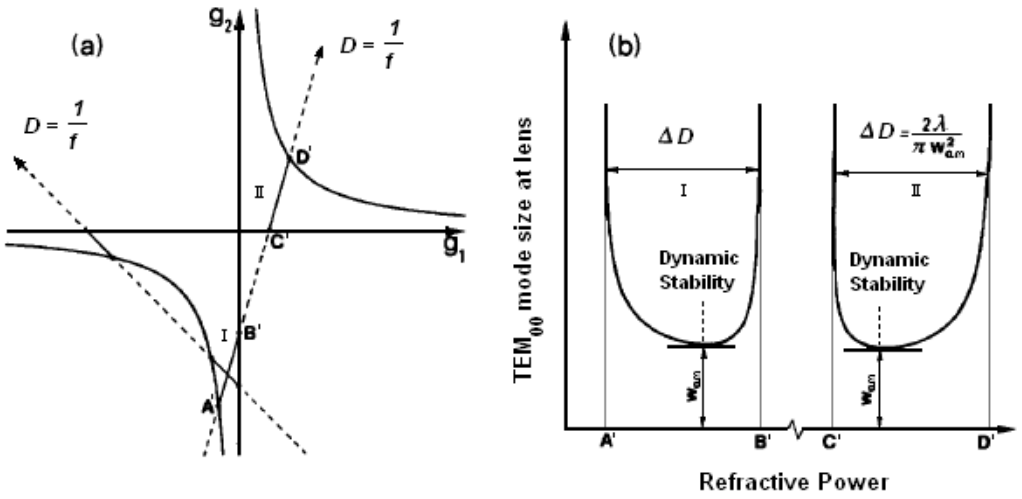

Figure 3.7 (a) Example stability diagram on the (g_1, g_2) plane. The stability zones are illustrated by solid black lines that intersect the stability regions (arbitrarily labelled I and II) and (b) The fundamental mode radius at the lens as a function of lens power. A', B', C' and D' represent the boundaries of resonator stability [3.15].

In order to maximise fundamental mode volume in the active medium and promote the efficient extraction of stored energy it is necessary to produce a minimum waist size at the laser rod that is comparable to its radius a. To avoid

introducing excessive diffraction loss due to beam truncation by the limiting aperture [3.16; 3.17], which is in this case set by the laser rod, we can apply the constraint

$$2a \cong \pi w_a \tag{3.26}$$

It is now possible to obtain a set of resonator parameters R_1, R_2, L_1 and L_2 that satisfy this mode fill condition and the condition for dynamic stability defined by equation (3.23).

3.1.4 Multi-spatial-mode resonator design

We will now consider laser resonators that are capable of supporting multiple higher-order spatial modes. As previously discussed, efficient operation is promoted if the beam generated inside the resonator is made to fill the active medium and exploit as much of the inverted population as possible. The beam generated in a resonator that is designed to allow the proliferation of higher order spatial modes will naturally fill the limiting aperture, which is usually characterised by the cross-section of the laser rod. This essentially means that we are no longer concerned with maximising the size of the fundamental mode at the gain medium. However, we are still interested in maintaining efficient high-power operation with the required beam properties despite small variations in pump power, mechanical alignment and component performance. For industrially robust multi-spatial-mode operation it is therefore prudent to identify a more relevant, measurable condition for dynamic stability and to define this condition as a function of the controllable resonator dimensions and parameters. At this point we will include rod end curvatures as another controllable resonator parameter. This means that the gain-module may be considered as a lensing element with both a dynamic, positive thermal lens induced component and a static, positive or negative facet-curvature related component. The result is a net thin lens equivalent of refractive power D_n that can be given an offset by altering the rod facet radius of curvature R such that

$$D_n = \left(\frac{2(n_r - 1)}{R} + C_t P \right) \tag{3.27}$$

where n_r is the first order refractive index of the rod, P is the total pump power and C_t is a proportionality constant introduced in chapter 2, which describes the thermal lensing characteristics of the gain-module in terms of the refractive power per unit of incident pump under oscillating conditions. In this case the same rod facet curvature is applied to both rod ends.

In a similar step to that seen in the treatment of fundamental mode operation we can apply this equivalent thin lens approximation to a thick rod-like lens system [3.18] by referencing the cavity mirror positions relative to the principle planes P_1 and P_2, which are located at distances h_1 and h_2 from the corresponding rod ends where

$$h_1 = h_2 = \frac{L}{2n_r} \tag{3.28}$$

This first order approximation is valid in the majority of practical cases when the focal length is greater than the rod length. Note that in this condition the position of the principle planes can be assumed to be independent of the pump power. The resultant resonator configuration is illustrated in figure 3.8.

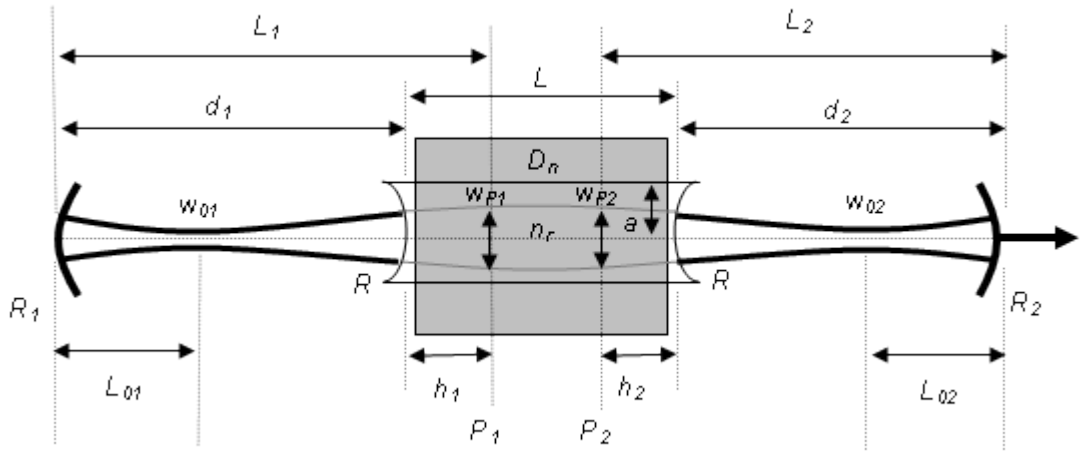

Figure 3.8 Schematic of the multi-mode resonator model showing the controllable cavity dimensions and a resultant embedded gaussian (not to scale).

Using equations (3.21) and (3.27) we can now define the g_1 and g_2 stability parameters as a function of rod facet radius of curvature R (in meters), cavity mirror curvatures R_1 and R_2 (in meters), total pump power P (in watts) and distances between the principle planes P_1 and P_2 and the cavity mirrors L_1 and L_2 (in meters), such that

$$g_i = \left[1 - \frac{\left(L_i + L_j\right)}{R_i}\right] - \left[D_n L_j \left(1 - \frac{L_i}{R_i}\right)\right]$$
$$= \left[1 - \frac{\left(L_i + L_j\right)}{R_i}\right] - \left[L_j \left(\frac{2\left(n_r - 1\right)}{R} + C_t P\right)\left(1 - \frac{L_i}{R_i}\right)\right] \qquad (3.29)$$

again where $i = 1$ when $j = 2$ and $i = 2$ when $j = 1$.

The distances between the principle planes and the cavity mirrors L_1 and L_2 can be simply calculated using equation (3.28) and two easily measurable distances from the rod facets to the corresponding cavity mirrors d_1 and d_2 such that

$$L_i = h_i + d_i = \frac{L}{2n_r} + d_i \qquad (3.30)$$

Using this model we can extract an expression for the size of the two embedded gaussian waists w_{oi} and their positions in the resonator relative to the corresponding end mirror L_{oi} for an operating wavelength λ whereby

$$w_{oi}^2 = \frac{\lambda L^*}{\pi n_r} \cdot \frac{\left[g_i g_j \left(1 - g_i g_j\right)\right]^{1/2}}{g_j \left(\frac{L^*}{R_i}\right)^2 + g_i \left(1 - g_i g_j\right)} \qquad (3.31)$$

and $$L_{oi} = L^* \cdot \frac{g_j \left(\frac{L^*}{R_i}\right)}{g_j \left(\frac{L^*}{R_i}\right)^2 + g_i \left(1 - g_i g_j\right)} \qquad (3.32)$$

L^* is the effective length of the equivalent cavity, which for a single-rod resonator is given by the expression

$$L^* = L_1 + L_2 - D_n L_1 L_2 \tag{3.33}$$

By combining equations (3.31) and (3.32) we can further derive an expression for the size of the embedded gaussian at the principle planes w_{Pi}, which can also be represented as a function of the Rayleigh range z_R. This yields the expression

$$w_{Pi}^2 = w_{oi}^2 \left[1 + \frac{(L_i - L_{oi})^2}{\left(\frac{n_r \pi w_{oi}^2}{\lambda_0} \right)^2} \right] = w_{oi}^2 \left[1 + \frac{(L_i - L_{oi})^2}{z_R^2} \right] \tag{3.34}$$

Importantly, for a resonator designed to support multiple spatial modes, the variation in resonator stability determines the number of stable modes that the laser will operate on given sufficient gain. This can be characterised by the resulting M^2 factor for the resonator, which is in turn related to the embedded gaussian via equation (3.20). We can also define the M^2 as a ratio between the square of the embedded gaussian beam size at the limiting aperture and the square of the multi-mode beam size at the same plane. It is reasonable to assume that the limiting aperture will always be confined within the cylindrical Nd:YAG rod and is therefore located close to one of the principle planes of the rod-like lens, each of which imposing the same aperture size. The extent of the M^2 is thus limited by the maximum embedded gaussian beam radius generated at the principle planes such that

$$M^2 = \min\left\{ \frac{{W_{P1}}^2}{w_{P1}^2}; \frac{{W_{P2}}^2}{w_{P2}^2} \right\} \tag{3.35}$$

To obtain an accurate relationship between the hard aperture of the rod and W_{Pi}, the multi-mode beam-size produced at the principle planes, we must apply a constraint similar to that defined by equation (3.26). Although there will be a difference in the field distribution of the higher order spatial mode structure at the hard aperture, to the first approximation, it is assumed that

$$2a \cong \pi W_{Pi} \tag{3.36}$$

where a is the radius of the laser rod. Using equations (3.35) and (3.36) we can now obtain a final expression for the M^2 whereby

$$M^2 = \min\left\{\frac{1}{w_{P1}^2}\left(\frac{2a}{\pi}\right)^2; \frac{1}{w_{P2}^2}\left(\frac{2a}{\pi}\right)^2\right\} \tag{3.37}$$

Note that for asymmetric resonators the limiting aperture can alternate between the principle planes with changing internal lens, thus more accurately reflecting what will occur in practice. Substituting equations (3.29 – 3.34) into (3.37) therefore gives us a rather substantial but very useful expression for the beam propagation parameter as a function of all controllable resonator dimensions R_1, R_2, d_1, d_2, R, a and L. This provides us with a powerful mathematical model that can be used to define the output properties of a stable laser resonator and investigate conditions under which they may become dynamically stable. This is discussed at length in chapter 4.

3.2 Temporal characteristics: CW-pumped, actively Q-switched laser resonators

Q-switching is a well known method for generating short, high-energy output pulses from a laser resonator [3.19]. In a Q-switched laser the onset of stimulated emission is temporarily inhibited by increasing the cavity loss. This enables the build-up of a large population inversion that is well above the threshold required for oscillation at a subsequent point when the cavity loss is reduced. At this point the stimulated radiation is allowed to rapidly build-up, exhausting the surplus excitation. The light generated then decays from the resonator as a function of the inherent parasitic and output coupling losses before the excess cavity loss is reintroduced in order to repeat the process.

For this work we will concentrate on the investigation of active Q-switching using compression mode acousto-optic modulators (AOMs). When engaged with RF (radio frequency) power these modulators induce changes in the cavity

Q-factor through the production of a diffractive phase grating. The way by which a Q-switched pulse is developed depends on the ratio of the pulse build-up time and the finite switching time of the AOM within the resonator. For the gain, loss and spatial mode characteristics expected to be produced in this work, we can assume that the pulse build-up time is approximately equal to or greater than the switching time. Operation will therefore be in the *fast Q-switching* regime. Theoretical quantitative comparisons of these parameters are made in section 4.2.

A number of salient industrial applications, detailed in chapter 1, are known to require particularly consistent Q-switched pulse generation. Pulse-to-pulse inconsistency can manifest as a variation in the timing of the pulse with respect to the switch (jitter) and as a variation in the pulse energy. For active Q-switching these forms of pulse variability can be interrelated and may also affect an irregularity in the pulse duration. The following sections provide a summary of the controllable and non-controllable conditions that limit consistent pulsing and highlight how these conditions are influenced by multi-spatial-mode operation. Initially, the circumstances that promote the reduction of free-running Q-switched pulse inconsistency in CW-pumped resonators are addressed. This is followed by the design principles used to ensure consistent pulse generation during time-gated bursts of resonator Q-switching.

3.2.1 Repetitively Q-switched pulsing consistency

Figure 3.9 illustrates the conditions that influence the Q-switched pulse consistency of a thermally active resonator operating at the fundamental (TEM_{00}) spatial mode only. There is a minimum level of inversion and corresponding pump power P_{min} required for oscillation given the output coupling and parasitic cavity loss. In addition to this, the resonator must also be stable with suitable cavity dimensions for the pump dependent internal lensing that is present. In this particular arbitrary case the minimum pump level needed for resonator stability P_s is shown to be above P_{min}. The threshold for oscillation

therefore lies at this resonator stability condition. It follows that another oscillation terminating condition will be present at a higher pump power $P_{s'}$ where the resonator again becomes unstable. In this case we will consider operation within a single resonator stability zone, as defined in section 3.1.3. It is useful to note that power $P_{s'}$ will vary between a thermal lens condition close to that observed without oscillation at low pulse repetition frequency f_R and a thermal lens condition that tends toward that associated with CW oscillation at multiple kilohertz PRF. Figure 3.9 also illustrates the effect that occurs when the ability of the Q-switch to hold-off oscillation is reduced. This can occur due to AOM misalignment, decrease in RF power to the AOM or increased cavity gain. The result is a loss of Q-switched pulse consistency at the upper limiting conditions for oscillation and is initially observed at low PRF. In this case the maximum pump power must be reduced to a level P_H to maintain consistent pulsing.

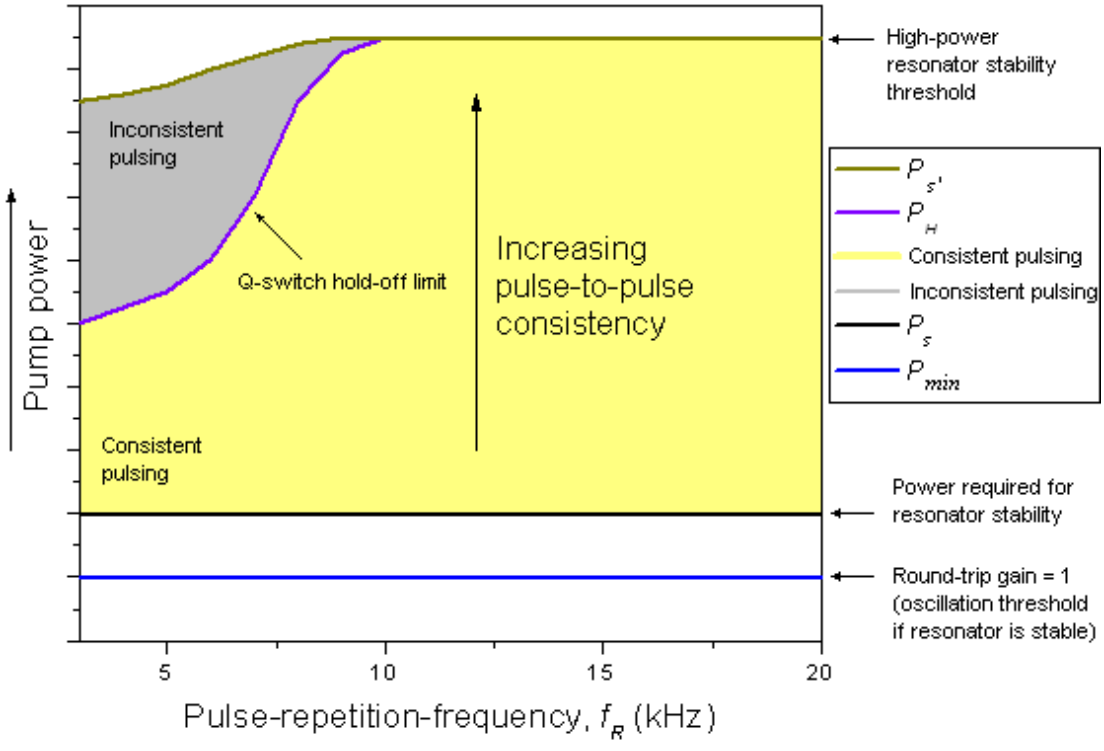

Figure 3.9 An illustration of the pump-power related conditions that influence Q-switched pulse consistency as a function of PRF for a single-spatial-mode thermally active resonator.

As the gain is increased above the threshold for oscillation the pulse moves forward in time with respect to the Q-switch. The pulse also exhibits shorter durations and higher energies, as illustrated in figure 3.10. At increased gain the statistical likelihood that a pulse evolving from spontaneous emission will develop in a similar manner to the previous will increase, thus reducing the pulse-to-pulse inconsistency.

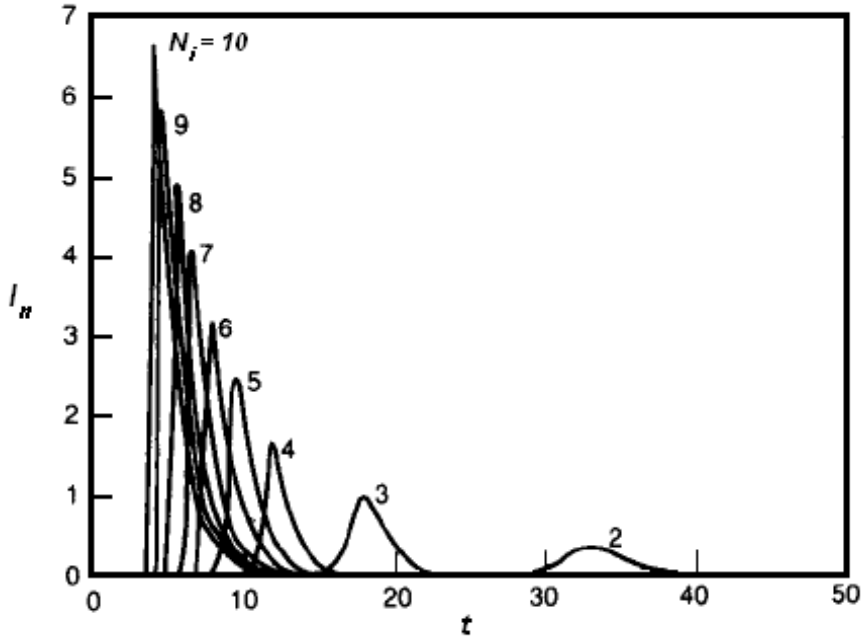

Figure 3.10 Normalised optical intensity I_n of Q-switched pulses as a function of time for an arbitrary single-spatial-mode resonator calculated for an initial inversion that is N_i number of times above the spatially averaged threshold inversion density (optical intensity normalised to the N_i = 3 case) [3.20].

We can now consider the effect of multi-spatial-mode oscillation on the conditions for consistent Q-switched pulsing. Unexpectedly, empirical observation has revealed that at low pump power the evolution of Q-switched pulses can become inconsistent in the presence of numerous spatial modes. This is characterised by a pulse build-up time that may vary by several times that of the average pulse duration, which also exhibits a significant variation along with

a corresponding fluctuation in the pulse energy. Moreover, at lower pump-powers the beam size at the AOM is generally increased, which slows the switching time. This can become troublesome for longer cavities at low PRF where double-pulsing may also occur. At a pump level P_{m1} above P_{min} and P_s the Q-switched pulse consistency increases to a level similar to that observed with single-spatial-mode operation, whereby the timing jitter is only a fraction of the pulse duration and the energy fluctuation is fraction of the average pulse energy. Although the reasons for the spatial-mode-related pulsing inconsistency at low gain are not clear the observed trends with changing pump-power and PRF are illustrated in figure 3.11.

For multi-spatial-mode operation the Q-switched pulse inconsistency is usually observed to reach a minimum at a specific pump power P_o. This level generally corresponds to a maximum in the product between the number of spatial modes generated, as characterised by the M^2 and equation (3.37), and the gain that the pulse will experience, which increases with pump power and decreases with PRF. It is hypothesised that for a given level of gain a larger number of spatial modes will increase the statistical likelihood of a pulse building up sooner with respect to the Q-switch and in the same manner as the previous pulse. As the gain available for pulse development decreases at higher PRF the spatial-mode-related partition noise can also be seen to affect the upper limiting conditions for pulse consistency. At this point both the upper P_{m2} and lower P_{m1} spatial-mode related limits for non-chaotic pulsing tend toward P_o. This essentially restricts the pump power over which consistent pulsing can occur and imposes an upper limit on the operating PRF. This can be lower than the maximum PRF limit conventionally set by the florescence-lifetime related energy-storage capacity. Note that the reduction in pulse consistency due to insufficient Q-switch hold-off can limit operation at P_o, particularly for lower PRF (although in this case the pulse consistency is inherently improved for a given pump power due to the increased gain that is accumulated between pulses).

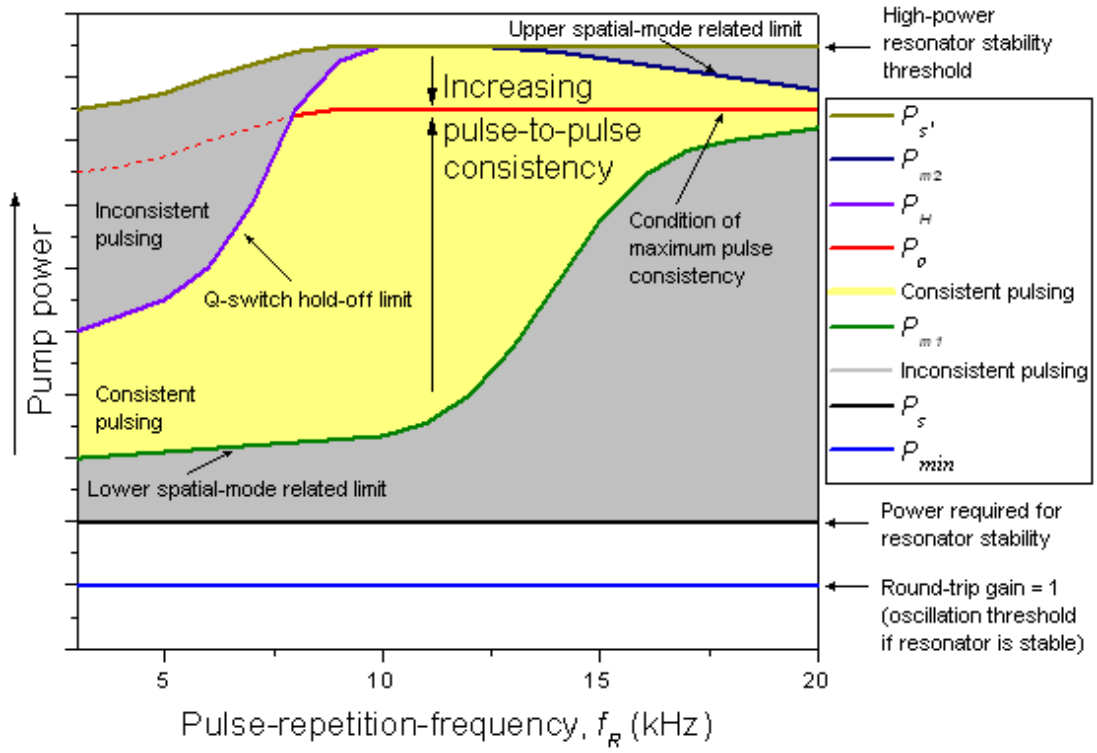

Figure 3.11 An illustration of the pump-power related conditions that influence Q-switched pulse consistency as a function of PRF for a multi-spatial-mode thermally active resonator.

3.2.2 First pulse suppression and transient thermal lens control

The minimisation of pulse inconsistency in free-running repetitively Q-switched operation is often not sufficient for process applications that require highly repeatable pulsing over intermittent periods. In this case there are two additional factors that can adversely affect pulse consistency. The extent to which these factors manifest is related to the on-off (duty) cycle of the gated pulsing and the operating PRF. When an Nd:YAG laser operating at kHz repetition frequencies is inhibited for durations longer than the pulsing period the additional gain build-up will result in an anomalous subsequent first pulse. When this occurs the first pulse in a burst of pulses can exhibit higher energy and shorter duration compared to the typical free-running case, thus tending toward the limiting conditions associated with single-shot operation (which is

further discussed in section 4.2). This effect will arise for process cycle off-times in the order of the fluorescent life-time (~ 230 μs for Nd:YAG) and longer. Moreover, an anomalous first pulse can also affect the subsequent gain available to a number of following pulses.

Various tried and tested methods for first pulse suppression are commercially available from AOM driver manufacturers. All of these methods essentially involve altering the RF power supplied to the AOM Q-switch in order to control the gain available to the initial pulse, or pulses. For example, this can be achieved by limiting the reduction in RF power used to generate the first pulse. In this case the remaining residual cavity loss restricts the amount of energy that is extracted on pulse build-up. However, the remaining diffraction may result in a first pulse that has dissimilar spatial characteristics to the following pulses. Another method of first pulse suppression that resolves this peripheral effect but adds another is to bleed-out a controlled amount of surplus gain via low power CW oscillation over a period prior to the first pulse. This is typically achieved by gradually reducing RF power over a few hundred microseconds (typically 200 μs) so that a Q-switched pulse is not generated and is commonly referred to as pre-pulse kill (PPK).

The second factor that adversely affects gated pulse consistency, particularly at higher PRF, is the change in thermal lens that can occur between oscillating and non-oscillation conditions. This issue will transpire on initial start-up of the laser and for long process-cycle on and off times. Generally, the thermalisation of Nd:YAG with change in heat load takes place over large fractions of a second. For gated pulse operation with on and off times in the order of the thermalisation time or greater the effect on laser output manifests as a deviation from the expected pulse energy, duration and timing jitter over many Q-switched pulses. However, we have shown that it is possible to eliminate these transient changes in thermal lensing by means of a novel pump power control technique.

When using laser diodes it is possible to rapidly modulate the pump level in order to maintain a constant refractive power at the rod with or without the presence of laser oscillation. During periods of Q-switched pulsing the laser is allowed to operate at the optimum pump power for maximum reliable diode output. When the laser is gated-off for long periods without oscillation the CW pump power is reduced to a level that contributes an equivalent amount of heat load as the conditions with oscillation. As discussed in chapter 2, previous investigations suggest increases of around 10 % in the amount of absorbed pump that contributes to thermal lensing between oscillating and non-oscillating conditions. For the gain-modules used here the optimum pump level is set at 50 A drive current, which therefore requires modulation in order of 5 A for transient lens control.

Figure 3.12 shows a triggering scheme for gated pulse operation that incorporates pre-pulse kill and pump diode modulation. This scheme enables consistent pulsing for any arbitrary duty cycle. The specially designed process electronics simply require a TTL input gate signal to produce a controlled burst of Q-switched pulses, which are triggered by an internal signal generator. A predetermined duration of around 500 μs is typically set between the input gate and output pulsing to accommodate the response time of the pump-diode power-supply and the required PPK delay. This is long enough in advance for the pump to reach the operating level before pulsing starts and a short enough to avoid thermalisation. Commercial laser-diode power-supplies are able to operate as current sources with slew rates of around 100 $A.ms^{-1}$. A modulation of 5 A gives a minimum required ramp time of around 50 μs and is initiated on receipt of the input gate signal. A trigger for PPK is generated an amount of time after the input gate so that an adequate PRF dependent delay can be provided to the RF driver before pulsing begins. This delay typically ranges between 250 μs and 450 μs. Practical investigation of PPK and transient thermal lens control by pump diode modulation is reported in section 5.2.4.

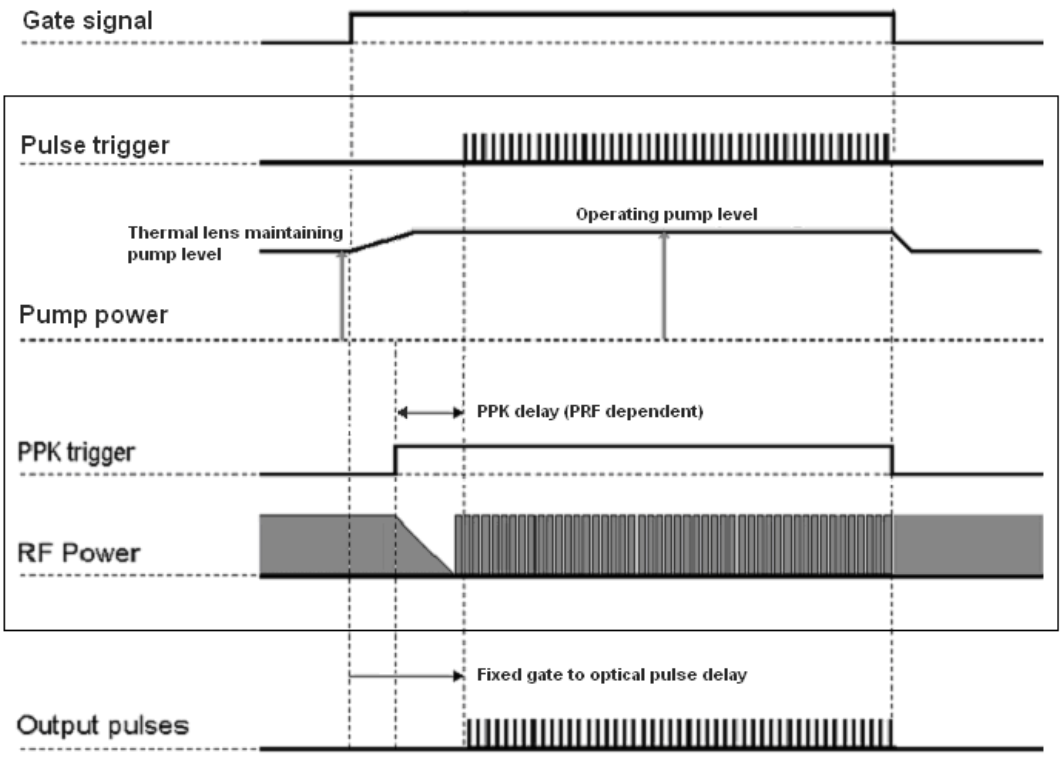

Figure 3.12 An illustration of the input, process and output signals associated with pre-pulse kill (PPK) and transient thermal lens control by diode modulation.

3.3 Product engineering and cost control

The previous sections outline the theoretical background used to design multi-spatial-mode lasers with optimised performance. Total optimisation is achieved when all output spatial and temporal beam characteristics required by the target application are produced with the highest efficiency, maximum dynamic stability, minimum misalignment sensitivity and at a sufficient margin from self-induced optical damage (all of these characteristics are addressed in the following chapter). Indeed if this were purely an academic exercise then we would attempt to satisfy all of these desired characteristics simultaneously. However, for industrial applications where the developed laser will be marketed and sold as a product, it is essential to consider the engineering implications of using the optimum design and its impact on the overall cost per

unit. It is often found that the best performing laser design is not the most cost effective option for manufacture. Cost control is an important part of commercial research and development as there is generally little business advantage gained in designing an ideal laser for an application that costs more than the market is willing to pay for it. The key is therefore to achieve the specified performance characteristics for the target application and where possible selectively compromise others in order to limit production costs. It should be stressed that this does not mean that the laser performance is made to be deficient for the target process. Any cost control compromise that takes away from an optimum state should be made outside of the minimum requirements for the application. For this work the objective is to satisfy all of the application process requirements detailed in chapter 1 while keeping the production costs as low as possible.

There are a number of 'value engineering' methods that can be used to control the production cost of complex optical systems. The first is to limit the number of required components where possible. Any component should be removed from the optimum design as long as it is without detriment to the minimum performance requirements for the laser. A more flexible method for reducing excess cost is to assess the required performance characteristics of each component part in an attempt to relax any over-specified tolerances. The specifications that can affect cost will vary depending on the component in question, such as the reflectivity tolerance of a dielectric mirror or the diffraction efficiency tolerance of an AOM Q-switch. In addition to this, there are also tolerances associated with the mechanical location of the resonator components relative to each other and the laser housing. Tolerance rationalisation can be extended to all resonator components.

There are two particular resonator components that are considerably more expensive and the most cost sensitive to changes in specified performance. The first of these components is the laser diode pump source, with particular reference to the wavelength and output power specifications. The second

component which has a significant bearing on cost control is the Nd:YAG rod. Current single crystal manufacturing techniques exhibit an inevitable variation in doping concentration between rods. This means that tight tolerancing may require increased selectivity, a reduction in useable rod yield and a resultant incurred cost premium. A further cost implication for rod manufacture is associated with the specified optical finish. As previously discussed, rod manufacturers are able to grind and polish rod facets to a plane finish or with limited curvature. This process however exhibits imperfect levels of accuracy and reproducibility, particularly with respect to facet perpendicularity and curvature centration. Again, this means that tight tolerancing on the optical finish may require increased selectivity, further reducing the useable rod yield or increasing the need for repeated processing, both of which result in another significant cost premium.

Another important point to note is that the mechanical tolerances in component position and optical finish can vary for the same component depending on the resonator design. This implies that the most cost effective laser may not be achieved by simply redefining component specifications for the optimised resonator but that actually changing the resonator design to allow further relaxation of specified tolerances may also be useful. Of particular interest is the possibility for reducing rod facet perpendicularity and curvature centration tolerances, which will aid in the implementation of a plug-and-play design whereby components can be serviced and/or replaced without the need to re-align.

3.4 Summary

In this chapter we have introduced various fundamental principles of laser design and brought together a number of known and new concepts for the optimisation of thermally active solid-state laser resonators. Particular reference was given to those pertaining to spatial or ‘transverse’ laser modes

and resonator stability. The concept of dynamic resonator stability was introduced and used to formulate the early stages of a mathematical model that can be used to simulate the output properties of a solid-state laser.

The temporal characteristics of CW pumped, actively Q-switched laser oscillators were explored and discussed with specific reference to the conditions that govern pulse consistency. A number of concepts for first pulse suppression and transient thermal lens control were highlighted.

Finally, consideration was given to the methods by which the design concepts can be refined for the commercial development of industrial laser products. In the next chapter we will expand on all of these fundamental principles and concepts to set out a novel framework for high-power, multi-spatial-mode, Q-switched laser design.

4 Multi-spatial-mode resonators: Part II – Mathematical modelling

When developing lasers for industrial applications it is important that the optical design is carried out quickly, accurately and with minimum cost. This enables the manufacture of laser products that are not only fit for purpose but are also available to the market in time to meet demand and preferably ahead of the competition. A number of mathematical models that can be used to facilitate successful laser design and optimisation are presented in the following sections. Of central concern are the conditions for resonator stability and the spatial characteristics of the resultant output beam. Related to these properties are other important considerations such as misalignment sensitivity, Q-switched pulse optimisation and laser induced optical damage control, all of which will be assessed through mathematical simulation.

4.1 Spatial simulation

We can now use the mathematical model presented in section 3.1.4 to investigate the individual effect that each controllable cavity dimension has on resonator stability and the properties of the generated multi-spatial-mode beam.

4.1.1 Resonator stability optimisation: Single-rod configuration

Figures 4.1 – 4.3 show the change in M^2 with total pump power for varying cavity length, mirror curvature, and rod facet curvature. To highlight the two permissible stability zones the modelled resonators have been given an arbitrary degree of asymmetry in cavity arm length such that $d_2 = 0.75d_1$. The rod length L is constant and for simplified illustration the resonator mirror radius of curvature $R_1 = R_2$.

Figure 4.1 illustrates that changing the total physical cavity length $L' = (d_1 + d_2 + L)$ will alter the range and magnitude of the M^2 curve with respect to the total pump power, except at a single common point where all propagation factors are equivalent. For the illustrated case, which comprises a plane-plane resonator with no rod facet curvature, this point corresponds to a zero net lens condition occurring at a total incident pump power $P = 0$.

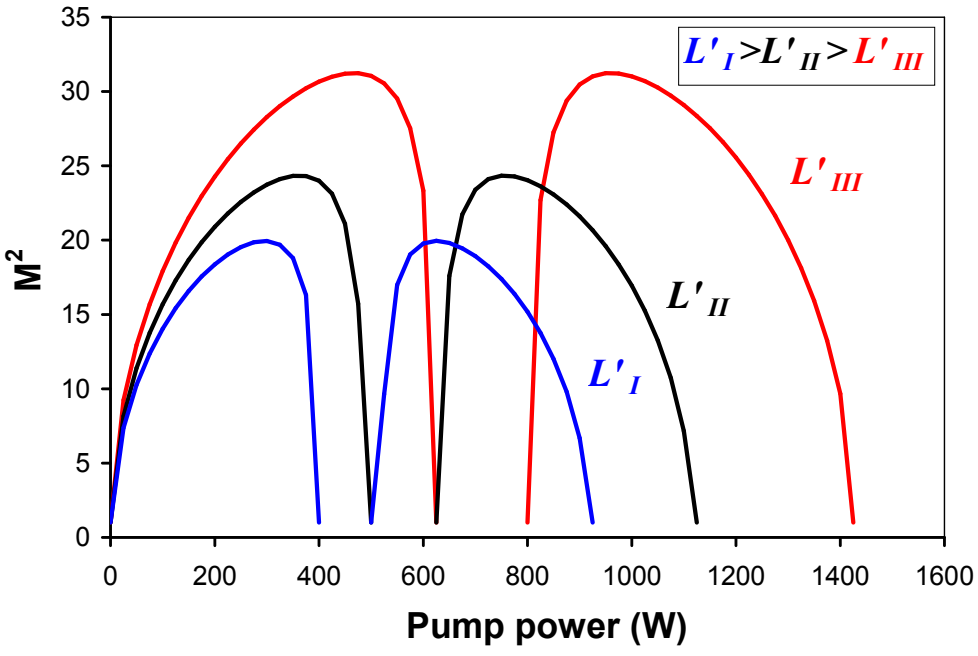

Figure 4.1 Simulated M^2 as a function of total incident pump power for a range of physical resonator lengths $L' = (d_1 + d_2 + L)$. Here $R = \infty$, $d_2 = 0.75d_1$, $L = 97$ mm, $a = 2.25$ mm, $C_t = 0.0084$ D.W^{-1} and $R_1 = R_2 = \infty$.

Similarly, figure 4.2 illustrates the variation in M^2 with changing cavity mirror curvatures R_1 and R_2 for a symmetrically concave-concave resonator ($R_1 = R_2 = R'$). The general trend corresponds to configurations by which $u_2/u_1 > 0$, where $u_1 > 0$ and $u_2 > 0$ (as described by equation (3.22) and figure (3.6). Again we see that both the range and magnitude of the M^2 curve are affected but in this case the plots share a common point at the maximum stable pump power. This corresponds to a condition where the beam size is smallest at both cavity mirrors, regardless of R'.

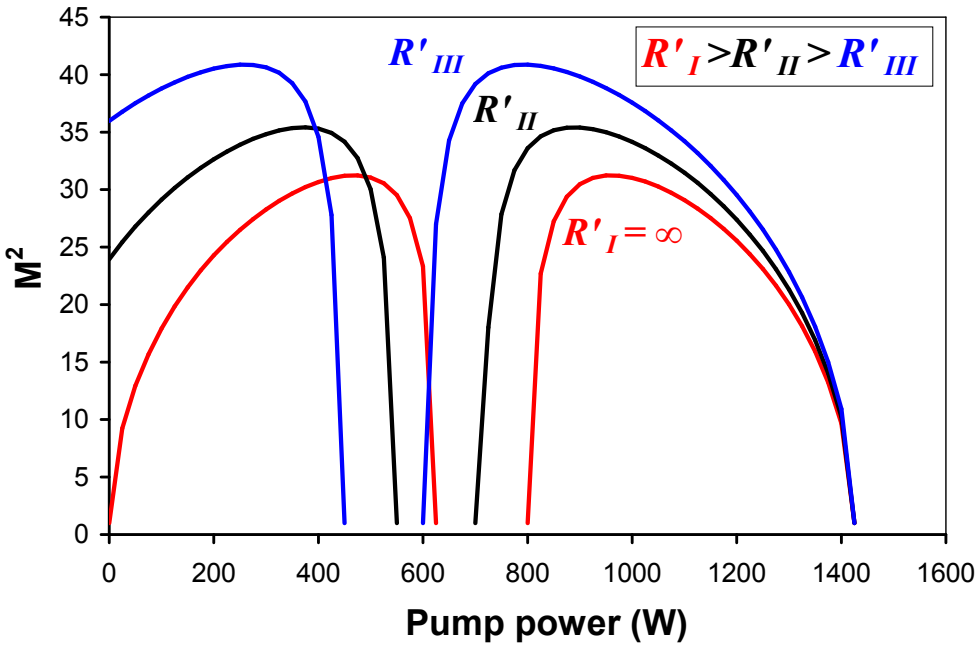

Figure 4.2 Simulated M^2 as a function of total pump power for a range of concave-concave resonator mirror radii of curvature where $R_1 = R_2 = R'$. Here $R = \infty$, $d_1 = 150$ mm, $d_2 = 0.75d_1$, $L = 97$ mm, $a = 2.25$ mm and $C_t = 0.0084$ D.W^{-1}. Importantly, in this case $u_2/u_1 > 0$, where $u_1 > 0$ and $u_2 > 0$.

It should be noted that it also possible to create an alternative trend for symmetrically concave-concave resonator configurations that satisfy $u_2/u_1 > 0$, where $u_1 < 0$ and $u_2 < 0$. In this regime the effect of increasing pump power on M^2 is identical to that seen with changing cavity length (see figure 4.1) although

the common stability condition corresponds to a physically different state whereby the beam waists are located closest to the cavity mirrors.

The influence of changing the rod facet curvature and therefore the static component of the internal lens is shown in figure 4.3. This particular alteration leads to a simple uniform translation of the M^2 plot with respect to the total input pump power.

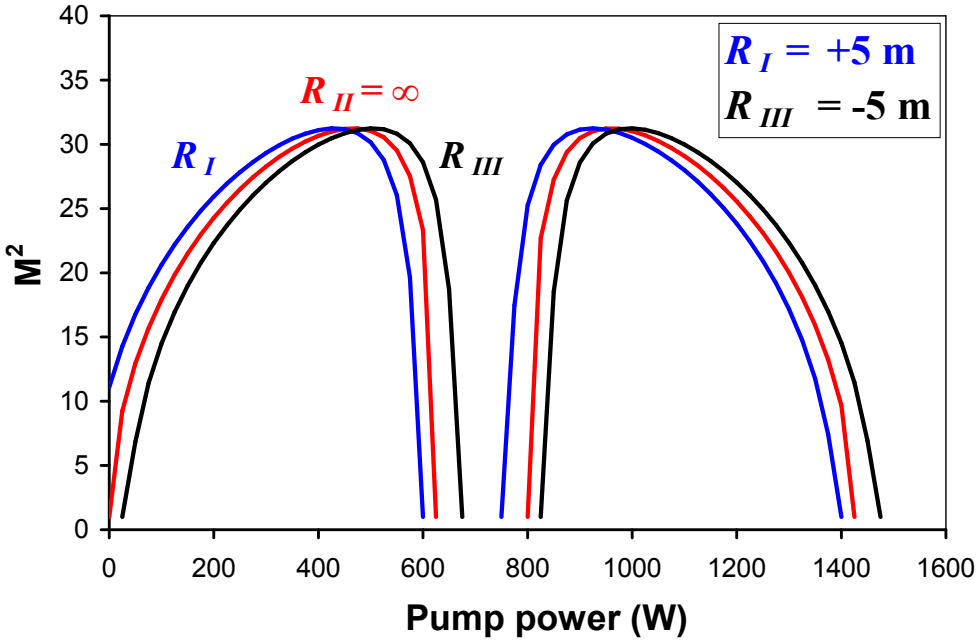

Figure 4.3 Simulated M^2 as a function of total pump power for a range of rod facet radii of curvature R (present equally on both ends of the rod). Here $R_1 = R_2 = \infty$, $d_1 = 150$ mm, $d_2 = 0.75d_1$, $L = 97$ mm, $a = 2.25$ mm and $C_t = 0.0084$ D.W^{-1}. A negative curvature denotes concave facet profiles.

The effects of changing the controllable dimensions on resonator stability and the resultant properties of the generated beam are further explained in the following illustrations. Figure 4.4 (a) shows the general trends in lens-power-governed stability and the associated spatial-mode-envelope profiles for plane-plane resonators with various arbitrary resonator arm lengths d_1 and d_2. In this configuration the condition $u_2/u_1 > 0$, where $u_1 > 0$ and $u_2 > 0$ is always satisfied, which is also the case for all convex-convex resonators. Figures 4.4 (b) and (c)

illustrate how resonator stability changes with variation in mirror curvatures R_1 and R_2 for an otherwise symmetrical cavity of static length. In this case (b) obeys the condition $u_2/u_1 > 0$, where $u_1 > 0$ and $u_2 > 0$ and for (c) $u_2/u_1 > 0$, where $u_1 < 0$ and $u_2 < 0$.

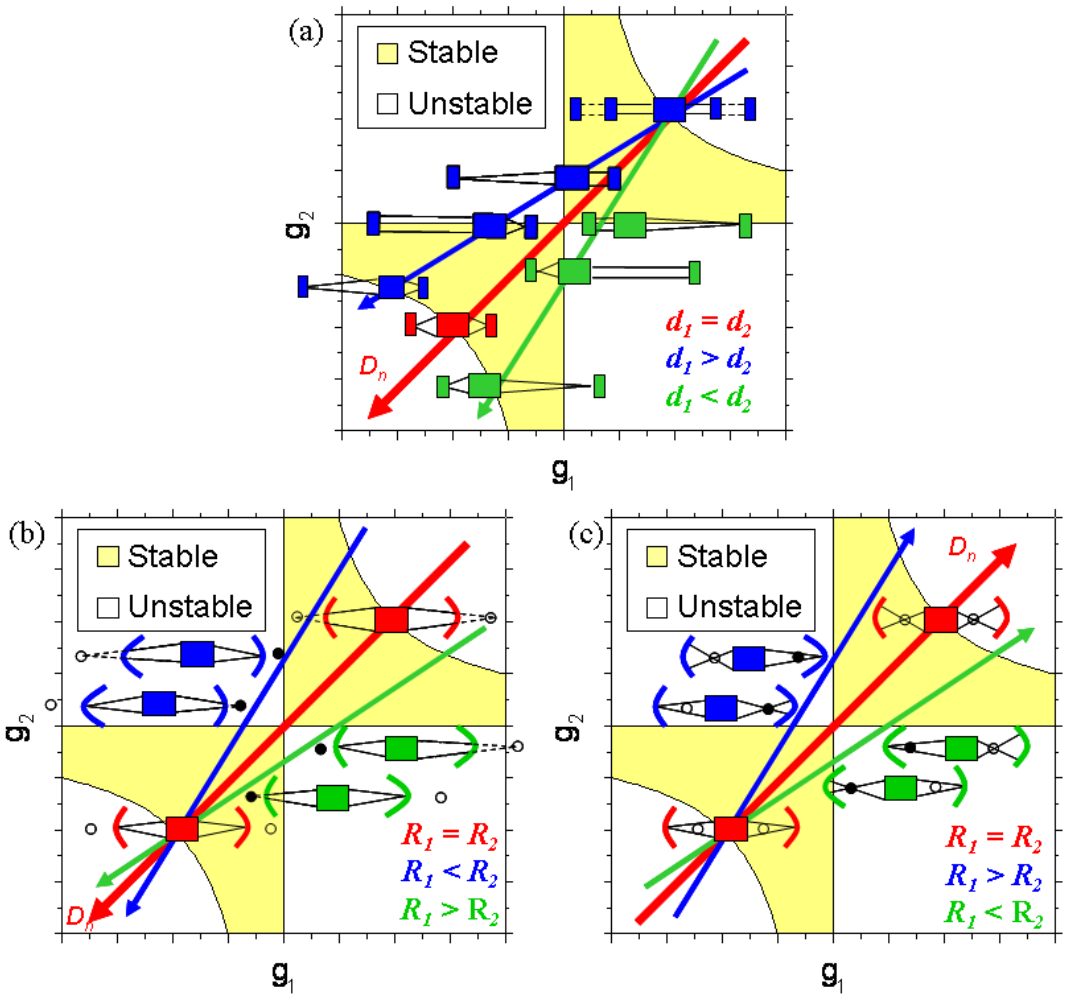

Figure 4.4 Simulated stability diagrams and spatial-mode-envelope profiles at the boundaries of the stability zones for (a) plane-plane resonators of various d_1 and d_2 arm length combinations, and a range of concave-concave resonator mirror curvatures R_1 and R_2 for a symmetrical cavity of static length such that (b) $u_2/u_1 > 0$, where $u_1 > 0$ and $u_2 > 0$, and (c) $u_2/u_1 > 0$, where $u_1 < 0$ and $u_2 < 0$.

Now that we have an understanding of how the level of stability for a multi-spatial-mode resonator changes with its controllable dimensions, it is possible to investigate how this relates to other important beam properties. Of particular

interest are the far-field divergence, waist size and waist position, all of which are important for effective relay and re-imaging of the beam outside of the resonator. These parameters are also of interest to the laser designer when calculating intra-cavity intensities at optic surfaces for laser induced damage investigation, or in non-linear crystals for wave mixing applications (as discussed in section 4.3 and chapter 7 respectively). The waists of the multi-mode beam are located at the same planes as that of the embedded gaussian, which are defined by equation (3.32). We can obtain the multi-mode waist sizes W_{oi} and the corresponding half-angle far-field divergences Θ_i by combining equation (3.17) with (3.31) and the result with equation (3.16). This gives

$$W_{oi} = \left(\frac{4}{3}\right) M \; w_{oi} \tag{4.1}$$

and $$\Theta_i = \left(\frac{3}{4}\right) M^2 \frac{\lambda}{\pi W_{oi}} \tag{4.2}$$

The variation in these beam properties with changing pump power for an arbitrary plane-plane resonator is summarised in figure 4.5. In this case the maximum radius for both multi-mode beam waists W_{omax} is the same. This parameter is governed by the largest permissible beam size at the limiting aperture W_P whereby

$$W_{o_{\max}} = W_P \cong \frac{2a}{\pi} \tag{4.3}$$

The maximum multi-mode half-angle far-field divergences can also be generally approximated using the limiting aperture and the distance of the waist position from the aperture such that

$$\Theta_{i_{\max}} \cong \frac{a}{\left(L_i - L_{oi}\right)} \tag{4.4}$$

For a plane-plane resonator the waists are always located at the cavity mirrors (i.e. $L_{oi} = 0$).

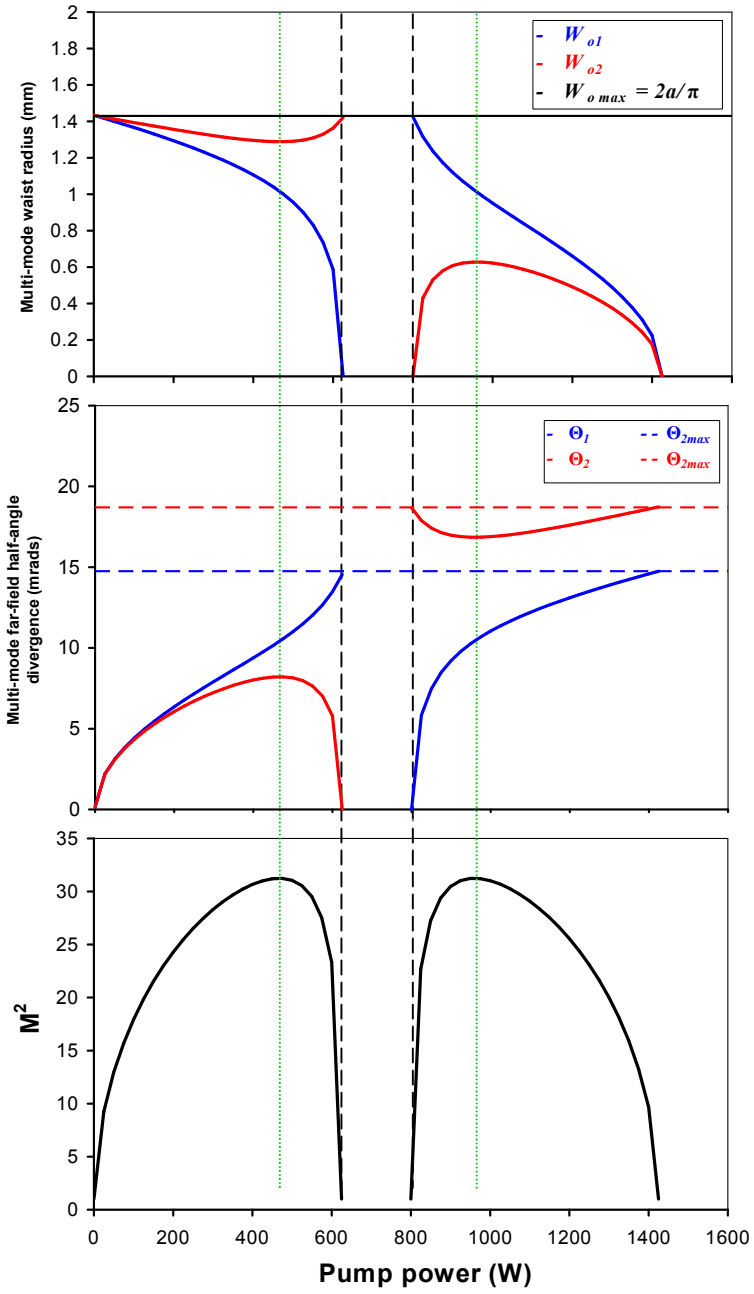

Figure 4.5 The variation in multi-mode waist radius, half-angle far-field divergence and M^2 with changing pump power for an arbitrary plane-plane resonator. Here d_1 = 150 mm, d_2 = 0.75d_1, L = 97 mm, a = 2.25 mm and C_t = 0.0084 D.W^{-1}. The vertical green dashed lines indicate points of dynamic stability for the output beam that occur when $|u_2| < |u_1|$.

At this point it is useful to note the labelling convention used, which is the same as that for the resonator schematic shown in figure 3.8 whereby a '*1*' subscript

has been used to denote the beam properties at the rear (high-reflector side) of the cavity and a '*2*' subscript denotes the beam properties at the front (output-coupler side). For consistent laser performance we are particularly interested in designing a resonator capable of maintaining its divergence and waist characteristics at the output side. Dynamic stability in the *output beam* waist size and divergence for any arbitrary single-rod resonator is seen to occur at the points of maximum M^2 when the condition $|u_2| < |u_1|$ is satisfied. That is, in this configuration the waist and divergence values exhibit minimum rates of change (at the points of dynamic stability) for the beam at the front of the resonator, rather than at the rear.

As we are no longer practically interested in the fundamental mode size and are actually unable to directly measure its properties in a multi-mode beam we must find an alternative method of defining the dynamic stability. The data presented in figure 4.5 suggests that a convenient approach may be to define this condition as a function of the beam propagation parameter M^2 whereby

$$\frac{dW_{o2}}{dP} = \frac{d\Theta_2}{dP} = \frac{dM^2}{dP} = 0 \qquad (4.5)$$

For the single-rod case this provides two points of dynamic stability in the output divergence and waist size that coincide with the conditions for peak M^2, the magnitude of which is also of interest for controlling the operating beam quality.

In theory, we may now use the controllable resonator dimensions to generate any number of dynamically stable combinations of output waist size, divergence and beam quality that satisfy the relation set by equation (4.2). However, to effectively simulate the spatial characteristics of real laser resonators it is necessary to extend the model. It is important to accurately represent the lensing that occurs as a result of stress-induced birefringence, which has been found to be a significant effect at the pump powers employed here. Until this point the experimentally derived net lens power D_n comprised a static facet-

curvature related component and dynamic thermally and stress-induced elements. This value represents an average over all polarisations and can be calculated using equation (3.27). It is however possible to formulate two modified net lens powers D_{nr} and $D_{n\varphi}$ that account for the variation in the stress-induced components D_r and D_φ that affect radial and tangential polarisations respectively, as defined by equation (2.12). These modified net refractive powers exhibited for radial and tangential polarisations can be expressed by

$$D_{n_r} = D_n + \left(\frac{D_r - D_\varphi}{2} \right) \tag{4.6}$$

and $$D_{n_\varphi} = D_n - \left(\frac{D_r - D_\varphi}{2} \right) \tag{4.7}$$

In this case D_r and D_φ must be calculated using the projected power dissipated as heat under oscillating conditions such that

$$P_h = \eta_h \eta_{h'} P_{abs} = \eta_h \eta_{h'} \eta_c P \tag{4.8}$$

where P is the total pump power, η_h is the fractional heat loading measured under non-oscillating conditions, $\eta_{h'}$ is the change in fractional heat loading between non-oscillating and oscillating conditions and η_c is the pump coupling efficiency, as defined in section 2.1.2. From the modelling and characterisation of the gain-modules developed in chapter 2 we may suppose that $\eta_h = 0.39$, $\eta_{h'} = 0.90$ and $\eta_c = 0.80$. The corresponding difference in temperature between the surface and the centre of the rod ΔT_{rod}, required to assess D_r and D_φ using equation (2.12), can be calculated for oscillating conditions by substituting equation (4.8) into equation (2.11), whereby we obtain

$$\Delta T_{rod} = \frac{\eta_h \eta_{h'} \eta_c P}{4\pi K L_p} \tag{4.9}$$

Here, the thermal conductivity $K = 0.103$ W.cm^{-1}.K^{-1} and the length over which the rod is pumped $L_p = 4.6$ cm. The thermal component of the net lens can be defined using the expression

$$D_{n_{therm}} = D_{n_r} - D_r = D_{n_\varphi} - D_\varphi \tag{4.10}$$

although in reality this component will never exclusively exist without the corresponding stress-induced lensing elements. Figure 4.6 illustrates the change in net lens power affecting radial and tangential polarisations as a function of total pump. The experimentally determined average net lens power D_n (between the radial and tangential components) that has been used for modelling up to this point is also shown. For this example the laser rod has been given concave facet curvatures of 1.0 m radius to illustrate the resulting zero offset induced in the net lens power values. Note that for the gain-modules developed here the lensing contribution from facet deformation as a result of axial rod expansion, commonly known as the 'end effect', is considered negligible due to the sufficiently lengthy un-pumped sections at both ends of the Nd:YAG rod [4.1].

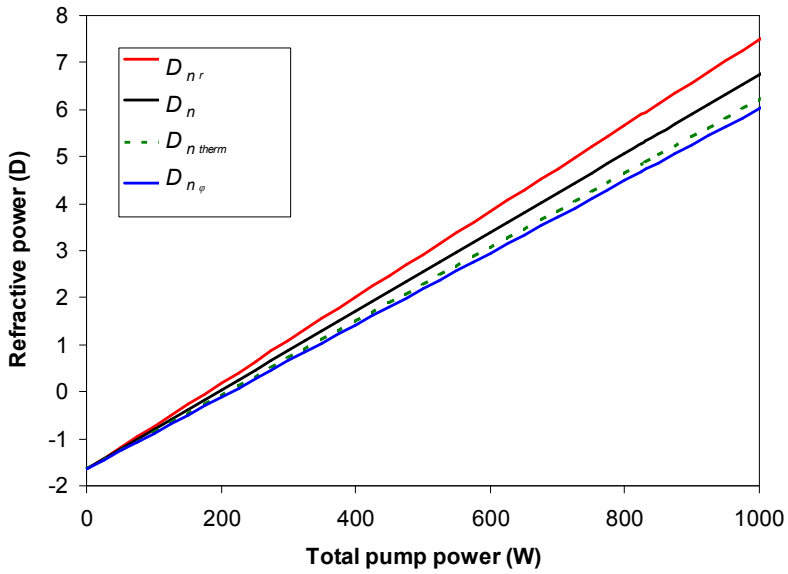

Figure 4.6 Net lens power as a function of total pump for radial D_{nr} and tangential $D_{n\varphi}$ polarisations. The average net lens between radial and tangential components D_n is shown (calculated using the experimentally determined average lens constant for oscillating conditions C_t = 0.0084 D.W^{-1}). In this case the rod has been given concave facet curvatures of R = 1.0 m to illustrate the zero offset induced in the net values. The embedded thermal component for the net lens D_{ntherm} is also illustrated.

For the high-power gain-module developed in chapter 2 the stress-induced lens component affecting radial polarisation adds around +1.07 dioptres to the +6.53 dioptres of refractive power contributed by the thermal component, at 831 W optimum pump. In contrast, the stress-induced component affecting tangential polarisation constitutes a negative lens power of approximately -0.16 dioptres at optimum pumping. The change in M^2 as a function of pump power for the polarisation dependent net lens conditions is illustrated in figure 4.7 (the red and blue lines show the resultant M^2 for radial and tangential polarisations respectively).

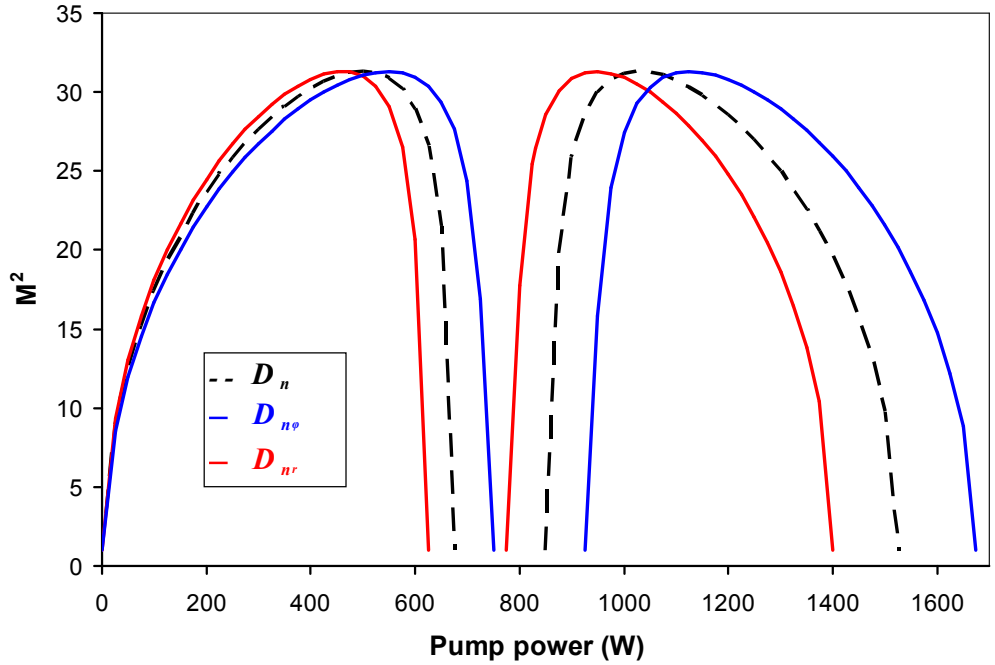

Figure 4.7 Simulated M^2 as a function of total pump power for the unmodified average net lens (dashed black) and the modified, polarisation dependent, net lens conditions (radial in red and tangential in blue). Here $R = \infty$, $d_1 = 150$ mm, $d_2 = 0.75d_1$, $L = 97$ mm, $a = 2.25$ mm, $C_t = 0.0084$ D.W^{-1} and $R_1 = R_2 = \infty$.

A consequence of this polarisation bifocusing is the creation of two separate M^2 to pump-power relations for the same resonator. For a single-rod configuration this produces two pairs of dynamically stable conditions, as defined by equation (4.5). However, we can extend the concept of dynamic stability by

combining the contributions of both polarisations to define a maximum output beam propagation parameter M^2_{max} for a given pump power. This means that real resonators using such gain-modules will exhibit broadened M^2 curves effectively creating *regions* of dynamic stability around the conditions where the maximum M^2 for each polarisation overlap. Here we have arbitrarily defined the region limits as the pump powers at which the M^2 drops to 95% of the maximum dynamically stable value. Note that these regions of dynamic stability can be made to be larger for one stability zone than the other. For a plane-plane resonator the second stability zone (corresponding to the third quadrant on the (g_1, g_2) plane) shows greater broadening and therefore a larger dynamic stability region, as illustrated in figure 4.8.

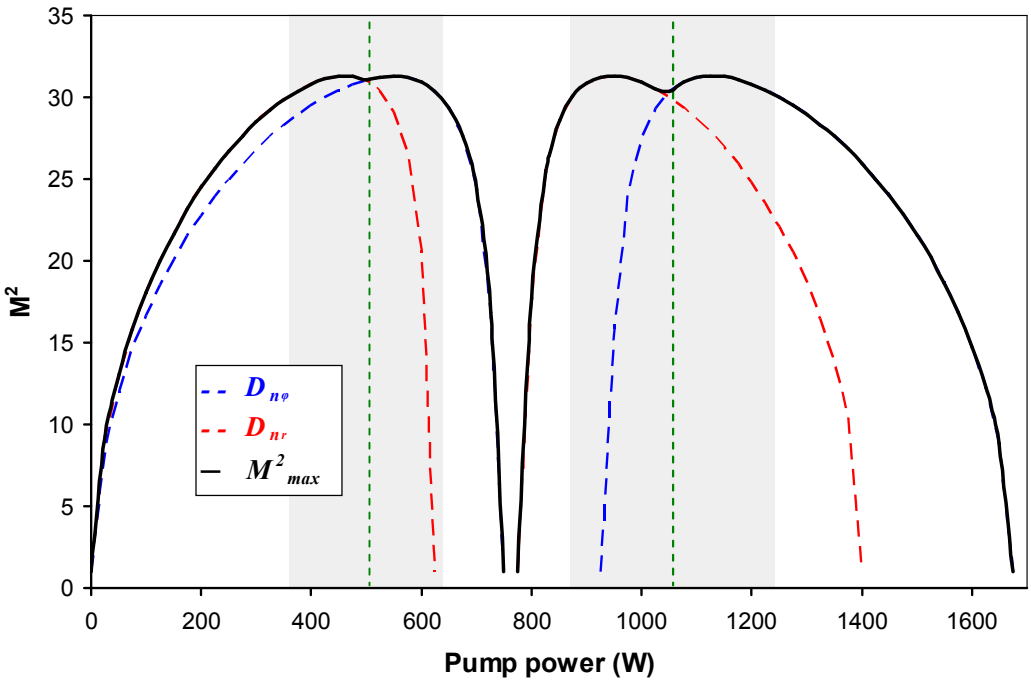

Figure 4.8 Simulated maximum M^2 as a function of total pump power for the modified polarisation dependent net lens conditions. 'Regions' of dynamic stability are shown by grey shaded areas with central optimum design points (vertical dashed green lines). Here $R = \infty$, $d_1 = 150$ mm, $d_2 = 0.75d_1$, $L = 97$ mm, $a = 2.25$ mm, $C_t = 0.0084$ D.W^{-1} and $R_1 = R_2 = \infty$ (plane-plane resonator).

Now that we are able to influence the multi-mode waist size, divergence, beam quality and region over which these properties are considered to be dynamically stable we can attempt to optimise the performance of a multi-spatial mode resonator. This is realised by selecting a combination of R_1, R_2, d_1, d_2, R, a and L that both generates the required output beam properties and satisfies the conditions for dynamic stability such that the central point of the selected stability region (in this case the broader second region) is aligned to the optimum pump power of 830 W. Here the optimum pump power is considered to be the maximum power that the laser diodes can be operated without compromising their working lifetime, which for industrial applications is required to be > 15,000 hours. Note that operating at dynamically stable pump powers less than the central design point can result in predominantly radial polarisation and dynamically stable pump powers more than the central design point can result in predominantly tangential polarisation. Operation in either of these states of unpolarised output is considered to be acceptable for the target applications outlined in chapter 1.

4.1.2 Resonator stability optimisation: Multi-rod configurations

To increase the output power generated by a single resonator an additional gain-module can be introduced, creating a dual-rod configuration. The multi-spatial-mode resonator model presented in section 3.1.4 can be extended for the treatment of dual-rod configurations by simply modifying the stability parameters. For a dual-rod resonator, where both rods exhibit the same lensing properties, the g-parameters can be redefined as

$$g_i = \left[1 - \frac{L_1 + L_2 + L_3}{R_i}\right] + L_3 D_n \left[\frac{L_j\left(L_3 D_n - 2\right)}{L_3}\left(1 - \frac{L_i}{R_i}\right) - \left(1 - \frac{L_1 + L_2}{R_i}\right)\right] \tag{4.11}$$

where L_3 is the distance between the facing principle planes of the two identical rod-like lenses, each with average net refractive power D_n [4.2]. A cavity schematic for this dual-rod model is illustrated in figure 4.9.

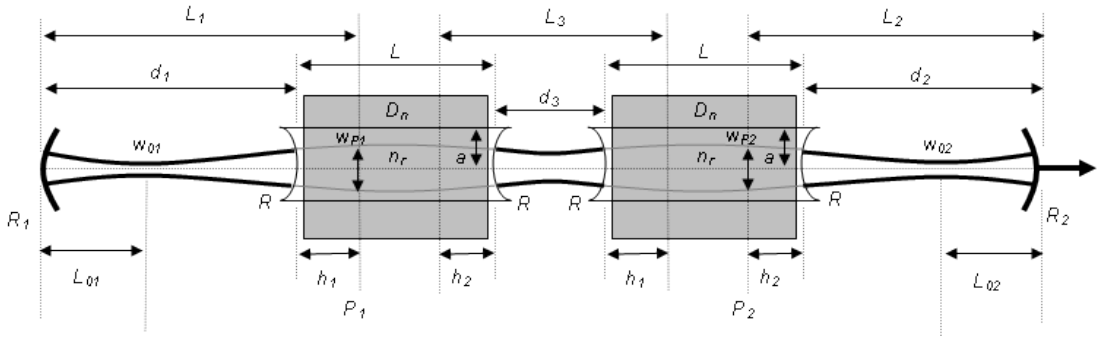

Figure 4.9 Schematic of the dual-rod multi-spatial-mode resonator model showing the controllable cavity dimensions and resultant embedded gaussian. Not to scale.

On investigation of equation (4.11) we see that generally, in contrast to the single-rod case, the stability of a dual-rod resonator follows a parabolic line on the (g_1, g_2) plane. This results in four permissible stability zones and eight corresponding boundary conditions. An example of this is shown in figure 4.10, which highlights the differences in the stability relations between arbitrary single and dual-rod resonators.

In some exceptional dual-rod configurations it is possible to create three stability zones whereby the axis of the parabola is parallel with either $g_1 = 0$ or $g_2 = 0$. For example, this can occur when one of the rods is located at a corresponding cavity mirror, when $L_2 \to 0$ or $L_1 \to 0$ respectively. Importantly, when both rods are located at the cavity mirrors, where $L_2 = L_1 \to 0$ or when the gap between the two rods is removed such that $L_3 \to 0$, the parabola degenerates toward a condition similar to that of the single-rod case whereby a linear relation with two stability zones and four boundary conditions is obtained [4.2].

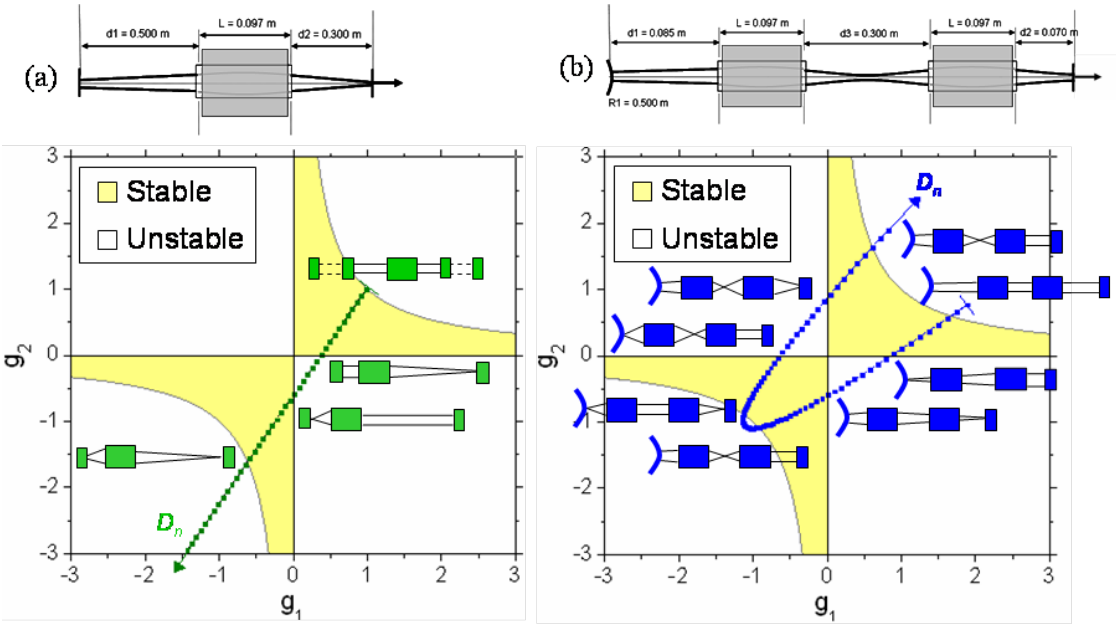

Figure 4.10 Simulated resonator stability illustrated on the (g_1, g_2) plane for (a) an arbitrary single-rod resonator showing a linear variation in stability with increasing average net lens power and (b) an arbitrary dual-rod resonator represented by a parabolic variation in stability with increasing refractive power (in this case the four permissible stability zones are shown with eight corresponding boundary conditions). The markers on both model generated lines indicate equal pump power intervals of (a) 25 W and (b) 50 W.

We can further compare the dual-rod configuration with the single-rod case by investigating the resultant trends in output far-field divergence, waist size and dynamic stability with change in pump power. The spatial beam characteristics for a dual-rod resonator can be determined using equations (3.31) and (3.32). However, in order for the model to hold we must redefine both the stability parameters, given in equation (4.11) and the effective resonator length, which is now of the form

$$L^* = L_1 + L_2 + L_3 - D_n L_3 \left[L_1 + L_2 - \left(\frac{(D_n L_3 - 2) L_1 L_2}{L_3} \right) \right] \qquad (4.12)$$

For single-rod configurations the points of dynamic stability in the output beam waist size and divergence, as defined by equation (4.5), occur when $|u_2| < |u_1|$. However, this is not always the case for the output beam generated with a dual-

rod configuration. At this point it is useful to introduce the concepts of full and partial output dynamic stability. In this case we define full output dynamic stability as the complete satisfaction of equation (4.5) whereby the output beam exhibits dynamic stability in waist size, far-field divergence and beam quality at the same pump power. Multi-rod resonators can however exhibit conditions of both full and partial dynamic stability whereby only one of the three spatial beam characteristics is dynamically stable with pump power. These partial dynamic stability conditions can be useful for product engineering or cost control purposes when designing lasers intended for use in applications that are only sensitive to a particular spatial characteristic. It is also possible to create dual-rod configurations that exhibit dynamic stability in all three spatial characteristics within a given stable zone, but not simultaneously.

Figure 4.11 illustrates the variation in the spatial beam characteristics with change in total pump power for a plane-plane dual-rod resonator where $L_3 > L_1 + L_2$. In this case, zones I and IV exhibit points of full dynamic stability for the beam at the rear of the cavity and zones II and III show useful conditions of full *output* dynamic stability (illustrated by the vertical dashed green lines).

Similarly, figure 4.12 illustrates the variation in the spatial beam characteristics with change in total pump power for a plane-plane dual-rod resonator where $L_3 < L_1 + L_2$. Here zones I and IV exhibit points of full dynamic stability for the output beam (again illustrated by the vertical dashed green lines) but zones II and III only have points of partial output dynamic stability. For dual-rod configurations in general, stability zones I and IV are seen to be equal in width with respect to total input pump power. The same is observed for zones II and III, which are typically significantly wider than I and IV. Zones III and IV tend to produce points of dynamic stability with smaller waist sizes and larger divergences. Smaller waist sizes are normally undesired in high-power lasers for reasons relating to laser induced optical damage (discussed in section 4.3). It follows that for a dual-rod resonator it is generally advantageous to operate at points of dynamic stability in stability zone II where possible.

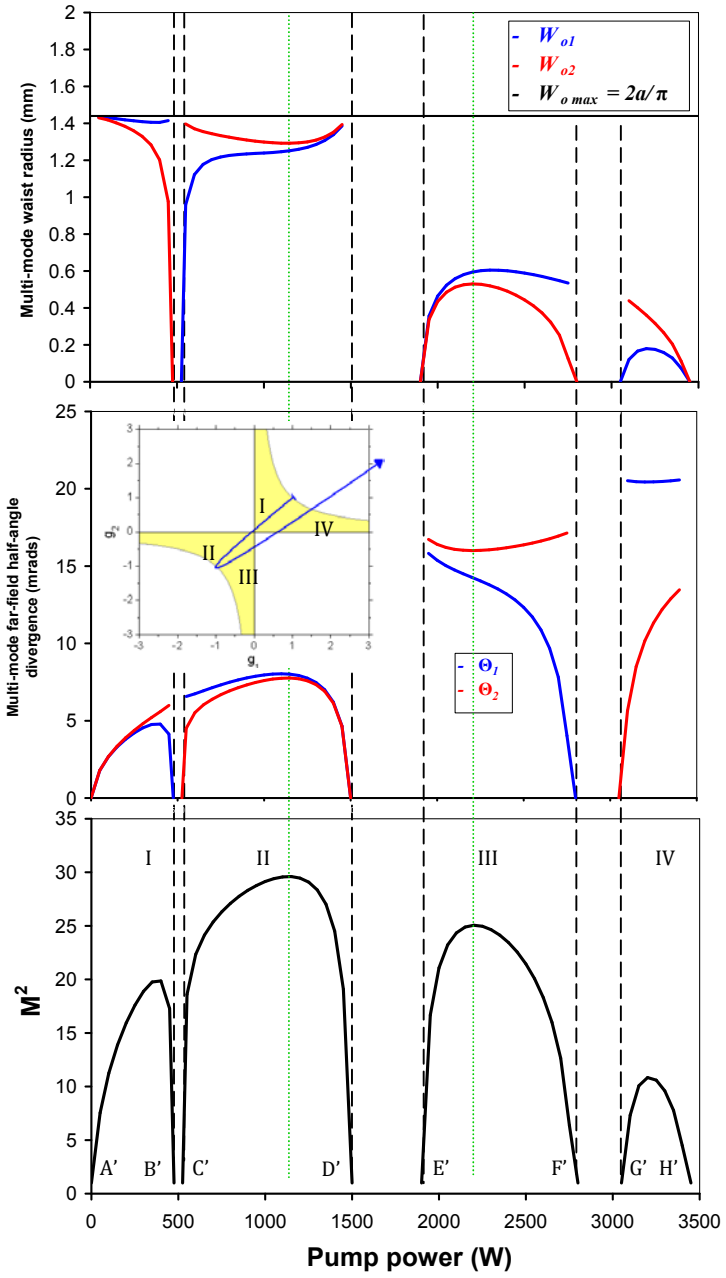

Figure 4.11 The variation in multi-mode waist radius, half-angle far-field divergence and M^2 with changing pump power for an arbitrary dual-rod resonator. Here d_1 = 100 mm, d_2 = 125 mm, d_3 = 300 mm, $R_1 = R_2 = \infty$, L = 97 mm, a = 2.25 mm, $R = \infty$ and C_t = 0.0084 D.W^{-1}. Stability zones I to IV and zone boundaries A' to H' are labelled. Vertical green dashed lines indicate the points of dynamic stability for the output beam. The corresponding cavity stability on the (g_1, g_2) plane is inset.

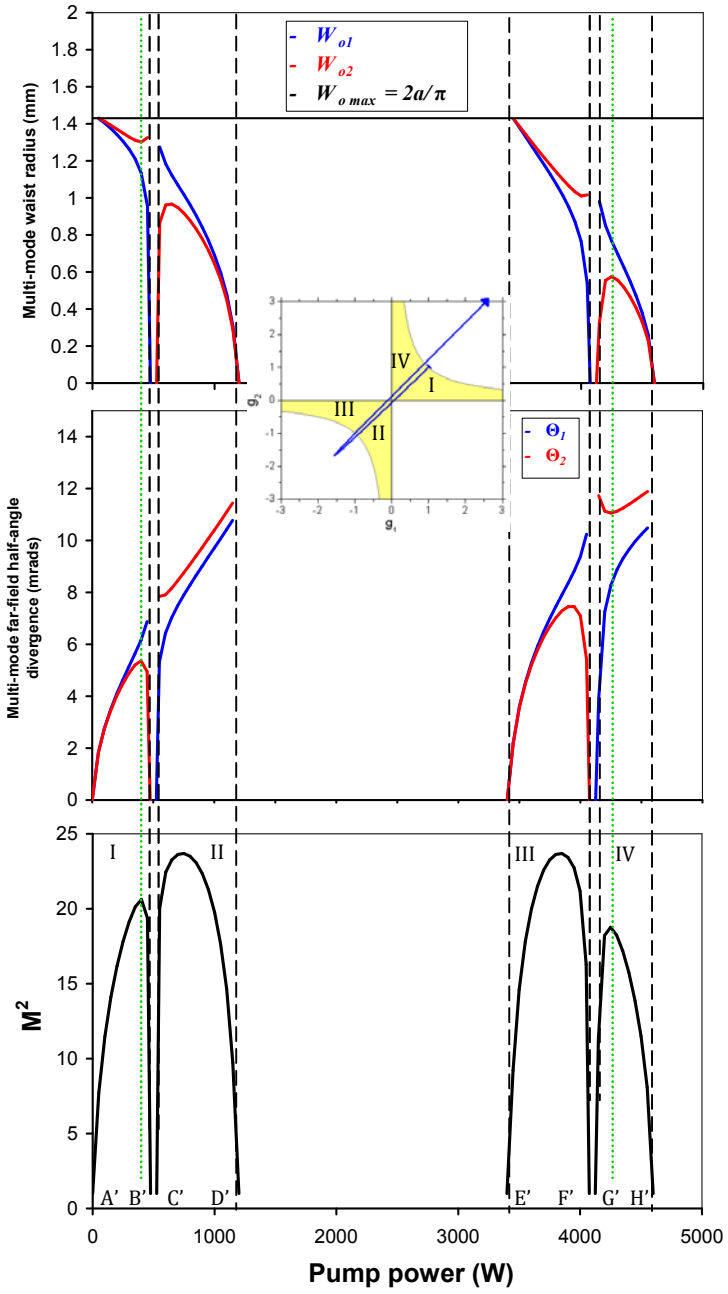

Figure 4.12 The variation in multi-mode waist radius, half-angle far-field divergence and M^2 with changing pump power for an arbitrary dual-rod resonator. Here d_1 = 210 mm, d_2 = 190 mm, d_3 = 100 mm, $R_1 = R_2 = \infty$, L = 97 mm, a = 2.25 mm, $R = \infty$ and C_t = 0.0084 D.W^{-1}. Stability zones I to IV and zone boundaries A' to H' are labelled. Vertical green dashed lines indicate the points of dynamic stability for the output beam. The corresponding cavity stability on the (g_1, g_2) plane is inset.

Figure 4.13 illustrates how the limiting aperture can alternate between the gain-modules in a dual-rod resonator as the internal lens power is increased and the stability altered. The effect is observed when tending toward boundary conditions B', C', F' and G' and can result in an under-fill of one rod, which may in turn reduce the overall energy extraction efficiency. This effect is reduced for resonators with smaller rod separations.

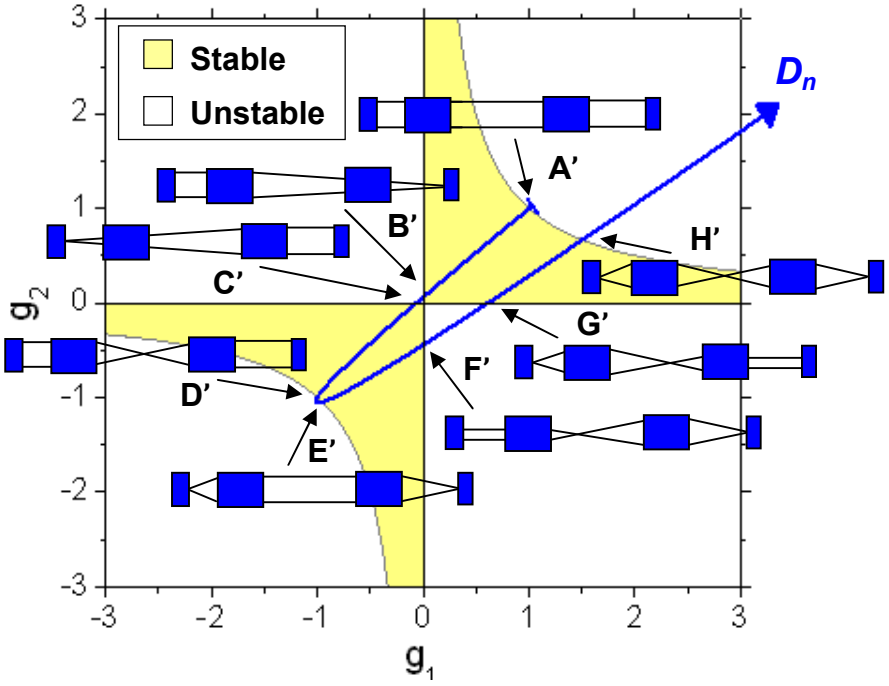

Figure 4.13 Simulated resonator stability and boundary condition spatial-mode-envelopes shown on the (g_1, g_2) plane for the arbitrary plane-plane dual-rod resonator previously illustrated in figure 4.11 where d_1 = 100 mm, d_2 = 125 mm, d_3 = 300 mm, $R_1 = R_2 = \infty$, L = 97 mm, a = 2.25 mm, $R = \infty$ and C_t = 0.0084 D.W^{-1}.

In order to effectively model the stability of real dual-rod laser resonators we can again extend the model to include the variation in lensing that occurs as a result of stress-induced birefringence. As an example we will apply the treatment to the cavity configuration illustrated in figures 4.11 and 4.13, which demonstrates a condition full output dynamic stability in zone II. In this case we can once again use the M^2 factor as an indication of dynamic stability. Figure 4.14 shows the change in M^2 as a function of total pump power for the

polarisation dependent net lens components and the maximum output beam propagation parameter M^2_{max} for either radial or tangential polarisations. As observed in the single-rod resonator model, regions of full dynamic stability are created around the conditions where the maximum M^2 for the two polarisation dependent components overlap. Comparing this dual-rod resonator example to the single-rod case in 4.1.1 with similar arm lengths we see that, for the same operating beam quality, the region of dynamic stability is increased.

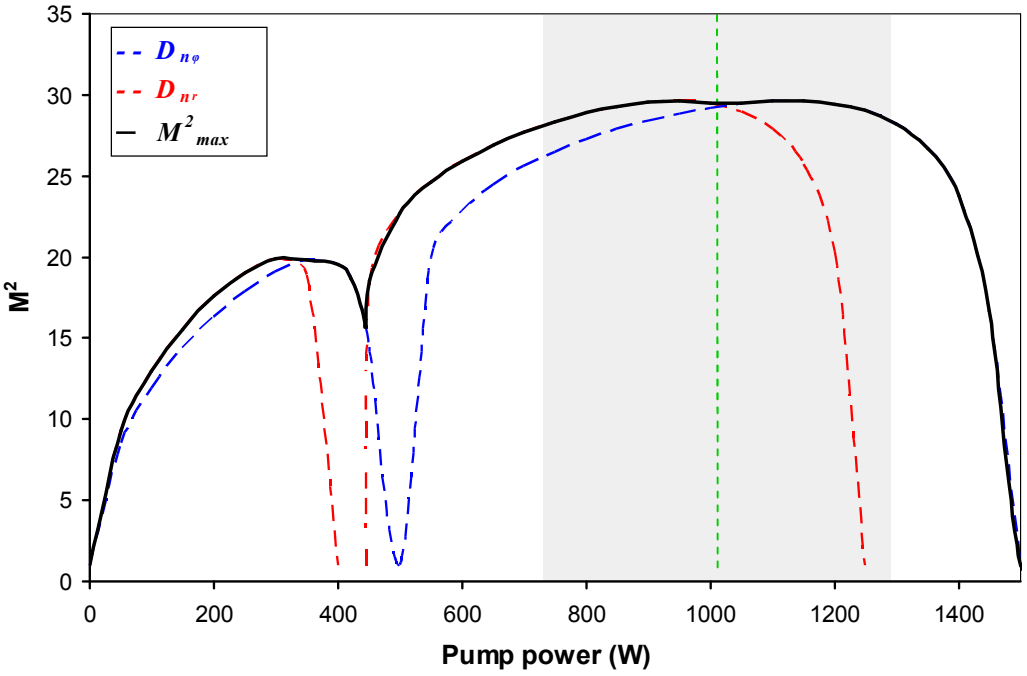

Figure 4.14 Simulated maximum M^2 as a function of total pump power for the polarisation dependent net lens conditions. The region of output dynamic stability for zone II is shown by the grey shaded area with a central optimum design point (vertical dashed green line). Here d_1 = 100 mm, d_2 = 125 mm, d_3 = 300 mm, $R_1 = R_2 = \infty$, L = 97 mm, a = 2.25 mm, $R = \infty$ and C_t = 0.0084 D.W^{-1}.

As there are now two gain-modules the optimum total pump power is doubled to 1660 W, at which point the above example is unstable. To translate the illustrated design point in zone II to the optimum pump level we must induce a static negative lens at the rod by fabricating adequate facet curvatures. In this

case, equal concave rod facet curvatures R of approximately 600 mm would be required.

In the dual-rod case it is possible to remove the birefringence-induced polarisation bifocusing and depolarisation by using mutual compensation between the pumped rods. This can be carried out using a number of methods [4.3], including the simple addition of a 90° quartz rotator placed between the rods. The general objective is to achieve equal phase retardation at each point of the rod cross-section for radially and tangentially polarised components [4.4]. However, for multi-spatial-mode lasers this may only be required if the radial and tangential lensing components of a particular gain-module design are sufficiently separated to cause a split in the selected region of dynamic stability, or for resonators that are required to produce a given polarisation.

The mathematical model presented will also allow us to investigate the effects of having dissimilar lensing properties at the two rods in a dual-rod system. For a plane-plane cavity with two different rod-like lenses of average net power D_{n1} and D_{n2} the stability parameters would be modified [4.5] such that

$$g_i = 1 - L_j\left(D_{n_1} + D_{n_2}\right) + L_3\left(L_j D_{n_1} D_{n_2} - D_{n_i}\right) \tag{4.13}$$

We can also use this modification to assess the effects of variation in gain-module characteristics on resonator performance. However, with sufficient component tolerancing the overall variation in gain-module features can be reduced or if required matched in pairs for use in dual-rod cavities. In this case, the gain-modules should be matched with respect to the total power dissipated as heat in the rod. As discussed in previous sections, this thermal loading is particularly difficult to accurately assess but may be expressed by combining equations (2.8) and (4.8) as follows

$$P_h = \eta_h \eta_{h'} P_{abs} = \eta_h \eta_{h'} \eta_c P = \eta_h \eta_{h'} \eta_T \eta_a P \tag{4.14}$$

The key is to pair gain-modules with similar pump absorption efficiency η_a.

Theoretically, the output power of a single resonator can be further scaled by adding more gain-modules. In general, the addition of *N* rods to a single-rod resonator will increase the output power by at least a factor of *N*. It can be shown that three and four-rod resonator configurations will exhibit stability relations that move across the (g_1, g_2) plane on third and fourth order polynomial lines respectively [4.2]. An example of this is shown in figure 4.15. The mathematical model presented in this thesis can be extended to simulate the beam characteristics for resonators with any number of rods provided that relevant definitions for the stability parameters and effective cavity length are used.

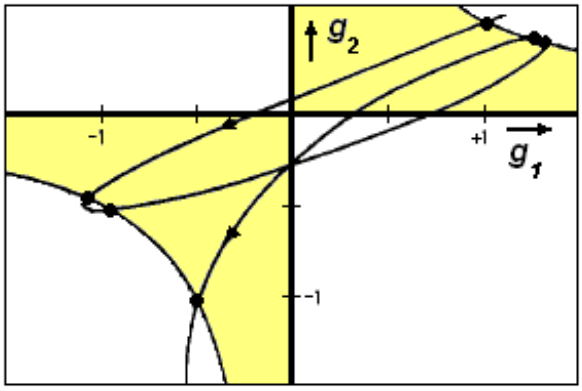

Figure 4.15 Simulated resonator stability with increasing refractive power for an arbitrary four-rod resonator moving in the (g_1, g_2) plane along a fourth-order polynomial [4.2].

In practice however, the number of resonator rods is generally limited by the ability to control the cumulative thermal lensing at the optimum pump level and/or the inevitable cavity length restrictions imposed by packaging requirements. The scope of the work presented in this thesis on multi-rod resonator development will be confined to a maximum of two gain-modules per cavity.

4.1.3 Misalignment sensitivity

It has long been recognised that deviations in the alignment of the optical components that make up a laser resonator can have an impact on its

performance. Misalignment of the resonator mirrors can cause asymmetry in the spatial mode structure, which leads to greater diffraction losses [4.6; 4.7]. It is therefore advantageous to create resonator configurations that obey the conditions for efficient dynamic stability but are also relatively insensitive to misalignment. This means that the laser as an optical system will be most likely to withstand any long-term creep or mechanical shock. Alternatively, a lower sensitivity to misalignment can allow a relaxation in manufacturing tolerances, providing possible routes for cost reduction.

Theoretical treatments for the analysis of resonator misalignment have been suggested by investigation of the fractional re-coupling of reflected gaussian beams [4.8; 4.9]. However, a more practical approach is to define an expression that characterises misalignment sensitivity as a function of the controllable resonator parameters [4.10]. A resonator's sensitivity to misalignment can be simply related to the displacement of the geometrical mode axis and field pattern at the plane of the limiting aperture that is caused by tilting one or both of the cavity mirrors [4.11]. In this case the limiting (mode selecting) aperture is at the cross-section of the lens-like Nd:YAG rod. Figure 4.16 shows the displacement x_1 of the mode axis at the lens with misalignment of mirror 1 by an angle Ψ_1 for an arbitrary equivalent resonator.

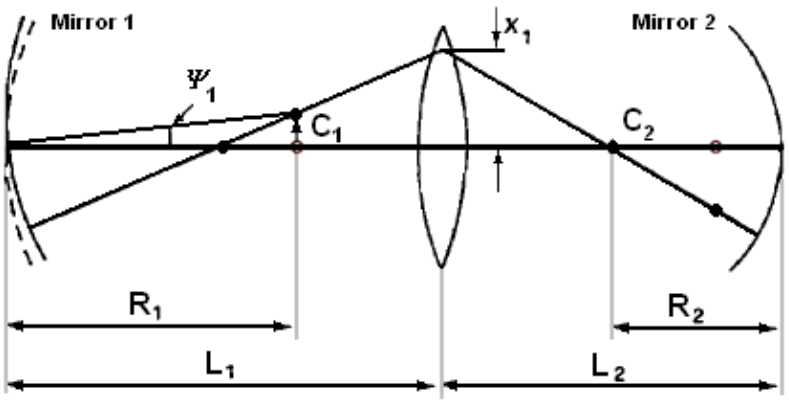

Figure 4.16 Mode axis of a resonator with misalignment of mirror 1 by an angle Ψ_1 [4.11].

For this optical system we can assume that the additional diffraction losses due to misalignment are a function of the mode axis displacement with respect to the mode size at the lens w_a for a given cavity mirror rotation. We can therefore define two misalignment sensitivity factors corresponding to the misalignment of mirror 1, S_1, and mirror 2, S_2, as follows

$$S_1 = \frac{x_1}{w_a \psi_1} \quad \text{and} \quad S_2 = \frac{x_2}{w_a \psi_2} \tag{4.15}$$

It is possible to express these sensitivity factors as a function of the controllable resonator parameters by investigating their relation to the spatial mode axis. Since the axis is required to be normal to the mirror surface it must follow the line toward the centre of curvature denoted C_1 for mirror 1 on figure (4.16). The mode axis is then conjugated at the other side of the lens so that it passes along a line that intersects the centre of curvature C_2 for mirror 2. The displacement at the lens for a given misalignment can be calculated using the lens-maker's formula in the small-angle approximation. For a multi-spatial-mode resonator the mode size at the lens W_{Pi} is static at the limiting aperture and can be related to the radius of the rod a by equation (3.36). This yields a more useful equation for the misalignment sensitivity, given by

$$S_i = \frac{\pi}{2a} \frac{R_i}{L_i - R_i} \left(\frac{1}{L_i - R_i} + \frac{1}{L_j - R_j} - D \right)^{-1} \tag{4.16}$$

where $i, j = 1, 2$; $i \neq j$ [4.12]. The overall misalignment sensitivity S for the resonator can be obtained by combining S_1 and S_2 as follows

$$S = \left(S_1^2 + S_2^2 \right)^{1/2} \tag{4.17}$$

Figure 4.17 illustrates a general trend in misalignment sensitivity as a function of the incident pump power (which is proportional to the internal lens power) for three general single-rod resonator conditions. The corresponding resonator stability on the (g_1, g_2) plane is shown for each. Although there are two permissible zones of resonator stability, invariably one zone exhibits greater

tolerance to cavity mirror misalignment. Moreover, the disparity in misalignment sensitivity between the two zones is increased the further they are apart in terms of lens power. This should be borne in mind when optimising the spatial characteristics of the resonator and selecting the preferred operating stability zone.

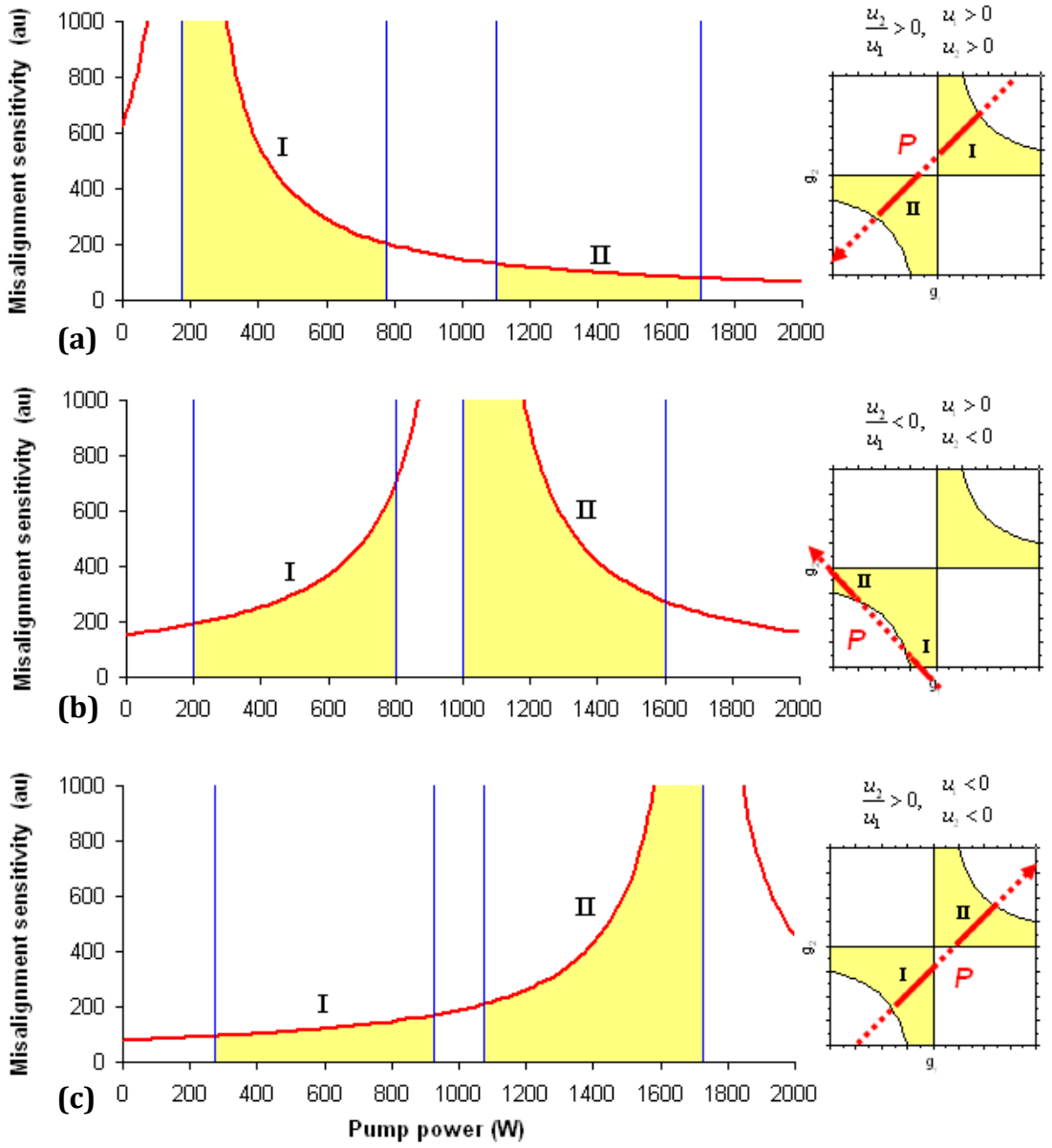

Figure 4.17 Qualitative representation of the misalignment sensitivity as a function of incident pump for three general single-rod resonator conditions; (a) $u_2/u_1 > 0$ where $u_1 > 0$, $u_2 > 0$ (b) $u_2/u_1 < 0$, where $u_1 > 0$ and $u_2 < 0$ and (c) $u_2/u_1 > 0$ where $u_1 < 0$, $u_2 < 0$. Stability on the (g_1, g_2) plane is illustrated for each case. Stability zones are shown by the shaded areas [4.12].

An interesting result of this investigation is that, contrary to some reports, an increasing internal lens does not always correspond to a stabilisation of the resonator, as illustrated in figure 4.17 (c).

The additional diffraction losses due to misalignment are difficult to quantitatively evaluate but to the first order can be considered proportional to $(\Psi_1 S_1)^2$ or $(\Psi_2 S_2)^2$. As a rule of thumb it can be assumed that the angle of misalignment required to produce a 10% increase in the cavity losses is $\sim 1/S$ [4.10; 4.11].

A similar approach for investigating the effects of misalignment has been presented with emphasis on the spatial mode structure rather than the increase in diffraction losses [4.13]. Again, a simple geometrical model can be formulated for assessing the misalignment sensitivity. In this case, it is suggested that the reduction in output power due to misalignment of a multi-spatial-mode resonator is only caused by a corresponding decrease in the mode volume inside the active medium. This model also assumes that the spatial structure remains symmetrical with respect to the mode axis. For a single-rod resonator, the angle by which mirror *i* can be tilted in order to produce a 10% reduction in the mode volume within the rod can be defined as

$$\psi_{i_{10\%}} = 0.025\pi a \frac{L_i - R_i}{R_1}\left(D_n - \frac{1}{L_1 - R_1} - \frac{1}{L_2 - R_2}\right) \qquad (4.18)$$

This method allows a more quantitative assessment of a resonators response to misalignment, providing the assumptions hold. In this case we see that $\Psi_{i10\%}$ varies proportionally with change in net refractive power and incident pump. A significant observation is that this model returns the same trends in misalignment sensitivity as the previous with respect to stability zone selection for all of the general conditions illustrated in figure 4.17.

Both of the geometrical models presented above have been extended to consider the additional factors associated with multi-rod laser resonators [4.14; 4.15]. In this case there are two main components to the misalignment

sensitivity. Again, titling of the cavity mirrors is of primary concern but this time we are also interested in the possible transversal displacement of the two rods with respect to the mode axis and each other. For mirror tilt investigation, equations (4.16) and (4.17) hold for dual-rod resonator configurations as long as the relative placement of the stability zones on the corresponding misalignment sensitivity curve is calculated using the modified stability parameters and effective resonator length, as defined by equations (4.11) and (4.12) respectively. The sensitivity in diffraction loss induced due to misalignment by transversal displacement of the rods with respect to one another can be estimated by assessing the relative size of the multimode beam at each rod. In multimode operation one of the rods will always be filled as the limiting (mode selecting) aperture. Using the model presented in section 3.1.4 we can derive an expression for the total transversal misalignment sensitivity of a rod relative to the other as a function of the controllable resonator parameters such that

$$S_{rod} = \frac{2a}{\pi} - \left| Mw_{P1} - Mw_{P2} \right| \tag{4.19}$$

where w_{P1} and w_{P2} are the radii of the embedded gaussian at principle planes P_1 and P_2 as defined by equation (3.34) and illustrated by figure 4.9. This model assumes that the direction of the mode axis is unchanged by the transversal displacement of either rod and that any translation in the mode axis with respect to the mirror centres is small. Figures 4.18 and 4.19 show the misalignment sensitivity associated with mirror tilt and transverse rod displacement for the dual-rod resonator previously presented in figures 4.11, 4.13 and 4.14.

For the treatment of compound misalignment sensitivity associated with multi-internal-element stable resonators the reader is directed to reference [4.16].

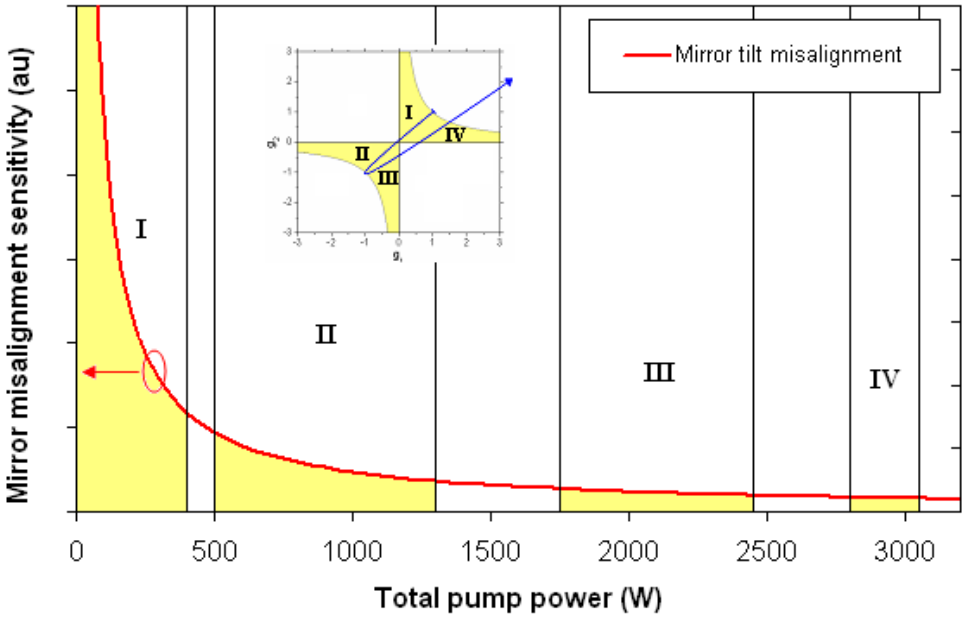

Figure 4.18 Qualitative representation of the misalignment sensitivity with mirror tilt as a function of total incident pump (proportional to internal lens power) for a dual-rod resonator.

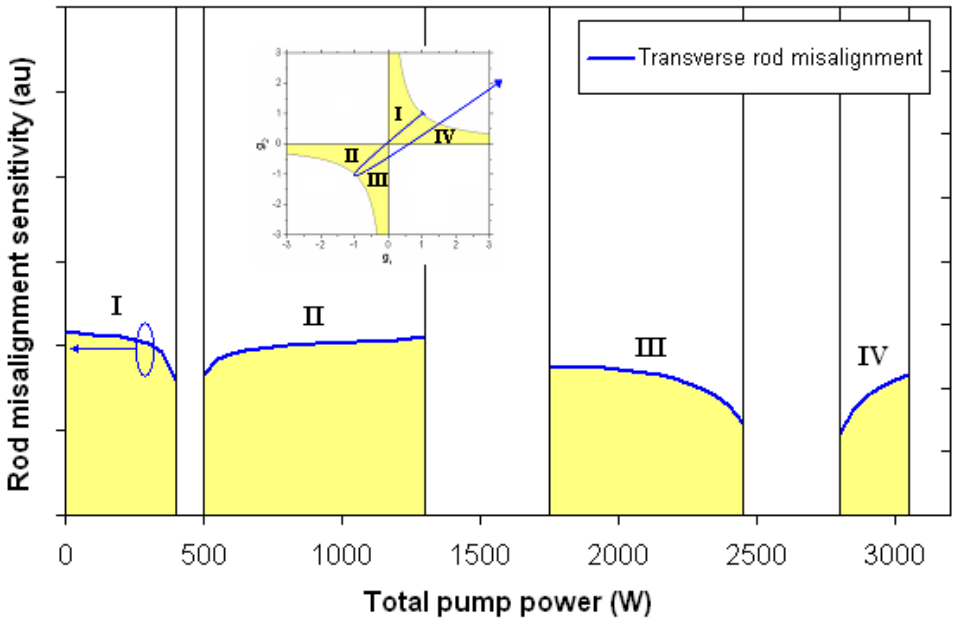

Figure 4.19 Qualitative representation of the misalignment sensitivity with transverse rod displacement as a function total incident pump (proportional to internal lens power) for a dual-rod resonator.

4.2 Temporal simulation: Q-switched pulse model

Rigorous mathematical analysis of Q-switched pulse evolution requires the simultaneous solution of the coupled differential equations that represent the relative rates of change in the population inversion and the intra-cavity photon density [4.17]. In practice however, laser designers are more interested how this Q-switching theory can be related to more useful parameters such as efficiency, pulse energy, peak power and pulse duration. It has been shown that simple analytic expressions for these key parameters can be mathematically derived using a Lagrange multiplier technique [4.18]. We can use these expressions to build a model based on the static and controllable conditions for gain and loss that will enable general simulation of Q-switched performance.

This Q-switched pulse model assumes unsaturated pump absorption such that the doping concentration is always in excess of the initial population inversion density n_i, which can be related to the total pump power P using the equation

$$n_i = \frac{P\eta_c\eta_u\tau_s\lambda}{Vhc} \tag{4.20}$$

where η_c is the pump coupling efficiency (this is the proportion of pump that is transferred into and absorbed by the laser rod). In section 2.2 a pump coupling efficiency η_c = 0.8 was obtained for the particular gain-modules used here. η_u is the upper-state efficiency, which is a product of the branching-ratio related quantum efficiency and the stokes factor. τ_s is the spontaneous emission lifetime, V is the pumped volume of the rod and λ is the free-space wavelength associated with the laser transition, resulting in an emitted photon energy of hc/λ. For the Nd:YAG transition in question η_u = 0.68, τ_s = 230 μs and λ = 1.064 μm. The total pump power should be set by the optimum output power of the pump diodes, which for the gain-modules used corresponds to approximately 830 W of continuous pumping.

At this point we can introduce a useful dimensionless parameter *Z*, which is defined as the ratio of the round-trip logarithmic small-signal gain to the parasitic (non-useful) round-trip cavity loss *l* and can be expressed as

$$Z = \frac{2\sigma n_i L_p}{l} = \frac{2g_0 L_p}{l} \tag{4.21}$$

where σ is the effective stimulated emission cross-section, L_p is the pumped length of the rod and g_0 is the unsaturated small-signal gain coefficient. For Nd:YAG the effective stimulated emission cross-section for the relevant manifold transition ($^4F_{3/2}$ - $^4I_{11/2}$), σ = 2.8 x 10^{-23} m^2. The logarithmic single-pass small-signal gain can be expressed as $g_0L_p = \sigma n_i L_p$, which leads to a single-pass power gain for the pumped rod G_0 given by

$$G_0 = \exp\left(g_0 L_p\right) \tag{4.22}$$

The first parameter of practical interest is the value of output mirror reflectivity that will maximise the output energy and therefore the efficiency of a standing-wave resonator for a given initial population inversion density or pump power. Assuming that the rear cavity mirror is highly reflective, the optimum output coupler reflectivity ρ_{2opt} can be defined as

$$\rho_{2_{opt}} = \exp\left[-l\left(\frac{Z-1-\ln Z}{\ln Z}\right)\right] \tag{4.23}$$

We can calculate the threshold inversion for oscillation with the optimum output coupler reflectivity, n_{th}, using the following expression

$$n_{th} = \frac{1}{2\sigma L_p}\left[\ln\left(\frac{1}{\rho_{2_{opt}}}\right) + l\right] \tag{4.24}$$

From this we are able to determine the pump threshold P_{th} defined as the total pump power required to compensate for the population loss at the upper state due to spontaneous emission. For a four-level system this is given by

$$P_{th} = \frac{hcn_{th}V}{\lambda \eta_c \eta_u \tau_s} \tag{4.25}$$

The number of times above threshold the population inversion is at the start of the Q-switched pulse build-up is thus given by $N_i = n_i/n_{th} = P/P_{th}$.

We can define an expression for the maximum possible output pulse energy at the optimised output coupling as

$$E_{\max} = \eta_B \frac{Ahcl}{2\lambda\sigma\gamma}\left[Z - 1 - \ln Z\right] \tag{4.26}$$

where A is the cross-sectional area of the rod and γ is an inversion reduction factor that corresponds to the net reduction in the population inversion resulting from the stimulated emission of a single photon. The value of γ not only depends on energy state degeneracies, but also on the speed of the various relaxation mechanisms in the active medium relative to the build-up time of the Q-switched laser pulse. If the relaxation time of the lower multiplet state ($^4I_{11/2}$) is slow compared to the Q-switched pulse duration then $\gamma = 2$, reflecting the fact that the population inversion is reduced by 2 for each stimulated emission of a photon. This is because, in the absence of any rapid relaxation mechanisms, the emitting atom remains trapped in the lower laser level during the remainder of the pulse. However, if the relaxation time of the lower multiplet state is slow but the thermalisation times within the multiplet states are rapid compared to the Q-switched pulse duration then the bottleneck is partially removed. At pulse durations greater than the 12 ns thermalisation time of the multiplet states for Nd:YAG the inversion reduction factor satisfies the inequality $0.6 < \gamma < 2$ [4.18]. For pulse durations of greater than 30 ns we have found that $\gamma = 1.1$ is appropriate. At this point we have also introduced another efficiency parameter η_B which represents the beam overlap efficiency. This is the degree by which the volume of the spatial mode matches the distribution of gain within the Nd:YAG rod. This can be approximated by comparing the cross-sectional gain-profile

$g_r(x)$ to the radial intensity profile of the beam $I_B(x)$ in the rod by using the overlap integral

$$\eta_B = \frac{\int g_r(x) I_B(x) 2\pi a.dx}{\int I_B^2(x) 2\pi a.dx} \tag{4.27}$$

where a is the radius of the rod. However, for this model we have assumed that the gain-profile is fixed for a given gain-module design and that the beam profile will not vary greatly between arbitrary multi-spatial-mode resonators that generate 10 - 100 times diffraction limited beams. Therefore, from the short test resonators used to characterise the gain-modules developed in chapter 2 we can calculate a typical value for $\eta_B = 0.7$.

In the limit of large Z, the output pulse energy approaches the total useful energy available to the laser mode E_u, which is given by

$$E_u = \eta_B \frac{Ahcl}{2\lambda\sigma\gamma} Z \tag{4.28}$$

We can therefore define an energy extraction efficiency for the Q-switched pulse η_E, expressed as

$$\eta_E = \frac{E_{\max}}{E_u} \tag{4.29}$$

This indicates that a fraction of the initial inversion may remain after the generation of a Q-switched pulse and that this is governed by the level of initial inversion and the threshold value.

In order to evaluate the average Q-switched output power P_Q we must also define a pulse-repetition-frequency related power efficiency η_Q, which compares the period between pulses t_p to the spontaneous emission lifetime [4.19] such that

$$\eta_Q = \frac{\tau_s}{t_p}\left[1 - \exp\left(-\frac{t_p}{\tau_s}\right)\right] \tag{4.30}$$

Therefore, the repetition-frequency dependent average Q-switched output power P_Q and corresponding pulse energy E_Q at the optimised output coupling are given by the expressions

$$P_Q = \eta_c \eta_u \eta_B \eta_E \eta_Q \eta_{ASE} P \tag{4.31}$$

and $$E_Q = P_Q t_p = \frac{P_Q}{f_R} \tag{4.32}$$

where f_R is the pulse repetition frequency. Also note that a final efficiency coefficient η_{ASE} has been introduced. This factor accounts for the fractional loss of upper-state population due to amplified spontaneous emission (ASE). This is required in the model to equate the correct proportion of the total pump that contributes to the Q-switched pulse and is implied within the inversion reduction factor γ previously used to calculate E_{max}. η_{ASE} can therefore be assessed in the limit of small f_R where the condition $E_Q = E_{max}$ must be met. For the system modelled here where $\gamma = 1.1$, we find that $\eta_{ASE} = 1/\gamma = 0.91$.

Also of great practical interest is the Q-switched pulse duration. The minimum permissible full-width-half-maximum (FWHM) pulse duration at the optimised output coupling t_{min} can be assessed using the expression

$$t_{\min} = \frac{t_R}{l}\left(\frac{\ln Z}{Z\left[1 - y'\left(1 - \ln y'\right)\right]}\right) \tag{4.33}$$

Here $t_R = 2L_r/c$ represents the round-trip time of the cavity where L_r is the effective (refractive index dependent) optical path length of the resonator and

$$y' = \frac{Z - 1}{Z \ln Z} \tag{4.34}$$

Thus, we can define a maximum extra-cavity peak power for the pulse as

$$P_{p_{\max}} = \frac{E_{\max}}{t_{\min}} \tag{4.35}$$

In a final step we can attempt to calculate the repetition-frequency dependent pulse duration t_Q. To a first order approximation we can assume that this duration will increase with inverse proportionality to the calculated Q-switched pulse energy from the minimum duration value, which will occur in the single-shot condition limit. We therefore obtain the expression

$$t_Q \cong t_{\min} \frac{E_{\max}}{E_Q} \tag{4.36}$$

The corresponding repetition-frequency dependent extra-cavity peak power for each Q-switched pulse is consequently given by

$$P_p = \frac{E_Q}{t_Q} \tag{4.37}$$

4.3 Laser-induced optical damage control

When developing a high-power laser for industrial operation it is not sufficient to simply design a resonator that satisfies the output requirements for the target applications. For reliable operation it is also important to consider how susceptible the components of the resonator may be to optical damage. Having developed theoretical models for both the spatial and temporal characteristics we can now combine the two in order to investigate the operating limits associated with laser induced optical damage.

High intra-cavity irradiances will occur at any waists generated in the spatial mode envelope, the size and position of which are described by equations (4.1) and (3.32) respectively. For a concave-concave cavity these waists are located between the rod and the cavity mirrors. It is therefore, in this case, sensible to install any additional cavity optics such as Q-switches away from the waist position in order to negate optical damage, unless the higher intensities generated are otherwise useful (in some non-linear frequency conversion configurations for example). For all plane-plane and convex-convex laser

resonators the maximum intra-cavity irradiances will occur at the surfaces of the cavity mirrors.

By further extending the resonator stability model presented in section 3.1.4 we can define the second moment multi-spatial-mode beam radius at cavity mirror m_i for all resonator configurations using the following exression

$$W_{m_i}^2 = M\left|\frac{\lambda L^*}{\pi}\left[\frac{g_j}{g_i\left(1-g_1g_2\right)}\right]^{1/2}\right| \tag{4.38}$$

This equation holds for resonators with any number of rods as long as the relevant g-parameters and effective cavity length L^* are used.

The two-way intra-cavity peak power at the resonator mirrors can be defined by extension of the Q-switched pulse model presented in section 4.2. At the output coupler mirror m_2 the PRF dependent two-way intra-cavity peak power is given by

$$P_{m_2} = \left(\frac{1+\rho_{2_{opt}}}{1-\rho_{2_{opt}}}\right)P_p \tag{4.39}$$

where ρ_{2opt} is the power efficiency optimised output coupler reflectivity and P_p is the PRF dependent extra-cavity peak power for the pulse, as defined by equation (4.37). The maximum two-way intra-cavity peak power will occur in the limit of low pulse-repetition-frequency, tending toward the single-shot conditions. Similarly, for the rear cavity mirror m_1, which is assumed to have a reflectivity ρ_1 close to unity, the PRF dependent two-way intra-cavity peak power can be defined as

$$P_{m_1} = \left[\frac{\left(1+\rho_1\right)\sqrt{\rho_{2_{opt}}}}{1-\rho_{2_{opt}}}\right]P_p \cong \left(\frac{2\sqrt{\rho_{2_{opt}}}}{1-\rho_{2_{opt}}}\right)P_p \tag{4.40}$$

Therefore, by combining equations (4.39) and (4.40) with equation (4.38) we can formulate an expression for the PRF dependent intra-cavity irradiance I_{mi} at the cavity mirrors with optimum output coupling such that

$$I_{m_i} = \chi \frac{P_{m_i}}{\pi W_{m_i}^2} \tag{4.41}$$

Here we have introduced a spatial form-factor χ, which is required to return a peak value of irradiance. This form-factor is used to account for the non-uniform spatial profile of the multi-mode beam at the cavity mirrors, which is likely to be super-gaussian with an order that is dependent on the spatial mode content. Typically we see that $1 \leq \chi \leq 2.3$ where $\chi = 1$ represents a uniform, top-hat spatial distribution that correponds to an infinately low beam quality and $\chi = 2.3$ represents the normal distribition observed at the waist of a diffraction limited beam. Without this form- factor, equation (4.41) would return the average irradiance across the beam diameter at the cavity mirror. General observation has revealed that 15 – 30 times diffraction limited beams generated by multimode rod lasers exhibit a form-factor $\chi \approx 2$. The corresponding PRF dependent peak fluence (energy density) at the cavity mirrors can be simply expressed as

$$F_{m_i} = \chi \frac{P_{m_i}}{\pi W_{m_i}^2} t_Q = I_{m_i} t_Q \tag{4.42}$$

The calculated peak irradiance and corresponding fluence values for a given cavity design can now be compared against the laser-induced damage thresholds (LIDT) specified by the optic substrate and dielectric coating manufacturers. In practice the LIDT depends on a number of factors. These include the dielectric material and stack design used to fabricate the reflective or anti-reflective coating, which can in turn depend on the wavelengths and angles of incidence required. Another related factor is the method by which the dielectric layers are deposited, which is also influenced by the materials being used. This essentially means that there can be varying combinations of dielectric material, stack design and layer deposition method that give the highest LIDT for different operating wavelengths, angles of incidence and reflectivities. The

details of complex coating design are beyond the scope of this thesis and are usually proprietary to the coating manufacturer.

The LIDT of an optic or coating is largely dependant on the damage mechanisms involved. For CW lasers and long pulse durations (> 10^{-6} s) the predominant causes of damage are a result of thermal effects. Conversely, at very short pulse durations (< 10^{-9} s), dielectic materials can experience avalanche ionisation or even multiphoton ionisation. For the applications described in this thesis we are interested in generating pulses that are tens of nanoseconds in duration. In this case the principal cause of laser induced optical damage is dielectric breakdown [4.20].

Typically, the LIDT reported by the coating manufacturers is specified as either an irradiance or fluence at the required wavelength for a single-shot test-pulse duration t_T. This test-pulse duration is invariably different to the minimum or repetition frequency dependent pulse durations t_{min} or t_Q associated with the laser being designed. However, in the nanosecond, high repetition frequency regime we may apply a number scaling factors to the specified LIDT that have been derived from empirical observations. Firstly, we can scale the LIDT proportionally with $t^{1/2}$ to generate a modified damage threshold fluence F_{Tsc} given by

$$F_{T_{SC}} = \frac{\sqrt{t_{\min}}}{\sqrt{t_T}} F_T \tag{4.43}$$

where F_T is the tested fluence value specified by the coating manufacturer. For example, a specified LIDT of 50 J.cm^{-2} at 8 ns would scale to 71 J.cm^{-2} for 16 ns minimum operating pulse duration (t_{min}). This scaling is also applicable to specified irradiance damage thresholds.

An additional rule-of-thumb scaling factor can be implemented to account for operation at high pulse-repetition-frequencies where the average power becomes sufficient to cause thermally induced damage mechanisms. In this case, the pulse duration scaled LIDT should be carried out using the repetion-

frequency dependent pulse duration t_Q and then given a further scaling factor of $1/N_f$, where N_f is the PRF order of magnitude with respect to the single-shot condition (i.e. $N_f = 1$ for 1 Hz PRF and $N_f = 5$ for 10 kHz PRF). For the repetitively Q-switched nanosecond pulse regime we therefore have an overall specified LIDT fluence scaling law expressed as

$$F_{T_{SC}} = \frac{\sqrt{t_Q}}{\sqrt{t_T}} \frac{1}{N_f} F_T \tag{4.44}$$

Extending the previous worked example, a manufacturer specified LIDT fluence of 50 J.cm^{-2} at 8 ns would therefore scale to 20 J.cm^{-2} for 32 ns pulse duration operating at 10 kHz PRF. This threshold value can now be compared to that predicted by the Q-swtiched pulse model presented in section 4.2 to ascertain whether or not self-induced optical damage should be expected for a given resonator design. Again, this LIDT fluence scaling law holds for manufacturer specified irradiance values also.

4.4 Summary

In chapter 4 we have reported on the refinement of two mathematical models for the optimisation of actively Q-switched, multi-spatial-mode resonators. As an extension of the basic concepts presented in chapter 3, the first model was used to simulate the spatial properties of non-diffraction limited beams generated in thermally active laser cavities. Here we introduced the notion of dynamic stability regions generated by stress-induced polarisation bifocusing. Methods for resonator stability optimisation were given for a single-rod case and extended to include multi-rod configurations. The spatial model was then augmented to include the ability to evaluate various forms of cavity misalignment sensitivity.

A second model was then presented that facilitates the temporal simulation and optimisation of CW pumped, actively Q-switched resonators. This model enables calculation of the inversion levels and corresponding energy-extraction-

efficiency-optimised output coupling. Using these parameters we can project the PRF-dependent average output power, pulse energy, FWHM pulse duration and peak power for a given oscillator design.

Whilst the temporal optimisation of Q-switched pulsing is not new, when integrated with the spatial model it becomes a much more useful tool for industrial laser development. By combining the two models we are able to assess the susceptibility of a laser resonator to self-induced optical damage and alter the fundamental design to avoid this effect.

5 Multi-spatial-mode resonators: Part III – Experimental results

In this chapter we detail the experimentally determined performance characteristics for single and dual-rod resonators that have been constructed using the design principles and mathematical models presented in chapters 3 and 4. For the target industrial applications (detailed in chapter 1) the objective is to produce cost-effective, dynamically stable laser resonators with M^2 beam propagation parameters in the order of 15 – 30. These resonators must also exhibit tens of nanosecond pulse durations and the highest reliably achievable pulse energies when operating at kilohertz repetition frequencies.

5.1 Single-rod resonator design and characterisation

The following single-rod resonator configuration has been proposed in an attempt to validate the mathematical models and satisfy many of the performance requirements outlined in chapter 1. This design makes use of the gain-module developed and characterised in chapter 2.

5.1.1 Resonator design

Given a fixed rod diameter, the resonator arm lengths and mirror curvatures should be first optimised to obtain the required operating beam quality, as characterised by the M^2 factor. In order to achieve full *output* dynamic stability (defined by equation (4.5) and illustrated in figure 4.5) we must also set the cavity arm lengths and mirror curvatures such that $|u_2| < |u_1|$ (Ref. equation (3.22)). The position of the dynamic stability design point can then be translated to coincide with the optimum pump power, in this case ~ 830W, by changing the rod facet curvatures in the resonator model. Conveniently, for the gain-modules developed in chapter 2, which has a fixed rod diameter of 4.5 mm and a thermal lens constant under oscillating conditions C_t = 0.0084 D.W^{-1}, the criteria for full output dynamic stability at a suitable operating $M^2 \sim 25$ can be met using a plane-plane resonator with plane-plane rod facets. The use of plane-parallel optics will also help minimise the component cost of the resonator and allow the specification of standard optical tolerances. In this case, operation is centred at the largest dynamic stability region associated with the second resonator stability zone (as illustrated in figure 4.8). Zone II also exhibits reduced sensitivity to misalignment relative to zone I (see figure 4.17 (a)). The corresponding physical arm lengths (distance between cavity mirror and rod facet) for the resonator, as generated by the stability model, are d_1 = 0.200 m and d_2 = 0.175 m.

Using equation (4.20) of the Q-switched pulse model, presented in section 4.2, we can evaluate the initial population inversion n_i prior to Q-switching. At the optimum pump power of 831 W, n_i = 7.64 x 10^{23} m^{-3}. This value is below the limit for gain saturation set by the Nd^{3+} doping concentration, which in this case is 9.01 x 10^{25} m^{-3} (corresponding to 0.65 % at. Nd). Following the Q-switched pulse model we see that this level of initial inversion leads to an unsaturated small-signal gain coefficient g_0 = 0.214 cm^{-1}. A pump length L_p = 4.6 cm results in a logarithmic single-pass small signal gain g_0L_p = 0.98 and a corresponding single-pass power gain G_0 = 2.68.

Assuming a reasonable roundtrip parasitic loss of 3 % we can use equation (4.23) to calculate the power-efficiency-optimised output coupler reflectivity ρ_{2opt}. For the single-rod resonator at optimum pump ρ_{2opt} = 64.8 % (or 35.2 % output coupling). From equations (4.24) and (4.25) we can also evaluate the population inversion at the threshold for oscillation n_{th} = 1.80 x 10^{23} m^{-3} and the corresponding total pump for this threshold condition P_{th} = 196 W, given the optimum output coupling. These values are a factor N_i = 4.24 times below those associated with the initial inversion at the optimum pump of 831 W.

For this laser, compression mode acousto-optic modulators (AOMs) have been implemented to enable sufficiently fast Q-switching of the resonator. The AOM Q-switch used has a commercially standard configuration, which comprises a fused-silica cell and a piezoelectric transducer for production of a travelling-wave phase grating (driven with 100 W RF power at 27.1 MHz modulation). Practically, we are restricted to the use of fused-silica as an AOM cell substrate due to the damage thresholds required for operation at very high intra-cavity irradiances. It is common practice to locate the AOM at the rear of the resonator to prevent residual diffracted light emerging at the laser output. This requirement is not as critical for master-oscillator power-amplifier systems where the amplifier rods can act as an aperture stop for unwanted diffracted light (this is further discussed in chapter 6).

Although the AOM used here had the highest commercially available diffraction efficiency for its type (90% +0, -5 for 1.064 μm wavelength at the Bragg angle) it became immediately apparent that a single Q-switch was not sufficient to hold-off oscillation in the resonator. In fact the addition of a second AOM only eliminated CW leakage (pre-lasing) when they were specifically positioned with respect to the gain-module and cavity mirror. It is hypothesised that this is because the diffraction angle of 5 mrads was not enough to prevent re-coupling of the light into higher order resonator modes. The extent of this re-coupling was found not only to be dependent on the location but also on the orientation of the Q-switches. Increased hold-off was observed when one AOM was rotated

about the axis of beam propagation so that the phase gratings are perpendicular to one another. It is thought that this may be due to the elimination of crossed-coupling between the AOMs whereby diffracted light from one cell is re-coupled into a resonator mode by the other, when diffracting in the same plane. For this resonator, maximum hold-off is observed when perpendicular AOMs are positioned together and in the centre of the rear cavity arm. Although 100% modulation depth is not required for Q-switching, the elimination of pre-lasing can be advantageous from an application process stand-point. Pre-lasing is assumed not to occur between pulses in the Q-switched resonator model presented in section 4.2.

At this point it is important to note that the addition of transmitting resonator components that have refractive indices greater than 1 (such as fused-silica AOM cells) will affect the spatial and temporal models in opposing ways. In the Q-switched pulse model the addition of a component with higher refractive index will increase the effective optical path length L_r and consequently the round-trip time of the resonator t_R. Conversely, in the spatial model the addition of such a component will be seen by the paraxial rays as an effective shortening of the cavity arm lengths L_1 and L_2 and therefore the referenced physical lengths d_1 and d_2 [3.3]. This will in turn affect the stability and spatial characteristics of the resonator. The actual physical arm lengths $d_{1'}$ and $d_{2'}$ required to compensate for the effective shortening of the cavity observed with installation of two AOM Q-switches are thus given by

$$d_{1'} = d_1 + 2\left(L_q - \frac{L_q}{n_q} \right) = 0.200 + 2\left[0.04 - \left(\frac{0.04}{1.449} \right) \right] = 0.225 \text{ m} \qquad (5.1)$$

and $$d_{2'} = d_2 = 0.175 \text{ m} \qquad (5.2)$$

where L_q = 0.04 m is the physical length of the Q-switch cell and n_q = 1.449 is the refractive index of fused-silica at 1.064 μm wavelength. These resulting physical cavity dimensions for the final optimised resonator are shown in figure 5.1. The effective total optical path length L_r for this resonator is given by

$$L_r = d_{1'} + 2\left(L_q n_q - L_q\right) + n_r L + d_{2'}$$

$$= 0.225 + 2\left[0.04\left(1.449\right) - 0.04\right] + 1.823\left(0.097\right) + 0.175 = 0.612 \text{ m} \quad (5.3)$$

where n_r and L are the first order refractive index and length of the laser rod respectively.

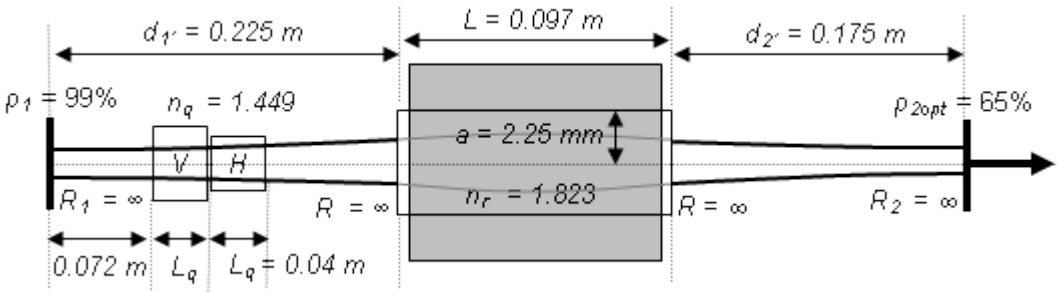

Figure 5.1 Schematic of the optimised single-rod multi-spatial-mode resonator showing all cavity components and physical dimensions including the vertically (V) and horizontally (H) orientated acousto-optic modulators. Not to scale.

As a final check before this laser is constructed we must employ the models to assess its possible susceptibility to laser induced optical damage. Using equation (4.38) we can calculate the average multi-mode beam radius for radial and tangential polarisations at the cavity mirrors. For the optimum pump power of 831 W this yields W_{m1} = 1.06 mm and W_{m2} = 0.88 mm (although at this pump level the spatial model indicates that the polarisation may be predominantly tangential with slightly larger beam radii). The corresponding peak fluence at each mirror as function of pulse-repetition-frequency is calculated using equation (4.42). Figure 5.2 shows this peak operating fluence relative to the pulse duration and PRF scaled laser induced damage threshold F_{TSC}, as defined by equation (4.44) and given a manufacturer specified threshold fluence F_T = 50 J.cm^{-2} (at a single-shot test pulse duration t_T = 8 ns), for both mirrors.

Note that the scaled damage threshold shown on figure 5.2 moves through a minimum as the PRF (and PRF dependent pulse duration) increases. Theoretically, reliable operation should be guaranteed as long as the peak

fluence lies below the scaled threshold at all intended operating PRF. In practice however it is sensible to operate at a predetermined safety factor below the scaled threshold in order to account for any variation in damage performance from mirror to mirror. We have found that a safety factor of $0.75F_{TSC}$ is adequate for reliable industrial operation. Moreover, if first pulse suppression is not implemented then, as a second requirement, the peak fluence for a single-shot pulse must also be below the corresponding scaled damage threshold. In this case, the proposed resonator design satisfies the conditions for damage-free operation as the intended working PRF is above 5 kHz for all target applications detailed in chapter 1.

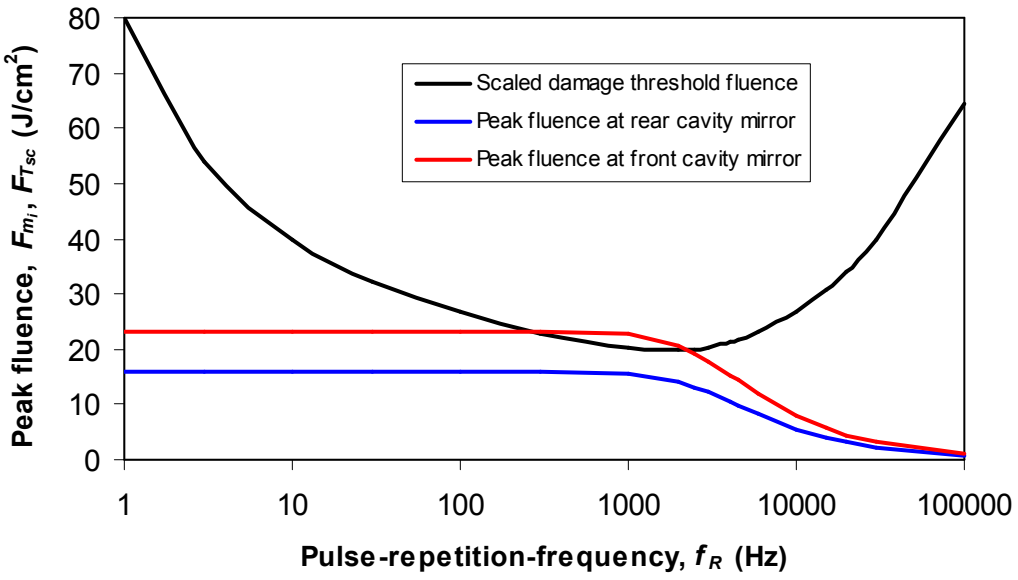

Figure 5.2 Peak operating fluence at each cavity mirror for the single-rod resonator as function of PRF relative to the pulse duration and PRF scaled laser induced damage threshold F_{TSC} (given a manufacturer specified threshold fluence F_T = 50 J.cm^{-2} at t_T = 8 ns for both mirrors).

5.1.2 Spatial beam characterisation

Now that we have a full theoretical design for the single-rod resonator we can compare the simulated output characteristics with the experimentally

determined resonator performance. A 66 % output coupler reflectivity was used as the best available match for the theoretical optimum of 64.8 %. The spatial characteristics of the beam were measured using ~ 5 W of light coupled out of the high reflector at the rear of the cavity, which was in fact given 99 % (±0.2 %) reflectivity to provide a reproducible source for real time power monitoring of the laser product. This output is also useful for diagnostic measurement when the high-power beam is being otherwise used or when means of attenuation are unavailable or impractical. The resonator beam characteristics were experimentally determined using a commercially available Spiricon (M^2-200) beam propagation analyser, which conforms to the ISO standard (ISO 11146) for such measurement. This apparatus operates by creating a waist that is axially translated through the plane of an appropriate camera sensor. The second moment beam size is recorded at predetermined steps through the waist for both *x* (horizontal) and *y* (vertical) cross-sections. This produces two caustic curves that can be used to calculate the beam propagation parameter for each plane to within ± 5 % fractional error.

Figure 5.3 shows the graphical representation of the caustic curves given by the user interface of the beam propagation analyser. Also shown is the data for this particular measurement and a spatial profile of the beam taken at a point along the caustic curve. The selected spatial profile in figure 5.3 shows an image of the beam within the laser rod. Note that a small degree of 5-fold symmetry is exhibited in the beam profile that reflects the orientation of the pump diodes with respect to the rod. This suggests that the absorbed pump distribution may not be as homogeneous as predicted in chapter 2. The spatial mode shaping may therefore be due to a combination of an irregular distribution of gain and any consequential aberrations induced in the thermal lens by uneven heat deposition.

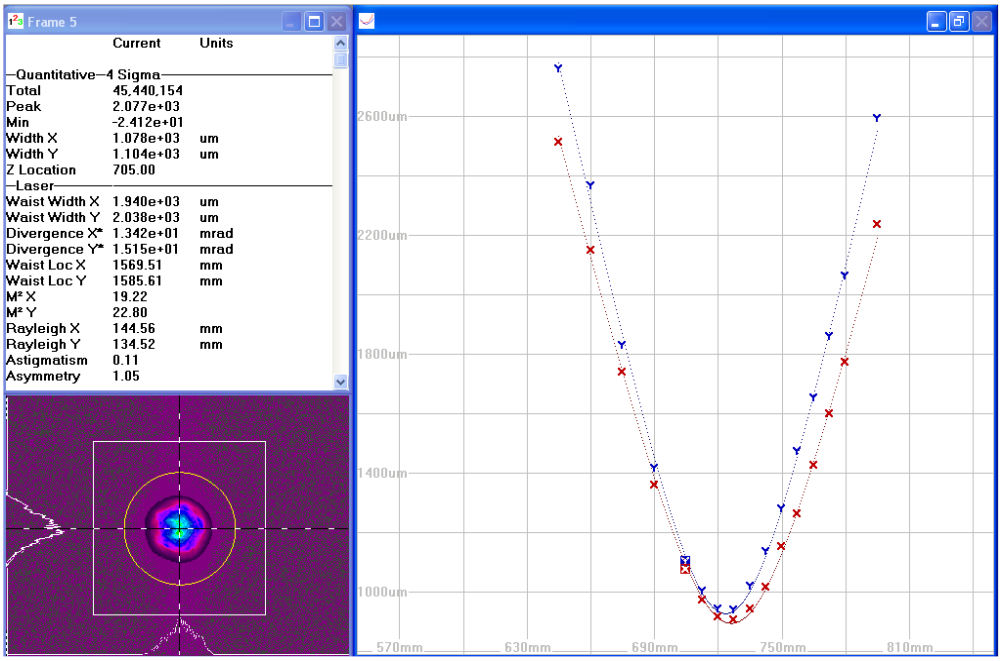

Figure 5.3 Spiricon M^2-200 user interface showing a graphical representation of the experimentally measured caustic curves, beam propagation data and a spatial profile taken at a rod image plane.

Figure 5.4 shows the expected beam propagation parameter (M^2) generated by modelling the resonator stability and spatial mode content associated with the internal lensing experienced by both radial and tangential polarisations, under oscillating conditions. The corresponding experimental data for CW operation measured in the *x* (horizontal) and *y* (vertical) axes of the beam profile is superimposed.

The data shown in figure 5.4 demonstrates that this cavity may actually benefit from a slight negative lensing via long-radius concave rod-facet curvatures in order to centralise the second stability region on the optimum pump. The variation in the measurements between the *x* and *y* axes outside of the normal fractional error is likely to be due to residual astigmatism in the thermal lens and the fact that the resonator was aligned for maximum output power, which may not be perfectly plane-parallel. This is made evident by a small (5 %) asymmetry in the output beam (relative to the measurement axes).

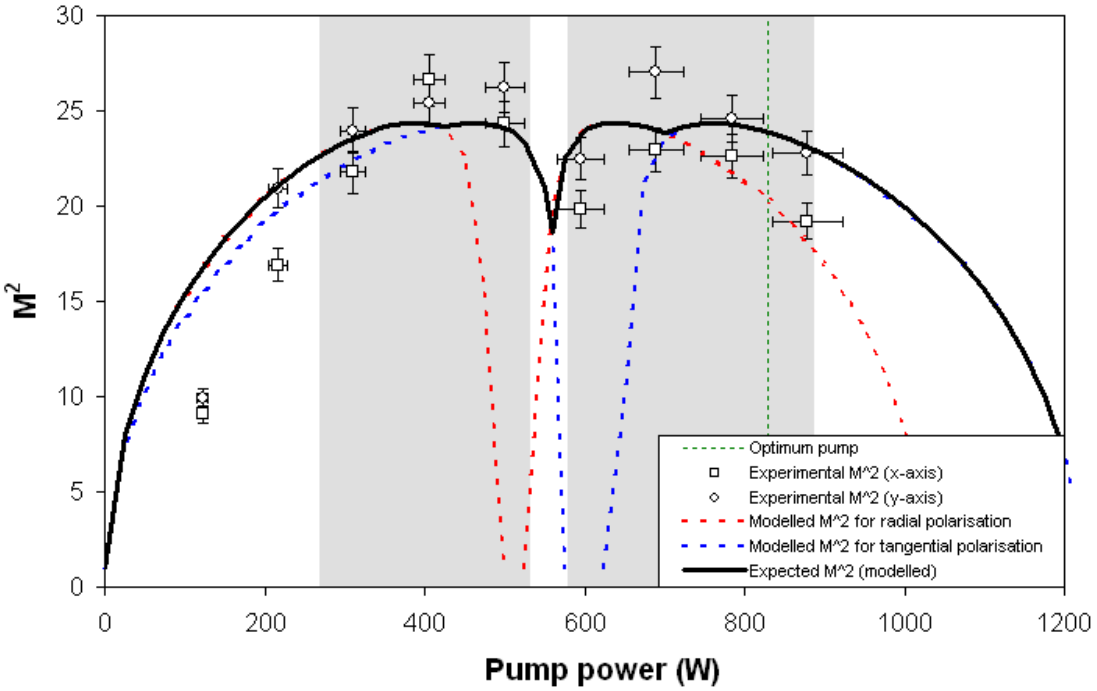

Figure 5.4 Mathematically simulated and experimentally measured beam propagation parameter as a function of pump power for the constructed single-rod resonator. The regions of output dynamic stability are shown by the grey shading.

Notice that the experimentally determined M^2 is seen to deviate from the theoretical model below 200 W pump power. This is as expected and believed to be caused by the loss of higher order spatial modes due to the lack of gain available to them. In fact, the Q-switched pulse model (Ref. equation (4.25)) predicts a total pump power at oscillation threshold P_{th} = 196 W, thus correctly indicating that the threshold for oscillation should be limited by the population inversion rather than resonator stability. In reality the threshold for oscillation is observed slightly lower at around 160 W total pump, which suggests that the parasitic losses are likely to be moderately less than the 3% assumed in the model. This result is illustrated in figure 5.5, which shows the CW output power as a function of the total pump. A line of best fit indicates a slope efficiency of 36.2 (± 0.5) % and an optical to optical efficiency of 29 (± 3) % at optimum pump.

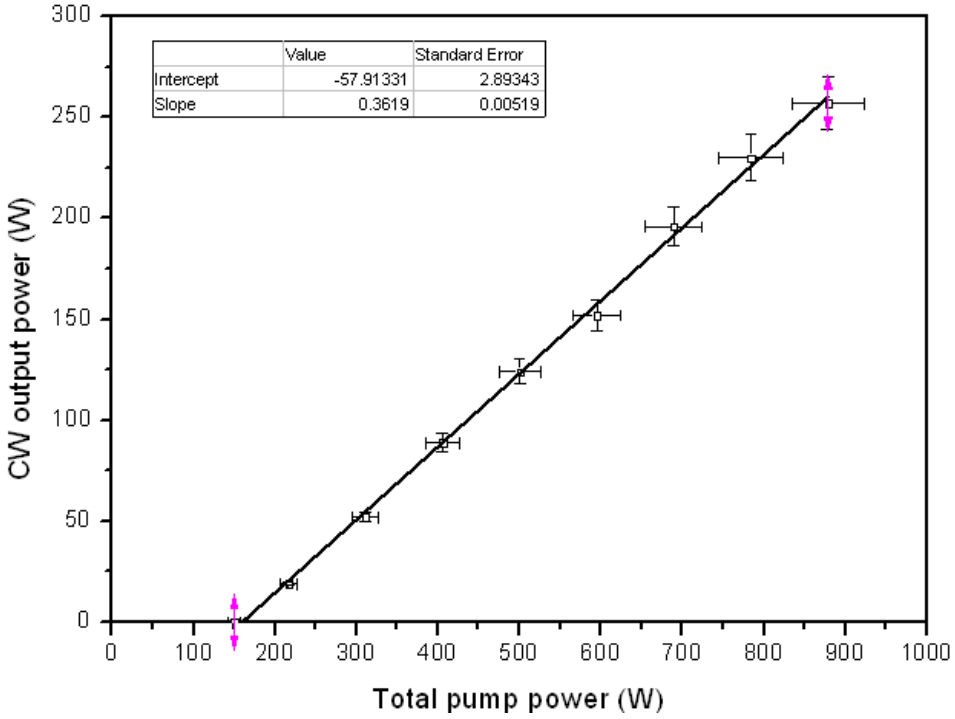

Figure 5.5 Experimentally measured CW output power as a function of total incident pump power for the constructed single-rod resonator with optimum output coupling.

For further verification of the resonator stability model we can compare other simulated spatial beam characteristics to that measured using the beam propagation analyser. Figure 5.6 shows the multi-mode waist radius and far-field half-angle divergence as a function of total pump power, again measured at the rear of the cavity.

The mathematically modelled spatial data shown in figure 5.6 illustrates a general agreement with the experimentally determined trends. However, the inherent errors in the experimental measurements lead to uncertainty as to whether the data follows the radial component, tangential component or some weighted average of the two. It is likely that above the oscillation threshold for all permissibly stable higher order modes the beam will comprise some mixture of both radial and tangential polarisations. Interestingly, the model shows very good correlation with the experimental results at the points labelled A and B

where only one of the polarisation components is allowed to propagate under the conditions for stable self-sustained oscillation.

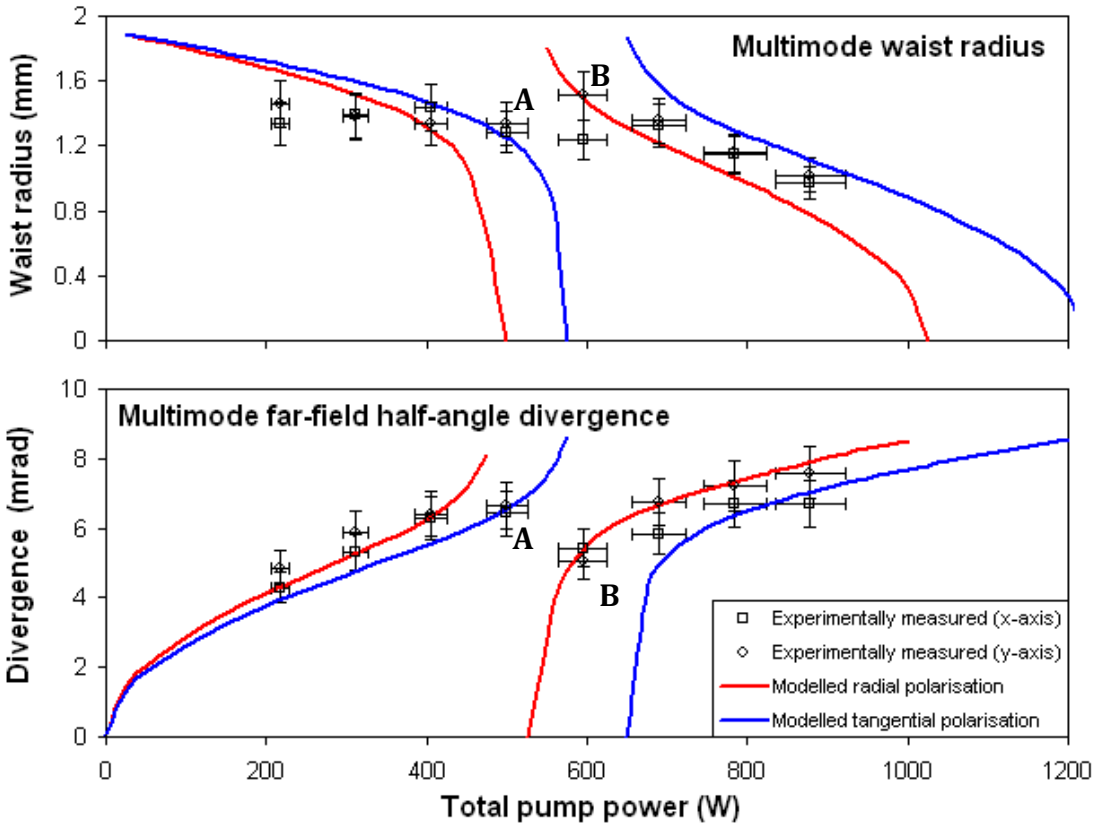

Figure 5.6 Mathematically simulated and experimentally measured multimode waist size and far-field half-angle divergence as a function of pump power at the rear of the single-rod resonator.

Having ascertained that the resonator model can adequately predict the properties of a multi-spatial-mode beam we would expect the output at the front of the laser to follow the full dynamically stable trends illustrated in figure 5.7.

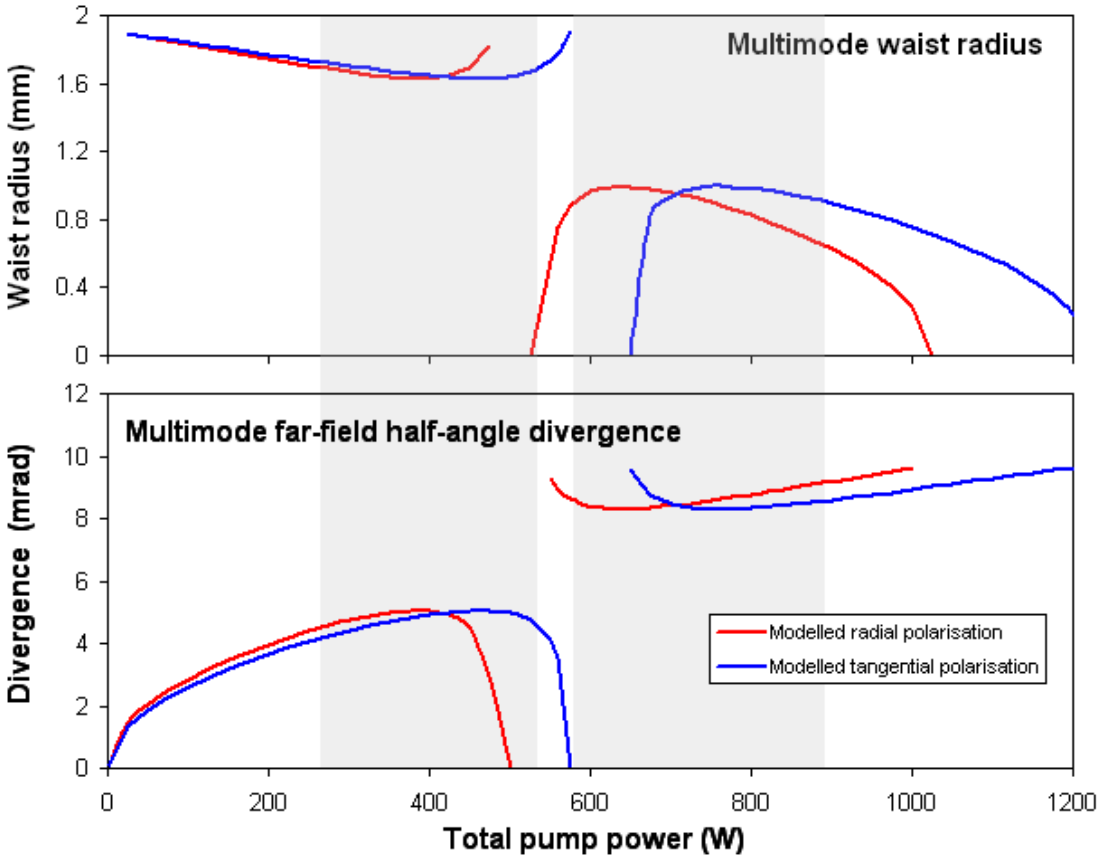

Figure 5.7 Mathematically simulated multimode waist size and far-field half-angle divergence as a function of pump power at the front the single-rod resonator. The regions of full output dynamic stability are shown by the grey shading.

5.1.3 Q-switched performance

The experimentally measured Q-switched performance of the single-rod resonator can now be compared to the data generated by the model presented in section 4.2. To ensure fastest Q-switching the AOMs were synchronised such that the two travelling-wave phase-gratings are simultaneously coincident with the laser beam. This condition can be approximately set by selecting a pump power at which the resonator is able to generate stable pulses with either one of the AOMs operating in isolation. One AOM is then translated so that the pulse that it generates occurs at the same time as a pulse generated when the alternate AOM is switched only. Figure 5.8 shows the results for the resonator output when both AOMs are used for Q-switching at the optimum pump power

of 831 W. The average power was measured to within ± 5 % fractional error using a Coherent LM-1000 thermopile power-meter head and compatible field-master display. As there was no pre-lasing between pulses the pulse energy can be determined by simply dividing the average power by the PRF f_R.

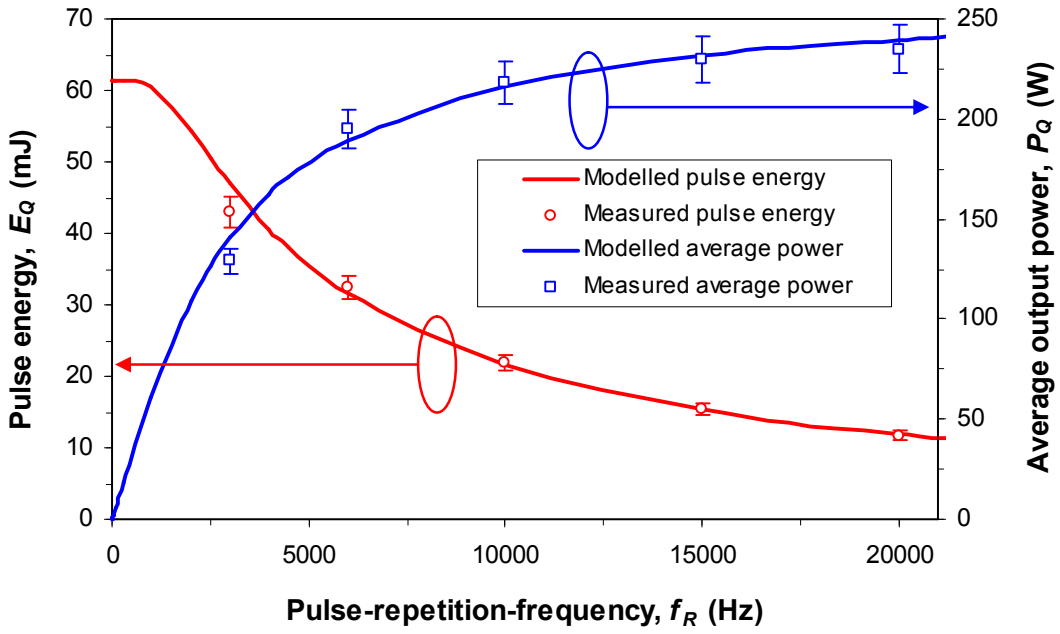

Figure 5.8 Mathematically simulated and experimentally determined average power and pulse energy as a function of pulse repetition frequency for the constructed multimode single-rod resonator.

The experimental results demonstrate a very good match with the mathematically simulated data. This is also the case in figures 5.9 and 5.10, which illustrate the PRF dependent full-width-half-maximum (FWHM) pulse duration, peak output power and corresponding peak fluence at the cavity mirrors (relative to the previously determined scaled damage threshold F_{TSC}).

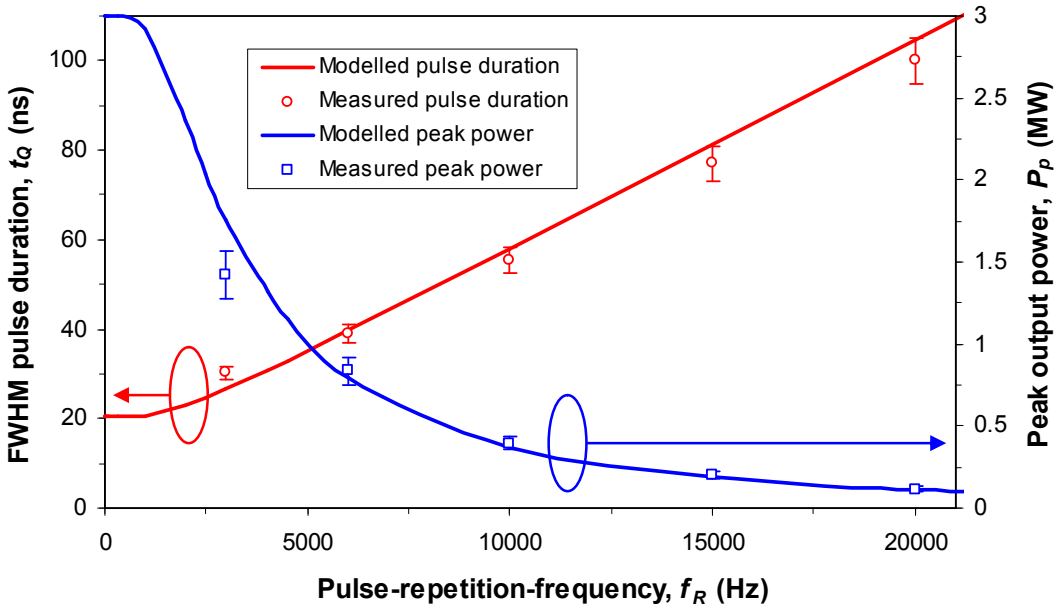

Figure 5.9 Mathematically simulated and experimentally determined full-width-half-maximum (FWHM) pulse duration and peak output power as a function of pulse repetition frequency for the multimode single-rod resonator.

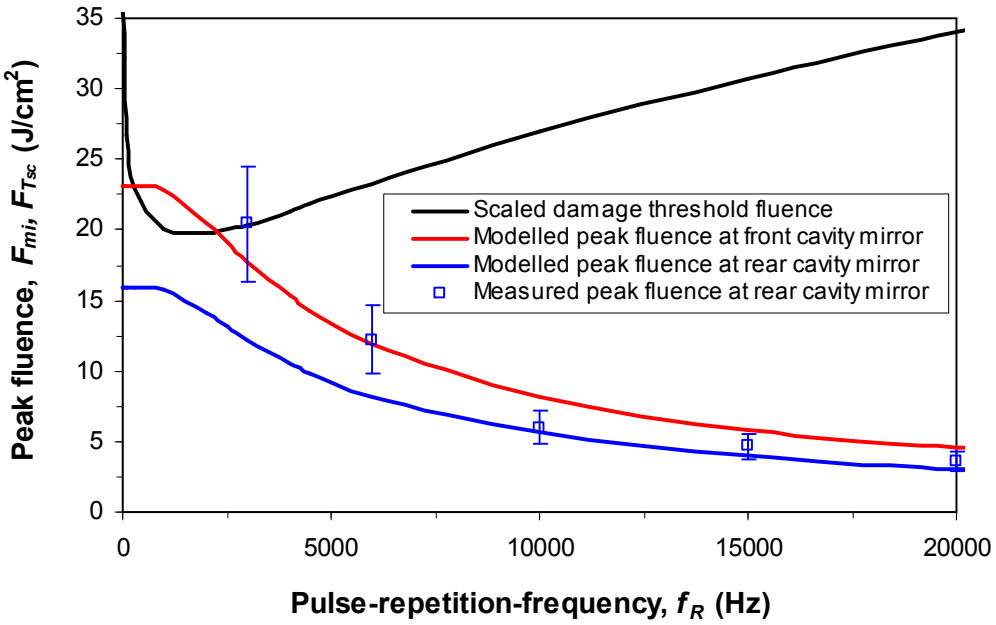

Figure 5.10 Mathematically simulated and experimentally determined peak fluence at the cavity mirrors relative to the scaled damage threshold as a function of pulse repetition frequency for the multimode single-rod resonator.

Figures 5.8 and 5.9 indicate that the experimental data begins to deviate from the mathematical model below ~ 5 kHz PRF. This is predominantly due to a reduction in the expected gain or extraction of gain, which leads to reduced average power, pulse energy and increased pulse duration. As a result the peak power values are also lower than expected. A change in the efficiency of energy extraction can be brought about by a variation in the beam-to-gain overlap as a result of change in spatial mode structure due to the increased thermal lensing at lower PRF (as discussed in section 3.2.1 and illustrated in figure 3.11). This hypothesis may be substantiated by the fact that the rear beam waist size is also observed to decrease at lower PRF, which maintains a high peak fluence at the cavity mirror despite the reduction in peak power (see figure 5.10). It is also significant that the spatial characteristics at 3 kHz PRF are similar to those at much higher PRF when the pump power is decreased by 10 %, thus emulating the expected difference in thermal loading between non-oscillating (or low PRF) and CW oscillating (or high PRF) conditions. This effect will be less evident at the front (main output) beam, which has been designed to be dynamically stable with respect to the multi-mode waist size.

In this case, to ensure reliable operation below the scaled threshold for optical damage the PRF should be kept above 5 kHz. However, when operating at both high peak and high average powers there is another damage issue that should also be considered and accounted for. The intra-cavity average power P_{Qin} for these resonators can become very large, increasing at higher PRF. P_{Qin} can be calculated by extending the Q-switched pulse model, yielding the expression

$$P_{Q_{in}} = \frac{P_{m_2}}{P_p} P_Q = \left(\frac{1+\rho_{2_{opt}}}{1-\rho_{2_{opt}}} \right) P_Q \qquad (5.4)$$

At 20 kHz PRF, for example, the average power of the constructed single-rod resonator is in excess of 1.1 kW. Although this average power is accounted for in the optical damage calculations it has other implications for the design and specification of the mounts, holders, apertures and retaining methods for optics

and components in the vicinity of the laser beam. The opto-mechanics used in the construction of the laser should be selected such that they are able to cope with extended heating and thermal cycling without detrimental levels of movement or chemical out-gassing.

Figure 5.11 provides an illustration of the pump-power related conditions that influence Q-switched pulsing consistency as a function of PRF for the single-rod multi-spatial-mode resonator. The measured data agrees with the general trends highlighted in section 3.2.1 (and illustrated in figure 3.11). Here, the maximum operating pump power P_{max} was limited to 880 W to conserve laser diode lifetime. This meant that the terminating condition present at a higher pump power where the resonator becomes unstable $P_{s'}$ could not be investigated. Note that the loss of pulse stability at high pump power and low PRF was not observed as the AOM Q-switches were capable of complete oscillation hold-off at the tested pump levels.

For this resonator the minimum pump level needed for resonator stability (P_s = 0 W) is below the minimum level for inversion and the corresponding pump power P_{min} required for oscillation. Therefore, the threshold for oscillation lies at P_{min}. The pump power that corresponds to the conditions for maximum pulsing consistency P_o is seen to occur close to the optimum laser diode output and lies within the region of output dynamic stability, as illustrated in figure 5.4. This data suggests that the best conditions for Q-switched operation are obtained when the optimum pump level is located slightly toward the upper limit of the output dynamic stability region rather than centralised on it (as happens to be the case for the resonator constructed here, see figure (5.4)).

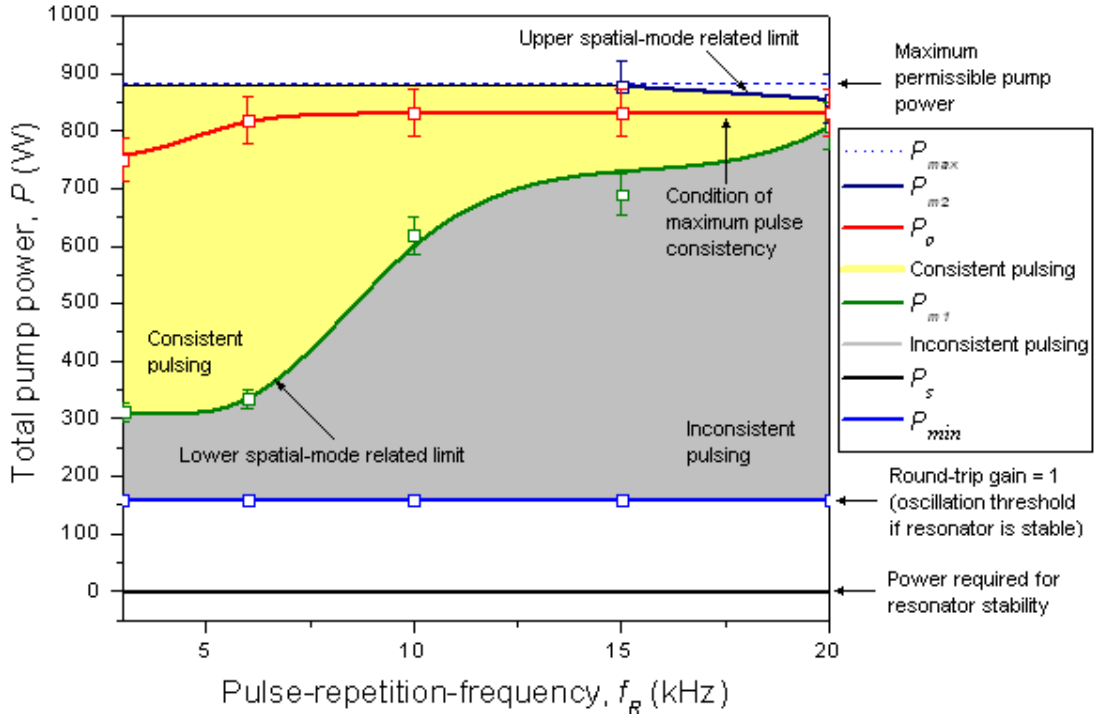

Figure 5.11 Experimentally investigated pump-power related conditions that influence Q-switched pulse consistency as a function of PRF for the proposed single-rod multi-spatial-mode resonator.

5.2 Dual-rod resonator design and characterisation

The following dual-rod resonator configuration was proposed in an effort to scale the output power while generally maintaining the spatial and temporal characteristics exhibited by the previously presented single-rod arrangement. We have once again utilised the gain-module design developed in chapter 2.

5.2.1 Resonator design

An optimised dual-rod cavity design has been determined by applying the resonator stability and Q-switched pulse models in the same manner as that described in the previous section. At the optimum total pump power of 1662 W (831 W per gain module), the initial population inversion density prior to

Q-switching is the same as the single-rod case whereby $n_i = 7.64 \times 10^{23}$ m^{-3}. Again, this is well below the limit for gain saturation set by the Nd^{3+} doping concentration. It follows that the unsaturated small-signal gain coefficient is also the same as the single-rod case, such that $g_0 = 0.214$ cm^{-1}. In the dual-rod configuration however, a total pump length of $L_p = 9.2$ cm leads to a logarithmic single-pass small signal gain $g_0 L_p = 1.96$, which corresponds to a single-pass power gain $G_0 = 7.16$.

The model also returns a power-efficiency-optimised output-coupler reflectivity for the dual-rod resonator at optimum pump $\rho_{2opt} = 43.2$ % (or 56.8 % output coupling), assuming a reasonable roundtrip parasitic loss of 5 %. Given this optimum output coupling the population inversion at the threshold for oscillation $n_{th} = 1.73 \times 10^{23}$ m^{-3} and the corresponding total pump for this threshold condition $P_{th} = 376$ W, or 188 W per gain-module (Ref. equation (4.25)). These threshold values are a factor $N_i = 4.42$ times below those associated with the initial inversion at the optimum pump.

The spatial model shows that optimisation of the spatial output may be achieved using a linear resonator configuration where the gain-modules are separated such that $L_3 > L_1 + L_2$ and $L_1 < L_2$ (Ref. figures 4.9 and 4.11). In this arrangement the dual-rod resonator will exhibit full output dynamic stability (in multi-mode waist size, far-field divergence and beam quality) and satisfy the cavity length requirements for keeping the pulse duration low and the $M^2 \sim 25$. A proposed configuration for dynamically stable operation at the optimum pump power of 1662 W (831 W per gain module) is illustrated in figure 5.12. For best Q-switched pulse consistency the optimum pump level is located just above the centre of zone II stability region. In this construction the AOM Q-switches may be positioned either between or outside of the gain-modules, whichever combination exhibits the best performance in terms of fastest switching speed and maximised oscillation hold-off.

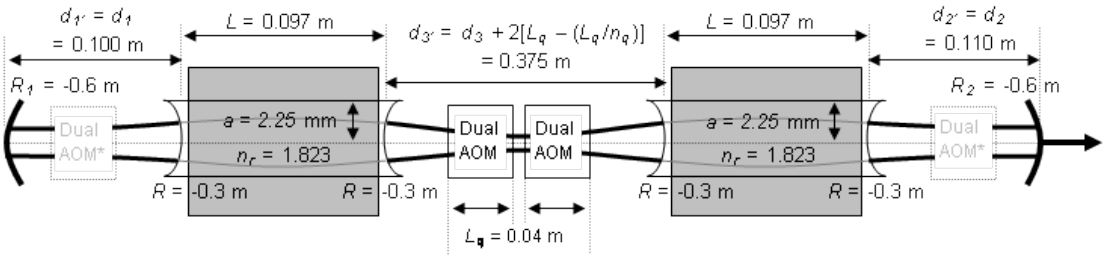

Figure 5.12 Schematic of a fully optimised dual-rod multi-spatial-mode resonator showing all cavity components and physical dimensions including alternative acousto-optic modulator positions*. Negative radius values denote concave curvatures. Not to scale.

However, during development of the dual-rod laser resonator it was decided to make a number of compromises for product engineering and cost control purposes, the concepts of which are discussed in section 3.3. In order to achieve the mechanical tolerances required for relative gain-module alignment and reduce the complexity (and cost) of the laser housing a final cavity configuration was chosen whereby the two gain-modules were positioned closer together such that $L_3 < L_1 + L_2$. In addition to this, less expensive plane cavity mirrors were implemented at the cost of a 35 % reduction in the theoretical misalignment angle required to produce a 10 % increase in cavity loss (Ref. section 4.1.3). This reduced tolerance to misalignment was still considered to be greater than the expected angular movement of the mirror during transport and operating lifetime of the laser system. Moreover, a plane output coupler fixes the resonator waist position and therefore the position of any waist generated by an external focusing system, which was considered advantageous for most of the intended applications.

In this case we can make $L_1 > L_2$ to create a region of full output dynamic stability in zone I and a broader region of partial output dynamic stability (for the beam waist or propagation factor) in zone II, as illustrated in figure 4.12. In an attempt to hold off oscillation, given an increased intra-cavity gain, the standard Q-switches were replaced by two 'dual-actuator' acousto-optic modulators. Both AOMs comprised a pair of orthogonally orientated, compression-induced, phase-gratings within a single fused-silica cell. The AOMs

were driven with 50W RF power (modulated at 27.1 MHz) per channel, aligned for the Bragg conditions and located for maximum hold-off within the cavity arms of physical length $d_{1'} = d_1 + L_q - (L_q/n_q)$ and $d_{2'} = d_2 + L_q - (L_q/n_q)$. Here d_1 and d_2 are the modelled arm lengths, L_q is the physical length of the Q-switch cell and n_q is the refractive index of fused-silica at 1.064 µm wavelength. For optimised operation in stability zone II at $M^2 \sim 25$ we find that $d_1 = 0.185$ m, $d_2 = 0.180$ m, $d_3 = 0.115$ m, $L_q = 0.04$ m, $n_q = 1.449$ and the rod facet curvature R = -0.4 m. A schematic of the resulting resonator design is shown in figure 5.13.

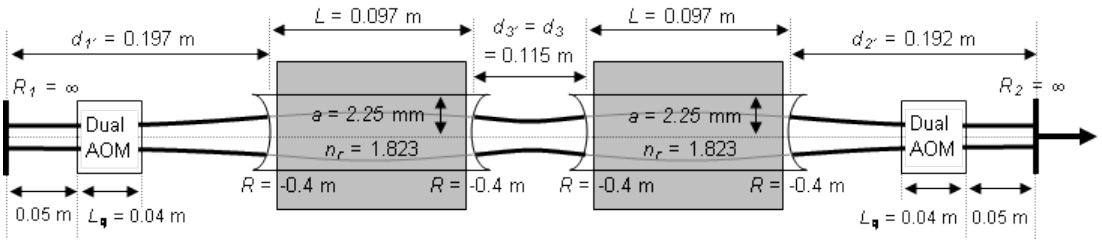

Figure 5.13 Schematic of the final product engineered dual-rod multi-spatial-mode resonator showing all cavity components and physical dimensions, including the experimentally determined optimum 'dual-actuator' acousto-optic modulator positions. Not to scale.

In this configuration it is possible that the positioning of the AOM Q-switch close to the resonator output may cause residual diffracted light to be seen in the periphery of the emitted beam. However, this is not of great concern here as this dual-resonator design is primarily intended for use with external power-amplifier modules (discussed in chapter 6) or fibre-delivery of the output beam, both of which can be used to aperture any unwanted non-axial light.

To assess the susceptibility of the dual-rod resonator design to laser induced optical damage we can calculate the average multi-mode beam radius for radial and tangential polarisations at the cavity mirrors for the optimum pump power of 1662 W such that $W_{m1} = 1.38$ mm and $W_{m2} = 1.33$ mm. Figure 5.14 shows the mathematically simulated peak operating fluence relative to the pulse duration and PRF scaled laser induced damage threshold F_{TSC} (as defined by equation (4.44) and given a manufacturer specified threshold fluence

F_T = 50 J.cm^{-2} at a single-shot test pulse duration t_T = 8 ns for both cavity mirrors). The results indicate that the dual-rod resonator should be able to comfortably function without damage at all operating pulse repetition frequencies due to the inherently larger beam sizes at the cavity mirrors when compared to the previously reported single-rod design.

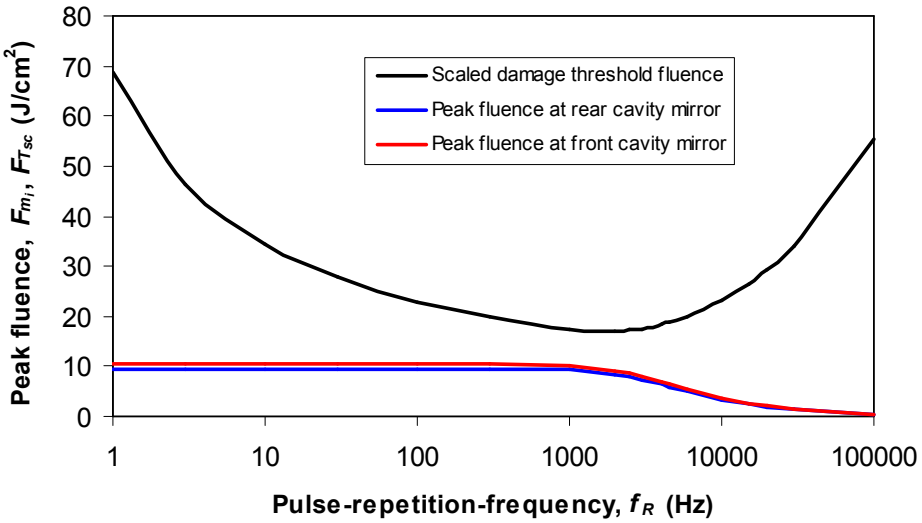

Figure 5.14 Peak operating fluence at each cavity mirror for the dual-rod resonator as function of PRF relative to the pulse duration and PRF scaled laser induced damage threshold F_{TSC} (given a manufacturer specified threshold fluence F_T = 50 J.cm^{-2} at t_T = 8 ns for both mirrors).

5.2.2 Spatial beam characterisation

We can now compare the simulated spatial output characteristics with the experimentally determined performance for the proposed dual-rod resonator design. For this cavity a 37 % output coupler reflectivity was used as the best available match for the theoretical optimum of 43.2 %. This time the spatial characteristics of the generated beam were measured using the primary output at the front of the resonator, which was heavily attenuated using polarisation-maintaining partial-reflectors. The rear cavity mirror was again given 99 % (± 0.2 %) reflectivity to provide a reproducible output of ~ 5 W for real time power monitoring of the laser product. The beam characteristics were

experimentally determined using the Spiricon (M^2-200) beam propagation analyser that was discussed in the previous section. Figure 5.15 shows the graphical representation of the caustic curves given by the user interface of the beam propagation analyser measured in the *x* (horizontal) and *y* (vertical) axes at optimum pump. Inset is a selected spatial profile that shows an image of the beam within the laser rod closest to the laser output.

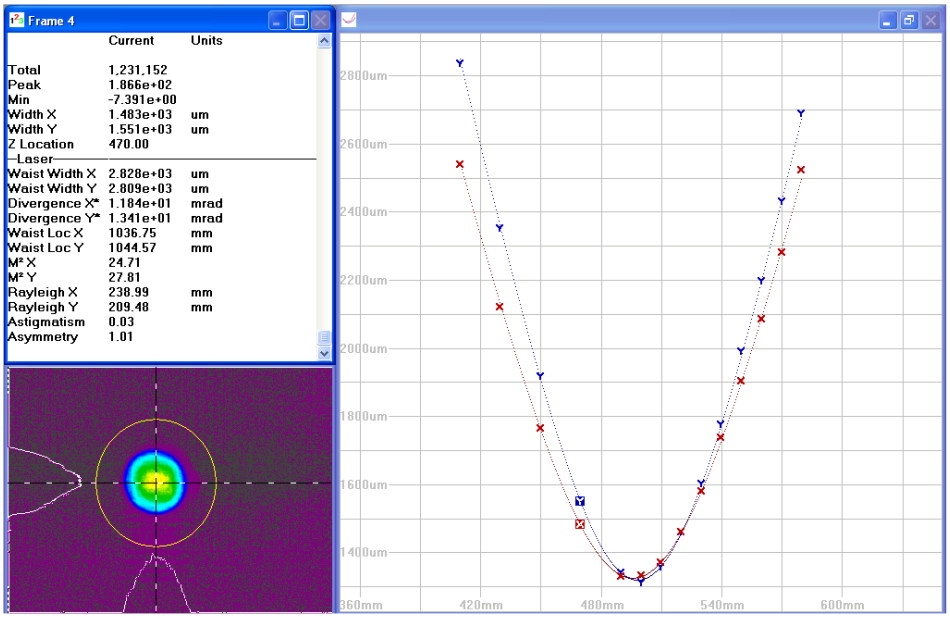

Figure 5.15 Spiricon M^2-200 user interface showing a graphical representation of the experimentally measured caustic curves, beam propagation data and a spatial profile taken at an image plane of the front laser rod for the constructed dual-rod resonator.

Note that very little 5-fold symmetry is exhibited in the beam profile at the front laser rod compared to the single-rod resonator case, regardless of the fact that the pump orientation is the same for front and back gain-modules. This may be caused by minor dissimilarities in the distribution of absorbed pump within the laser rods between gain-modules.

Figure 5.16 shows the expected beam propagation parameter (M^2) as a function of total pump power for the dual-rod resonator. This was generated by modelling the spatial-mode stability associated with the internal lensing

experienced by both radial and tangential polarisations under oscillating conditions (using a thermal lens constant C_t = 0.0084 D.W^{-1}). The corresponding experimental data for CW operation measured in the *x* and *y* axes of the beam profile are superimposed.

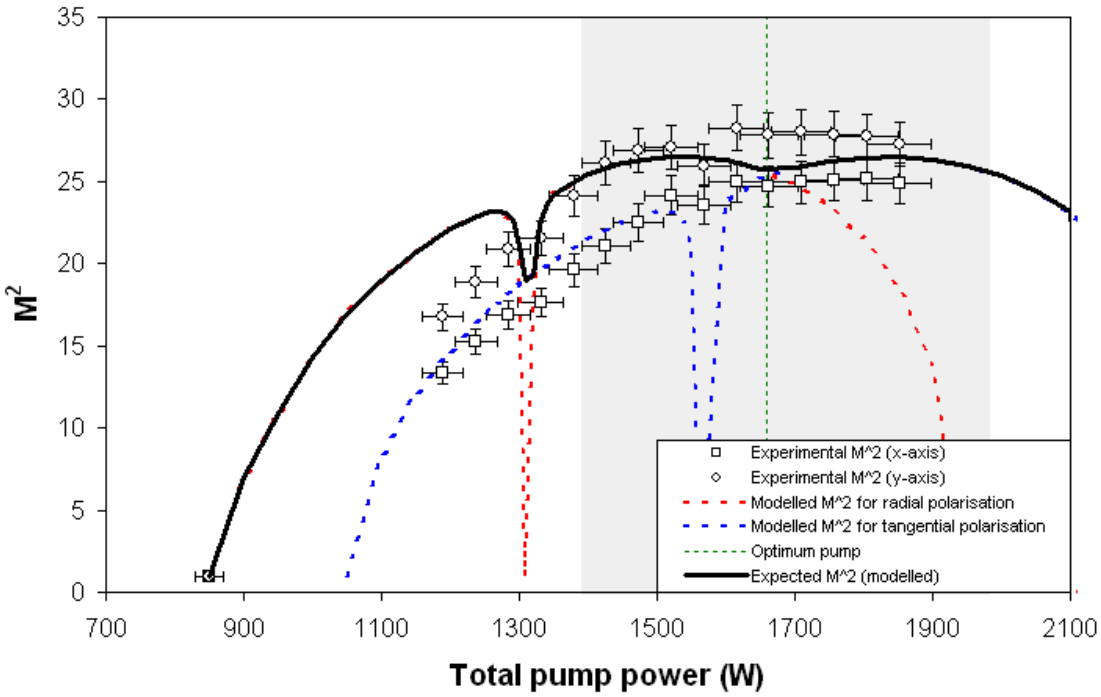

Figure 5.16 Mathematically simulated and experimentally measured beam propagation parameter as a function of pump power for the constructed dual-rod resonator. The region of partial output dynamic stability is shown by the grey shading.

On inspection it is found that, as expected, this particular cavity design locates the region of dynamic stability centrally on the optimum pump power. However, prior results with the single-rod resonator indicate that operating just above the centre of the spatial stability region can benefit Q-switched pulse stability, which is assessed in the following section. Variation in the measurements between the *x* and *y* axes outside of the normal fractional error may again be due to residual astigmatism in the thermal lens and the fact that the resonator may not be perfectly aligned as plane-parallel. Note that the experimentally determined M^2 is once more seen to deviate from the theoretical model at pump

powers approaching the oscillation threshold. As surmised in the single-rod case, this may be caused by the loss of higher order spatial modes due to the lack of gain available to them, rather than loss of stability. Interestingly however, in this case the model accurately predicts the threshold for oscillation at 850 W total pump. For the dual-rod resonator the oscillation threshold is cavity stability limited rather than inversion limited.

Figure 5.17 shows the CW output power as a function of total pump, measured above 1200 W. This data reveals a slope efficiency of 48.3 (± 1.0) % and an optical to optical efficiency of 30 (± 3) % at the optimum pump power, which is very similar to that measured with the single-rod configuration.

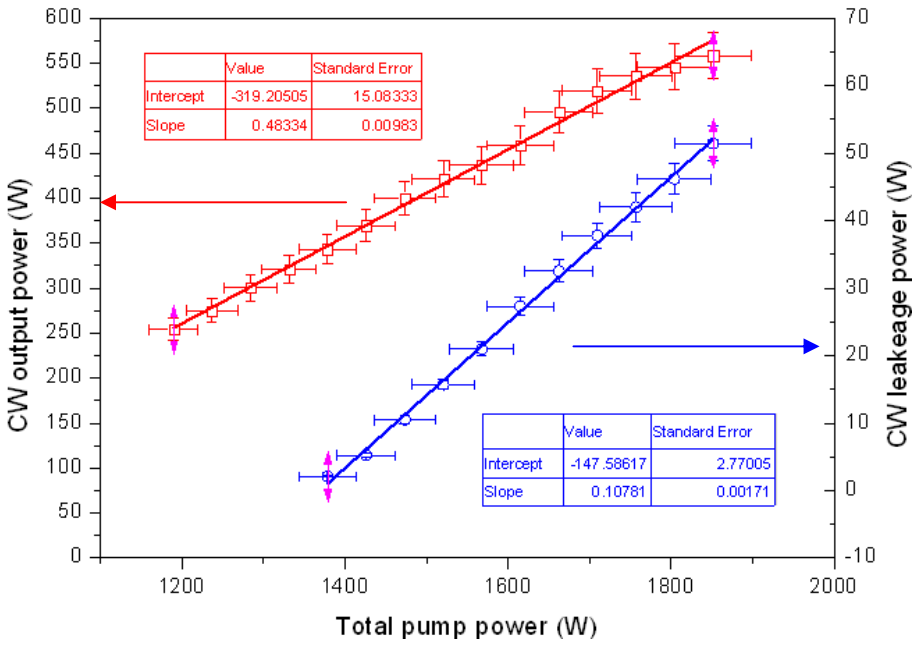

Figure 5.17 Experimentally measured CW output power and CW leakage as a function of total incident pump power for the constructed dual-rod resonator with near optimum output coupling.

Also illustrated on figure 5.17 is the CW leakage power that occurs at the resonator output when the AOM Q-switches are constantly engaged but are unable to hold-off oscillation. Note that CW leakage occurs above ~ 1350 W

total pump and that around 30 W of leakage is present at the optimum pump level.

Figure 5.18 shows the resulting multi-mode waist radius and far-field half-angle divergence as a function of total pump power for the dual-rod resonator, this time measured at the front (output) of the laser cavity.

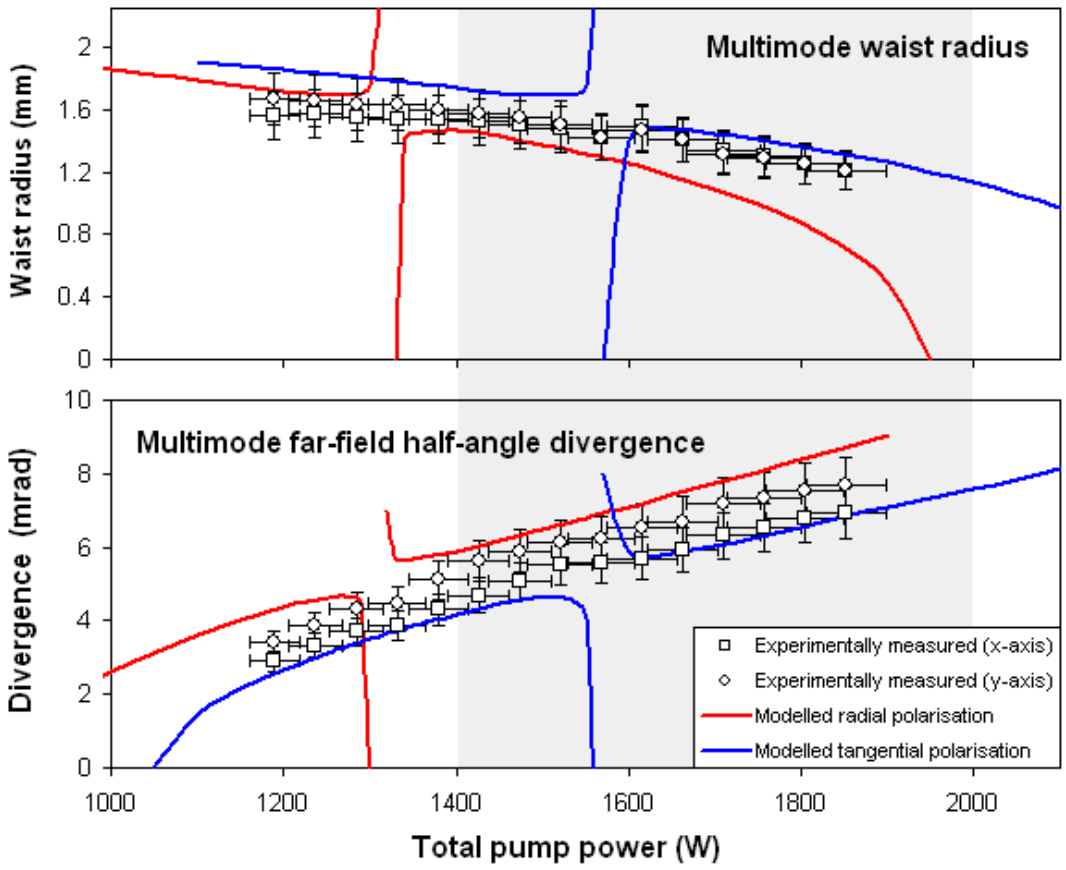

Figure 5.18 Mathematically simulated and experimentally measured multimode waist size and far-field half-angle divergence as a function of pump power at the front the dual-rod resonator. The region of partial output dynamic stability (in the beam propagation factor) is shown by the grey shading.

The modelled data again illustrates a general agreement with the trends exhibited by the experimentally determined results. However, as previously found for the single-rod resonator the inherent measurement error provides uncertainty as to whether the data follows the radial component, tangential

component or a weighted average of the two. Regardless of this, the theoretical model provides a good first order approximation of the spatial characteristics and enables an adequate assessment of resonator stability trends and intra-cavity fluence calculations.

5.2.3 Q-switched performance

The output from the constructed dual-rod resonator has been characterised with respect to its Q-switched performance over a working PRF range of 1 - 15 kHz. Figures 5.19 - 5.21 illustrate the measured pulse parameters as a function of PRF compared to mathematically simulated data produced using the Q-switched pulse model presented in section 4.2. In this case, pulsing consistency at the optimum total pump power of 1662 W was limited to lower PRF. The results were therefore taken at an increased pump power of 1800 W where the pulsing consistency is close to its maximum over the range of 6 - 15 kHz PRF.

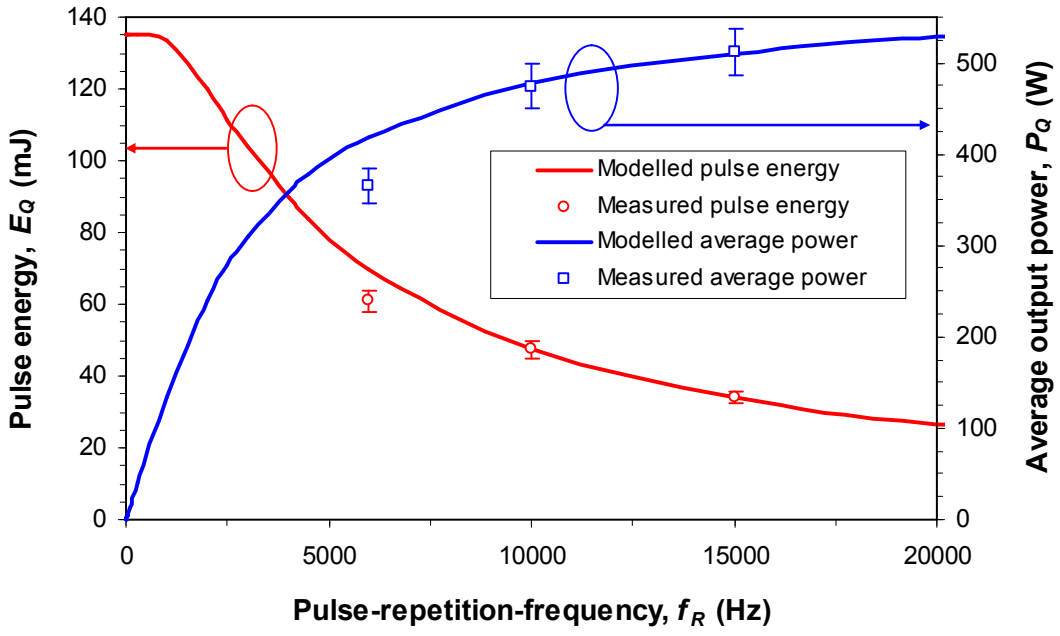

Figure 5.19 Mathematically simulated and experimentally determined average power and pulse energy as a function of pulse repetition frequency at 1800 W total pump power for the constructed multi-spatial-mode dual-rod resonator.

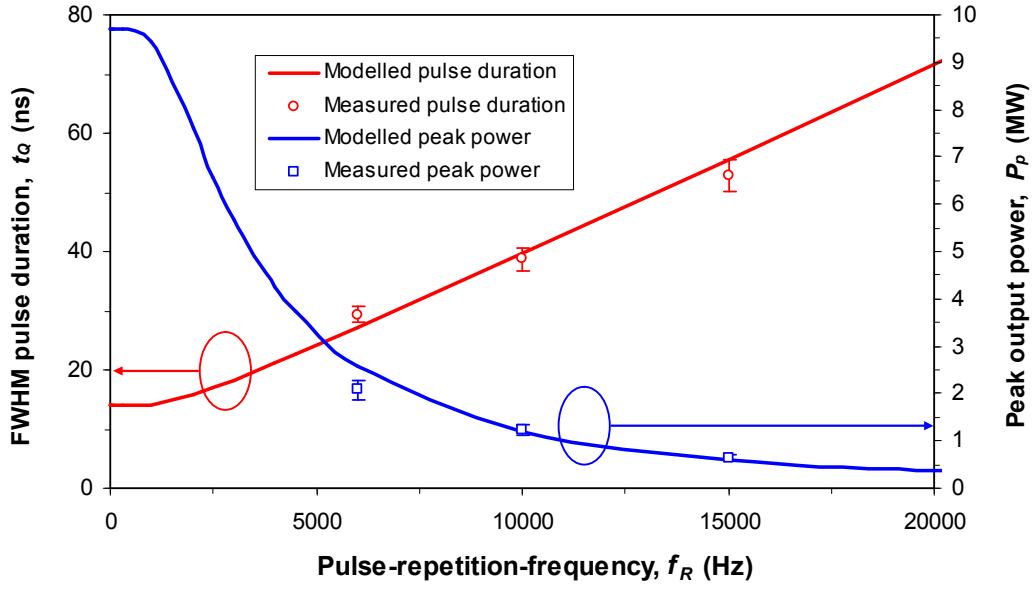

Figure 5.20 Mathematically simulated and experimentally determined full-width-half-maximum (FWHM) pulse duration and peak output power as a function of pulse repetition frequency (at 1800 W pump) for the multi-spatial-mode dual-rod resonator.

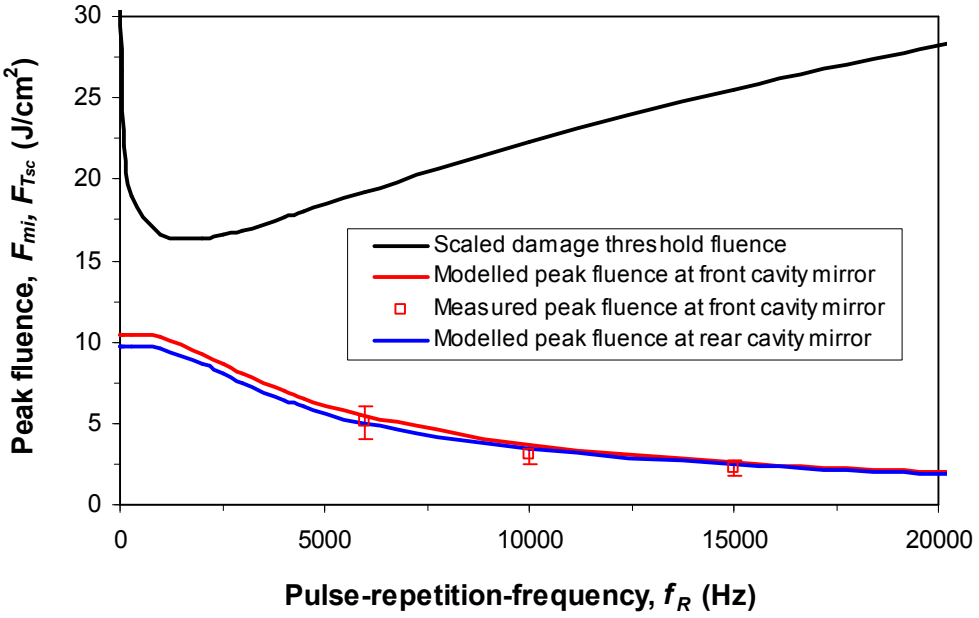

Figure 5.21 Peak operating fluence at each cavity mirror for the dual-rod resonator at 1800 W pump as function of PRF relative to the pulse duration and PRF scaled laser induced damage threshold F_{TSC} (given a manufacturer specified threshold fluence F_T = 50 J.cm^{-2} at t_T = 8 ns for both mirrors).

The effective optical path length for this resonator L_r has been calculated as follows

$$L_r = [d_{1'} + (L_q n_q - L_q)] + 2n_r L + d_3 + [d_{2'} + (L_q n_q - L_q)] = 0.894 \text{ m} \qquad (5.5)$$

where L and n_r are the physical length and first order refractive index of the laser rod at 1.064 μm wavelength.

The experimental results show a good degree of correspondence with the mathematical model at pulse repetition frequencies of around 10 kHz and above, despite a theoretically non-ideal output coupling. Below 10 kHz PRF the measured data is observed to deviate from the model. One contributing factor for this is a reduction in the expected gain or extraction efficiency due to the change in spatial mode structure as a result of the increased thermal lensing at lower PRF (as discussed in section 3.2.1 and illustrated in figure 3.11). In the dual-rod case however, there is a second contributing factor that will cause deviation from the model. This factor is the onset of CW leakage (or pre-lasing) between Q-switched pulses at lower PRF. Figure 5.22 presents an oscilloscope trace taken using a sufficiently fast photodiode showing the end of a gated set of 10 kHz pulses. Here, the vertical range was reduced to show only the bottom 5 % of the pulses and the background noise has been subtracted. The trace shows that at the optimum pump power a relaxation oscillation in output CW leakage will occur around 150 μs after the last 10 kHz pulse. As the PRF is decreased this duration is marginally increased (due to a more depleted inversion) but will inevitably approach the period between Q-switched pulses, at which point the pulsing becomes highly inconsistent. Consequently, at low PRF a reduction in the operating pump power is required to regain Q-switched pulse stability. This constitutes a deviation away from the optimum pump level for laser diode output and spatial dynamic stability. It is therefore necessary to assess the need for optimised function at low PRF relative to the increased cost and complexity associated with the elimination of the CW leakage oscillation (pre-lasing). This may, for example, involve the addition of more AOM

Q-switches if the exhibited loss of performance from the expected optimum state is not acceptable. The operating repetition frequencies for the target applications associated with this work are however expected to be greater than 6 kHz (Ref. chapter 1).

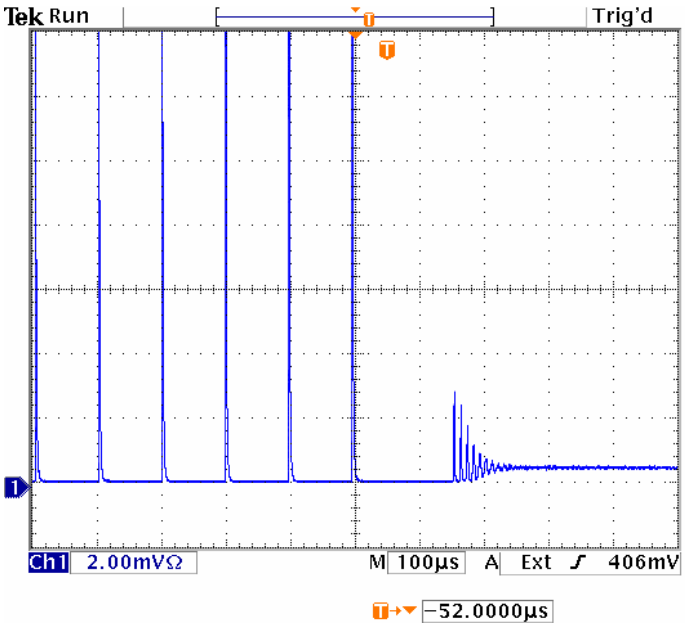

Figure 5.22 An oscilloscope trace showing the end of a gated set of 10 kHz pulses. The vertical range is reduced to show only the base 5 % of the pulses and the background noise has been subtracted.

5.2.4 Pulsing consistency and gated operation

As an important parameter for a number of the intended industrial applications the Q-switched pulsing consistency was further investigated and characterised for both free-running and gated operation. Here we are looking to assess the variation in peak power between consecutive pulses and gated bursts of pulses. Observations of the optical pulses reveal that although the timing jitter can be in the order of 10 % of the FWHM pulse duration at 10 kHz PRF, this is only around 3 % of the total build-up time (which is $\sim 1.4 \times 10^{-7}$ s for the effective cavity length and expected round-trip losses of the dual-rod resonator). It was

noted that the fractional variation in pulse duration was small compared to the pulse amplitude. Thus, the observed inconsistency in peak power was predominantly due to fluctuations in the pulse energy.

Figure 5.23 illustrates a typical temporal waveform trace of a single pulse taken at 10 kHz PRF in continuously Q-switched (free-running) operation for the dual-rod resonator. At 1 GHz sample rate the trace shows that there is some temporal ripple present on the pulse but that this is no larger than the background noise.

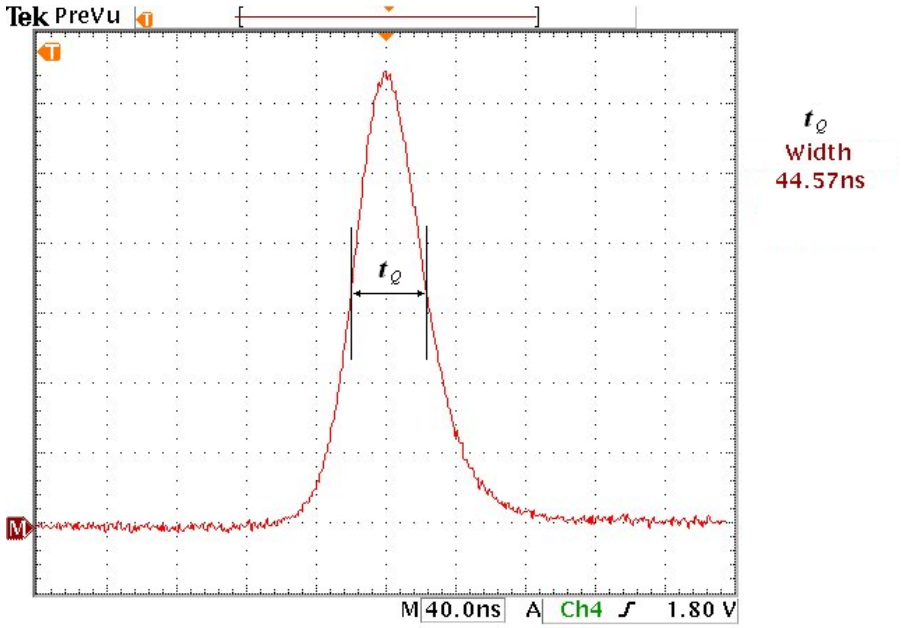

Figure 5.23 An oscilloscope trace showing a single pulse taken at 10 kHz PRF in continuously Q-switched (free-running) operation for the dual-rod resonator.

The pulse energy fluctuation can be calculated by assessing the statistical distribution of the integrated areas beneath a sufficiently large population sample of pulse waveforms. This is a computationally intensive process but has been applied to selected random pulses taken at large intervals for long-term reliability testing. However, for quantifying the repeatability between consecutive pulses an approximation can be made that defines the level of inconsistency Q_o as the noise subtracted peak-to-peak variation in pulse height expressed as a fraction of the average pulse height, such that

$$Q_o = \frac{J_h - Q_n}{Q_h} \tag{5.6}$$

where J_h is the peak-to-peak variation in pulse height, Q_n is the peak-to-peak noise measured before significant pulse build-up and Q_h is the mean pulse height over the tested sample. An illustration of this is given in figure 5.24 for 10,000 pulses taken in free-running operation at 10 kHz PRF. This approximation for the pulse energy fluctuation includes the assumption that any changes in the pulse shape or duration t_Q are small compared to the variation in pulse height.

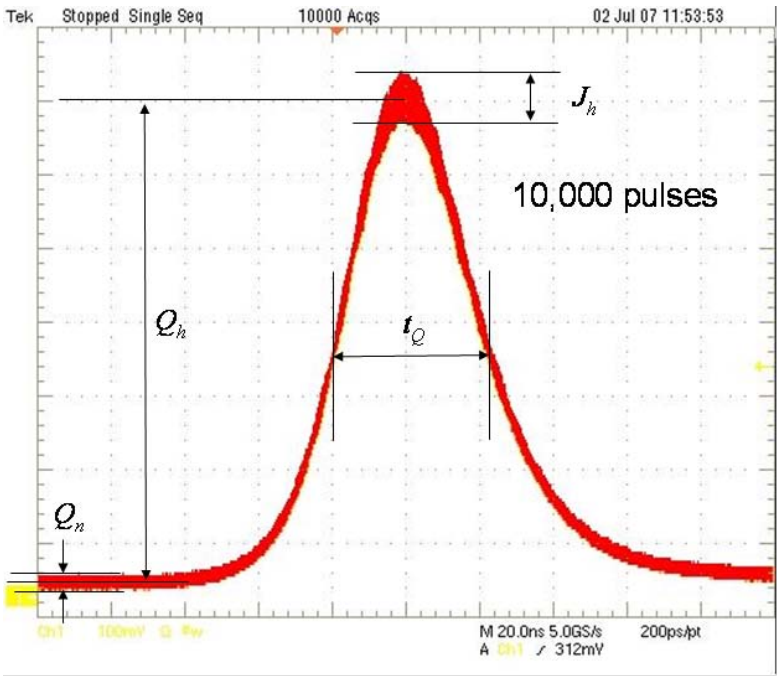

Figure 5.24 An oscilloscope trace showing the captured envelope of 10,000 consecutive pulses at 10 kHz PRF in continuously Q-switched operation (triggered by the optical pulse).

A temporary concession was made for the dual-rod resonator with respect to the pump diode lifetime to allow higher operating powers and investigation up to a maximum pump P_{max} = 925 W per gain-module (1850 W total pump power). Figure 5.25 illustrates the pump-power related conditions that influence Q-switched pulse consistency as a function of PRF for the dual-rod resonator. In

contrast to the single-rod cavity the dual-rod configuration shows a resonator-stability-related threshold for oscillation, at around 850 W pump. As expected, both the upper and lower spatial mode related pulse instability conditions P_{m1} and P_{m2} restrict operation at higher PRF. In this case the resonator was able to generate consistent Q-switched pulses over a pump range of only 30 W at 15 kHz. Also as predicted, the onset of CW oscillation between pulses led to pulse inconsistency at low PRF. This is shown in figure 5.25 by the hold-off limited condition P_H. Figure 5.26 illustrates how the pulsing inconsistency is reduced with increase in spatial mode content and available gain (as discussed in section 3.2.1). In this case the pulse consistency has been compared with the mathematically simulated CW beam propagation parameter, to which the modal characteristics at ~ 6 kHz PRF and greater will tend toward.

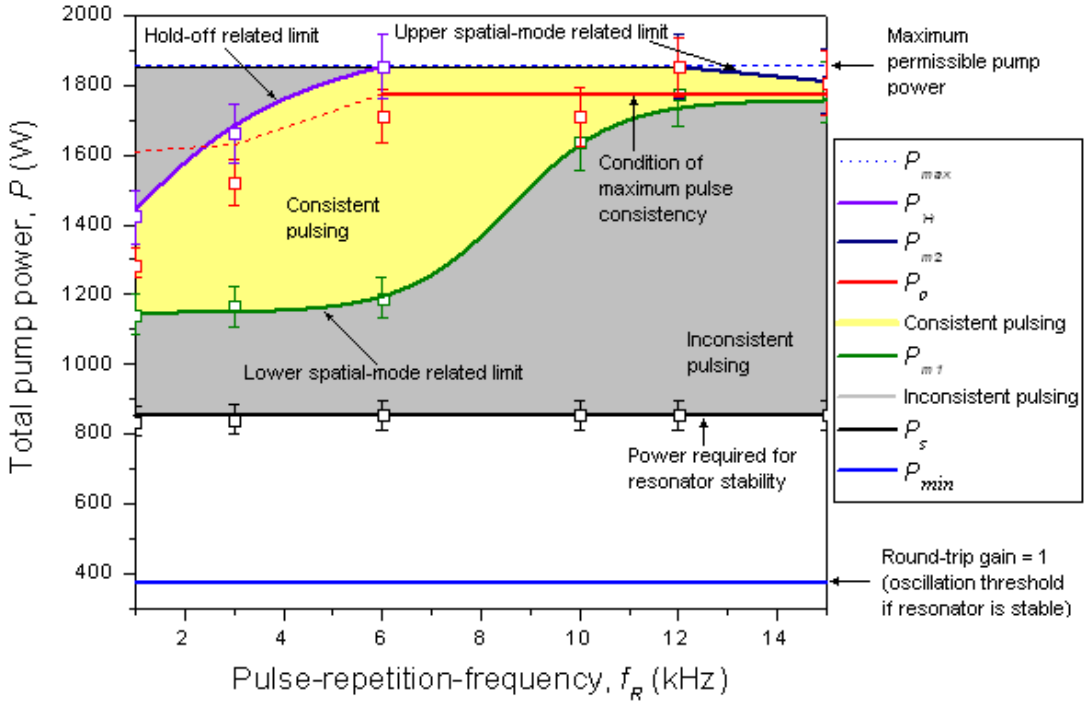

Figure 5.25 Experimentally investigated pump-power related conditions that influence Q-switched pulsing consistency as a function of PRF for the constructed dual-rod multi-spatial-mode resonator.

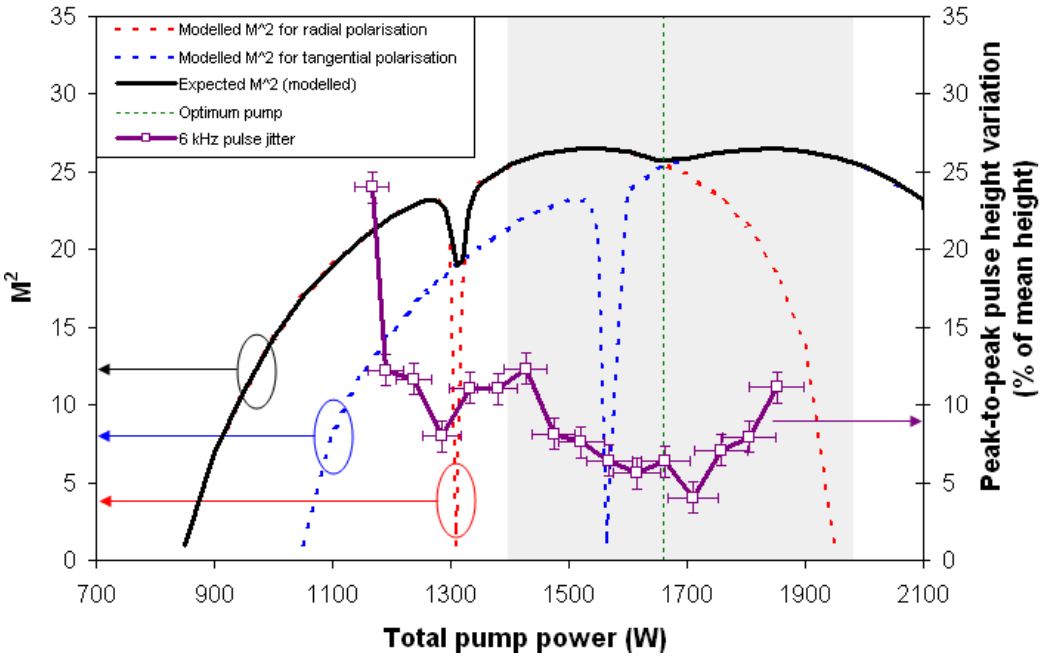

Figure 5.26 Experimentally measured Q-switched pulse inconsistency at 6 kHz PRF in relation to the mathematically simulated CW beam propagation parameter (M^2) as a function of pump power for the dual-rod resonator. The region of partial output dynamic stability in the spatial beam characteristics is shown by the grey shading.

Figure 5.27 illustrates the implementation of first pulse control and diode modulation for full gated pulse optimisation and inconsistency reduction, as discussed in section 3.2.2. Here, the pulsing gate (green trace) is used to initiate both the pre-pulse kill (PPK) control of the first pulse in a gated train and diode modulation for transient thermal lens management. The electrical trigger signal used to prompt a Q-switch is shown (magenta trace) along with the laser-diode drive-current modulation signal that has been remotely measured using a Hall effect sensor located near to the driver cable (blue trace). The resulting optical pulse train, detected using a fast photodiode, is shown for a thermally long gated cycle of 1 s on and 2 s off (brown trace).

The results show that without diode modulation the transient thermal lensing can cause anomalous pulsing over a period of ~ 0.3 seconds at the start of the gated pulse train. Figure 5.27 (a) shows the gated pulse train without diode modulation or fully optimised PPK delay that is required to control the first

pulse. In this case a random PPK delay is shown, which produces a slightly higher first pulse. Note that with no PPK delay the first pulse may be significantly larger than a typical 10 kHz pulse. In theory it is possible for the first pulse to have over 2.5 times the energy of an average 10 kHz pulse as it tends toward the single-shot condition. In practice however the maximum increase in pulse energy is nearer ~ 50 % due to the previously discussed mechanisms that result in deviation from the theoretical models (Ref. section 5.2.3). Figure 5.27 (b) illustrates a similar gated pulse train with a PPK delay optimised for 10 kHz PRF at 273 μs (with a linear RF power slope to zero over the initial 200 μs of this delay, Ref. figure 3.12). To maintain the thermal lens power between pulsing (oscillating) and non-pulsing (non-oscillating) conditions the diode output required a modulation of 164 W at the optimum pump. This constitutes a 9.9 % variation in heat loading, which agrees with the values reported by Brown [5.1] and validates the assumption of 10 % initially used in the thermal lens power calculations and resonator stability models presented in chapters 2 and 4 respectively. Using both first pulse control and diode modulation the peak-to-peak pulse height variation level Q_o for the dual-resonator, as defined by equation (5.6), is typically less than 5 % when operating at 6 kHz. This increases to around 10 % at the maximum operating PRF of 15 kHz and ~ 15 % at the minimum operating PRF of 1 kHz (due to the requirement for a reduced operating pump power of 1285 W to maintain hold-off).

Note that it is also possible to implement a third level of diode modulation that can be used as a 'standby' level to eliminate unwanted CW leakage between gated bursts of pulses at high PRF. Figure 5.17 suggests that CW leakage could be removed by modulating down to an inter-gate standby level of ~ 1350 W pump. The CW leakage will inevitably return a fraction of a second before pulsing when the operating thermal lens power is reinstated.

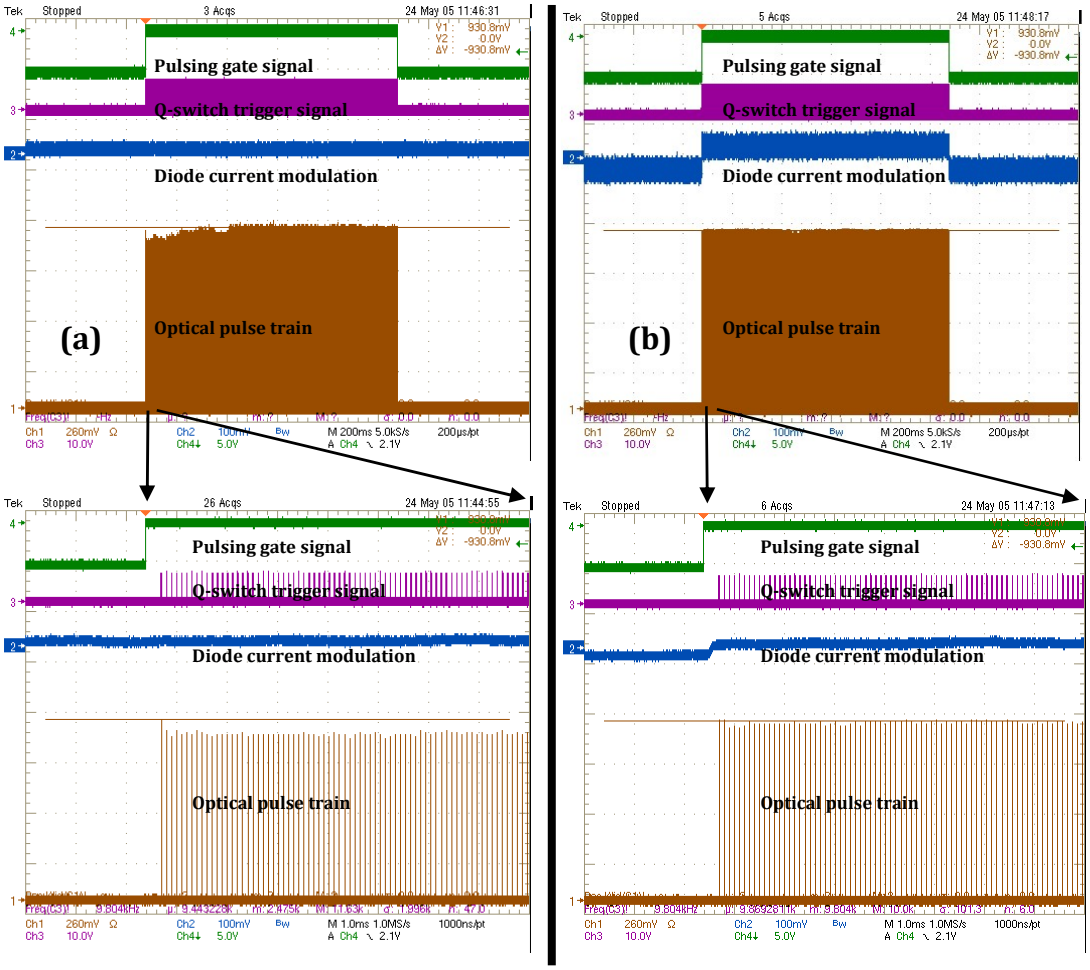

Figure 5.27 Oscilloscope traces that show a 1second-on, 2 second-off gated pulse train with (a) no optimised first pulse control or diode modulation and (b) optimised PPK delay and diode modulation depth.

5.3 Summary

In chapters 3 – 5 we have presented a range of development techniques that can be used for the cost-effective production of industrially robust, high-power, multi-spatial-mode laser oscillators. Based on a number of important laser design principles we have formulated a set of mathematical models that allow simulation of the spatial and temporal characteristics of thermally active resonators.

The first of the mathematical models facilitates investigation of the spatial mode content and resonator stability. This enables the theoretical quantification of the beam propagation parameter (beam quality), beam size and far-field divergence for a given cavity design. The model applies for any laser resonator configuration that has flat or curved reflectors and multi-element internal lensing with a cylidrical limiting aperture. Using the design principles outlined in chapter 3 we have derived conditions for full and partial dynamic stability in the output characteristics of a multi-spatial-mode solid-state laser resonator, such that they are resistent to change in the inevitable thermal lensing that occurs within the pumped gain medium. The resonator stability model presented will enable a laser designer to tailor the output characteristics of a multi-spatial-mode resonator through the manipulation of controlable dimensions, while maintaining dynamic stability. These controlable dimensions include resonator length, cavity mirror curvatures, number of laser rods, rod positions, rod length, rod facet curvature and pump parameters. In an advanced step we have related the spatial mode content and gain trends to Q-switched pulsing consistency, allowing further theoretical optimisation of the resonator. The spatial model has also been extended to include the consideration of relative and quantitative misalignment sensitivity of the simulated resonator configurations.

The second model, presented in chapter 4, was developed to aid the optimisation of CW pumped active Q-switching for a given resonator design. This model assumes operation in the fast Q-switching regime and enables calculation of the inversion levels and corresponding energy-extraction-efficiency optimised output coupling. These values are in turn used to project the PRF dependent average output power, pulse energy, FWHM pulse duration and peak power for the laser oscillator. Deviations from the model are seen to occur under conditions of changing beam-to-gain overlap and with the onset of CW leakage (pre-lasing) between Q-switched pulses.

It was also shown that the spatial and temporal models can be combined to assess the susceptibility of a laser resonator to self-induced optical damage. This was achived by relating the theoretical peak intra-cavity fluences or irradiances with the manufacturer specified damage threshold, which can be scaled to be representative at the intended operating PRF and projected PRF-dependent pulse duration.

Chapter 5 details the experimental investigation of various acousto-optically Q-switched resonators based on the gain-modules developed in chapter 2. In the first instance a single-rod resonator was designed and constructed to illustrate the design principles and validate the mathematical models. At an optimum pump power of 831 W this resonator generated a 25 times diffraction limited beam at the fundamental wavelength with a CW optical to optical efficiency of 29 (± 3) %. The resonator exhibited consistent Q-switching in the PRF range of 3 - 20 kHz with corresponding average powers of 130 - 235 W, pulse energies of 12 - 43 mJ and pulse durations of 30 - 100 ns. Damage analysis suggests that operation above 5 kHz should be maintained to ensure long term reliability.

The second resonator presented comprised a dual-rod configuration for increased power output. In this case the concepts of design compromise for product development and cost control were implemented. Again using the gain-module design developed in chapter 2 the dual-rod resonator produced a similar $M^2 \sim 25$ with a similar optical to optical efficiency of 30 (± 3) % at an optimum total pump of ~ 1660 W. The dual-rod resonator demonstrated consistent Q-switching over the PRF range 1 - 15 kHz with corresponding average powers of 56 - 510 W, pulse energies of 34 - 61 mJ and pulse durations of 22 - 53 ns. Although, in this case the pump power was increased above the optimum reliable pump for operation at 6 kHz or greater and reduced below 6 kHz in order to maintain maximum Q-switched pulsing consistency. The pulse energy consistency was confirmed to be related to the spatial mode content of the resonator and measured as < 5 % peak-to-peak at 6 kHz PRF. In addition to this, methods of first pulse control and transient thermal lens management by

diode modulation were proven to enable the presevation of optimised Q-switching consitency for gated pulse operation of the laser resonators. The resulting pump modulation depth of 9.9 % required for optimised transient lens management substantiates the thermal load defect between oscillating and non-oscillating conditions that was suggested in chapter 2.

The experimental results presented in chapter 5 illustrate that the models can be successfully used to optimise a multi-mode laser resonator to produce dynamic stability in the desired spatial charactesistics, while maximising Q-switched pulsing consistency. Resistance to perturbations in thermal lensing and cavity misalignment by design will also decrease the resonator's response to long-term pump degredation, gain-module performance variation and promote laser to laser reproducibility.

6 Power scaling at the fundamental wavelength

The laser resonators presented in chapter 5 illustrate how the previously formulated design principles and mathematical models can be used to optimise multi-spatial mode Q-switched operation. This optimisation has enabled production of the spatial and temporal output characteristics required by the infrared applications outlined in chapter 1. However, the resonators presented thus far fall short of providing sufficient pulse energies and average powers for these applications. For total satisfaction of the process requirements we must address the methods by which pulse energy and average power can be scaled at the fundamental wavelength, while keeping the beam quality, pulse duration and PRF to within the acceptable ranges. We have considered two approaches to this, the first of which involves straight forward power amplification of the dual-rod oscillator presented in chapter 5. The second approach requires a step back to chapter 2 and the redesign of power scaled laser gain-modules for use in both higher energy oscillators and power amplifier stages.

6.1 Master-oscillator power-amplifier systems

From a resonator stability stand point there is no limit to the number of thermally active gain-modules that can be added to an oscillator. For oscillators

with sufficient spacing between the gain-modules (where $L_3 > L_1 + L_2$), operation with additional modules is only limited by the increased intra-cavity fluence or irradiance, which can lead to optical damage at the interfaces of resonator components. Such resonators would also need to be a number of meters in length. This has practical implications with respect to system size and would inevitably lead to difficulties in the relative alignment of the gain-modules.

Alternatively, for oscillators with closely spaced gain-modules (where $L_3 < L_1 + L_2$), operation with additional modules (and therefore the output power scalability) is not only limited by the fluence related optical damage but also by the increase in rod facet or cavity mirror curvatures required to maintain resonator stability. In reality, for the plane-plane resonators presented in chapter 5, the restrictions associated with rod curvature fabrication (at the time of this investigation) limits the number of similar gain-modules to a maximum of 2 when operating in the second stability zone (Ref. section 4.1.2). It should however be noted that with alternative rod facet and cavity mirror curvatures it may be possible to obtain output dynamic stability with operation in the extra stability zones that would appear with the addition of oscillator gain-modules. Detailed investigation of this is beyond the scope of this work but would be facilitated by simple extension of the mathematical model presented in section 4.1.2 on multi-rod resonator stability optimisation.

To further scale the output power, additional gain-modules may be introduced in the form of extra-cavity amplifiers. The fundamental principles of laser pulse amplification are well documented [6.1; 6.2; 6.3; 6.4; 6.5]. In a Q-switched regime where the pulse duration is short compared to the fluorescent lifetime, the level of amplification is seen to be dependent on the energy density (or fluence) rather than the peak power density. For efficient extraction of the energy stored in an amplifier stage the input fluence should be greater than that associated with saturation [6.6]. For a 4-level system such as that exhibited by Nd:YAG the saturation fluence can be simply calculated using the expression

$$F_{sat} = \frac{hc}{\lambda\sigma} = \frac{E_{st}}{g_0} \tag{6.1}$$

where λ is the signal wavelength, σ is the stimulated emission cross section and E_{st} is the energy stored in the upper level of the transition per unit volume. For the gain-module developed in chapter 2, the saturation fluence is calculated to be 6.7 x 10^3 J.m^{-2}. This implies that input pulse energies of at least 43 mJ should be generated by the master-oscillator for efficient energy extraction from this gain-module, when used as a first-stage amplifier. Here, we have assumed that the spatial mode coupling into the amplifier is such that the beam radius to $1/e^2$ irradiance is at a maximum permissible value in relation to the amplifier rod diameter, constrained by the condition defined in equation (3.36). This condition ensures that the diffraction losses of a gaussian-like beam on transmission through the hard aperture are kept to a negligible level. It follows that at 10 kHz pulse repetition frequency the calculated saturation level leads to an average input power requirement of at least 430 W. The experimental results taken for the dual-rod resonator reported in section 5.2.3 show that, with optimum spatial coupling, the saturation fluence can be exceeded when operating across the stable PRF range of 6 – 15 kHz.

We can define the efficiency of extraction at the amplifier η_{Eamp} as the ratio of extracted energy to the energy stored per unit volume, such that

$$\eta_{E_{amp}} = \frac{F_{out} - F_{in}}{E_{st} L_p} = \frac{F_{out} - F_{in}}{g_0 L_p F_{sat}} \tag{6.2}$$

where L_p is the pumped length of the Nd:YAG rod in the amplifier. $g_0 L_p$ is the logarithmic single-pass small-signal gain, which has been assessed for this gain-module to be 0.98 at an optimum pump power of 830 W (Ref. section 5.1.1). F_{in} and F_{out} represent the average input and output fluence of the propagating pulse respectively. The corresponding power gain associated with this gain-module G can be expressed as

$$G = \left(\frac{F_{sat}}{F_{in}} \right) \ln\left(1 + \left[\exp\left(\frac{F_{in}}{F_{sat}} \right) - 1 \right] \exp\left(g_0 L_p \right) \right) \tag{6.3}$$

We can refine this formula to obtain a more realistic representation of the gain by including a number of known efficiency values. In this case the previously calculated small-signal gain coefficient g_0 already incorporates the upper state and pump coupling efficiencies η_u and η_c respectively. For comprehensive analysis we must also include the efficiency that accounts for the fractional loss of upper-state population due to amplified spontaneous emission (ASE) η_{ASE}, the Q-switched pulse-energy extraction efficiency η_E, a PRF dependent power extraction efficiency $\eta_{Q'} = (1 - \eta_Q)$ and a beam to gain-distribution overlap efficiency in the amplifier $\eta_{B'}$ (Ref. section 4.2). Equation (6.3) can therefore be recast as

$$G = \left(\frac{\eta F_{sat}}{F_{in}} \right) \ln\left(1 + \left[\exp\left(\frac{F_{in}}{\eta F_{sat}} \right) - 1 \right] \exp\left(g_0 L_p \right) \right) \tag{6.4}$$

where $\eta = \eta_{ASE}.\eta_E.\eta_{Q'}.\eta_{B'}$. This analysis assumes a rectangular pulse shape but holds, to a good approximation, for triangular-shaped pulses also [6.6]. Using equation (6.4) we can determine the gain produced by a power amplifier when applied to the dual-rod master-oscillator presented in section 5.2. For example, at 10 kHz PRF the efficiency values have been previously calculated or estimated such that $\eta_{ASE} = 0.91$, $\eta_E = 0.93$ and $\eta_Q = 0.81$. Here it has been assumed that the input beam fills the amplifier rod such that $\eta_{B'}$ is close to unity. Substituting these values into equation (6.4) gives an expected power gain of 1.37 for a single-stage amplifier (using an identical gain-module to those inside the resonator). For an oscillator output power of 430 W this level of gain would lead to an initial amplified power of 590 W, at 10 kHz PRF. Adding another identical gain-module as a second-stage amplifier will provide a further gain of 1.28, giving a total power gain of 1.75 for the 2-stage amplifier chain and a total output power of 753 W at 10 kHz PRF.

Amplification of a master-oscillator output can lead to a number of distortions. In general, the leading edge of an amplified pulse sees larger gain than the trailing edge, effectively resulting in a forward shift of the peak and a shortening of the pulse duration. The presence of gain saturation can influence this temporal distortion by further affecting how the amplification varies as the pulse evolves. In addition to temporal distortion of the signal, gain saturation can also cause a spatial distortion whereby the less intense outer sections of the beam are amplified to a greater extent than the central regions, thus effectively broadening the beam diameter. Other spatial distortions in the amplified signal can result from non-uniform pumping, in-homogeneities in the active medium, diffraction effects and thermal lens aberrations. All of these spatial distortion effects can have implications on the output beam quality. However, most of them can be minimised or eliminated through careful gain-module design and effective beam coupling within the amplifier chain.

Other considerations associated with the design of a power amplifier include the mitigation or accommodation of ASE, pre-lasing and parasitic oscillation. Again, these effects have been largely eliminated through considered gain-module design (Ref. chapter 2). At low signal levels the power gain tends toward the small-signal single-pass gain G_0, which was calculated for our gain-module to be 2.68 (Ref. equation 4.22 and section 5.1.1). This value suggests that low level back reflections are unlikely to be problematic and the need for optical isolation is not required.

6.2 Power-scaled laser gain-module development

To scale the average output power beyond 1 kW it is possible in principle to simply add further amplifiers stages in an extension of the master-oscillator power-amplifier (MOPA) configuration described in the previous section. In practice however, there are several reasons why this is not a desirable approach

for industrial laser design. System size and complexity are increased, component tolerances are tightened and robustness is reduced. A particularly important limitation is optical damage. At the exit to the second amplifier stage of the MOPA system described in section 6.1 the peak irradiance on the rod facet is similar to that inside the resonator. This means that the addition of more amplifiers with the same design will increase the peak irradiance to potentially destructive levels. At this point the amplifier chain begins to limit rather than increase the peak power of the system. To achieve our design goals of scaling to high average power with high peak power an alternative approach is required.

Using the same general design principles presented in chapter 2 a new, physically larger, higher-power gain-module has been developed. It was decided that this new gain-module should exhibit similar thermal lens powers at optimum pump as the original gain-module. This would allow the new unit to be used in place of the original without significant change in resonator stability or amplifier configuration. To enable further amplification at the maximum permissible irradiances the cross sectional area of the rod was doubled by increasing the diameter by a factor of $\sqrt{2}$ to 6.36 mm. The total pump was also doubled to maintain the thermal lens power and provide the additional gain. However, as there were no higher power diode bars available and there was little space to add more laser diode assemblies, the extra pump power was achieved by an increase in the number of diode bars per assembly. The new assemblies therefore each comprised an 8 bar linear array, instead of 4, and were positioned with the same 5-fold symmetry as those in the original gain-module. An increased rod length of 147 mm was used to take advantage of the doubled pumped length and maintain a similar un-pumped region at each rod end for mechanical location and cooling water seals. In an effort to increase the pump coupling efficiency the doping density was marginally increased to 0.8% at. Nd. Regardless of this, the distribution of the additional pump over a longer pump length maintains a safety factor of ~ 3 below the limit for thermal fracture. A 3-dimensional CAD model of the new power scaled gain-module

configuration is shown in figure 6.1, without the mechanical housing and cooling water manifolds.

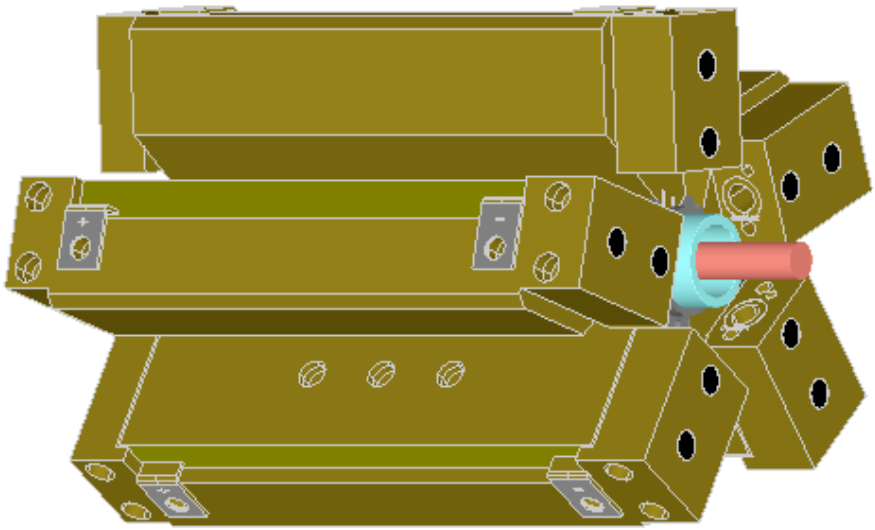

Figure 6.1 3-dimensional CAD model of the power scaled gain-module showing a pump chamber and directly coupled 8-bar diode assemblies in 5-fold symmetry (illustrated without the mechanical housing and cooling water manifolds).

6.3 Experimental results

The following sections detail the experimental results taken when characterising a number of master-oscillator power-amplifier systems. Initially, power amplification of a dual-rod oscillator was investigated using 1 and 2 amplifiers based on the original gain-module design presented in chapter 2. This is followed by the characterisation of a higher power MOPA system constructed using various power scaled gain-modules in the oscillator and a 3-stage amplifier chain.

6.3.1 MOPA system with 1 and 2-stage amplification

A master-oscillator power-amplifier (MOPA) system has been constructed by implementing 1 and then 2 additional gain-modules as power amplifier stages

for the dual-rod resonator design described in section 5.2. To achieve optimum beam coupling the amplifier gain-modules were given the same rod facet radius of curvature as those inside the resonator and placed at the same effective optical distance from the output coupler as the internal gain-modules d_2 = 0.180 m. To maintain cavity stability with addition of the AOM a physical cavity arm length $d_{2'}$ = 0.192 m is required (Ref. sections 5.1.1 and 5.2.1). The idea here is to create a closely spaced amplifier pair located in a position that reflects that of the gain-modules inside the master oscillator. This geometry effectively optimises the laser-mode to gain-distribution overlap in the amplifiers and prevents excess clipping of the beam by the hard aperture of the rod. That is, an optimum trade-off is made between increasing energy extraction and reducing diffraction loss. Moreover, in this configuration, the beam divergence generated by the oscillator can be closely replicated at the MOPA output when both amplifiers are installed.

There were however, a number of practical issues associated with the design of this MOPA system when considering that it must lend itself to volume production and industrial use where a high level of serviceability s required. It was found that when the gain-modules were aligned in a simple linear configuration the system had two major drawbacks. The first is that the overall size of the laser head was regarded as too large by many of the intended customers. Secondly, the mechanical tolerances required to achieve sufficiently accurate location of the oscillator and amplifier gain-modules were difficult to realise and significantly increased the cost of the laser enclosure. In a product engineering step, the MOPA system was folded such that the amplifier stages sat along side the oscillator with two plane turning mirrors installed for beam coupling and alignment. In the final design the distances from the internal and external gain-module pairs to the output coupler $d_{2'}$ and $d_{4'}$ were not exactly equal due to mechanical constraints associated with the location of the turning mirrors and power amplifiers, in this case $d_{4'}$ = 0.220 m. A schematic of the final MOPA configuration is shown in figure 6.2.

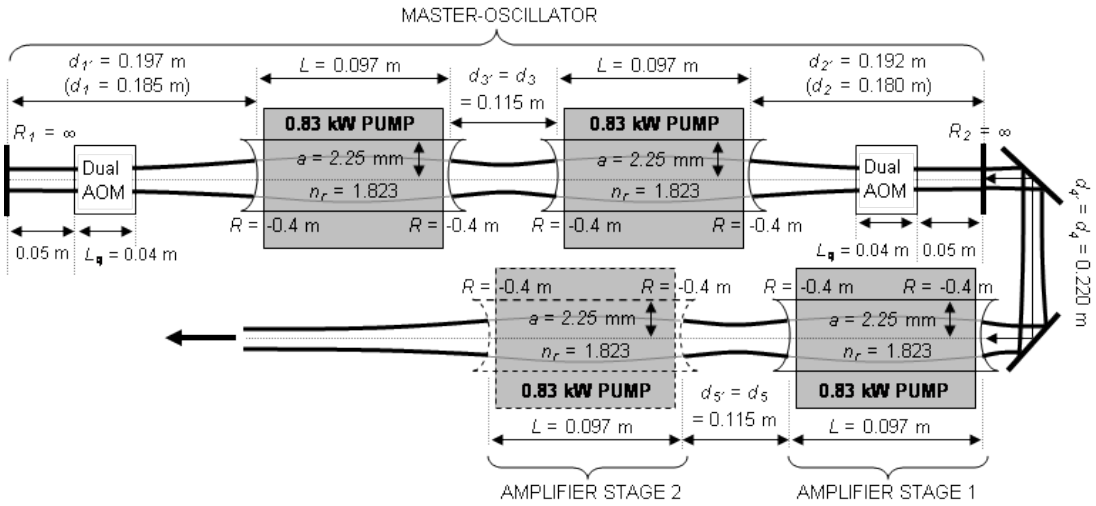

Figure 6.2 Schematic of the final MOPA configuration designed for volume production, industrial use and enhanced serviceability. Not to scale.

Figure 6.3 shows the average output power as a function of pulse repetition frequency for the dual-rod master-oscillator and with the addition of 1, and then 2 amplifier gain-modules. The modelled data illustrated for the oscillator output has been generated using the mathematical treatment detailed in section 4.2. We have then applied the standard theory for pulse amplification outlined in section 6.1 to simulate the output after 1 and 2 identical amplification stages. Experimentally, the master-oscillator was reproduced using alternative gain-modules to that reported in section 5.2, although these gain-modules were constructed to the original design. The resonator dimensions were set as presented in figure 6.2 to within 10 % error in measurement. Gain-module and laser performance reproducibility is further discussed in section 8.2.2. For this system the laser oscillator exhibited an output power of 431 W at 10 kHz PRF. The first amplifier stage demonstrated a gain of 1.36 resulting in average output power of 587 W at 10 kHz PRF. Addition of the second amplifier provided a further gain of 1.30 increasing the maximum output power to around 765 W, also at 10 kHz PRF. This final output corresponds to a total optical-to-optical efficiency (pump-to-fundamental) of ~ 23 %. The efficiency of energy extraction form the amplifier chain η_{Eamp}, as defined by equation (6.2), was 31 %. The experimental data collected is seen to be a good fit with the oscillator and

amplifier models with respect to the average power generated. This suggests that the imposed increase in amplifier distance from the oscillator has a relatively small affect on the amplified output power.

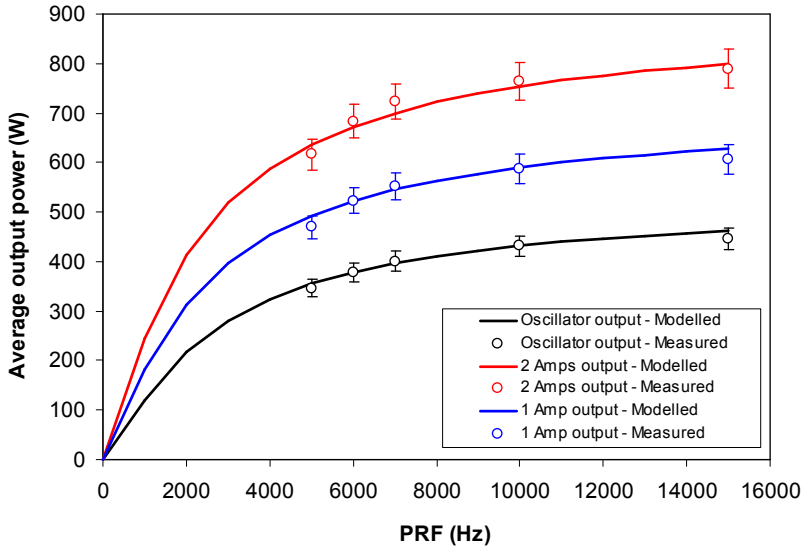

Figure 6.3 Average output power as a function of pulse repetition frequency (PRF) for a dual gain-module master oscillator, and with the addition of 1 and 2 power amplifier gain-modules.

The PRF dependent pulse durations for the oscillator were measured to be very similar to that reported in section 5.2.3. Empirical observations indicated that any distortions in the pulse duration due to gain saturation at the power amplifiers are small and within the error of measurement. This means that the increase in peak power generally follows the same gain trends as those outlined for the average power in figure 6.3.

The spatial distortion effects and optical aberrations present within the amplifier pair were assessed using a beam propagation analyser. In this case the beam propagation factor was increased from $M^2 = 23$ to $M^2 = 26$. It was observed that this increase in the factor of merit can be reduced to ~ 1 (resulting in $M^2 = 24$) with the implementation of a simple form of birefringence compensation. This was done by adding a quartz rotator of sufficient thickness to achieve 90° polarisation rotation between the first and second stage amplifier rods [6.8].

6.3.2 Power-scaled MOPA system with 3-stage amplification

In an attempt to further scale the output power at the fundamental wavelength a MOPA system was developed that comprised a combination of gain-module designs. Each of these gain-modules had twice the pump power of the original design outlined in chapter 2. To maintain the beam propagation parameter at $M^2 \sim 25$ the dual-rod resonator gain-modules detailed in section 5.2 were consolidated to produce a single, longer gain-module with double the pump length and the same rod diameter of 4.5 mm. Another of these gain-modules was used as the first stage amplifier, which effectively replicated the final MOPA system developed in the previous section, generating around 800 W average output power. In this case, each of the new gain-modules act like the original gain-module pairs but with effectively zero separation. As there are two less rod-ends per gain-module the thermal lens compensating concave facet curvatures were increased to give - 0.175 m ROC.

At this point the power amplifier stages 2 and 3 were added using the power-scaled gain-module design discussed in section 6.2. These gain-modules, with larger diameter rods, allow the peak irradiances at the rod facets to be maintained below a safe level as the power is amplified. A 90° quartz rotator was placed between the power-scaled gain-module pair for basic birefringence compensation (labelled 'QR' in the schematic of the final power-scaled MOPA system design is illustrated in figure 6.4).

The performance of the oscillator was found to be similar to that of the dual-rod resonator detailed in section 5.2 in terms of output power and beam propagation parameter. The pulse durations were around 7 ns shorter, at 18 - 58 ns across the stable PRF range of 4 – 20 kHz, due to the slightly reduced cavity length. Again, no significant temporal distortion in the pulse duration due to gain saturation in the amplifier chain was measured.

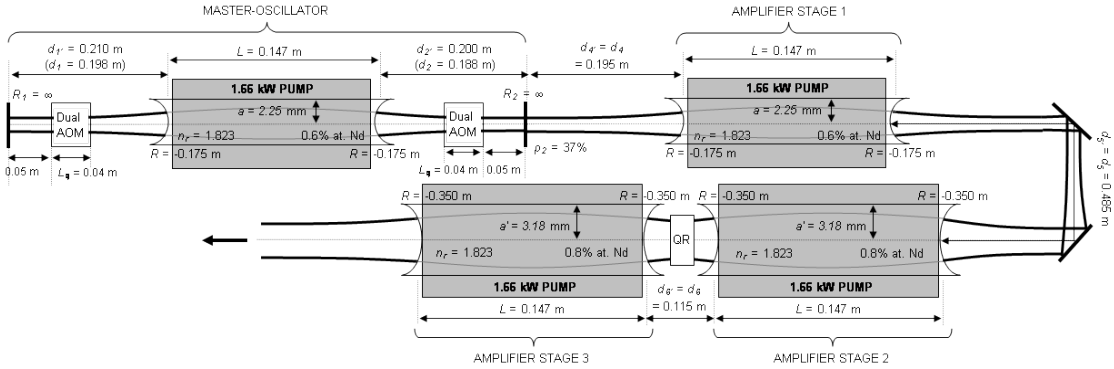

Figure 6.4 Schematic of the power-scaled MOPA configuration designed to produce an $M^2 \sim 25$ and average output powers up to 1600 W. Not to scale.

Figure 6.5 shows the resulting average and peak powers obtained at the output of the four gain-module MOPA system. These results show peak powers of up to 18 MW with an average power of 1261 W and pulse energies in excess of 0.32 J at 4 kHz PRF. At 20 kHz PRF an average power of 1580 W was produced giving an overall optical-to-optical efficiency of ~ 24 % (pump-to-fundamental). The beam propagation parameter at the optimum pump level was measured to be $M^2 = 23$, which is consistent with that predicted by the mathematical models for spatial mode evaluation presented in section 4.1.

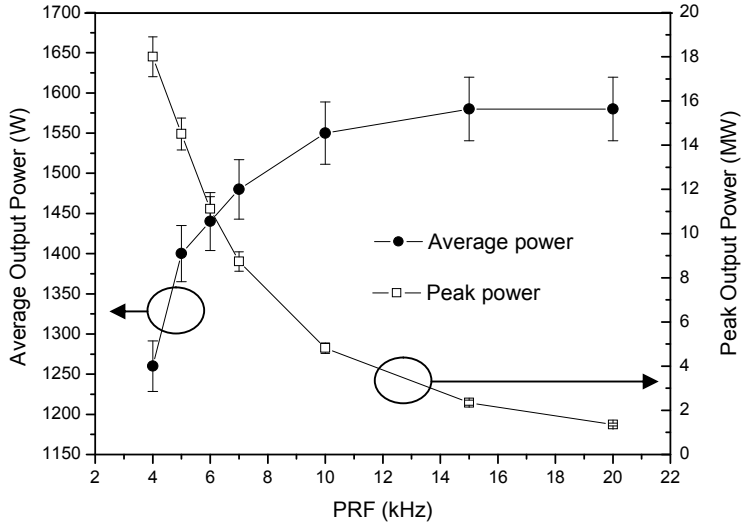

Figure 6.5 Average and peak output power as a function of PRF for the power-scaled infrared MOPA laser system with 3-stage amplification.

6.4 Summary

A number of methods for power-scaling at the fundamental wavelength of 1.064 μm have been presented. The first approach involved straight forward power amplification of the dual-rod oscillator presented in chapter 5. This led to output powers of around 800 W and pulse energies in excess of 0.12 J. The second approach involved designing a number of power scaled laser gain-modules for use in both oscillators and power amplifier stages. In this case a 3-stage power-scaled MOPA system was developed that was able to produce close to 1600 W average output power at pulse repetition frequencies of up to 20 kHz. At 4 kHz PRF this system was capable of producing pulse energies of around 0.32 J with 18 ns pulse durations, thus leading to peak powers of over 18 MW.

The laser systems developed in this chapter are capable of generating the pulse energies and average powers, as well as the spatial and temporal output characteristics required by the infrared applications outlined in chapter 1.

7 Wavelength conversion by non-linear wave mixing

To satisfy the application requirements stipulated in sections 1.1.3 and 1.1.4 it is necessary to convert the operating wavelength to around 0.5 μm. This can be done by applying non-linear wave mixing to generate a second-harmonic of the Nd:YAG fundamental produced by the laser configurations described in chapters 5 and 6. Although the generation of 0.532 μm laser light by this method is not new [7.1; 7.2; 7.3], the extension to kilowatt average powers with joule-level pulse energies has yet to be demonstrated. The following sections outline the considerations associated with such operation and detail the methods used to scale the output power and pulse energy. Techniques for refinement of the fundamental resonator platforms to optimise harmonic generation are initially discussed.

7.1 High-power intra-cavity harmonic generation using LiB_3O_5 (LBO)

There are many commercially available lasers that employ non-linear wave-mixing to generate higher photon energies and shorter wavelengths. Most of these lasers are, however, designed to operate at or near to the diffraction limit [7.4]. This facilitates generation of the small beam sizes and low angles of

divergence that are advantageous for efficient non-linear conversion. However, these systems are generally limited to tens of watts output due to inevitably low powers at the fundamental wavelength.

The challenge at higher M^2 operation is to generate the intensities required for efficient non-linear conversion while maintaining beam divergences low enough to stay within the acceptance angle for the converting media used. In an extra-cavity configuration the fundamental is typically focused to produce the intensities required for harmonic generation. However, at higher M^2 values the minimum achievable focus size for a given lens f-number is increased, thus reducing the intensity and conversion to the second harmonic. Compensating for this by using a lesser f-number to generate a smaller spot will tend to increase the beam divergence beyond the acceptance angle of the non-linear medium, again leading to reduced conversion efficiency. A solution to this problem is to use intra-cavity harmonic generation whereby the non-linear medium can take advantage of larger spots and lower angles of divergence, while maintaining sufficient intensity for wavelength conversion. Moreover, intra-cavity configurations can be shown to operate efficiently with a lower single-pass conversion as any uncoupled fundamental is 'recycled' for potential conversion on later passes.

At the commencement of this research in 2006, a number of higher power, higher M^2 green lasers had been reported including a 73 W oscillator by S. Lee et al [7.5], 100W systems by J. Yi et al [7.6] and E. C. Honea et al [7.7], and a 138 W configuration by S. Konno et al [7.8]. More recently, multi-spatial mode Q-switched oscillators operating at or around 0.532 μm have also become commercially available with up to 100 W average power.

At high average powers and peak irradiances we are predominantly limited in our choice of non-linear medium by the potential for laser induced damage and the optical transmission properties at 1.064 μm and 0.532 μm. In this case, single crystal lithium triborate LiB_3O_5 or 'LBO', was selected as a suitable

converting medium due to its combination of relatively high damage threshold, low absorption, high optical homogeneity and large acceptance angles at these wavelengths [7.9; 7.10; 7.11].

The single gain-module infrared oscillator detailed in section 5.1 was initially used to investigate intra-cavity harmonic generation in multi-spatial mode operation. At the fundamental wavelength this oscillator effectively produces random polarisation with respect to a given axis. Therefore, in order to utilise more than one polarisation component for non-linear conversion, the LBO was cut for type II critical phase matching at 25 °C. The crystal was thermally managed to within ± 0.1 °C using a thermo-electric cooler, thermistor and PID control loop. In this regime a component of the beam polarised parallel to the ordinary axis of the LBO crystal combines with an orthogonal component polarised parallel to the extra-ordinary axis to generate a second harmonic ordinary beam. Although LBO cut for type I critical phase matching has a larger effective non-linear coefficient (commonly referred to as d_{eff}), it also has a smaller acceptance angle and would only utilise one polarisation component of the fundamental, thus greatly restricting the number of photons available for conversion to the second harmonic. In the other extreme, the larger angles of acceptance seen with type I non-critical phase matching at ~ 150 °C may provide an increase in non-linear coupling. This however would require the implementation of a crystal oven, resulting in additional expense and undesirably lengthy system warm-up periods.

7.2 Infrared resonator refinement for optimum harmonic generation

In order to liberate the green light generated and ensure that little infrared (IR) is emitted the cavity output coupler was replaced by a dichroic optic coated for high reflection (HR) at 1.064 μm and anti-reflection (AR) at 0.532 μm. This also increases the intra-cavity power at the fundamental wavelength and the

intensity at the LBO crystal, thus promoting conversion to the second harmonic. Another consequence, however, is that the peak fluences at the resonator waists, in this case located at the cavity end mirrors, can readily exceed the limits for laser induced damage. These intra-cavity fluences can be reduced to safer levels by applying a partial reflectivity to the rear cavity mirror, thus discarding excess IR. For reliable operation the peak operating fluence at the cavity mirrors was not permitted to exceed a safety factor of 2 below the pre-determined damage threshold. A second dichroic optic was also installed to reflect the 0.532 μm light propagating toward the gain-module back in the direction of the green output, while allowing the resonating IR to be transmitted with negligible loss. The harmonic generation was observed to be unaffected by the resulting co-linear green beams that overlap within the 5 x 5 x 18 mm LBO crystal.

Using the method of spatial mode control outlined in section 4.1 it is possible to select an alternative design point that will maintain maximum resonator stability but also lead to a spatial mode envelope that produces larger beam waists at the cavity mirrors. This is illustrated in figure 7.1 below, which is a simplified version of figure 4.4 (a). The alternative stability condition will occur at the first apex of the stability curve (labelled 1 in figure 7.1), which corresponds to the left most of the M^2 maxima as previously illustrated in figure 4.5. The compromise required to operate at this alternative stability condition is a reduction in the size of the stability region with changing pump.

There are, however, a number of resulting benefits for intra-cavity harmonic generation. Firstly, the larger mode waists allow a safe peak intra-cavity fluence to be maintained when the rear cavity mirror reflectivity is increased back toward HR values. This enables the generation of higher intra-cavity powers for a given pump level. Furthermore, for the same peak M^2, the larger waists bring about lower divergences, which force a larger proportion of light into the acceptance angle of the LBO crystal. Ultimately, these effects lead to an increase in conversion to the second harmonic.

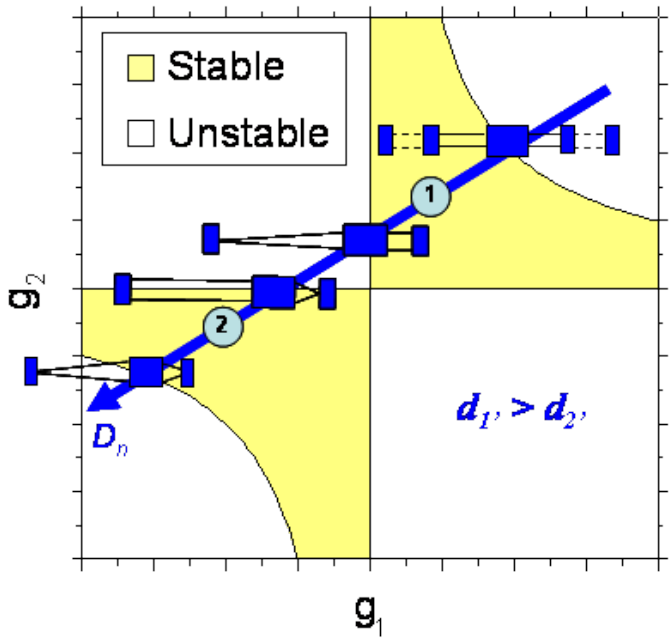

Figure 7.1 Simulated cavity stability diagram with spatial-mode-envelope profiles at the boundaries of the stability zones for a plane-plane resonator where arm length $d_{1'} > d_{2'}$. The positions of the first and second stability apexes are denoted 1 and 2 respectively.

In addition to the enhanced non-linear conversion observed with operation at the first resonator stability apex we can increase the overall efficiency of the green laser by attempting to match the harmonic conversion to the optimum output coupling for the fundamental resonator. There are three interrelated parameters that need to be considered here. The first and second are the rear cavity mirror reflectivity and the non-linear conversion to the second harmonic. Together these parameters represent the total output coupling. Changing the rear cavity mirror reflectivity will alter the intra-cavity power and therefore influence the non-linear conversion. The rear cavity mirror reflectivity will also govern the amount of IR light discarded at the rear of the cavity, which should be reduced where possible. The third parameter is the gain at the fundamental wavelength. This can be controlled by changing the pump level, which will in turn alter the optimum output coupling for the resonator. Changing the gain will also affect the intra-cavity power and therefore the non-linear conversion. For increased conversion efficiency, it is therefore advantageous to select a suitable

combination of pump level and rear cavity mirror reflectivity in order to match the total output coupling to the optimum for the fundamental resonator. For operation at high PRF (>20 kHz) we can approach this condition by decreasing the pump level from 830 W to 690 W and still obtain the same output power at 0.532 μm. Note that the efficiency is increased by eliminating the wasted IR light that is discarded from the rear of the cavity. To do this the rear cavity mirror reflectivity should be increased to a maximum level. In this case 99.0 ± 0.2 % reflectivity is chosen to allow the intra-cavity power to be reliably measured using the relatively small amount of escaping light. The resonator stability design point must then be re-optimised to accommodate for the new optimum pump level. For this resonator, the centre of the first stability apex can be translated to 690 W pump power by introducing a static negative lensing component. This is done by simply changing the rod facet radius of curvature for each rod end to – 0.9 m (concave-concave).

In summary, this optimisation process allows a reduction in pump power for the same 0.532 μm output through the elimination of wasted IR light at the rear of the cavity. The optimum condition ensures a maximum permissible intra-cavity power, which negates damage but maximises harmonic generation. The overall efficiency from pump to green output is effectively increased by closer matching the non-linear conversion to the optimum output coupling for the fundamental resonator.

The final optimised resonator design is illustrated in figure 7.2. Notice that the configuration comprises a single (in this case vertically orientated) AOM Q-switch. This is because the switch is not required to completely hold-off oscillation as little IR light is transmitted at the output coupler, which is HR coated for 1.064 μm. The residual IR that oscillates in the low-Q condition is only sufficient to produce milliwatts of green light (which can actually have a practical use as a rudimentary pointing or alignment aid). Moreover, the Q-switching modulation depth generated by a single AOM is suitable for efficient and repeatable pulsing up to 20 kHz PRF. The AOM was placed at the

rear of the cavity so that the increased beam size is captured within the active area and the switching speed is maximised.

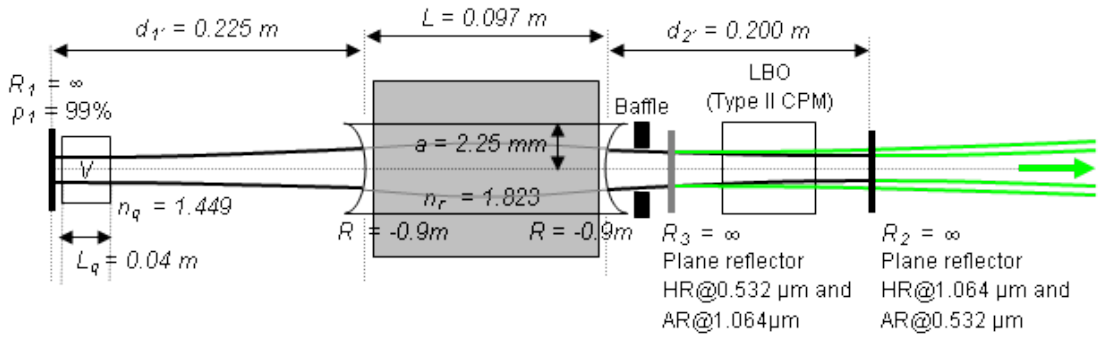

Figure 7.2 Layout of the single gain-module resonator optimised for intra-cavity second harmonic generation (not to scale).

Notice also that the cavity arm lengths are still set to maintain dynamic stability at the output of the oscillator (i.e. $d_{1'} > d_{2'}$). This will sustain the beam size and divergence at the LBO crystal with any drift in pump power and therefore promote stability in the non-linear conversion. A water cooled baffle was also introduced to capture any residual off-axis back-reflected light from the AR coated facets of the angle-tuned LBO crystal as this resonator can produce intra-cavity average powers of up to 6.8 kW in normal operation.

7.3 Extension to higher pulse repetition frequencies

To fully satisfy the process requirements set out in section 1.1.3 it is necessary to develop a second harmonic Nd:YAG laser capable of operating at pulse repetition frequencies of up to 50 kHz. There are two issues that arise when the PRF is increased to these levels. The first is that the conversion efficiency to the second harmonic and therefore the average output power at 0.532 µm is reduced. This is a result of the inherent reduction in gain build-up between

pulses, which leads to decreased pulse energy and increased pulse duration at the fundamental wavelength. Each of these affects a reduction in irradiance at the LBO crystal. The second issue is that the fundamental pulse-to-pulse energy begins to fluctuate as function of the gain and the spatial mode related inconstancy described in section 3.2.1. This effectively decreases pulse energy repeatability and increases timing jitter.

We have demonstrated a simple but novel method of obtaining and improving pulse constancy while simultaneously increasing intra-cavity irradiance and conversion to the second harmonic at high PRF. This technique involves optimisation of the off-time window in the RF power signal supplied to the acousto-optic modulator used for Q-switching. By reducing the RF off-time to an extent where the reinstated cavity loss terminates the tail of the optical pulse we can preserve a level of inversion and thus increase the gain available for build up of the following pulse. This effectively conserves energy storage within the gain media and emulates the gain properties of that seen with longer pulse repetition periods (lower PRF operation). The resultant increased gain improves the likelihood of obtaining repeatable pulse evolution and therefore aids pulse-to-pulse constancy. In addition to this, the increased gain leads to faster pulse build-up times and therefore an overall reduction in the pulse duration. This in turn increases the peak power of the fundamental which then promotes energy conversion to the second harmonic. The resulting increased second harmonic pulse energy leads to elevated peak and average powers for the same PRF. Figure 7.3 provides an illustration of the typical RF envelopes and corresponding optical signals that are generated when using this technique.

Basic software development has enabled automatic calibration of the RF off-time window as a function of PRF (via a PLC based laser control system). Here the principle has been demonstrated on intra-cavity frequency doubled Nd:YAG lasers but its application may also be extended to other Q-switched laser technologies.

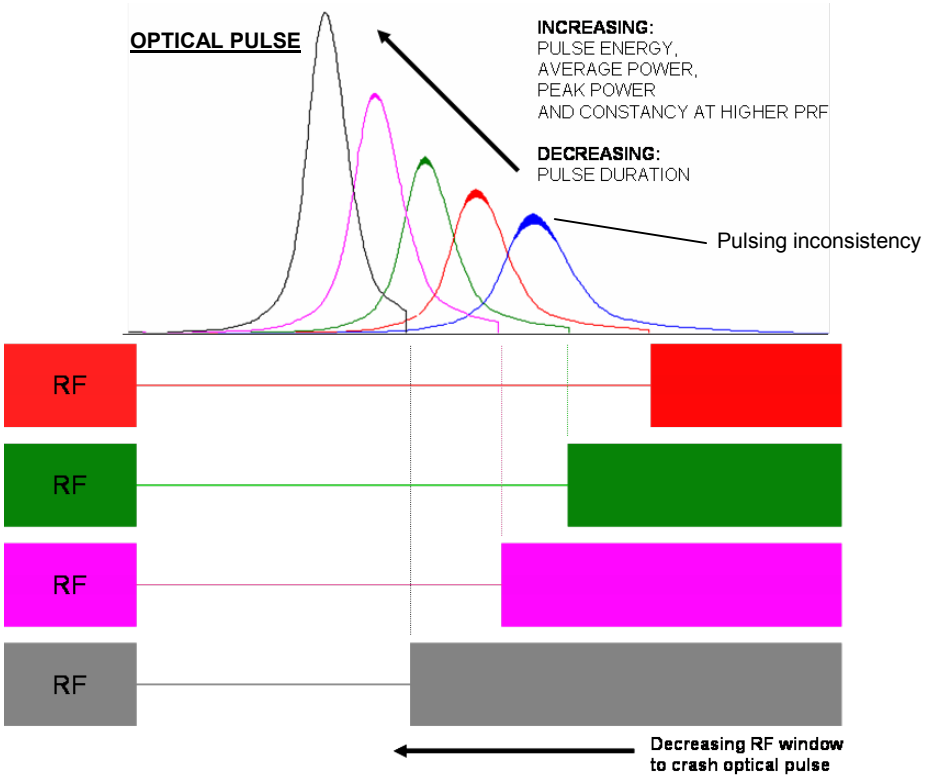

Figure 7.3 Diagrammatic representation of how the RF signal to the acousto-optic Q-switch can be altered to increase pulse energy, output power and promote pulse repeatability. The window in the RF envelope is reduced until it crashes the free running optical pulses, truncating them in the process.

7.4 Experimental results

The following sections outline the characterisation of a polarisation-multiplexed dual-resonator green laser system and a higher power version that utilises the power-scaled gain-module design presented in section 6.2.

7.4.1 Dual-resonator green system

The output power from a green laser system can be scaled by the combination of two independent linearly polarised oscillators. Here, outputs from two oscillators with the same design as that reported in the previous section are

made co-linear by multiplexing orthogonal polarisations from each oscillator at a thin film polariser. In this case the normally vertically polarised light from one oscillator is rotated 90° using a half-wave (λ/2) plate. It is important that the distances between the output of each oscillator and the combining polariser are equal. This ensures that the beams from each oscillator are the same size when combined. The amount of power that is transmitted by the polariser and therefore the power contribution of the first oscillator can be controlled by simply rotating the λ/2-plate. In the same way, the contribution from the second oscillator can also be controlled by subjecting its output to polarisation rotation and selection. This method of independent power control is further described in section 7.4.3. The final optical layout is illustrated in figure 7.4.

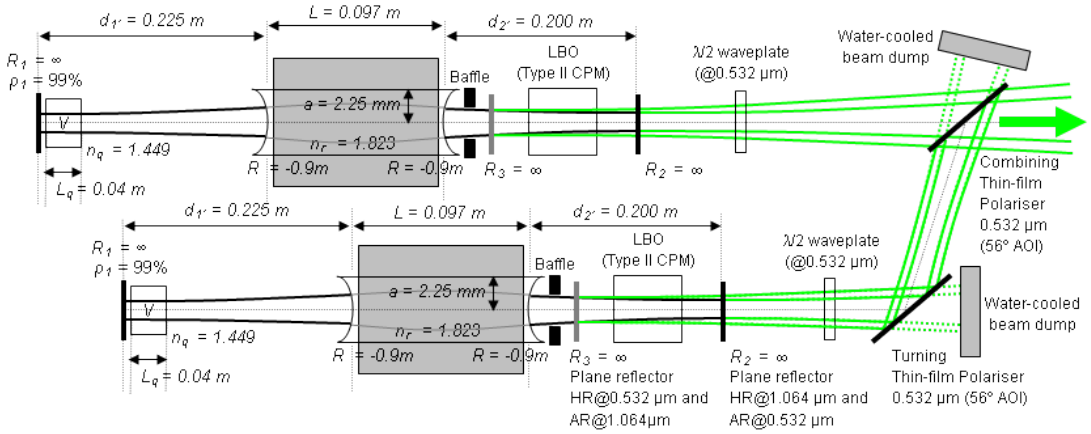

Figure 7.4 Layout of the polarisation multiplexed dual-resonator laser system incorporating intra-cavity second harmonic generation and independent oscillator output power control (not to scale).

For this system the beam pointing reproducibility from each oscillator was found to be insufficient for alignment-free multiplexing. Translation and rotation of the beam turning polariser was therefore required to obtain horizontal co-linearity, maintaining Brewster angle at both polarisers (~ 56° incidence for fused silica at 0.532 μm). Angular tilt on both polarisers is also required for co-linearity in the vertical plane.

At 690 W pump power the optimum total output coupling for the fundamental resonator was measured to be 16 %, which gave a maximum Q-switched output power of 240 W in the infrared (without the LBO crystal installed).

Implementation of the single intra-cavity SHG layout described in figure 7.2 and the PRF extension technique outlined in section 7.3 gave a maximum Q-switched output power of 121 W at 0.532 μm and 30 kHz PRF. This corresponds to an optical-to-optical efficiency of 18 % (pump-to-green) and indicates that the non-linear conversion did not fully match the optimum output coupling for the fundamental resonator. The optical-to-optical efficiency could be increased buy reducing the pump power but this would be at the expense of absolute output at 0.532 μm, which is undesirable for the targeted applications.

The addition of a second resonator and implementation of the layout described in figure 7.4 produced a single green beam of 240 W maximum average power and 60 kW maximum peak power, as illustrated in figures 7.5 and 7.6 (each plotted data set has been given an estimated line of best fit). A discontinuity in the data can be seen at 20 kHz due to that fact that the pump power was reduced to 525 W in order to maintain a factor of 2 below the damage threshold fluence at the cavity mirrors. There is also a reduction in the anticipated pulse duration at 60 kHz PRF, which leads to a corresponding increase in the expected peak power. This may be related to the fact that both oscillators only just pulse consistently at this PRF. The reduction in pulse duration may therefore be a symptom of the spatial mode related inconstancy described in section 3.2.1.

The two oscillators exhibited parity in output power to within ~ 5 % and the same pulse durations to within ~ 10 % over the measured PRF range. It is believed that this reproducibility in performance is facilitated by the dynamic stability that was incorporated as part of the fundamental resonator design (Ref. section 4.1). The beam propagation factor was largely maintained between the fundamental and green beams with an $M^2 \sim 23$ across the investigated range of PRF.

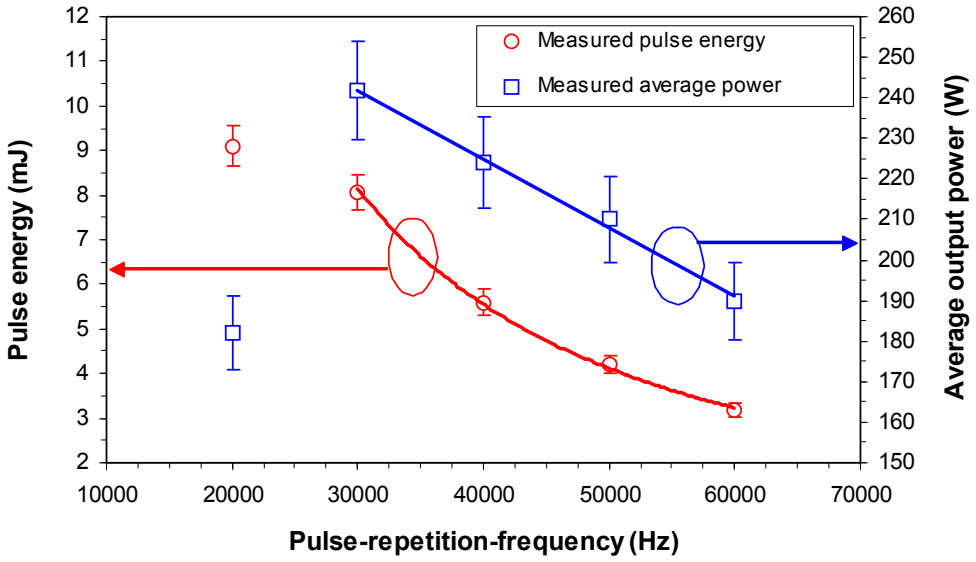

Figure 7.5 Experimentally measured average power and pulse energy as a function of PRF (optimised for pulsing at 30 - 50 kHz) at 0.532 µm for the dual-resonator laser system.

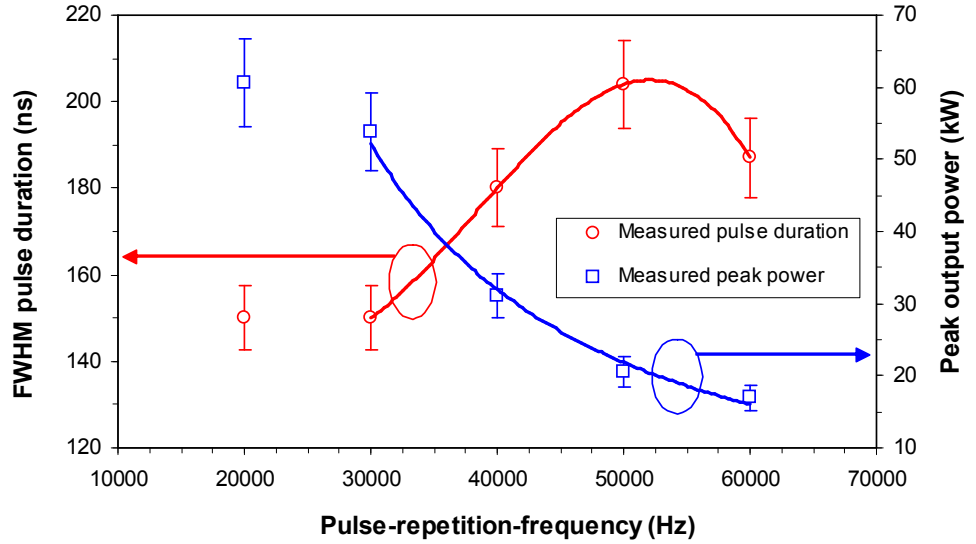

Figure 7.6 Experimentally measured pulse duration and subsequent peak power as a function of PRF (optimised for pulsing at 30 - 50 kHz) at 0.532 µm for the dual-resonator laser system.

7.4.2 Power-scaled dual-resonator green system

To produce a laser system capable of meeting the requirements demanded by the polysilicon annealing application detailed in section 1.1.4 it is necessary to

further scale the pulse energy and average power at 0.532 μm. This can be accomplished by using the power-scaled gain-module design presented in section 6.2 and the same resonator optimisation principles previously outlined in this chapter.

In line with the process requirements a power-scaled SHG resonator was optimised for maximum pulse energy at pulse repetition frequencies of 5 kHz or greater. As with the lower power oscillator this involved a single gain-module configuration and operation on the first apex of the beam propagation parameter curve, producing output dynamic stability (Ref. section 7.2). A suitable combination of pump level and rear cavity mirror reflectivity was selected to prevent optical damage and minimise discarded IR. Again, this led to a rear cavity mirror reflectivity of 99.0 ± 0.2 %, but this time at the optimum pump level for the laser diodes at 1660 W. To accommodate the larger spatial mode envelope the LBO crystal aperture was increased from 5 mm to 8 mm giving new crystal dimensions of 8 x 8 x 18 mm. The resulting intra-cavity wavelength converted oscillator produced a maximum average power of over 260 W at 0.532 μm when operating at 12 kHz PRF. This corresponds to an optical-to-optical efficiency of 16 % (pump-to-green). An expected reduction in pulse duration to around 66 ns at 8 kHz PRF provided a maximum operating peak-power of 0.4 MW for the single oscillator. Operation below 8 kHz PRF is not recommended for reliable operation as the minimum safety factor of 2 below the previously determined mirror damage threshold is not achieved.

In a final act of power scaling this wavelength converted oscillator was combined with another to produce a dual-resonator system by polarisation multiplexing, as described in section 7.4.1. This led to a maximum average power of 520 W and maximum peak powers in excess of 0.8 MW at 0.532 μm wavelength. Figures 7.7 and 7.8 illustrate the trends in output characteristics as a function of PRF for this laser system (each plotted data set has been given an estimated line of best fit). Again, the beam propagation factor was largely

maintained between the fundamental and green beams with an $M^2 \sim 32$ across the investigated range of PRF.

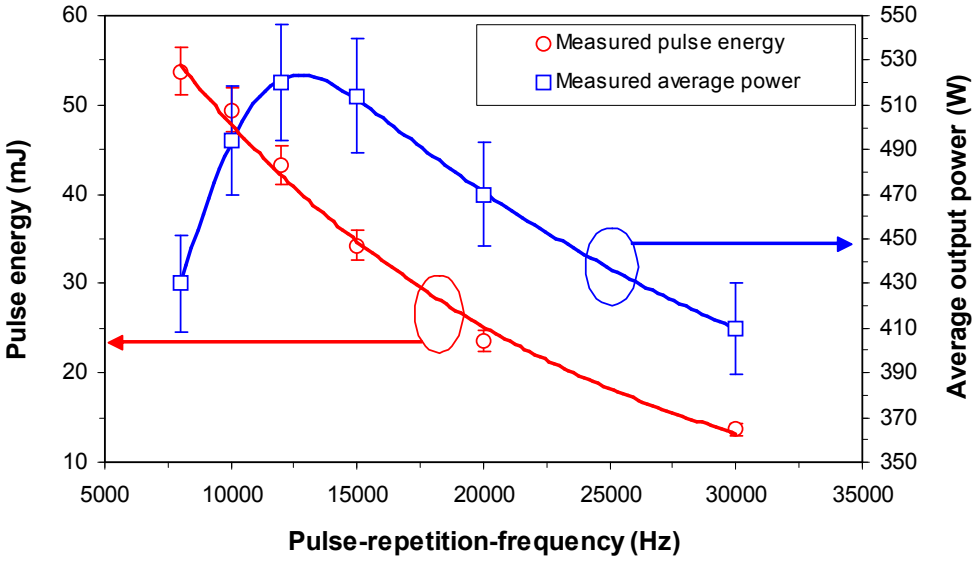

Figure 7.7 Experimentally measured average power and pulse energy as a function of PRF (optimised for pulsing at 8 – 30 kHz) at 0.532 µm for the power-scaled dual-resonator laser system.

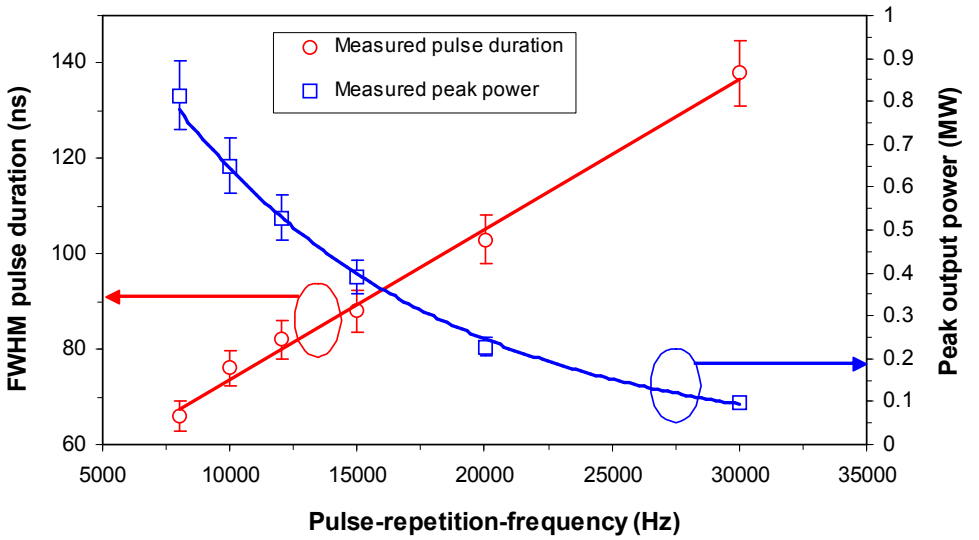

Figure 7.8 Experimentally measured pulse duration and subsequent peak power as a function of PRF (optimised for pulsing at 8 – 30 kHz) at 0.532 µm for the power-scaled dual-resonator laser system.

7.4.3 Output control and temporal pulse shaping

A method of temporal pulse shape control has been developed that uses independent manipulation of the Q-switched pulses generated from two polarisation multiplexed oscillators. Pulse shaping is achieved by altering the relative magnitude (energy) and timing of the pulses via the laser control system and user interface.

Independent control of the pulse energy, and therefore power, that each oscillator contributes to the combined output is achieved through the variable transmission of the laser beams through thin-film polarisers with change in incident polarisation. The polarisation from each resonator is rotated using half-wave plates, which are held in bespoke motorised opto-mechanical mounts. These mounts enable the polarisation rotation, and therefore attenuation to be manipulated via the laser control interface. Light that is not coupled into the laser output is transmitted or reflected onto water-cooled beam dumps, the resulting system layout is illustrated in figure 7.4. By using this means of power control, instead of pump level reduction, it is possible to maintain the optimum conditions for stable and consistent Q-switched operation and preserve all spatial properties of the beam, such as M^2 and divergence.

In terms of timing, this method of pulse control allows the oscillators to be either synchronously pulsed together (with no delay) or fully interlaced with a delay of half the pulse repetition period. The latter condition effectively produces double the pulse repetition frequency at the combined output and enables repetition frequencies in excess of 100 kHz. In addition to this coarse adjustment, a fine delay has also been implemented that allows the user to separate the pulses in time by 0 to 1000 ns, with a resolution of 5 ns.

Altering the timing of the pulses by sub pulse-length durations and changing the relative energy contribution from each resonator enables control of the temporal shape and duration of the pulse at the combined output. This pulse shaping technique has enabled the extension to output pulse durations in excess

of 300 ns full-width half-maximum. Figure 7.9 illustrates a number of temporal pulse shapes that can be produced using this technique.

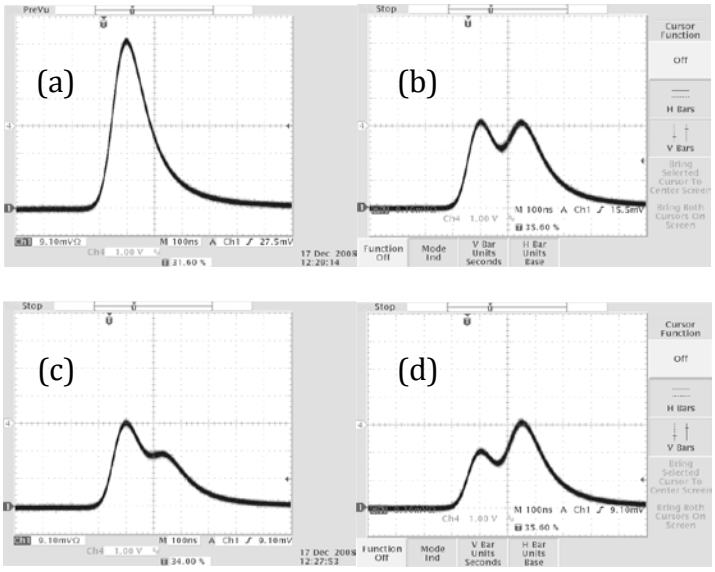

Figure 7.9 Temporal waveform envelopes for 10,000 pulses produced at the combined output of a dual-resonator green laser system showing (a) synchronised superposition of pulses 1 and 2 at full power, (b) separation of pulses 1 and 2 by 150 ns and their amplitudes set equal, (c) pulse 2 delayed and attenuated relative to pulse 1, and (d) pulse 2 delayed relative to an attenuated pulse 1.

7.5 Summary

High-power harmonic generation using LBO has been discussed with relevance to non-diffraction-limited beams and scaling toward kilowatt average powers at 0.532 μm wavelength. The resonator design tools presented in chapters 3, 4 and 5 were used to refine a number of infrared oscillators for the promotion of intra-cavity wavelength conversion.

A technique for extension to higher PRF has also been presented that involves novel control of the RF signal applied to the acousto-optic Q-switches. The innovative steps discussed have been shown to promote pulse-to-pulse constancy of Q-switched lasers, specifically those required to operate at pulse

repetition periods that would normally be too short for repeatable pulses to be generated. This technique facilitates a reduction in the pulse duration and increases peak power in the infrared, which in turn leads to elevated second harmonic pulse energy and thus, for the same PRF, an increase in average power output at 0.532 μm.

The implementation of these optimisation techniques has led to the generation of polarisation-multiplexed dual-resonator laser systems capable of producing 240 W average power, at 30 kHz PRF, with 18 % optical-to-optical efficiency (pump-to-green). Moreover, a similar system that utilises the power-scaled gain-module design presented in section 6.2 has enabled 520 W average power, optimised at 12 kHz PRF. At 8 kHz PRF this laser system can deliver maximum pulse energies of 54 mJ in 66 ns, leading to peak powers in excess of 0.8 MW at 0.532 μm wavelength.

Control over temporal pulse shape and duration has also been demonstrated that takes advantage of the flexible polarisation-multiplexing arrangement used. Pulse shaping is achieved through independent control of the output energy and timing of the pulses from two beam combined oscillators. This has enabled the generation of tailored pulse waveforms with full-width half-maximum durations ranging from 66 ns to over 300 ns.

The laser systems developed in this chapter are capable of producing all of the performance characteristics, including the pulse energies, average powers, pulse durations and spatial characteristics, required by green laser applications outlined in chapter 1.

8 Outlook and conclusions

8.1 Research overview

A number of specific industrial laser applications have been identified that require high-power pulsed operation at near-infrared and green wavelengths. These target applications (detailed in section 1.1) had been qualified in principle using the highest power, nanosecond-pulse, solid-state lasers that were commercially available at the beginning of this research in 2006. However, scaling of the power and pulse energy at both near-infrared and green wavelengths was needed to make the processes feasible for efficient industrial use. The objective of this research was to develop nanosecond-pulse, Nd:YAG lasers capable of producing these new levels of average power and pulse energy at the 1.064 μm fundamental and 0.532 μm second harmonic wavelengths. Importantly, the highlighted applications do not require near diffraction limited beam quality. They do however demand that the scaling to higher average powers is achieved at minimum cost and with the same or better standard of reliability and reproducibility than that offered by the existing highest power industrial laser systems.

In chapter 2 we discuss the concept, design and characterisation of a high-power laser gain-module that integrates Nd:YAG solid-state gain medium with an optimised high-power pump configuration. For long-term reliable operation the CW pump diodes are operated below the maximum rated drive current

giving an optimum total pump power of 830 W shared equally in 5-fold symmetry. The diode light is directly coupled without the use of expensive delivery fibres, micro-lenses or optical ducts into a pump chamber that has been designed to maximise absorption efficiency and promote homogeneous thermal loading (and gain distribution). Fractional heat loading with respect to the total absorbed pump was measured to be 0.39 (+ 0.05, - 0.04). This led to the calculation of an average lens constant for the gain-module under oscillating conditions $C_t = 8.4 \times 10^{-3}$ dioptres per watt of total incident pump, which includes the effects of birefringence observed for radial and tangential polarisations. The fraction of pump power dissipated as heat per unit length was determined to be a factor of 3.6 (+ 0.4, - 0.3) below the experimentally measured limit associated with fracture of the Nd:YAG rod.

A number of important design principles are discussed in chapter 3 that enable the cost-effective production of industrially robust, high-power, multi-spatial-mode laser resonators. These resontors exhibit full or partial dynamic stability such that their output characteristics are resistent to change in the inevitable thermal lensing that occurs within the pumped gain medium.

In chapter 4 we present a suite of mathematical models that can be used to simulate the design principles and therefore optimise the output of thermally active solid-state resonators. This modelling is focused on the investigation of two sets of performance characteristics – spatial mode control and the subsequent temporal evolution of Q-switched pulses. The first of the mathematical models facilitates analysis of the spatial mode content and resonator stability. This enables theoretical quantification of the beam propagation parameter (M^2), beam size, far-field divergence and output dynamic stability for a given cavity design. In an advanced step the spatial mode content and gain trends were linked to Q-switched pulse jitter, allowing further theoretical optimisation of the resonator. This spatial model was also extended to consider relative and quantitative misalignment sensitivity of the simulated optical configurations. To complement the spatial model a temporal simulation

was also developed for the implementation and optimisation of active Q-switching with CW pumping. This enabled the projection of PRF dependent average output power, pulse energy, FWHM pulse duration and peak power for a given laser oscillator. Finally, the spatial and temporal models were combined to assess the susceptibility of each laser resonator design to self-induced optical damage.

Chapter 5 outlines experimental investigation for various examples of acousto-optically Q-switched resonators based on the gain-modules developed in chapter 2. At an optimum pump power of 830 W this resonator output a 25-times diffraction limited beam at the fundamental wavelength with a CW optical to optical efficiency of 29 (± 3) %. This resonator exhibited consistent Q-switching in the PRF range of 3 - 20 kHz with corresponding average powers of 130 - 235 W, pulse energies of 12 - 43 mJ and pulse durations of 30 - 100 ns. A second resonator was then presented that comprised a dual-rod configuration for increased power output, again using the gain-module design developed in chapter 2. This dual-rod resonator produced a similar $M^2 \sim 25$ with an almost identical optical to optical efficiency of 30 (± 3) %, at an optimum total pump of 1660 W. The dual-rod resonator demonstrated consistent Q-switching over a PRF range of 1 - 15 kHz with corresponding average powers of 56 - 510 W, pulse energies of 34 - 61 mJ and pulse durations of 22 - 53 ns. Deviations from the models generated in chapter 4 are only seen to occur under conditions of changing beam-to-gain overlap and with the onset of CW leakage (pre-lasing) between Q-switched pulses. A number of methods for first pulse control and transient thermal lens management by diode modulation have also been demonstrated that promoted Q-switched pulse repeatability in gated operation.

In chapter 6, a number of standard methods for power-amplification were applied to the optimised resonators. Power-scaling at the fundamental wavelength was needed to produce lasers capable of generating the output characteristics required by the infrared applications outlined in chapter 1. The first approach involved straight forward power amplification of the dual-rod

oscillator presented in chapter 5 using additional gain-modules of the same design. Single-stage amplification resulted in average output powers approaching 600 W above 10 kHz PRF. In this case, a maximum of 2 amplification stages were permitted due to the fluence limits for optical damage at the output rod facet. This 2-stage amplification led to output powers of around 800 W and pulse energies in excess of 0.12 J. The second approach to further power-scaling at 1.064 μm involved designing a number of larger gain-modules for use in both the oscillator and power amplifier chain. In this case a 3-stage power-scaled MOPA system was developed that was able to produce close to 1600 W average output power at pulse repetition frequencies of up to 20 kHz. At 4 kHz PRF this system was capable of producing pulse energies of around 0.32 J with 18 ns pulse durations, thus leading to peak powers of over 18 MW. Figure 8.1 illustrates the state-of-the-art for commercially available high-power, nanosecond-pulse, solid-state lasers operating at ~1 μm wavelength in 2009. This is an updated version of figure 1.5, which showed the technology landscape before this research in 2006. The annotated lines represent the output characteristics with changing PRF for the infrared laser systems developed during this work.

It is evident that the 600 W and 800 W MOPA systems developed are capable of meeting the minimum requirements for the rapid laser patterning (RLP) of ITO in plasma display panel production. In addition to this, the 1600 W power-scaled MOPA system demonstrates the requirements for EUV generation by laser produced plasma (LPP), particularly when 2 or more of these lasers are multiplexed to the same focus. Note also that the 1600 W power-scaled MOPA system may also be capable of meeting the 0.1 J pulse energy requirement for increased productivity in the RLP application, at around 16 kHz PRF.

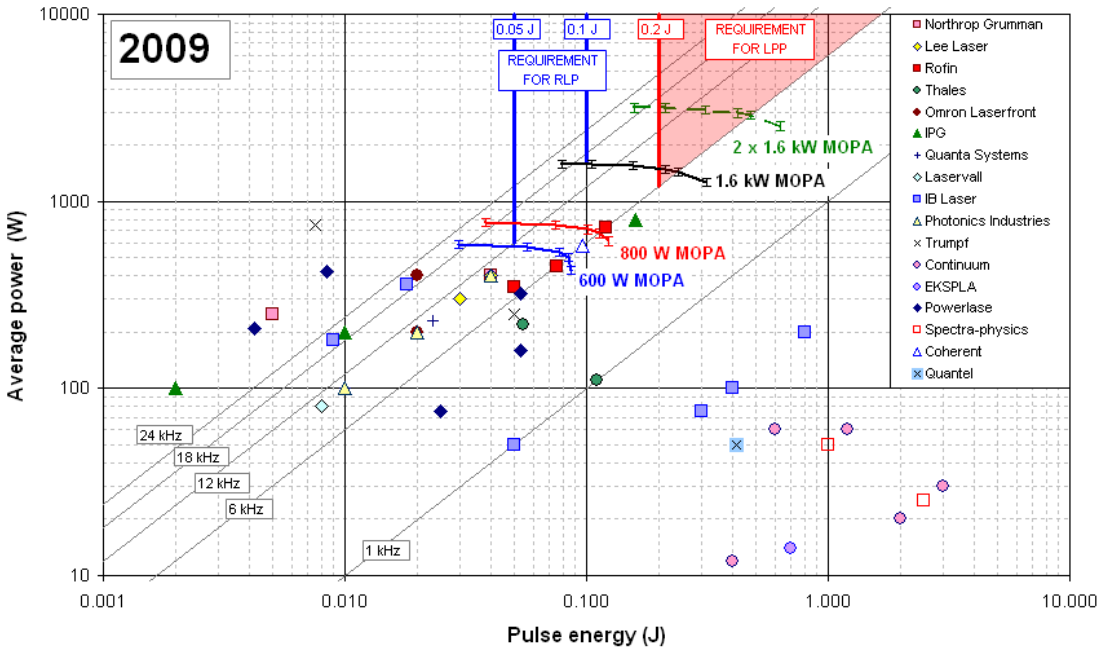

Figure 8.1 State-of-the-art for commercially available high-power, nanosecond-pulse, solid-state lasers operating at ~ 1 µm wavelength in 2009. The requirements for RLP and LLP applications are illustrated in blue and red respectively.

Chapter 7 outlines the implementation of high-power harmonic generation using LBO and non-diffraction-limited beams. The novel resonator design tools presented in the previous chapters were used to refine a number of infrared oscillators for the promotion of intra-cavity conversion to 0.532 µm wavelength. A technique for extension to higher PRF led to the realisation of a polarisation-multiplexed dual-resonator laser system capable of producing 240 W average power at 30 kHz, with 18 % optical-to-optical efficiency (pump-to-green). A similar system that utilised the power-scaled gain-module design presented in section 6.2 demonstrated a maximum average power of 520 W at 0.532 µm, when optimised at 12 kHz PRF. Operating at 8 kHz PRF this laser system can deliver maximum pulse energies of 54 mJ in 66 ns, leading to peak powers in excess of 0.8 MW. Figure 8.2 illustrates the state-of-the-art for commercially available high-power, nanosecond-pulse, solid-state lasers operating at ~ 0.5 µm wavelength in 2009. This is an updated version of figure 1.6, which showed the performance limits of the commercial laser systems available before

this research in 2006. Here the annotated lines represent the output characteristics as a function of PRF for the green laser systems developed during this work.

Figure 8.2 shows that the 240 W dual-resonator green system, optimised at 30 kHz PRF, is able to meet the process requirements for the laser micro-jet application detailed in section 1.1.3. The 260 W single resonator power-scaled green laser system meets the minimum requirements for the low temperature poly-silicon annealing (LTPS) application below 10 kHz PRF. Moreover, the 520 W that result from combining two of these resonators is sufficient to satisfy the 0.05 J pulse energies needed to efficiently anneal the thickest p-Si films. Notice that the 260 W single-resonator green system may be capable of satisfying the requirements for both LTPS and micro-jet applications (assuming that the increase in beam propagation parameter can be tolerated).

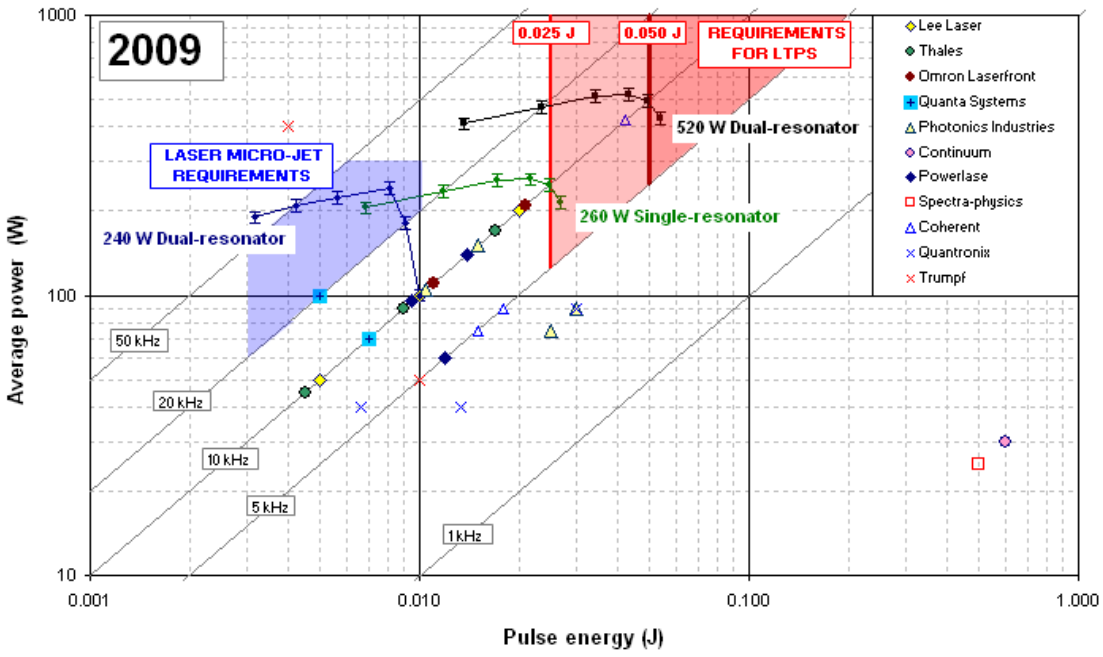

Figure 8.2 State-of-the-art for commercially available high-power nanosecond-pulse solid-state lasers operating at ~ 0.5 µm wavelength in 2009. The laser micro-jet and LTPS application requirements are highlighted in blue and red respectively.

8.2 Further work

Although the laser systems developed during this work meet the application requirements set out in chapter 1, there are still a number of areas that would benefit from continued effort. Now that lasers have been designed to enable commercialisation of the target applications the next step will be to make the processes more cost-effective to the laser user. This inevitably requires the design of laser systems that facilitate increased productivity and reduced cost of ownership. Moreover, these advancements must be done ahead of, or better than, the competing companies and technologies. With exception of the micro-jet process, all of the target applications highlighted would benefit in terms of productivity with further scaling of the average power and pulse energy. Efforts can also be made to keep the cost of ownership to a minimum by consideration of the efficiencies involved in the design, manufacturing and performance of the laser as a system.

8.2.1 Scaling to higher powers and pulse energies

Scaling to higher average powers and pulse energies at the common fundamental wavelength of Nd:YAG is straight-forward in principle. This can done by simple reapplication of the rules used to generate the power-scaled gain-module and MOPA system presented in sections 6.2 and 6.3.2 respectively. However, experience shows that this may become more and more difficult to put into practice from an engineering standpoint. For example, at very high peak and average powers we must be wary of optical damage and thermal management. Failure modes at high powers often emerge in the form of catastrophic damage resulting from contamination of the optical surfaces with dust or other airborne particles. Inadequate capture and dissipation of the significant amounts of heat in the form of stray or residual back reflected light can cause melting or burning of components close to the beam. This can be particularly troublesome when using rubber or plastic based o-rings and seals

for mounting or water cooling. It has been known that optical and thermal damage mechanisms can cascade whereby the heating of a seal causes out-gassing and contamination of nearby optical surfaces. In short, the cost of implementation (the extra cost over that required to provide the additional gain) is likely to increase as the power is scaled.

Increasing the power and pulse energy at the second harmonic is more difficult, particularly for the same beam propagation parameter. However, with no spatial mode constraints, power scaling using the concepts proposed in this work can be extended through greater pump powers and larger limiting apertures (Nd:YAG rod diameters). To scale the power and pulse energy while maintaining M^2 it is necessary increase the total gain but keep the irradiances and fluences below the level associated with optical damage. This can only be achieved by increasing the beam size at the relevant optical interfaces and/or increasing the pulse duration. This may be possible with further investigation of the resonator design and use of the mathematical models presented in chapter 4. Particular emphasis should be given to the possibility of adding resonator gain-modules, increasing the total oscillator length and the use of spherical cavity mirrors to control beam size and waist positions. As part of this investigation, it would be beneficial to clarify the efficacy of using alternative resonator stability zones to enable the use of more than 2 highly thermally active gain-modules in a single resonator (Ref. section 4.1.2).

8.2.2 Design optimisation for cost-effective industrial operation

In addition to increased productivity through improved process speed and yield, laser users expect to see a reduction in the cost of ownership for a given level of performance as the technology matures. It is therefore up to the laser manufacturer to develop and employ universal methods for cost reduction. There are many factors that govern the cost of ownership for the laser system as

a whole. The factors that are based on engineering principles can be partitioned into 3 general groups:

1) Fundamental laser system design,
2) Design for manufacturing and
3) Reliability and serviceability.

Fundamental laser system design - Here we have defined the fundamental design of a laser system as that required to achieve the minimum output requirements for the application processes (in terms of power, pulse energy, PRF, pulse duration, spatial beam quality, etc.). Depending on the volume to be manufactured, the fundamental design of the laser has arguably the greatest impact on the cost of ownership. It is the fundamental design that has the largest influence on material cost, which is usually the primary driver for setting the capital cost of purchase for the laser system. Importantly, the fundamental design of the laser also has the most significant effect on the system efficiency. Laser users are often interested in the 'wall-plug' efficiency, which is defined as ratio of power output by the laser to the electrical power required. Increasing the efficiency of the laser by fundamental design can reduce the cost of ownership in two ways. Lower electrical power consumption for a given output will obviously reduce utility bills. Moreover, increased efficiency can lead to a reduction in the number of pump diodes required for a given output, which can significantly reduce the material cost and therefore selling price of the laser system. A list of the efficiencies associated with the transfer of energy from electrical to the output of an infrared resonator is shown in table 8.1. The parameters highlighted in blue are controllable by fundamental laser design. The aim for further work would be to look at the optimisation of these parameters for increased wall-plug efficiency, which is currently around 12 % for the infrared resonators presented (when Q-switched at 10 kHz PRF). This model could also be refined to include power amplification at the fundamental wavelength and intra-cavity harmonic generation.

EFFICIENCY PARAMETER				MEASURED OR CALCULATED VALUE	CW OPERATION	Q-SWITCHED OPERATION (10kHz PRF)	WHERE THE LOST ENERGY GOES
		η_D	Diode driver electrical efficiency	0.85	0.85	0.85	Heat in the PSU.
		η_P	Pump diode electrical to optical efficiency	0.5	0.5	0.5	Heat in the pump diodes.
	η_c Pump coupling efficiency	η_T	**Optical transfer efficiency of pump into the laser rod**	**0.95**	**0.81**	**0.81**	Heat dissipation in, or light lost from the pump chamber
		η_a	**Absorption efficiency into pump bands**	**0.85**			
		η_d	Dead site ratio (typical fraction of non-dead Nd sites)	0.85	0.85	0.85	Heat in the rod.
η_u Upper level (stokes & quantum) efficiency	η_s Stokes shift (quantum defect)	η_w	Branching quantum efficiency from absorption bands to the upper laser level	1	0.68	0.68	Heat in the rod.
		η_x	Transfer efficiency to the upper laser level from the absorption bands	0.92			
		η_y	Branching quantum efficiency to ground level from lower laser level	1			
		η_z	Transfer efficiency to the ground level from the lower lasing level	0.82			
		η_{qe}	Branching quantum efficiency from the upper to lower laser levels when oscillating (in the presence of stimulated emission)	0.9			Lost to fluorescence (via other available transitions).
η_{st} Stimulated emission extraction efficiency		η_{ASE}	ASE efficiency (fraction not lost to ASE when oscillating)	0.91	0.91	0.91	Lost due to amplified fluorescence.
		η_B	**Beam overlap - mode volume to gain volume distribution**	**0.82**	**0.82**	**0.82**	Lost due to fluorescence in unstimulated regions.
	η_{ext} Q-switch dependent extraction efficiency	η_E	Pulse extraction efficiency (how much of the available inversion is used over the duration of the pulse)	0.92		0.92	Lost as fluorescence between pulses.
		η_Q	Q-switch PRF dependent efficiency (calculated here for 10 kHz PRF)	0.85		0.85	Lost as fluorescence between pulses.
			WALL-PLUG EFFICIENCIES:		**0.15**	**0.12**	

Table 8.1 A list of efficiency parameters associated with an Nd:YAG resonator operating at the fundamental wavelength (assuming optimum output coupling). The total wall-plug efficiency for CW and Q-switched operation at 10 kHz PRF is given. The parameters highlighted in blue are controllable through fundamental laser design.

Further work on fundamental laser design could also be extended to continued investigation of resonator stability. It is still unknown why there is a spatial-mode related inconstancy in the generation of Q-switched pulses. Investigations into the temporal evolution of the spatial modes over the pulse duration may provide an insight into this phenomenon.

Design for manufacturing – Another area for further work is design for manufacturing (DFM). This type of design has roots in high volume manufacturing where the effort and time taken to construct a laser system can have a significant impact on the labour cost and therefore selling price. It is therefore advantageous to refine the fundamental laser design to aid the manufacturing process. In doing this it may also be possible to reduce the bill of materials through product or 'value' engineering and cost control. Intrinsic to

product engineering is the concept of component tolerance rationalisation, which can be used to control the material costs and the reproducibility in performance from unit to unit, as discussed in section 3.3. The requirements for this will vary depending on the target application.

Reliability and serviceability – The final group of factors that can have significant implications for cost of ownership are related to the long-term performance of the laser system. Increasingly, laser users seek added value from increased operating lifetimes and reduced maintenance. When implemented, the design principles presented in this work can promote both reliability and serviceability. Resistance to perturbations in thermal lensing by design will decrease the resonator's response to long-term pump degredation and gain-module performance variation. This will in turn increase the mean time to failure (MTTF). The MTTF will then ultimately depend on the lifetime of the least reliable component. Futher work should be done to indentify and improve the performance critical components. In addition to this, maximising the resistance to perturbations in cavity misalignment by design would aid the ability to replace (or 'plug-and-play') failed components in the field with minimum realignment, thus reducing the mean time to repair (MTTR).

8.3 Concluding remarks

It is often difficult to gauge the success of scientific or engineering research. In pure academic research, acceptance of the work done is usually measured through peer review and publication. In a commercial context however, the open dissemination of intellectual property or proprietary knowledge is regarded as a loss of competitive advantage. Therefore, the success of commercial research and development is measured by the ability of the emerging product to meet the needs of the customer and their application. By the end of this research in 2009, the MOPA system design presented in chapter 6 was being used by the industry leaders in plasma display panel

manufacturing, producing over 10,000 panels per month by rapid laser patterning. Power scaled MOPA systems have also been sold to customers for the development of microlithography EUV sources, for which trials have been successful. The wavelength converted laser systems presented in chapter 7 have now been used within the semiconductor industry for both micro-jet machining and poly-silicon annealing. By the end of 2009 laser systems based on the designs presented in this work had demonstrated over 1 million cumulative hours of industrial operation with over 200 units in use across the globe.

References

CHAPTER 1

[1.1] A. L. Schawlow and C. H. Townes, “Infrared and optical masers”, Phys. Rev., 112 (6), 1940-1949 (1958).

[1.2] A. Einstein, "Zur quantentheorie der strahlung" (On the quantum theory of radiation), Physika Zeitschrift, (18), 121-128 (1917).

[1.3] T. H. Maiman, “Stimulated optical radiation in ruby”, Nature (187), 493-494 (1960).

[1.4] K. J. Gasvik, *Optical Metrology*, John Wiley & Sons Ltd (2002).

[1.5] J. M. Senior, *Optical Fiber Communications: Principles and Practice*, Prentice Hall, (1985).

[1.6] M. Tabak, J. Hammer, M. E Glinski, W. L. Kruer, S. C. Wilks, J. Woodworth, E. M Campbell, M. D Perry and R. J. Mason, “Ignition and high-gain with ultrapowerful lasers”, Phys. Plasmas, 1 (5), 1626-1634 (1994).

[1.7] M. Roth, T. E. Cowan, M. H. Key, S. P. Hatchett, C. Brown, W. Fountain, J. Johnson, D. M. Pennington, R. A. Snavely, S. C .Wilks, K. Yasuike, H. Ruhl, F. Pegoraro, S. V. Bulanov, E. M. Campbell, M. D. Perry and H. Powell, “Fast ignition by intense laser-accelerated proton beams”, Phys. Rev. Lett., 86 (3):436-439 (2001).

[1.8] J. F. Ready, *LIA Handbook of Laser Materials Processing*, Laser Institute of America, Magnolia Publishing/Springer, Berlin, (2001).

[1.9] W. M. Steen, *Laser Material Processing*, Springer-Verlag, (1991).

[1.10] M. Hoheisel, A. Mitwalski and C. Mrotzek, "Microstructure and etching properties of sputtered indium-tin oxide (ITO)", Phys. Status Solidi, A123, 461 (1991).

[1.11] M. Mohri, H. Kakinuma, M. Sakamoto and H. Sawai, "Plasma etching of ITO thin films using a CH_4/H_2 gas mixture", Jap. J. Appl. Phys., 29 (L), 1932 (1990).

[1.12] P. Harrison and S. Ellwi, "Industrial applications of high average power, high peak power nanosecond pulse duration Nd:YAG lasers", Proc. SPIE Vol. 7193 71932A-4 (2009).

[1.13] M. Takai, D. Bollmann and K. Haberger, "Maskless patterning of indium tin oxide layer for flat panel displays by diode-pumped Nd:YLF laser radiation", Appl. Phys. Lett. 64 (19) 2560 – 2562 (1994).

[1.14] S. Venkat and C. Dunsky, "Laser patterning of ITO in flat panel display manufacturing", Proc. SPIE, 6106 (2006).

[1.15] M. Henry, P. M. Harrison and J. Wendland, "Laser direct write of active thin-films on glass for industrial flat panel display manufacture", Proc. LAMP (2006).

[1.16] R. Usui, R. Satoh, Y. Iwata, K. Nakagawa, E. Morinaga and S. Takaki, "Research on direct laser patterning of thin-films for flat-panel display", Proc. ICALEO (2005).

[1.17] V. Bakshi, *EUV Sources for Lithography*, SPIE Press (2005).

[1.18] V. Y. Banine, J. P. H. Benschop and H. G. C. Werij, "Comparison of extreme ultraviolet sources for lithography applications", Microelectronic Eng., 53, 681-684 (2000).

[1.19] K. Takenoshita, R. Bernath, R. Kamptraprasad, J. Szilagyi, S. A. George, J. Cunado, M. Richardson, S. Ellwi, B. Fulford, I. Henderson and N. Hay, "High power multiplexed EUV source development", SEMATECH EUV Source Workshop 8408-08 (2008).

[1.20] S. Ellwi, A. J. Comley and M. Brownell, "Spatially and temporally multiplexed laser modules for LPP sources", *EUV Sources for Lithography*, SPIE Press, 563-576, (2005).

[1.21] R. Pakula, "Dimensional analysis and laser produced plasmas", Phys. Fluids B3 (1), 176-185 (1991).

[1.22] J.D. Huba NRL Plasma Formulary, NRL/PU/6790-98-358, Naval Research Laboratory, Washington DC (1998).

[1.23] R. C. Spitzer, T. J. Orzechowski, D. W. Phillion, R. L. Kauffman and C. Cerjan, "Conversion efficiencies from laser-produced plasmas in the extreme ultraviolet regime", J. Appl. Phys. (79), 2251 – 2258 (1996).

[1.24] T. Ariga, H. Hoshino, T. Miura and A. Endo, "High power pulsed CO_2 laser for EUV lithography", SPIE Emerging lithographic technologies conference No10, vol. 6151 (2), (2006).

[1.25] U. Stamm and K. Gabel, "Technology for LPP sources", *EUV Sources for Lithography*, SPIE Press, 537 - 559 (2005).

[1.26] M. Schmidt, B. Barthod, T. Ceccotti, G. Cheymol, J-F. Hergott, O. Sublemontier, P-Y. Thro, P. Cormont, J. Skrzypczak and T. Auguste, "Modular LPP source", *EUV Sources for Lithography*, SPIE Press, 577 - 605 (2005).

[1.27] P. Couty, F. Wagner and P. Hoffmann, "Laser coupling with a multimode water-jet waveguide", SPIE Opt. Eng., 44 (6), 068001 (2005).

[1.28] P. Couty, A. Spiegel, N. Vago, B. I. Ugurtas and P. Hoffmann, "Laser-induced break-up of water jet waveguide", Experiments in Fluids 36, 919-927 (2004).

[1.29] A. Spiegel, N. Vago and F. Wagner, “High efficiency Raman scattering in micrometer sized water jets”, SPIE Opt. Eng., 43 (2), 450 – 454 (2004).

[1.30] T. Sameshima, S. Usui and M. Sekiya, “XeCl excimer laser annealing used in the fabrication of poly-Si TFT’s”, IEEE Elec. Dev. Lett., 7 (5), 276 – 278 (1986).

[1.31] H-J. Kahlert, B. Burghardt, F. Simon and M. Stopka, “High resolution optics for thin Si-film crystallization using excimer lasers: present status and future development”, Electronic Imaging, SPIE Vol. 5004 (2003).

[1.32] R.S. Sposili and J.S. Im, “Line-scan sequential lateral solidification of Si thin films”, Appl. Phys., A 67, 273 – 276 (1998).

[1.33] A. T. Voutsas, “A new era of crystallization: advances in polysilicon crystallization and crystal engineering”, Appl. Sur. Sci., 208-209, 250 – 262 (2003).

[1.34] R. B. Bergmann, J. Kohler, R. Drassow, C. Zaczek, J. H. Werner, “Nucleation and growth of crystalline silicon films on glass for solar cells”, Phys. Stat. Sol. (a) 166, 587 - 602 (1998).

[1.35] G. Andrä, J. Bergmann, F. Falk and E. Ose, “Preparation of single crystalline regions in amorphous silicon layers on glass by Ar^+ laser irradiation”, Applied Surface Science, (154-155), 123 - 129 (2000).

[1.36] Z. Yuan, Q. Lou, J. Zhou, J. Dong, Y. Wei, Z. Wang, H. Zhao and G. Wu, “Numerical and experimental analysis on green laser crystallization of amorphous silicon thin films”, Optics & Laser Technology, 41, 380–383 (2009).

[1.37] R. Dassow, J. R. Kohler, Y. Helen, K. Mourgues, O. Bonnaud, T. Mohammed-Brahim and J. H. Werner, “Laser crystallization of silicon for high-performance thin-film transistors”, Semicond. Sci. Technol. 15, L31-L34 (2000).

[1.38] T. Okamoto, K. Morikawa, A. Sono, Y. Sato and J. Nishimae, "Development of line-shaped optical system for green laser annealing used in the manufacture of low-temperature poly-Si thin-film transistors", Appl. Opt., 45 (19), 4709 – 4714 (2006).

[1.39] K. Nishida, R. Kawakami, J. Izawa, N. Kawaguchi, F. Matsuzuka, M. Masaki, M. Morita, A. Yoshinouchi and Y. Kawasaki, "Performance of solid green laser annealing system for LTPS TFTs", IDW'06 (2006).

CHAPTER 2

[2.1] W. Koechner, *Solid-State Laser Engineering*, 5th Edition, Springer (1999).

[2.2] W. Koechner, "Rupture stress and modulus of elasticity for Nd:YAG crystals", Appl. Phys. 2, 279 – 280 (1973).

[2.3] R. Weber, B. Neuenschwander and H. P. Weber, "Thermal effects in solid-state laser materials", Opt. Materials 11, 245 – 354 (1999).

[2.4] H. S. Carslaw and J. C Jaeger, *Conduction of heat in solids*, Oxford Univ. Press, London, 191 (1948).

[2.5] S. Timoshenko and J. N. Goodier, *Theory of elasticity*, 3rd Edition, McGraw-Hill, Singapore, (1982).

[2.6] T. Y. Fan, "Heat generation in Nd:YAG and Yb:YAG", IEEE J. Quantum. Elec., 29 (6), 1457 – 1459 (1993).

[2.7] D. P. Devor, L. G. DeShazer and R. C. Pastor, "Nd:YAG quantum efficiency and related radiative properties", IEEE J. Quantum. Elec., 25 (8), 1863 – 1873 (1989).

[2.8] M. Pollnau, P. J. Hardman, M. A. Kern, W. A. Clarkson and D. C. Hanna, "Up-conversion induced heat generation and thermal lensing in Nd:YLF and Nd:YAG", Phys. Rev. B, 58 (24), 16076 – 16092 (1998).

[2.9] D. C. Brown, “Heat, fluorescence and stimulated-emission power densities and fractions in Nd:YAG”, IEEE J. Quantum. Elec., 34 (3), 560 – 572 (1998).

[2.10] D. C. Brown, “Ultrahigh-average-power diode-pumped Nd:YAG and Yb:YAG lasers”, IEEE J. Quantum Elec., 33 (5), 861-873 (1997).

[2.11] J. Marion, “Strengthened solid-state laser materials”, Appl. Phys. Lett., 47 (7), 694 – 696 (1985).

[2.12] K. E. Shafer, D. E. Eakins, D. F. Bahr, M. G. Norton and K. G. Lynn, “Strength enhancement of single crystal laser components”, J. Mater. Res., 18 (11), 2537–2539 (2003).

[2.13] R. Feldman, Y. Shimony, E. Lebiush and Y. Golan, “Effect of hot acid etching on the mechanical strength of ground YAG laser elements”, J. Phys. and Chem. of Solids, 69, 839–846 (2008).

[2.14] Nature Photonics 1, p385, *Technology Focus: Semiconductor lasers*, Nature publishing group, July (2007).

[2.15] D. G. Hall, “Optimum mode size criterion for low-gain lasers”, Appl. Opt., 20 (9), 1579 – 1583 (1981).

[2.16] R. J. Koshel and I. A. Walmsley, “Optimal design of optically side-pumped lasers”, IEEE J. Quantum. Elec., 33 (1), 94 – 102 (1997).

[2.17] F. W. Quelle, “Thermal distortion of diffraction-limited optical elements”, Appl. Opt., 5 (4), 633 – 637 (1966).

[2.18] E. P. Riedel and G. D. Baldwin, “Theory of dynamic optical distortion in isotropic laser materials”, J. Appl. Phys., 38 (7), 2720 – 2725 (1967).

[2.19] G. D. Baldwin and E. P. Riedel, “Measurements of dynamic optical distortion in Nd-doped glass laser rods”, J. Appl. Phys., 38 (7), 2726 – 2738 (1967).

[2.20] J. D. Foster and L. M. Osterink, “Thermal Effects in a Nd:YAG Laser”, J. Appl. Phys., 41 (9), 3656 – 3663 (1970).

[2.21] W. Koechner, “Thermal lensing in a Nd:YAG laser rod”, Appl. Opt., 9 (11), 2548 – 2553 (1970).

[2.22] T. Kimura and K. Otsuka, “Thermal effects of a continuously pumped Nd^{3+}:YAG laser”, IEEE J. Quantum. Elec., 7 (8), 403 – 407 (1971).

[2.23] D. C. Burnham, “Simple measurement of thermal lensing effects in laser rods”, Appl. Opt., 9 (7), 1727 – 1728 (1970).

[2.24] T. J. Gleason, J. S. Kruger and R. M. Curnutt, “Thermally induced focusing in a Nd:YAG laser rod at low input powers”, Appl. Opt., 12 (12), 2942 - 2946 (1973).

[2.25] H. J. Eichler, A. Haase, R. Menzel and A. Siemoneit, “Thermal lensing and depolarization in a highly pumped Nd:YAG laser amplifier”, J. Phys. D: Appl. Phys., 26, 1884 – 1891 (1993).

[2.26] S. Fan, X. Zhang, Q. Wang, S. Li, S. Ding and F. Su, “More precise determination of thermal lens focal length for end-pumped solid-state lasers”, Opt. Comm., 266, 620–626 (2006).

[2.27] Q. Lu, N. Kugler, H. Weber, S. Dong, N. Muller and U. Wittrock, “A novel approach for compensation of birefringence in cylindrical Nd:YAG rods”, Opt. Quantum Elec., 28, 57-69 (1996).

[2.28] I. Moshe and S. Jackel, “Correction of thermally induced birefringence in double rod laser resonators – Comparison of various methods”, Opt. Comm., 214, 315-325 (2002).

[2.29] B. Neuenschwander, R. Weber and H. P. Weber, “Determination of the thermal lens ion solid-state lasers with stable cavities”, IEEE J. Quantum. Elec., 31 (6), 1082 – 1087 (1995).

[2.30] C. Jacinto, T. Catunda, D. Jaque, L. E. Bausá and J. García-Solé, "Thermal lens and heat generation of Nd:YAG lasers operating at 1.064 and 1.34 μm", OSA Opt. Exp., 16 (9), 6317 – 6323 (2008).

CHAPTER 3

[3.1] A. G. Fox and T. Li, "Resonant modes in a maser interferometer", Bell Sys. Tech. J., 40, 489 – 508 (1961).

[3.2] W. Koechner, *Solid-State Laser Engineering*, 5th Edition, Springer (1999).

[3.3] H. Kogelnik and T. Li, "Laser beams and resonators", Appl. Opt., 5 (10), 1550 – 1566 (1966).

[3.4] A. E. Siegman, "Laser beams and resonators: The 1960s", IEEE J. Select. Topics in Quantum Elec., 6 (6), 1380 – 1388 (2000).

[3.5] A. E. Siegman, "Laser beams and resonators: Beyond the 1960s", IEEE J. Select. Topics in Quantum Elec., 6 (6), 1389 – 1399 (2000).

[3.6] C. M. Stickley, "Laser brightness, gain and mode control by compensation for thermal distortion", IEEE J. Quantum Elec., 2 (9), 511 – 518 (1966).

[3.7] L. M. Osterink and J. D. Foster, "Thermal effects and transverse mode control in a Nd:YAG laser", Appl. Phys. Lett., 12 (4), 128 – 131 (1968).

[3.8] A. E. Siegman, "How to (maybe) measure laser beam quality", OSA TOPS, 17, 184 – 199 (1998).

[3.9] ISO 11146:2005 "Lasers and laser-related equipment — Test methods for laser beam widths, divergence angles and beam propagation ratios", Published by the International Organization for Standardization (2005).

[3.10] T. F. Johnston, "Beam propagation (M^2) measurement made as easy as it gets: The four-cuts method", Appl. Opt., 37 (21), 4840 – 4850 (1998).

[3.11] R. B. Chesler and D. Maydan, "Convex-concave resonators for TEM_{00} operation of solid-state ion lasers", J. Appl. Phys., 43 (5), 2254 – 2257 (1972).

[3.12] J. Steffen, J. P. Lortscher and G. Herziger, "Fundamental mode radiation with solid-state lasers", IEEE J. Quantum Elec., 8 (2), 239 – 245 (1972).

[3.13] J. P. Lortscher, J. Steffen and G. Herziger, "Dynamic stable resonators: A design procedure", Optical and Quantum Elec., 7, 505 – 514 (1975).

[3.14] V. Magni, "Resonators for solid-state lasers with large-volume fundamental mode and high alignment stability", Appl. Opt., 25 (1), 107 – 117 (1986).

[3.15] S. De Silvestri, P. Laporta and V. Magni, "The role of the rod position in single-mode solid state resonators: Optimisation of a CW mode-locked Nd:YAG laser", Opt. Comm., 57 (5), 339 – 344 (1986).

[3.16] O. Svelto, *Principles of Lasers*, 4th edition, p185 (1998).

[3.17] A. E. Siegman, *Lasers*, University Science Books, p666 (1986).

[3.18] H. P. Kortz, R. Ifflander and H. Weber, "Stability and beam divergence of multimode lasers with internal variable lenses", Appl. Opt., 20 (23), 4124 –4134 (1981).

[3.19] F. J. McClug and R. W. Hellwarth, "Giant optical pulsations from ruby", J. Appl. Phys., 33, 828 (1962).

[3.20] J. J. Zaynowski and P. L. Kelley, "Optimisation of Q-switched lasers", IEEE J. Quantum Elec., 27 (9), 2220 – 2225 (1991).

CHAPTER 4

[4.1] R. Weber, B. Neuenschwander and H. P. Weber, "Thermal effects in solid state laser materials", Opt. Materials 11, 245 – 354 (1999).

[4.2] K. P. Driedger, R.M. Ifflander and H. Weber, “Multirod resonators for high-power solid-state lasers with improved beam quality”, IEEE J. Quantum Elec., 24 (4), 665 – 674 (1988).

[4.3] Q. Lu, N. Kugler, H. Weber, S. Dong, N. Muller and U. Wittrock, “A novel approach for compensation of birefringence in cylindrical Nd:YAG rods”, Opt. Quantum Elec., 28, 57-69 (1996).

[4.4] I. Moshe and S. Jackel, “Correction of thermally induced birefringence in double rod laser resonators – Comparison of various methods”, Opt. Comm., 214, 315-325 (2002).

[4.5] R. C. Sam, J-J. Yeh, K. R. Leslie and W. R. Rapoport, “Design and performance of a 250Hz Alexandrite laser”, IEEE J. Quantum Elec., 24 (6), 1151 – 1166 (1988).

[4.6] A. G. Fox and T. Li, “Modes in a maser interferometer with curved and tilted mirrors”, Proc. IEEE, 51, 80 – 89 (1963).

[4.7] R. J. Freiberg and A. S. Halsted, “Properties of lower order transverse modes in argon ion lasers”, Appl. Opt., 8 (2), 355 – 362 (1969).

[4.8] R. L. Sanderson and W. Streifer, “Laser resonators with tilted reflectors”, Appl. Opt., 8 (11), 2241 – 2248 (1969).

[4.9] J. A. Arnaud, “Degenerate optical cavities II: Effect of misalignments”, Appl. Opt., 8 (9), 1909 – 1917 (1969).

[4.10] R. Hauck, H. P. Kortz and H. Weber, “Misalignment sensitivity of optical resonators”, Appl. Opt., 19 (4), 598 – 601 (1980).

[4.11] V. Magni, “Resonators for solid-state lasers with large-volume fundamental mode and high alignment stability”, Appl. Opt., 25 (1), 107 – 117 (1986).

[4.12] S. De Silvestri, P. Laporta and V. Magni, "Misalignment sensitivity of solid-state laser resonators with thermal lensing", Opt. Comm., 59 (1), 43 – 48 (1986).

[4.13] N. Hodgson and H. Weber, "Misalignment sensitivity of stable resonators in multimode operation", J. Modern. Opt., 39 (9), 1873-1882 (1992).

[4.14] R. Hua, S. Wada and H. Tashiro, "Analytical method for design a TEM_{00} mode resonator of a dual-rod Nd:YAG laser with full birefringence compensation", Opt. Comm., 232, 333 – 341 (2004).

[4.15] Hodgson and Weber, *Laser Resonators and Beam Propagation*, 2nd Edition, Springer publishing (2005).

[4.16] V. Magni, "Multi-element stable resonators containing a variable lens", J. Opt. Soc. Am. A., 4 (10), 1962 – 1969 (1987).

[4.17] W. G. Wagner and B. A. Lengyel, "Evolution of the giant pulse in a laser", J. Appl. Phys., 34 (7), 2040 – 2046 (1963).

[4.18] J. J. Degnan, "Theory of the optimally coupled Q-switched laser", IEEE J. Quantum Elec., 25 (2), 214 – 220 (1989).

[4.19] J. J. Zayhowski and P. L. Kelley, "Optimization of Q-switched lasers", IEEE J. Quantum Elec., 27 (9), 2220 – 2225 (1991).

[4.20] R. M. Wood, *The Power and Energy Handling Capability of Optical Materials, Components and Systems*, SPIE Press (2003).

CHAPTER 5

[5.1] D. C. Brown, "Ultrahigh-average-power diode-pumped Nd:YAG and Yb:YAG lasers", IEEE J. Quantum Elec., 33 (5), 861-873 (1997).

CHAPTER 6

[6.1] L. M. Frantz and J.S. Nodvik, "Theory of pulse propagation in a laser amplifier", J. Appl. Phys., 34 (8), 2346 (1963).

[6.2] R. Bellman, G. Birnbaum and W. G. Wagner, "Transmission of monochromatic radiation in a two-level material", J. Appl. Phys., 34 (4), 780 (1963).

[6.3] W. W. Rogrod, "Gain saturation and output power of optical masers", J. Appl. Phys., 34 (9), 2602 (1963).

[6.4] E. L. Steele and W. C. Davis, "Laser amplifiers", J. Appl. Phys., 36 (2), 348 (1965).

[6.5] W. D. Fountain, "Far-field brightness of amplified laser systems", Appl. Opt., 11 (10), 2383 (1972).

[6.6] N. P. Barnes, V. J. Corcoran, I. A. Crabbe, L. L. Harper, R. W. Williams and J. W. Wragg, "Solid-state laser technology", IEEE J. Quantum Elec., 10 (2), 195 – 201 (1974).

[6.7] W. Koechner, *Solid-State Laser Engineering*, 5th Edition, Springer (1999).

[6.8] I. Moshe and S. Jackel, "Correction of thermally induced birefringence in double rod laser resonators – Comparison of various methods", Opt. Comm., 214, 315-325 (2002).

CHAPTER 7

[7.1] J. A. Armstrong, N. Bloembergen, J. Ducuing and P. S. Pershan, "Interactions between light waves in a nonlinear dielectric", Phys. Rev. Lett., 127, 1918 – 1939 (1962).

[7.2] F. Zernike and J. E. Midwinter, *Applied Nonlinear Optics*, John Wiley and Sons (1973).

[7.3] G. S. He and S. H. Liu, *Physics of Nonlinear Optics*, World Scientific Publishing (1999).

[7.4] H. Zhang, P. Shi, D. Li and K. Du, "Diode-end-pumped, electro-optically *Q*-switched Nd:YVO4 slab laser and its second-harmonic generation", Appl. Opt. 42 (9), 1681 – 1684 (2003).

[7.5] S. Lee, Y. G. Kim, B. H. Cha and Y. K. Kim, "A diode-pumped linear intracavity frequency doubled Nd:YAG rod laser with 40 ns pulse width and 73 W green output power", Optics & Laser Tech. (36), 265 – 271 (2004).

[7.6] J. Yi, H-J. Moon and J. Lee, "Diode pumped 100W green Nd:YAG rod laser", Appl. Opt., 43 (18), 3732 – 3737 (2004).

[7.7] E. C. Honea, C. A. Ebbers, R. J. Beach, J. A. Speth, J. A. Skidmore, M. A. Emmanuel and S. A. Payne, "Analysis of an intracavity-doubled diode-pumped Q-switched Nd:YAG laser producing more than 100 W of power at 0.532 μm", Opt. Lett., 23 (15), 1203 – 1205 (1998).

[7.8] S. Konno, T. Kojima, S. Fujikawa and K. Yasui, "High-brightness 138 W green laser based on an intra-cavity frequency-doubled diode-side-pumped Q-switched Nd:YAG laser", Opt. Lett., 25 (2), 105 – 107 (2000).

[7.9] S. P. Velsko, M. Webb, L. Davis and C. Huang, "Phase Matched Harmonic Generation in Lithium Tiborate (LBO)", J. Quantum. Elec., 27 (9), 2182 – 2192 (1991).

[7.10] V. G. Dmitriev, G. G. Gurzadyan and D. N. Nikogosyan, *Handbook of Nonlinear Optical Crystals*, Springer Science and Business Media (1991).

[7.11] D. N. Nikogosyan, *Nonlinear Optical Crystals*, Springer Science and Business Media (2005).

Symbols and Abbreviations

SYMBOLS

(α, ϕ)	Polar coordinates in the plane transverse to the beam direction.
a	Radius of the laser rod.
A	Cross-sectional area of the rod.
$ABCD$	2 x 2 ray transfer matrix components.
A_{surf}	Area of the barrel surface for the pumped section of the laser rod.
b	Gaussian beam confocal parameter.
C	Specific heat coefficient.
c	Speed of light in free-space.
$C_{r,\varphi}$	Functions relating to the radial and tangential photoelastic coefficients.
c_s	Plasma sound speed.
C_t	Lens constant under oscillating conditions.
C_t'	Lens constant under non-oscillating conditions.
d	Resonator mirror spacing.
D	Refractive power of a gain-module under non-oscillating conditions.
$d_{1'}$ and $d_{2'}$	Physical cavity arm lengths with transmitting optical components installed.
$d_{4'}$	Distance from resonator output coupler to first (extra-cavity) power amplifier.
D_{exp}	Experimentally measured lens power.
D_n	Net refractive power of an equivalent thin lens for the laser rod.
dn/dT	Coefficient of the refractive index dependence on the temperature.

D_{n1}	Average net lens power for rod 1 in a dual-rod resonator.
D_{n2}	Average net lens power for rod 2 in a dual-rod resonator.
D_{nr}	Modified net lens power for radial polarisation.
D_{ntherm}	Thermal component of the net lens power in the presence of stress-induced birefringence.
$D_{n\varphi}$	Modified net lens power for tangential polarisation.
D_r	Radial stress-induced lens power component.
d_t	Initial diameter of a target for LPP.
D_{therm}	Thermal lens refractive power.
D_φ	Tangential stress-induced lens power component.
E	Complex electric field amplitude.
E_{max}	Maximum possible output pulse energy with optimised output coupling.
E_{st}	Energy stored in the upper level of the transition per unit volume within a power amplifier.
E_u	Total useful energy available to the laser mode during Q-switched pulse generation.
f	Focal length (or the distance from the focus of least confusion between radial and tangential polarisations and the nearest principle plane of the rod-like lens).
F_{in} and F_{out}	Average input and output fluence of a pulse propagating through a power amplifier respectively.
F_{max}	Total mechanical load at failure (rod fracture).
F_{mi}	PRF dependent peak fluence (energy density) at the cavity mirror m_i.
f_R	Pulse repetition frequency (PRF).
F_{sat}	Saturation fluence.
F_T	Tested laser induced damage threshold fluence value (specified by the optical coating manufacturer).
F_{Tsc}	Modified (scaled) laser induced damage threshold fluence.
g_0	Unsaturated small-signal gain coefficient.
g_1 and g_2	Resonator stability parameters.
$g_r(x)$	Cross-sectional gain-profile in the laser rod.
h	Planck's constant.
h_1 and h_2	Distances from a laser rod facet to the corresponding principle planes P_1 and P_2.
H_m and H_n	mth and nth-order Hermite polynomials respectively.

h_t	Laser rod surface heat transfer coefficient.
I	Irradiance.
i and j	Interchangeable index parameters such that $i, j = 1, 2; i \neq j$.
I_0	Surface irradiance of an incident laser beam.
$I_B(x)$	Radial intensity profile of the beam in the laser rod.
I_{mi}	PRF-dependent intra-cavity irradiance at mirror m_i.
I_n	Normalised optical intensity.
K	Thermal conductivity.
k	Wave number.
L	Laser rod length.
l	Parasitic round-trip cavity loss.
L^*	Effective spatial cavity length for paraxial ray propagation.
L'	Total physical cavity length.
L_1	Position of mirror 1 with respect to principle plane P_1
L_2	Position of mirror 2 with respect to principle plane P_2
L_3	Distance between the facing principle-planes of the two rod-like lenses in a dual-rod resonator.
L^l_p	Generalised Laguerre polynomial of order p and index l.
L_{oi}	Positions of an embedded gaussian-beam waist relative to the corresponding resonator end mirror.
L_p	Pumped length of the laser rod.
L_q	Physical length of the AOM Q-switch cell
L_r	Effective (refractive index dependent) optical path length of the resonator.
m and n	Number of zero irradiance nodes normal to the beam axis in the vertical and horizontal directions, using Cartesian coordinates.
M^2	Beam propagation parameter, or figure of merit.
$M^2_{\max}$	Maximum output beam propagation parameter for a given pump condition.
n	Refractive index.
N	Number of rods in a resonator.
n_2	Second order refractive index coefficient.
n_{cr}	Critical electron density.
n_{e0}	Electron density of unperturbed plasma,
N_i	Initial inversion factor above the spatially averaged threshold inversion density.
n_i	Initial population inversion density.

n_q	Refractive index of the fused-silica AOM Q-switch cell at 1.064 μm wavelength.
n_r	First order refractive index coefficient.
n_{th}	Threshold inversion for oscillation.
P	Total power output by the pump laser diodes.
p and l	Number of radial and angular nodes respectively.
P_1	Principle plane 1 of the rod-like lens.
P_2	Principle plane 2 of the rod-like lens.
P_{abs}	Total pump power absorbed in the laser rod.
P_h	Power dissipated as heat in the laser rod.
P_H	Pump power required to maintain consistent Q-switched pulsing with reduced hold-off.
P_{m1}	Lower spatial-mode related limit for consistent pulsing.
P_{m2}	Upper spatial-mode related limit for consistent pulsing.
P_{max}	Maximum total operating pump power.
P_{min}	Minimum total pump power required for oscillation (given a stable resonator) - equivalent to P_{th} in the temporal pulse model.
P_o	Pump power for maximum Q-switched pulse consistency in multi-spatial-mode operation.
P_p	Repetition-frequency dependent extra-cavity peak power of a Q-switched pulse.
P_{pmax}	Maximum extra-cavity peak power for a Q-switched pulse.
P_Q	Average Q-switched output power.
P_{Qin}	Intra-cavity average power.
P_s	Minimum pump level needed for resonator stability.
$P_{s'}$	Maximum pump level at which resonator stability is maintained.
P_{th}	Threshold pump power for oscillation - equivalent to P_{min} in the spatial mode and resonator stability model model.
Q	Constant heating rate per unit volume.
R	Laser rod facet curvature (applied to both ends).
R'	Cavity mirror radius of curvature when both are equal.
R_0	Reflectivity at a thin-film interface.
R_1 and R_2	Radius of curvature for the two mirrors that make up a laser resonator.
S	Overall misalignment sensitivity of a two-mirror resonator.

$S(x, t)$	Energy imparted by a laser pulse as a function of thin-film depth x and time t.
S_1	Resonator misalignment sensitivity factor corresponding to the misalignment of mirror 1.
S_2	Resonator misalignment sensitivity factor corresponding to the misalignment of mirror 2.
S_{rod}	Total transversal misalignment sensitivity of the rods in a dual-rod resonator.
T	Temperature.
t	Time.
t'	Time at which an optical pulse reaches maximum irradiance.
$T_{coolant}$	Coolant water temperature.
t_{max}	Finite lifetime of optically thick, critically dense plasma.
t_{min}	Minimum permissible FWHM pulse duration at the optimised output coupling.
t_p	Period between Q-switched pulses.
t_Q	Repetition frequency dependent Q-switched pulse duration.
t_R	Round-trip time of the cavity.
$T_{rod}(0)$	Temperature at the centre of the laser rod.
T_{surf}	Temperature of the barrel surface for the pumped section of the laser rod.
t_T	Single-shot test-pulse duration.
u	Transverse radial displacement from the axis of beam propagation.
u_1 and u_2	Secondary resonator stability parameters.
V	Pumped volume of the rod.
$w(z)$	Beam radius at which the irradiance of the TEM_{00} mode drops to $1/e^2$ of its peak value.
$W(z)$	Radius at which the irradiance of a non-diffraction limited beam drops to $1/e^2$ of its peak value.
w_0	Beam radius at a waist positioned at $z = z_0 = 0$.
W_0	Radius of a non-diffraction limited beam at the waist.
w_a	Gaussian-beam waist radius at an equivalent thin lens for the laser rod (similar to that at the mid-point of the rod).
w_{am}	Minimum achievable fundamental mode size at a resonator lens.
W_{mi}	Second moment multi-spatial-mode beam radius at cavity mirror i.

w_{oi}	Embedded gaussian-beam waist radius.
W_{omax}	Maximum permissible radius for any multi-mode resonator beam waist.
W_P	Largest permissible beam radius at the limiting aperture of a resonator.
w_{Pi}	Embedded gaussian-beam radius at the rod lens principle plane P_i.
W_{Pi}	Multi-mode beam-size produced at the rod lens principle plane P_i.
x	Distance or depth in the x axis (perpendicular to both y and z axes).
x_1	Displacement of the mode axis at the lens with misalignment of mirror 1 by an angle Ψ_1.
x_2	Displacement of the mode axis at the lens with misalignment of mirror 2 by an angle Ψ_2.
y	Distance or depth in the y axis (perpendicular to both x and z).
y_1	Paraxial ray input position.
y_1'	Paraxial ray input angle with respect to the axis of propagation.
y_2	Paraxial ray output position.
y_2'	Paraxial ray output angle with respect to the axis of propagation.
Z	Ratio of the round-trip logarithmic small-signal gain to the parasitic round-trip cavity loss l.
z	Distance or direction of beam propagation (perpendicular to both x and y).
z_0	Beam waist position.
z_l	Distance between the laser rod end support and the nearest load point.
z_R	Gaussian beam Rayleigh range.
α	Absorption coefficient.
$\beta(z)$	Radius of curvature exhibited by the wavefront of a beam.
Γ	Full-width half-maximum duration of the laser pulse.
γ	Population inversion reduction factor due to stimulated emission.
ΔD	Change in refractive power over which resonator stability is maintained in a stability zone.
ΔT_{rod}	Difference in temperate between the surface and centre of the laser rod.
$\zeta(z)$	Gouy phase delay.

η_a	Pump absorption efficiency.
η_{ASE}	Upper-state population efficiency accounting for loss due to ASE = $1/\gamma$.
η_B	Beam volume to gain distribution overlap efficiency in a resonator.
$\eta_{B'}$	Beam volume to gain-distribution overlap efficiency in a power amplifier.
η_c	Pump radiation coupling efficiency.
η_E	Q-switched pulse-energy extraction efficiency.
η_{Eamp}	Efficiency of energy extraction from a power amplifier.
η_h	Fractional heat loading measured under non-oscillating conditions.
$\eta_{h'}$	Change in fractional heat loading between non-oscillating and oscillating conditions.
η_Q	Pulse-repetition-frequency (PRF) related power efficiency.
$\eta_{Q'}$	PRF dependent power extraction efficiency from a power amplifier.
η_s	Stokes shift related efficiency (quantum defect).
η_T	Efficiency by which the pump is transferred to the laser rod.
η_u	Upper-state efficiency.
Θ	Far-field half-angle divergence of non-diffraction limited beam.
θ	Far-field half-angle divergence for a Gaussian beam
Θ_{imax}	Maximum multi-mode half-angle far-field divergence of a resonator beam.
λ	Free-space wavelength.
μ	Thermal coefficient of expansion.
ν	Poisson's ratio.
ξ	Young's modulus.
ρ	Mass density.
ρ_1	Rear cavity mirror reflectivity at the fundamental wavelength.
ρ_2	Output coupling cavity mirror reflectivity at the fundamental wavelength.
ρ_{2opt}	Optimum output coupler reflectivity.
σ	Effective stimulated emission cross-section.
σ_{max}	Maximum circumferential hoop stress.
σ_r	Radial normal stress component.
σ_u	Ultimate tensile strength (fracture limit).

σ_{x0}	Power density variance at a beam waist.
σ_z	Axial normal stress component.
σ_θ	Variance of the angular distribution for a beam leaving the waist.
σ_φ	Tangential normal stress component.
τ_s	Spontaneous emission lifetime.
χ	Spatial beam profile form-factor relative to a uniform, top-hat spatial distribution (where $\chi = 1$).
Ψ_1	Misalignment angle of cavity mirror 1.
Ψ_2	Misalignment angle of cavity mirror 2.
$\Psi_{i10\%}$	Misalignment angle of cavity mirror *i* that causes a 10 % reduction in mode volume within the rod.

ABBREVIATIONS

AMLCD	Active-matrix liquid-crystal displays.
AOM	Acousto-optic modulator.
Ar^+	Argon ion.
ArF	Argon fluoride.
ASE	Amplified spontaneous emission.
CAD	Computer aided design.
CO_2	Carbon dioxide.
CW	Continuous wave.
DFM	Design for manufacturing.
ESA	Excited state absorption.
EUV	Extreme ultraviolet.
FE	Finite element (modelling).
FWHM	Full-width half-maximum.
GB	Grain-boundaries.
HAZ	Heat-affected-zone.
ISO	International Organization for Standardization.
ITO	Indium tin oxide.
LIDT	Laser-induced damage threshold.
LPP	Laser produced plasma.
MOPA	Master-oscillator power-amplifier.
MTTF	Mean time to failure.
MTTR	Mean time to repair.

Nd:YAG	Neodymium-doped yttrium aluminium garnet ($Nd^{3+}:Y_3Al_5O_{12}$).
Nd:YLF	Neodymium-doped lithium yttrium fluoride ($Nd^{3+}:LiYF_4$).
OPD	Optical path-length difference.
PDP	Plasma display panel.
PID	Proportional-integral-derivative controller.
PPK	Pre-pulse kill.
PRF	Pulse repetition frequency.
p-Si	Poly-crystalline silicon.
RF	Radio frequency.
RLP	Rapid laser patterning.
Si	Amorphous silicon.
SLS	Sequential lateral solidification.
Sn	Tin.
SRS	Stimulated Raman scattering.
TEM	Transverse electro-magnetic.
TFT	Thin-film transistor.
TTL	Transistor-transistor logic.
Xe	Xenon.
XeCl	Xenon chloride.
Yb:glass	Ytterbium-doped glass (Yb^{3+}:glass).

Dissemination

1. Industrial Doctorate Centre Annual Conference, 8th August 2007: Academic progress report and poster presentation on “Advanced high-power solid-state laser sources – Design, performance and use in engineering”.
2. Industrial Doctorate Centre Annual Conference, 19th August 2008: Academic progress report and presentation on “Nanosecond-pulse solid-state laser development: Achieving high average and high peak power operation”.
3. Presentation at Photonics West International Conference, LASE 2009 (Solid-State Lasers XVIII: Technology and Devices): “Q-switched Nd:YAG lasers for high average-power and high peak-power operation”.
4. Invited presentation at Photonics West International Conference, LASE 2009 (Solid-State Lasers XVIII: Technology and Devices): “industrial applications of high average power, high peak power nanosecond pulse duration Nd:YAG lasers”. Paper 7193-89.
5. SPIE conference proceeding publication: Mike Poulter, Nick Hay, Ben Fulford, Paul Campton, and Mike Mason, “Q-switched Nd:YAG lasers for high average-power and high peak-power operation”, Solid-State Lasers XVIII: Technology and Devices, Proc. of SPIE Vol. 7193-9, 719309.

6. Industrial Doctorate Centre Annual Conference, 11th August 2009: Academic Progress Report and presentation on “High Average and Peak Power Solid-State Lasers for Industrial Applications”.
7. Presentation to the industrial advisory board to the Institute of Photonics on “The development of high-power, nanosecond-pulse Nd:YAG lasers for industrial applications”, 27th November 2009.
8. Tech-hub seminar at the Institute of Photonics on “The development of high-power, nanosecond-pulse Nd:YAG lasers for industrial applications”, 27th November 2009.
9. Formulation of numerous internal technical reports and updates for dissemination to key customers and suppliers. Monthly update meetings and joint quarterly review meetings held with both academic and industrial supervisors.